Discontinuous Galerkin Time Domain

by

J. Alvarez

A thesis submitted in partial fulfillment for the
degree of Doctor of Philosophy

in the
Facultad de Ciencias
Departamento de Electromagnetismo y Fisica de la Materia

August 2012

Declaration of Authorship

I, AUTHOR NAME, declare that this thesis titled, 'THESIS TITLE' and the work presented in it are my own. I confirm that:

- This work was done wholly or mainly while in candidature for a research degree at this University.

- Where any part of this thesis has previously been submitted for a degree or any other qualification at this University or any other institution, this has been clearly stated.

- Where I have consulted the published work of others, this is always clearly attributed.

- Where I have quoted from the work of others, the source is always given. With the exception of such quotations, this thesis is entirely my own work.

- I have acknowledged all main sources of help.

- Where the thesis is based on work done by myself jointly with others, I have made clear exactly what was done by others and what I have contributed myself.

Signed:

Date:

"Write a funny quote here."

If the quote is taken from someone, their name goes here

UNIVERSIDAD DE GRANADA

Abstract

Facultad de Ciencias
Departamento de Electromagnetismo y Fisica de la Materia

Doctor of Philosophy

by J. Alvarez

The Thesis Abstract is written here (and usually kept to just this page). The page is kept centered vertically so can expand into the blank space above the title too. . .

Acknowledgements

The acknowledgements and the people to thank go here, don't forget to include your project advisor...

Contents

List of Figures

List of Tables

List of Acronyms

ABC   **A**bsorbing **B**oundary **C**ondition

ADE   **A**auxiliary **D**ifferential **E**quation

ADER   **A**rbitrary **DER**ivatives in space and time

BI   **B**oundary **I**ntegral

C   **C**onformal

CAD   **C**omputer-**A**ided **D**esign

CASA   **C**onstrucciones **A**eronauticas **S**ociedad **A**nónima

CCCIE   **C**ombined **C**urrent and **C**harge **I**ntegral **E**quations

CEM   **C**computational **E**lectro**M**agnetics

CFD   **C**omputation **F**luid-**D**ynamics

CG   **C**ontinuous **G**alerkin

CPU   **C**entral **P**rocessing **U**nit

D   **D**imensions

dB   **d**eci**B**el

DG   **D**iscontinuous **G**alerkin

DGTD   **D**iscontinuous **G**alerkin in **T**ime **D**omain

DMCWF   **D**ual-**M**ode **C**ircular **W**aveguide **F**ilter

EADS   **E**uropean **A**eronautic **D**efence and **S**pace company

EM   **E**lectro**M**agnetism

EMC   **E**lectro**M**agnetic **C**ompatibility

EMI   **E**lectro**M**agnetic **I**nterference

FD   **F**requency **D**omain

FDFD   **F**inite **D**ifference in **F**requency **D**omain

FDTD   **F**inite **D**ifference in **T**ime **D**omain

FEM   **F**inite **E**lement **M**ethod

FETD	**F**inite-**E**lement **T**ime-**D**omain
FIT	**F**inite **I**ntegral **T**echnique
FVTD	**F**inite **V**olume in **T**ime **D**omain
GHz	**G**iga**H**ert**z**
GO	**G**eometrical **O**ptics
GPR	**G**ground **P**enetrating **R**adar
GPU	**G**raphics **P**rocessing **U**nit
GTD	**G**eometrical **T**heory of **D**iffraction
HIRF	**H**igh **I**ntensity **R**adiated **F**ields
IBC	**I**mpedance **B**oundary **C**ondition
LDG	**L**ocal **D**iscontinuous **G**alerkin
LF	**L**eap-**F**rog
LFDG	**L**eap-**F**rog **D**iscontinuous **G**alerkin
LLSF	**L**ow **L**evel **S**wept **F**ield
LO	**L**ow **O**bservability
LSRK	**L**ow-**S**torage **R**unge-**K**utta
LTS	**L**local **T**ime **S**tepping
MHz	**M**ega**H**ert**z**
MLFMM	**M**ultilevel **F**ast Multipole Method
MLFMA	**M**ultilevel **F**ast Multipole **A**lgorithm
MoM	**M**ethod **o**f **M**oments
MPI	**M**essage **P**assing **I**nterface
ODE	**O**rdinary **D**ifferential **E**quation
OMP	**O**pen Multi-**P**rocessing
O2	**O**rder **2**
PBC	**P**eriodic **B**oundary **C**ondition
PEC	**P**erfect **E**lectric **C**onductor
PMC	**P**erfect **M**agnetic **C**onductor
PML	**P**erfectly **M**atched **L**ayer
PO	**P**hysical **O**ptics
PTD	**P**hysical **T**heory of **D**iffraction
RADAR	**RA**dio Detection **A**nd **R**anging
RMA	**R**adar **A**bsorber **M**aterial

RCS	**R**adar **C**ross-**S**ection
RK	**R**unge-**K**utta
RK4	4th-order **R**unge-**K**utta
RKDG	**R**unge-**K**utta **D**iscontinuous **G**alerkin
SFZ	**S**cattered-**F**ield **Z**one
SM	**S**ilver-**M**üller
SMA	**S**ub**M**iniature version **A**
SSP	**S**trong **S**tability **P**reserving
TD	**T**ime **D**omain
TEM	**T**ransverse **E**lectro**M**agnetic
TFZ	**T**otal-**F**ield **Z**one
TLM	**T**ransmission **L**ine **M**atrix
TWTD	**T**hin **W**ire **T**ime **D**omain
UHF	**U**ltra **H**igh **F**requency
UPML	**U**niaxial **P**erfectly **M**atched **L**ayer
UTD	**U**niform **G**eometrical **T**heory of **D**iffraction
VHF	**V**ery **H**igh **F**requency
VSWR	**V**oltage **S**tanding-**W**ave **R**atio

List of Symbols

x, X Scalar

$\boldsymbol{x}$, $\boldsymbol{X}$ Vector

A_x, $\boldsymbol{A}|_x$ Component x of the vector A

$\hat{\mathbf{x}}$ Unit vector

$\hat{\mathbf{n}}$ Outward-pointing normal vector of a referred surface or face of a tetrahedron

$\mathbb{M}$ Matrix

$\bar{\bar{R}}$ Tensor

$\tilde{X}$ Numerical approximation of X

$\mathcal{T}_m$ Volume of the mth element

$\partial\mathcal{T}_m$ Boundaries of the mth element

$\mathbb{R}^3$ Three space dimension

J Jacobian matrix

$\boldsymbol{\phi}_i^m$ Vector-basis function of index i, defined in the element m

$\frac{d}{dx}$, d_x Differential operator with respect to variable x

$\frac{\partial}{\partial x}$, ∂_x Partial differential operator with respect to variable x

$\nabla \times \boldsymbol{X}$ Curl operation on a vector $\boldsymbol{X}$

∇X Gradient operation on a variable X

$\langle \boldsymbol{u}, \boldsymbol{v} \rangle_{\mathcal{T}_m}$ Inner product in the volume $\mathcal{T}_m$

$\|\boldsymbol{u}\|_{\mathcal{T}_m}^2$ Norm in the volume $\mathcal{T}_m$

$\langle \boldsymbol{u}, \boldsymbol{v} \rangle_{\partial\mathcal{T}_m}$ Inner product in the surface $\partial\mathcal{T}_m$

$\boldsymbol{B}$ Magnetic flux density (Wb m^{-1})

$\boldsymbol{D}$ Electric flux density (C m^{-2})

$\boldsymbol{E}$ Electric field intensity (V m^{-1})

$\boldsymbol{H}$	Magnetic field intensity (A m^{-1})
$\boldsymbol{J}$	Polarization current (A m^{-2})
$\boldsymbol{M}$	magnetization current (V m^{-2})
$\boldsymbol{J}_{imp}$	Impressed electric current density (A m^{-2})
$\boldsymbol{J}_s$	Surface electric current density (A m^{-1})
$\boldsymbol{M}_s$	Surface magnetic current density (V m^{-1})
μ	Magnetic permeability (H m^{-1})
μ_0	Magnetic permeability of vacuum (4π 10^{-7} H m^{-1})
μ_r	Relative magnetic permeability
ε	Electric permittivity (F m^{-1})
ε_0	Electric permittivity of vacuum (8.854187805806633 10^{-12} F m^{-1})
ε_r	Relative electric permittivity
c	Speed of a electromagnetic wave (m s^{-1})
c_0	Speed of a electromagnetic in vacuum (299792458.2 m s^{-1})
σ_e	Electric conductivity (S m^{-1})
σ_m	Magnetic conductivity (H s^{-1} m^{-1})

For/Dedicated to/To my...

Chapter 1

Introduction and Previous Work

This thesis is the product of research conducted in the Department of Electromagnetism and Matter Physics at the University of Granada, and EMI/EMC Department at Cassidian, EADS-CASA, both in Spain. The research of this thesis focuses on developing efficient and accurate time-domain electromagnetic computational techniques and their application to real and practical engineering problems. A brief overview of the most relevant methods, from this standpoint, is provided in this introductory chapter. In addition, the reasons, alternatives, and capabilities of the specific technique chosen for the current research are discussed, together with the current state of the art. A detail description of the proposed technique is left for the subsequent chapters.

1.1   Overview of Computational Electromagnetics

Prior to the 1960s, the computation of electromagnetic (EM) fields was more confined to analytical methods involving closed-form expressions or the solving-by-series approach. However, with the advent of powerful computers and the development of sophisticated algorithms, the art of computational electromagnetics (CEM), as in many other scientific disciplines, have enabled exponential growth during the last five decades. Nevertheless, the EM community has suffered without a unique and suitable method, able to solve all real-world EM problems, such as radiation, scattering, coupling, or waveguiding. Furthermore, the wide spectrum of engineering applications of CEM, design and modelling of antenna and microwave devices, for RADAR or communication systems, electromagnetic compatibility (EMC) studies, such as High Intensity Radiating Fields (HIRF), cross-talk or lightning strikes against large structures, nanophotonic devices, medical imaging, among other applications, makes the expertise of the user crucial in choosing
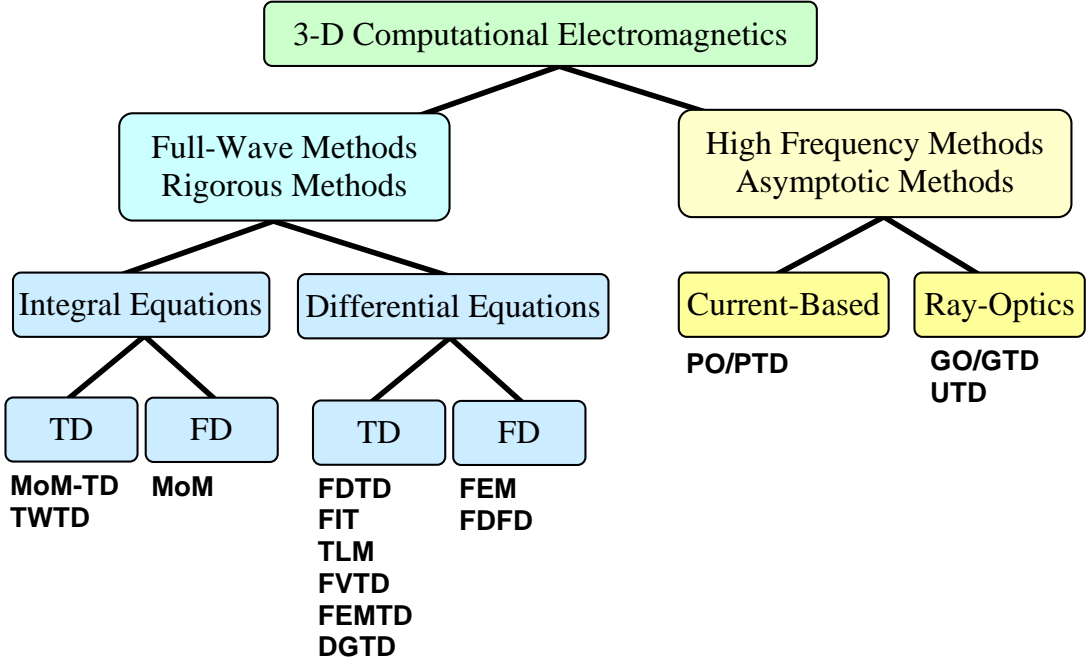
FIGURE 1.1: Classification of purely numerical 3-D computational electromagnetic methods.

the most appropriate method for a given problem. Hence, many different purely numerical 3-D CEM techniques have been proposed, a conceptual classification of the most relevant appears in figure 1.1.

Although many different numerical EM methods and classifications can be found in the literature, we consider those of figure 1.1 the most relevant, which can be classified on three different levels. At the highest level, we distinguish between asymptotic and full-wave methods. The former permit numerical solutions with low computational cost in the frequency domain (FD), converging to the physical ones as frequency increases. The full-wave methods, however, rigorously solve Maxwell's equations and the sources of differences between numerical and physical solutions come from discretization and numerical errors, finding convergence when those errors tend to zero. The asymptotic methods are based on simplified versions of Maxwell's equations or EM scattering models, such as Physical Optics (PO), which locally applies the equivalent principle, computing an approximated solution regardless of other effects, or considered in a simplified way, as in Physical Theory of Diffraction (PTD), or methods based on Ray-Optics, such as geometrical optics (GO) extended to Geometric Theory of Diffraction (GTD) methods, and Uniform Theory of Diffraction (UTD).

Full-wave methods can be classified in two ways: by the form (integral or differential) in which Maxwell's equations are solved, or according to the domain (frequency or time)

where the equations are solved. One of the main advantages of methods based on the integral form is that only the surfaces, interfaces of the materials where boundary conditions must be fulfilled, e.g. as Method of Moments (MoM), and/or lines, e.g. Thin-Wire Time-Domain (TWTD) method, have to be discretized, reducing the number of unknowns compared to volumetric methods. The accuracy of these methods, which make use of the Green functions, is usually very high. The main drawbacks appear when dealing with complex materials, composites, anisotropic, etc., where the applicability of the method becomes complex, and also solving electrically large problems, since the condition number of the resulting linear system grows with the number of unknowns. Methods based on differential forms include those based on fully structured meshes, such as Finite Differences in Time or Frequency Domain (FDTD, FDFD), Finite Integral Technique (FIT) or Transmission-Line-Matrix (TLM), or those based on unstructured meshes, such as Finite Volume (FV), Finite Element (FE) or Discontinuous Galerkin (DG) methods. The interest of FE and DG methods, compared to FV, is the possibility of combining different orders of the basis functions, achieving faster convergence rates. The main advantage of volumetric methods is its versatility to deal with any EM problems, limited only by the computational resources.

Typical frequency domain (FD) methods, such as MoM or FEM, are able to deal with large structures with electrically small details, but become computationally inefficient in the computation of wideband frequency responses, since one frequency needs one complete simulation requiring the resolution of a linear system. Time domain (TD) methods are an attractive alternative in such contexts. However, TD methods based on structured meshes, such as FDTD, FIT and TLM, imposes significant constraints on the geometrical discretization of complex objects, and on the accuracy and convergence of the methods. To overcome these limitations, finite-element time-domain (FETD) methods constitute useful alternatives. Nevertheless, classical FETD methods are still computationally unaffordable for electrically large problems. In this work, alternatives based on Discontinuous Galerkin Time Domain (DGTD) methods are proposed. DGTD approaches have most of the advantages of FDTD, FIT and TLM, providing a spatially explicit algorithm, simplicity, easy parallelization, and memory and computational cost, growing only linearly with the number of elements. At the same time, DGTD schemes retain most of the benefits of FEM: adaptability of the unstructured meshes and spatial super-convergence.

1.2 Discontinuous Galerkin Time Domain Survey

In this section, we give a brief overview of the most relevant finite element time domain methods (FETD). Then, a survey of the specific FETD technique, Discontinuous Galerkin Time Domain method, discussed in this work, is presented.

1.2.1 Background

During the 1980s, advances in meshing technology together with the finite element method (FEM) made it possible to solve Maxwell's equations in complex geometries by using an unstructured mesh based on tetrahedral tessellation. In this kind of mesh, complex objects, having arbitrary curvatures and intricate details, are accurately discretized, which is a major change from cube-based space partitioning of the previous methods, FDTD which appeared in 1966 [1], transmission-line-matrix (TLM) method in 1971 [2] and finite integral technique (FIT) proposed in 1977 [3]. This novel approach was initially applied to two-dimension (2-D) or axisymmetric problems [4, 5, 6, 7] and later to three-dimension (3-D) [8, 9, 10], but always to solve Maxwell's equation in the frequency-domain (FD). Thus, the application of FEM in FD has been to calculate S-parameters, radiation patterns, RCS, and so on, and are ideal methods for low-frequency problems, highly resonant structures, and eigenmode computations. However, time-domain (TD) methods, as FDTD, FIT and TLM, are advantageous to deal with transient fields effects and arbitrary time-signal excitation, such as lightning strikes, or broadband frequency domain simulations, such as EMC coupling estimation or wideband antennas, or with non-linear behavior of materials or components, where TD methods offer more direct and efficient approach.

During the 1990s, a variety of time-domain FEM schemes were proposed [11], these methods being based on both; Maxwell's curl-curl equation (Helmholtz equation), and the hyperbolic system of curl equations (Ampere's and Faraday's Laws). A detailed review of the different approaches appears in Chapter 2, briefly summarized below.

A second-order vector-wave (Helmholtz) equation is the one typically solved in frequency domain methods, and can be easily posed in the time domain. In these kinds of schemes, a single field, electric or magnetic, has to be computed. The major drawback is that a linear system of equations has to be solved at each time-step. To reduce the number of time-steps, an implicit time integration scheme, e.g. Newmark-beta, can be used, but the resulting system matrix becomes quite ill-conditioned. This family of methods has been widely studied by Lynch, Mur, Lee, Gedney, Carpes, Jin et al., [12, 13, 14, 15, 16, 17, 18, 19, 20, 21, 22].

The system composed of the first-order coupled Maxwell curl equations can be formulated considering electric field intensity $\boldsymbol{E}$ and magnetic flux density $\boldsymbol{B}$, or electric field intensity $\boldsymbol{E}$ and magnetic field intensity $\boldsymbol{H}$. In the case of E-B formulation, different expansion functions are used for the $\boldsymbol{E}$ and $\boldsymbol{B}$ fields, offering certain advantages with respect to the single-field formulation, such as avoiding spurious solutions or the fact that the first-order time derivatives allow the use of conventional Leap-Frog time-integration method, which avoids maintaining in memory previous states. The main drawback, again, is the need to solve a sparse linear system at each time-step, and its computational cost is therefore comparable to the single-field scheme. A worthwhile proposal was reported by Rieben et al. in [23]. The major developments of the E-B methods are currently being carried out by Texeira et al. [24, 25, 26, 27].

If E-H formulation is used, two different family methods can be identified by considering how the continuity of the tangential components of $\boldsymbol{E}$ and $\boldsymbol{H}$ fields are treated. Hence, if the continuity of the tangential components is assured in a strong way, as in the previous FEM methods, we have Continuous Galerkin (CG) methods. In this case, the resulting schemes are equivalent to the single-field ones, with the same limitations that both single-field and E-B formulations have, a linear system will be necessary to be solved each time-step. In case tangential components are not enforced to be continuous between elements, jumps are allowed, and we find Discontinuous Galerkin (DG) methods. Instead, continuous numerical fluxes are defined at the interface in order to connect the solution between them in the manner used in Finite Volume Time Domain (FVTD) methods, which is the main idea of Discontinuous Galerkin Time-Domain (DGTD) methods. In this case, the limitation concerning the resolution of a complete linear system is overcome, which is the main motivation for developing of numerical methods based on DG spatial discretization.

The main advantage of DGTD over FVTD is its higher order in space, while the advantage over other FEM methods in TD resides in the fact that the matrix of the linear system to be solved becomes diagonal and DGTD needs only the inversion of M square matrices of $Q \times Q$ elements (with M the number of elements and Q the number of basis functions per element), while larger matrices ($\simeq MQ \times MQ$) are involved in FEM in TD.

DGTD can be seen as a generalization of FVTD and also FDTD methods, [28]. Thus, many of the ideas already developed in FVTD and FDTD can be adapted to DGTD.

Since the beginning of this century, the number of scientific publications on DGTD methods applied to CEM have been growing linearly, and today this is becoming an active research area. The efforts on the application of DGTD methods to solve Maxwell's equations, have followed two main different directions:

- Analysis of the different alternatives or improvements offered by DGTD technique, and analysis of the method itself.

- Capabilities and application of the method. To adapt previous capabilities from FDTD or FVTD, or develop new ones to prove the method in real applications.

1.2.2 Analysis, Improvements and Alternatives of the Discontinuous Galerkin Methods

Discontinuous Galerkin (DG) techniques have been broadly used in other disciplines. The analysis, improvements, and alternatives of DG methods can be found mainly in the mathematics community. Most authors refer in this subsection as belonging to this community.

The first DG method was introduced in 1973 by Reed and Hill [29] in the framework of neutron transport. Lesaint and Raviart [30] were the first to place this method on a firm mathematical basis. Since then, there has been an active development of DG methods for hyperbolic and nearly hyperbolic problems. In the case of linear equations, the nature of the method has been rigorously analyzed by Johnson and Pitkäranta [31], Richter [32], Peterson [33], and Bey and Oden [34]. For nonlinear equations, a major development was made by Cockburn, Shu and collaborators, in a series of papers [35, 36, 37, 38, 39], in which they established a framework for easily solving nonlinear time-dependent hyperbolic conservation laws using explicit, nonlinearly stable high-order Runge-Kutta time discretizations (RKDG). Thus, in 1997, Bassi and Rebay [40] introduced a DG method for the Navier-Stokes equations, in computation fluid-dynamics (CFD), and in 1998, Cockburn and Shu [41] introduced the so-called Local Discontinuous Galerkin (LDG) methods, extending their approach to deal with time-dependent scalar advection-diffusion equation, and suggested how the approach could be applied to the Navier-Stokes equations, which generalize the original DG method of Bassi and Rebay. Around the same time, Oden and Bauman [42] introduced another DG method for diffusion problems and many other authors, since then, started to apply DG in CFD.

Lowrie et al. [43, 44] considered the space-time Discontinuous Galerkin, which involves discontinuous elements in both time and space. In [44] a Fourier analysis of the scheme was performed which shows a "super-convergence" property; i.e., the evolution error is $O\left(h^{2p+1}\right)$ if the order of the polynomial space used is p while h is a measure for the size of elements. Nevertheless, the method requires excessive resources to be useful for practical applications. That property prompted Hu et al. to apply DG methods to advection and linearized Euler equations, in computational acoustics, in [45] and continue the analysis of DG applied to wave-propagation problems in [46, 47]. These researchers studied the

dissipation, dispersion, and anisotropy errors introduced by the space discretization in the wave-propagation problem. The results of these analyses can be easily extended to the electromagnetic case.

Since 2002, DG methods have begun to find their way into CEM. Kopriva et al. [48], Perugia and Schötzau [49], and also Houston [50], or even Cockburn, Li and Shu [51] proposed and tested methods in 2-D, applied to simple numerical cases, where hp-convergence of the semi-discrete spatial schemes were proved (see Chapter 3). However, it was Hesthaven and Warburton in [52] who established the basis for lengthy analyses that were performed before. Their proposal was predicated on nodal basis function, upwind flux evaluation (see Chapter 3 for a detailed analysis of different alternatives in the evaluation of the numerical fluxes) and Runge-Kutta (RK) time-integration scheme. These authors analyzed their proposal in [53] from the eigenvalue problem perspective, finding results similar to those of Hu for the advection equation. The important point was that non-physical solutions (spurious modes) appear with a centered flux-evaluation scheme. These spurious modes are dissipative in the case that upwind flux or penalty terms were considered, as are typically used in DG methods for other applications (a detailed analysis appears in Chapter 3). Warburton and Embree give more details on this topic in [54], and Ainsworth et al. in [55, 56] and Grote et al. in [57] investigated interior penalty (IP) properties considering the second-order wave equation.

Some "super-convergence" analyses were performed (this topic has also been addressed during this work in Chapters 3 and 4), considering time-integration schemes by Chen, Cockburn, and Reitich in [58] and Sármány et al. in [59]. Chen proposed the so-called m^{th}-order, m-stage strong stability preserving Runge-Kutta (SSP-RK) scheme for the time marching. The idea is relating the time integration order to the spatial order, in this case "super-convergence" is assured. Sármány made an in-depth study of the dispersion and dissipation error of this scheme in [59].

A 3-D scheme based on vector-basis functions (see Chapter 2), tetrahedral elements, non-dissipative centered flux evaluation (see Chapter 3) and second-order Leap-Frog scheme for advancing in time (see Chapter 4), was introduced and analyzed by Fezoui et al. in [60]. Cohen et al. in [61] used a similar scheme but with non-structured hexahedral meshes in order to save memory and also introduced a local time-stepping scheme for Leap-Frog time integration. Cohen and Duruflé in [62], and later Montseny et al. in [63] followed the same approach, but they introduced dissipative terms in order to improve accuracy, reducing the spurious modes present in centered flux schemes. Non-conforming locally refined grids were introduced in this scheme by Canouet et al. in [64] and Fahs et al. thoroughly analyzed this technique in 2-D and 3-D in [65, 66, 67], which can be

identified as the traditional sub-gridding of the FDTD method. Also Fahs analyzed the use of curvilinear elements in 2-D in [68].

Concerning time integration, Runge-Kutta (RK) and Leap-Frog (LF) are the most commonly used schemes (see Chapter 4 for details of these time-integration algorithms), although others have been proposed and analyzed. Two main issues should be borne in mind: (i) once arbitrary high-order accuracy in space is provided by DG methods in a natural way, arbitrary high-order accuracy in time is required, and (ii), local refinement of unstructured mesh can lead to a very restrictive and diverse time-step in order to preserve the stability of explicit time-integration schemes, clearly fully implicit schemes are avoided due to the computational cost.

RK methods have been traditionally used in such other disciplines as CFD, so those can be extended only to CEM. Hesthaven and Warburton made a detailed analysis of DGTD with RK schemes in their book [69]. Diehl et al. in [70] compared different Multi-Step Low-Storage Runge-Kutta methods of different orders. Chen, as mentioned above, introduced the SSP-RK scheme with the idea of attaining high-order accuracy in time, as well as in space. The solution for the second point with RK methods is the use of local time stepping (LTS) strategies (see Chapter 4 for the description of the LTS algorithm proposed in this work). LTS, in the context of DG schemes on unstructured meshes, was introduced firstly by Flaherty et al. [71]. Dumbser et al. [72] introduced the arbitrary high-order scheme using derivatives for DG (ADER-DG). Making use of ADER-DG, LTS can be implemented with RK methods, [69]. As an alternative to RK methods, ADER scheme is also used for the time integration, instead of RK, which was proposed by Taube et al. in [73], this method provides high-order accuracy in time and advance in a single step, so it does not need intermediate stages as RK schemes do.

In the case of LF methods, high-order in time, referred to as LF_N, was developed by Fahs in [74]. Concerning the latter issue, there are basically two directions to cure this efficiency problem. The first one consists of using a LTS strategy combined to an explicit time-integration scheme, while the second approach relies on the use of an implicit or a hybrid explicit-implicit time-integration scheme. Some LTS strategies have been proposed and tested by Canouet et al. in [64] and Montseny et al. in [63]. An implicit method was applied to DGTD by Catella et al. in [75], which used the Crank-Nicolson time-integration scheme. Afterwards, Dolean et al. in [76, 77] applied the same approach but locally, proposing a hybrid explicit-implicit time-integration scheme. Another possibility, quite similar to LF, known as symplectic time schemes originally developed for the numerical time integration of dynamical Hamiltonian systems (molecular dynamics, astronomy, etc. (Sanz-Serna et al., [78])), were introduced to CEM and applied to the

DGTD method by Piperno, [79, 80]. Piperno developed both solutions, a locally implicit symplectic scheme and a multi-scale fully-explicit symplectic scheme.

Finally, structured and unstructured mesh-domain decomposition has been explored by Davies et al. in [81] using triangles and Cartesian elements in 2-D. This idea has also been tested in 3-D, in the finite volume time domain (FVTD) context, hybridized with FDTD in [82] by Edelvik and Ledfelt, splitting the geometry into regions of hexahedral and tetrahedral elements, geometrically coupling all these regions with pyramidal elements. A hybrid approach DGTD/FDTD was also discussed by Garcia et al. in [28].

1.2.3 Capabilities and Applications of Discontinuous Galerkin Time Domain Methods

The extension of ideas already developed for finite volume methods (FVTD), which can be seen as an 0th order DGTD, and finite differences (FDTD), has allowed the vigorous development of DGTD during the last 10 years, and its application to the analysis of numerous electromagnetic problems.

Absorbing boundary condition

How to truncate space to deal with open/radiation problems or port terminations is a key point of all TD methods. Many techniques have been studied in depth in the FDTD context, applied to FVTD and can be straightforwardly extended to DGTD. Firstly, Mohammadian, Shankar and Hall in [83, 84] proposed the simplest absorbing boundary condition (ABC) in the FVTD context, which simply set the incoming flux to zero, equivalent to a first-order Silver-Müller ABC (SM-ABC). Kabakian in 2004, with Shankar and Hall, [85], extended this idea to DGTD and applied the method to antenna and scattering problems. The very well-known truncation technique, perfectly matched layer (PML), widely used in FDTD, were introduced to DGTD by Xiao in 2005, [86], based on Cartesian coordinates. The uniaxial PML (UPML) family has been widely studied in the FDTD, [87, 88, 89, 90], but with no real application in that context apart from Cartesian coordinates, but these techniques are very appropriate to FVTD and DGTD. The objective is to have a conformal PML layer in order to reduce the computational domain. Thus, they have been successfully tested in FVTD by Sankaran et al. in [91, 92, 93], and also used together by the same authors with SM-ABC with non-additional computational cost. Dosopoulos et al. in [94] formulated UPML in DGTD context for any conformal PML layer. Other implementations of UPML, based on Cartesian coordinates, are, Lu et al. in [95] and Niegemann et al. in [96], in 2-D, and Gedney et al. in [97] in 3-D with an extension to the so-called complex-frequency shifted PML in [98]. A noteworthy analysis performed by Niegemann et al. of their

2-D version appears in [70]. The typical implementation, in all cases, is based on the auxiliary differential equation (ADE) method (see Chapter 3).

Materials and sub-cell models

In 2004, Lu et al. [95], used the auxiliary differential equation (ADE) method, to handle material-dispersion properties in 2-D. Same authors in [99] applied the method to the ground-penetrating RADAR (GPR) in dispersive media and the same approach is used in [96, 100] by Stannigel and Niegemann et al. to study nano-photonic systems and metallic nanostructures, also in 2-D. König in [101] developed the formulation for the 2-D case for the anisotropic material case (see Chapter 3 for a 3-D general formulation). Thin-layer sub-cell models can be naturally modelled in FVTD and, therefore, in DGTD. Mohammadian et al. in [84] introduced resistive sheets and impedance surface models in FVTD. Following the same idea, Pebernet et al. in [102] proposed a low-frequency resistive model for thin composite materials in DGTD. Recently, Chun et al. in [103, 104] developed high-order accurate thin-layer approximations for DGTD for general metal-backed coatings and thin transmission layers. Concerning thin-wire sub-cell model, Pebernet et al. in [102], and very recently Gödel in [105], introduced the traditional approximation widely used in FDTD to DGTD methods. Dosopoulos et al. in [106] developed models for lumped elements.

High performance computing

DGTD method leads to a locally implicit, globally explicit difference operator that provides an efficient high-order accurate time-dependent solution. This fact makes algorithms based on DGTD methods ideal for their implementation in highly parallel environments. Bernacki et al. in [107, 108] showed a parallel implementation based on mesh partitioning and message passing, demonstrating good parallel speedup. Klöckner et al. in [109] implemented a DG method to run on off-the-shelf massively parallel graphics processors (GPUs). Dosopoulos et al. in [94] showed the efficiency of the method, solving electrically large electromagnetic problems as a complete aircraft. In appendix A the algorithms implemented during this work are described considering high performance computing (HPC) concepts, and tested in Chapter 5 with large electromagnetic problems.

Real applications

With all the above features, many electromagnetic (EM) problems have been addressed by DGTD methods (see Chapter 5 for the applications and validations carried out during this work). In 2004, Kabakian et al. [85] used DGTD to deal with antenna and RADAR cross-section (RCS) EM problems. In 2005, Ji et al. studied 2-D Waveguide-Coupled Microring Resonators in [110], and Lu et al. in [99] applied the method to ground-penetrating RADAR. In both cases, high-order accuracy is required so DGTD

proved superior to the traditional FDTD. Chauvière et al. in 2006 [111], discussed computationally efficient ways of accounting for the impact of uncertainty, e.g., lack of detailed knowledge about sources, materials, shapes, etc., in computational time-domain electromagnetics, he used the DGTD method to deal with this topic, and Shi et al. in [112] simulated left-hand medium in DGTD. Again, Ji et al. in 2007 [113], studied the cross sections of coupled nanowires. In 2008, Pebernet et al. [102] applied the DGTD method to electromagnetic compatibility (EMC) problems. In 2009, Niegemann, König, Stannigel and Busch [96, 100] used DGTD method to study nano-photonic systems and metallic nanostructures. In 2010, Songoro et al. reviewed the main ideas of the DGTD method in [114]. Finally, at the beginning of 2011, ANSYS released the first commercial software based fully on the DGTD method.

1.3 Motivation

The main contribution of this work is the development, analysis, implementation, and application of a Discontinuous Galerkin formulation to which the Leap-Frog time-integration scheme has been applied. The method uses arbitrary order vector-basis functions and is applied to unstructured meshes based on curvilinear tetrahedra. The simplicity of the time-integration method allows the application of an efficient Local Time Stepping (LTS) strategy. The generality and flexibility of the resulting method allow its application in a wide variety of electromagnetic problems such as microwave devices, antenna modelling, RADAR cross-section estimation, electromagnetic coupling, etc.. This technique has been implemented to be executed in modern and powerful parallel computers, providing good scalability performances. The capability of dealing efficiently with large differences in the element size, because of the LTS, maintaining an accuracy level throughout the computational domain, selecting different orders of the basis functions in each element, makes the Leap-Frog Discontinuous Galerkin (LFDG) a promising method, which combines the advantages of Time Domain and Finite Element methods. Moreover, the limitations of the LFDG method have also been assessed, opening new paths and broadening current knowledge in computational electromagnetism.

The finite-element time-domain method in developed during this thesis has been implemented in a Fortran code called SEMBA. This code is a fully parallelized (OMP-MPI) computational tool that has been successfully applied to the above-mentioned kinds of problems. The resulting tool fills a technological gap in computational electromagnetics, overcoming some limitations of the traditional time-domain methods (FDTD, TLM or

FIT). In particular, the stair-casing problem, which introduces limitation in the geometrical discretization and anisotropic errors, and the poor convergence rate of the spatial discretization of the electromagnetic fields.

1.4 Chapter Organization

The chapters in this thesis are organized as follows.

Chapter 2 briefly reviews the fundamentals of the finite element methods (FEM) for its application to time domain (TD) schemes. The basis for the implementation of a FETD method are drawn, considering the use vector-basis functions. The most relevant FETD methods are also reviewed.

Chapter 3 presents the proposed spatial discretization scheme, which is based on the Discontinuous Galerkin (DG) method. The semi-discrete form is formulated in a general framework, which unifies different flux-evaluation schemes successfully applied to DG methods. The main electromagnetic capabilities, which have been developed for this method, are described, such as boundary conditions treatment, anisotropic materials and absorbing boundary conditions (ABC); the so-called first-order Silver-Müller ABC and the conformal uniaxial perfectly matched layer (C-UPML). The spatial semi-discrete scheme is studied, analyzing numerical dispersion and dissipation, spuriousness and convergence.

In Chapter 4, the temporal integration scheme is applied to the semi-discrete DG formulation. The Leap-Frog Discontinuous Galerkin (LFDG) algorithm and the proposed local time stepping (LTS) strategy are described. Following a similar approach to that used for the semi-discrete scheme, the LFDG algorithm is studied, considering topics such as stability, spuriousness and global convergence of the method. A final assessment of the computational cost vs. accuracy is performed, and compared to the well-known FDTD method.

Chapter 5 validates the LFDG method with microwave filters, antennas, and scattering electromagnetic problems, comparing the results with measurements and other numerical techniques. It also explains some real applications of the LFDG method. Some important properties of the method are shown, such as robustness, accuracy, stability, versatility, efficiency, scalability, and accuracy.

Chapter 6 summarizes the main conclusions of this thesis and the futures lines of research and development.

Appendix A offers a description of the simulation tool SEMBA, and, finally, some information about the author of this thesis, a list of publications, and his curriculum vitae.

Chapter 2

Finite-Element Time-Domain Methods in Computational Electromagnetics

Finite element methods (FEM), to solve general electromagnetic problems, have been traditionally used in the frequency domain. Today, modern computation and memory resources enable FEM to be applied to real problems in the time domain. Finite-element time-domain (FETD) methods offer some major advantages over the classical approaches to time domain computation in CEM; FDTD, FIT and TLM. Firstly, the use of unstructured grids offers superior versatility in geometry discrimination, and permits the application of mesh refinement (h-refinement) to increase and control accuracy. Secondly, the Faedo-Galerkin procedure, used to develop the weak statement [11], provides a natural way to deal with continuity conditions at material interfaces, material properties such as anisotropy, different sources, and so on. Finally, the use of Galerkin formulation provides a huge variety of different choices, related to basis functions (p-refinement), including the use of different finite elements in the same mesh (e.g. tetrahedra, pyramids and hexahedra) or non-conforming meshes.

The main disadvantages compared to FDTD (or FIT and TLM) are mainly operative features. The increment in complexity of the algorithms makes it more difficult to apply some computational acceleration techniques, such as vectorization, cache management, or parallelization, which are very effective in FDTD. In the case of analyzing large and complex geometries, such as an aircraft, the generation of meshes requires more simplified geometry for finite element (FE) than finite difference (FD). Thus, the defeaturing or geometrical cleaning process, prior to the mesh generation, is much more difficult for FE, making the simulation setup more time consuming. Once the cell size, related to

the accuracy and the minimum wavelength analyzed in the problem, is chosen, a FD mesher parses out what is electrically irrelevant, compared to the cell size, and naturally simplifies the geometry. However, a FEM mesher painfully tries to resolve every detail, even irrelevant ones, from an electrical standpoint.

In this chapter, we lay the basis to deal with 3-D Maxwell equations in the time domain making use of FE methods. Then, the most relevant FETD approaches for electromagnetic modelling are reviewed.

2.1 Space Discretization

The numerical representation of a domain Ω under analysis by idealized elements determines how well that volume can be approximated (curvature, location, interfaces, etc.) with the materials and different objects inside. Any numerical analysis is limited by the geometrical discretization.

One objective of this study is to use of explicit schemes for the time integration. The maximum time-step in a particular element, imposed by the Courant stability condition, is restrained by its electrical size, and on the order of the basis functions employed in that particular element. The material of adjacent elements, boundary conditions on its faces, aspect-ratio, and curvature, also influence the stability condition. This means that when small elements are needed to mesh the geometry, the Courant condition may result in an oversampling in time, which would lead to lengthy computational times.

Scalar mappings to defined curved shapes are widely used in connection with the finite element solution of differential equations [115, 116, 117, 118, 119]. In this study, unstructured conforming meshes based on tetrahedral elements are used for the spatial discretization of the geometries. Hence, each of the four faces of a tetrahedron is the face of only one other tetrahedron. Non-conforming meshes have been used in Discontinuous Galerkin methods for more flexibility in the discretization of complex domains or heterogeneous media, a detail description of these approaches appears in [64, 65, 66, 67].

With the application of scalar mapping, the local coordinate system ($L1$, $L2$, $L3$, $L4$, with $L_1 + L_2 + L_3 + L_4 = 1$) is mapped to the global coordinate system (x, y, z), making use of Lagrangian expansion functions. In tetrahedra the reference element has the following vertexes: $V_1 \equiv (0,0,0)$, $V_2 \equiv (1,0,0)$, $V_3 \equiv (0,1,0)$, $V_4 \equiv (0,0,1)$. For the straight tetrahedron, the geometric transformation needs four first-order Lagrange polynomials. If the tetrahedron is curved, the mapping from reference to real elements makes use of Lagrange polynomials of higher orders. Higher-order elements provide better accuracy and permit larger elements.

The mapping expressions are the following:

$$x = \sum_{i=1}^{N_n} x_i B_i\left(L_1, L_2, L_3, L_4\right), \ y = \sum_{i=1}^{N_n} y_i B_i\left(L_1, L_2, L_3, L_4\right), \ z = \sum_{i=1}^{N_n} z_i B_i\left(L_1, L_2, L_3, L_4\right)$$

(2.1)

where $(x_i, \ y_i, \ z_i)$ are called the node coordinates of the real tetrahedron and N_n the number of Lagrange functions (4 for first order, 10 for second order, 20 for third order, ...) [115].
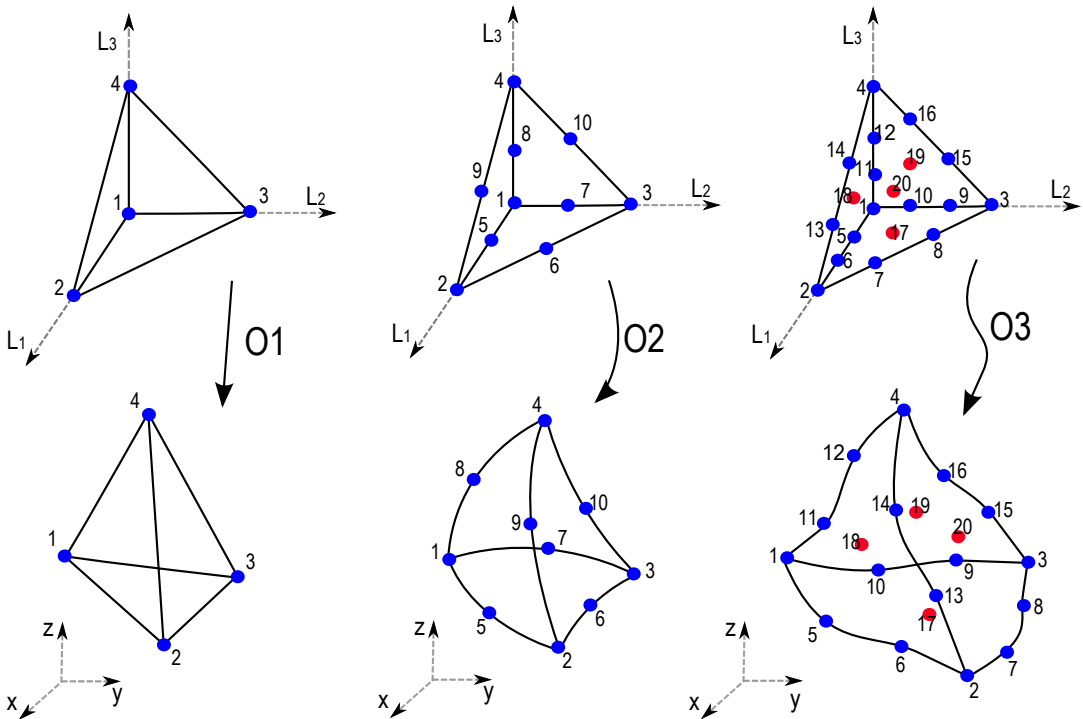
FIGURE 2.1: Mapping from the reference tetrahedra to the real elements for first (O1), second (O2) and third (O3) orders.

It is important to note that same expressions can be used for the mapping from the reference triangle to each curved face of the tetrahedron; just one of the four local tetrahedron coordinate will be zero, depending on the face.

The specific expressions for the tetrahedral element in local coordinates for the bi-quadratic mapping are:

$$
\begin{aligned}
B_1 &= \left(2L_1 - 1\right) L_1 & B_6 &= 4L_2 L_3 \\
B_2 &= \left(2L_2 - 1\right) L_2 & B_7 &= 4L_1 L_3 \\
B_3 &= \left(2L_3 - 1\right) L_3 & B_8 &= 4L_1 L_4 \\
B_4 &= \left(2L_4 - 1\right) L_4 & B_9 &= 4L_2 L_4 \\
B_5 &= 4L_1 L_2 & B_{10} &= 4L_3 L_4
\end{aligned}
$$

(2.2)

Some differential geometry is necessary to numerically solve Maxwell Equations, so the Jacobian matrix is defined to be able to numerically evaluate integrals or other spatial operators directly in the local coordinate system as,

$$
J = \begin{bmatrix} \frac{\partial x}{\partial L_1} & \frac{\partial y}{\partial L_1} & \frac{\partial z}{\partial L_1} \\ \frac{\partial x}{\partial L_2} & \frac{\partial y}{\partial L_2} & \frac{\partial z}{\partial L_2} \\ \frac{\partial x}{\partial L_3} & \frac{\partial y}{\partial L_3} & \frac{\partial z}{\partial L_3} \end{bmatrix}
\tag{2.3}
$$

Thus, the differential operator in the real coordinate system can be expressed as,

$$
\begin{bmatrix} \frac{\partial}{\partial x} \\ \frac{\partial}{\partial y} \\ \frac{\partial}{\partial z} \end{bmatrix} = [J]^{-1} \begin{bmatrix} \frac{\partial}{\partial L_1} \\ \frac{\partial}{\partial L_2} \\ \frac{\partial}{\partial L_3} \end{bmatrix}
\tag{2.4}
$$

The differential volume in the real coordinate system is evaluated making use of the determinant of the Jacobian matrix,

$$
dV = dxdydz = |J| \, dL_1 dL_2 dL_3
\tag{2.5}
$$

The normal vector to one face of the tetrahedron can be expressed as the following example for the face 3 ($L3 = 0$),

$$
\hat{\mathbf{n}} = \frac{\nabla L_1 \times \nabla L_2}{|\nabla L_1 \times \nabla L_2|} = \frac{\left(\frac{\partial x}{\partial L_1}\hat{\mathbf{x}} + \frac{\partial y}{\partial L_1}\hat{\mathbf{y}} + \frac{\partial z}{\partial L_1}\hat{\mathbf{z}} \right) \times \left(\frac{\partial x}{\partial L_2}\hat{\mathbf{x}} + \frac{\partial y}{\partial L_2}\hat{\mathbf{y}} + \frac{\partial z}{\partial L_2}\hat{\mathbf{z}} \right)}{|\nabla L_1 \times \nabla L_2|}
\tag{2.6}
$$

and the differential surface area is

$$
dS = |\nabla L_1 \times \nabla L_2| \, dL_1 dL_2
\tag{2.7}
$$

The magnitude of the cross product (2.6) plays the same role as the determinant of the Jacobian matrix for the differential volume.

$|\nabla L_1 \times \nabla L_2| =$

$$
\sqrt{\left(\frac{\partial y}{\partial L_1} \frac{\partial z}{\partial L_2} - \frac{\partial z}{\partial L_1} \frac{\partial y}{\partial L_2} \right)^2 + \left(\frac{\partial z}{\partial L_1} \frac{\partial x}{\partial L_2} - \frac{\partial x}{\partial L_1} \frac{\partial z}{\partial L_2} \right)^2 + \left(\frac{\partial x}{\partial L_1} \frac{\partial y}{\partial L_2} - \frac{\partial y}{\partial L_1} \frac{\partial x}{\partial L_2} \right)^2}
$$

$$
\tag{2.8}
$$

In this work, second-order (O2) tetrahedral elements have been used for the space discretization. This kind of elements permits the discretization errors to be reduced in typical cases, such as coaxial cables or double curved surfaces, compared to the commonly used straight or first-order elements. In those kinds of problems the space-discretization errors are critical for the accuracy of the electromagnetic solution. Commercial software able to generate good-quality second-order tetrahedral meshes is available [120].

2.2 Vector-Fields Discretization

Two main families of basis functions, scalar and vector basis, have been generally proposed to solve electromagnetic problems with finite element methods. In both cases, different piecewise polynomials are used to form the 3D vector space of order p. The typical choice, in the case of scalar basis, is the use of Lagrange polynomials, as in the space discretization, which gives rise to nodal finite elements. It is well-known that when a straightforward nodal Continuous Galerkin finite element scheme is used to approximate the Maxwell curl-curl equation (Helmholtz operator), nonphysical or spurious solutions appear, [121, 122], in frequency domain. The source of these problems is that there are solutions of the Helmholtz equation that do not consistently approximate the complete set of the Maxwell's equations, as the Gauss' law (divergence equal to zero) [123, 124, 125]. To overcome the spurious modes problem, special vector curl-conforming basis [126, 127] were proposed [123].

Currently, the dominant approach for finite element frequency domain methods is based upon curl-conforming elements, also known as Nédélec or edge elements, [20, 128]. The main advantages of curl-conforming basis in FEM, frequency domain and Continuous Galerkin are: (i) the schemes are free of spurious solutions, (ii) boundary conditions are easy to implement, (iii) normal discontinuity and tangential continuity between different media are automatically satisfied, and (iv) better behaviour in non-convex domains than nodal scalar basis, [129]. The main disadvantage is found in large problems with a high number of degrees of freedom, where more ill-conditioned matrices are obtained with curl-conforming than with nodal scalar basis.

In Discontinuous Galerkin methods, there are two important differences to bear in mind, compared to Continuous Galerkin methods:

(a) The nature and solutions of the spurious modes in Continuous and Discontinuous Galerkin approaches are different, and the lessons learned with the Continuous case are not straightforwardly extrapolated to the Discontinuous case.
Spurious modes or non-physical solutions topic was analyzed in [53] based on nodal

scalar functions. The conclusion was that there are no problems with spurious modes if upwind flux evaluation, penalty or stabilization with purely dispersive terms are introduced into the formulation. In the case that straightforward central fluxes are used, spectral pollution due to the presence of non-physical spurious modes will be found. Similar results were reported in [63], also with nodal scalar functions, where penalization of the centered fluxes by dissipative terms were also introduced to find more accurate results. In this work, a similar analysis has been done, which appears in 3.5.1, with vector-basis functions, finding similar results.

(b) The Discontinuous Galerkin method needs only the inversion of M small matrices of $Q \times Q$ elements (with Q the number of basis functions per element), while larger matrices ($\simeq MQ \times MQ$) are involved in Continuous Galerkin. Therefore, no problems with ill-conditioned matrices are expected in Discontinuous methods.

Due to these two facts, it is not clear which kind of basis functions present more advantages or disadvantages, and both families have been successfully applied in DG context, scalar [107] and vector basis [130]. In both cases, spurious modes can be avoided, applying the same solutions. From an implementation standpoint, both kinds of basis functions have advantages. In terms of matrix sharing between elements to save memory, both sets of functions have matrices which are identical, regardless of the element size and aspect ratio, and can be shared among elements during the updating algorithm, and some matrices, otherwise, are different and have to be kept in memory for each element. Therefore, there is not such a clear advantage, for nodal or vector-basis functions, as there is for FEM in frequency domain.

In any case, in this work, vector basis has been used and more specifically, hierarchical high-order vector-basis functions, [130, 131, 132], which present some implementation advantages in order to reduce computation and memory requirements.

2.2.1 Mapping Vector-Basis Functions to Curvilinear Elements

As noted above, vector-basis functions, hierarchical high-order ones in our case, are used to discretize the vector fields ($\boldsymbol{E}$ and $\boldsymbol{H}$). As has been introduced in section 2.1, second-order tetrahedra will be used for space discretization. Expressions (2.1) and (2.2) will be used to map the reference element to the curvilinear and real one. In the same way, a local mapping has to be established for the basis functions [122].

Let the reference element be defined by local coordinates, (L_1, L_2, L_3, L_4) with $L_1 + L_2 + L_3 + L_4 = 1$, and the specific mapping in (x, y, z) space as (2.1). To define and

manipulate vector quantities within a curvilinear element, we introduce the base vectors,

$$\boldsymbol{l}_i = \frac{\partial x}{\partial L_i}\hat{\mathbf{x}} + \frac{\partial y}{\partial L_i}\hat{\mathbf{y}} + \frac{\partial z}{\partial L_i}\hat{\mathbf{z}} \quad \text{with } i = \{1, 2, 3\} \tag{2.9}$$

and the reciprocal base vectors,

$$\boldsymbol{l}_i' = \nabla L_i = \frac{\partial L_i}{\partial x}\hat{\mathbf{x}} + \frac{\partial L_i}{\partial y}\hat{\mathbf{y}} + \frac{\partial L_i}{\partial z}\hat{\mathbf{z}} \quad \text{with } i = \{1, 2, 3\} \tag{2.10}$$

Note that the reciprocal base corresponds to the gradient of the local coordinates, and both notations ($\boldsymbol{l}_i'$, ∇L_i) are used indifferently.

In general, neither the base vector nor the reciprocal one are mutually orthogonal within an element. Even the three vectors of each base are not orthogonal. However, they always satisfied two important properties,

$$\boldsymbol{l}_i \cdot \boldsymbol{l}_i' = 1 \quad \text{with } i = \{1, 2, 3\} \tag{2.11}$$

$$\boldsymbol{l}_i \cdot \boldsymbol{l}_j' = 0 \quad \text{with } i = \{1, 2, 3\} \text{ and } j = \{1, 2, 3\} \text{ being } i \neq j \tag{2.12}$$

These properties enable us to express any vector $\boldsymbol{B}$ as a linear combination of any of the two bases, just projecting that vector over the other base,

- covariant components of a vector

$$\boldsymbol{B} = \sum_{i=1}^{3} \left(\boldsymbol{B} \cdot \boldsymbol{l}_i \right) \boldsymbol{l}_i' \tag{2.13}$$

- contravariant components of a vector

$$\boldsymbol{B} = \sum_{i=1}^{3} \left(\boldsymbol{B} \cdot \boldsymbol{l}_i' \right) \boldsymbol{l}_i \tag{2.14}$$

There are two kinds of vector-basis functions, known as div-conforming and curl-conforming. Div-conforming basis functions keep a known value of the normal component at the boundaries of the elements, tangential components being unknown and depending on element aspect. In the case of curl-conforming, the tangential component at the faces of the elements are known, independently of the element shape. Curl-conforming basis functions are used when the curl operation of the discretized fields is necessary to be evaluated, and div-conforming in case of divergence operation. In our case, $\nabla \times \boldsymbol{E}$ and $\nabla \times \boldsymbol{H}$ will be necessary to be evaluated, so a curl-conforming basis function is the right choice.

When a curl-conforming basis function is being constructed on a curvilinear element, the appropriate mapping is given by,

$$
\begin{pmatrix} B_x \\ B_y \\ B_z \end{pmatrix} = J^{-1} \begin{pmatrix} B_{\nabla L_1} \\ B_{\nabla L_2} \\ B_{\nabla L_3} \end{pmatrix}
\tag{2.15}
$$

J being the Jacobian matrix defined by (2.3).

Therefore, we need to define our basis functions expressed in covariant components. The curl operation can be expressed also considering the covariant components of the basis functions as,

$$
\nabla \times \boldsymbol{B} = \frac{1}{|J|} \left[\left(\frac{\partial B_{\nabla L_3}}{\partial L_2} - \frac{\partial B_{\nabla L_2}}{\partial L_3} \right) \boldsymbol{l}_1 + \left(\frac{\partial B_{\nabla L_1}}{\partial L_3} - \frac{\partial B_{\nabla L_3}}{\partial L_1} \right) \boldsymbol{l}_2 + \left(\frac{\partial B_{\nabla L_2}}{\partial L_1} - \frac{\partial B_{\nabla L_1}}{\partial L_2} \right) \boldsymbol{l}_3 \right]
\tag{2.16}
$$

this giving a vector expressed in contravariant components. Thus, the right mapping for curl operation is the following:

$$
\begin{pmatrix} \nabla \times \boldsymbol{B}|_x \\ \nabla \times \boldsymbol{B}|_y \\ \nabla \times \boldsymbol{B}|_z \end{pmatrix} = J^T \begin{pmatrix} \nabla \times \boldsymbol{B}|_{l_1} \\ \nabla \times \boldsymbol{B}|_{l_2} \\ \nabla \times \boldsymbol{B}|_{l_3} \end{pmatrix}
\tag{2.17}
$$

In summary, defining vector-basis functions in covariant components, which is the usual approach [132], and making use of equations (2.5), (2.7), (2.15), (2.16) and (2.17), we find that all the calculations to evaluate volumetric and superficial integrals, needed in any FEM implementation, can be performed in the local coordinate system (L_1, L_2, L_3, L_4).

2.3 Finite-Element Time-Domain Methods

The general procedure to develop numerical schemes for FETD is based on Faedo-Galerkin weak solutions of the 3-D Maxwell equations, supplemented with boundary conditions. It can be applied to both the hyperbolic system of the two curl equations, and the vector-wave equation. From this perspective, different approaches have been proposed [11], and the most relevant for this dissertation are reviewed in this section.

2.3.1 Single-Field Schemes

These schemes solve the second-order vector-wave or Helmholtz equation, also known as double-curl or curl-curl Maxwell equation [12, 13, 14, 15, 16, 17, 18, 19, 20, 21, 22]. Let a

material region Ω be characterized by the electric permittivity tensor $\bar{\bar{\varepsilon}}$ and the magnetic permeability tensor $\bar{\bar{\mu}}$. It is considered lossless, electric and magnetic conductivity equal to zero, for simplicity. The electric field $\boldsymbol{E}$ (a dual formulation could be expressed for $\boldsymbol{H}$) within the domain obeys the vector-wave equation given by,

$$\nabla \times \left(\bar{\bar{\mu}}^{-1}\nabla \times \boldsymbol{E}\right) + \bar{\bar{\varepsilon}}\frac{\partial^2 \boldsymbol{E}}{\partial t^2} = -\frac{\partial \boldsymbol{J}_{imp}}{\partial t} \qquad \text{in } \Omega \tag{2.18}$$

where $\boldsymbol{J}_{imp}$ is the impressed current, source of our problem. Let us formulate the most common boundary conditions, PEC, PMC, and ABC for unbounded media:

$$\hat{\mathbf{n}} \times \boldsymbol{E} = 0 \qquad \text{on } \partial_{PEC}\Omega \tag{2.19a}$$

$$\hat{\mathbf{n}} \times \nabla \times \boldsymbol{E} = 0 \qquad \text{on } \partial_{PMC}\Omega \tag{2.19b}$$

$$\hat{\mathbf{n}} \times (\hat{\mathbf{n}} \times \nabla \times \boldsymbol{E}) = \frac{1}{c}\hat{\mathbf{n}} \times \frac{\partial \boldsymbol{E}}{\partial t} \qquad \text{on } \partial_{\infty}\Omega \tag{2.19c}$$

For simplicity, we have adopted the Silver-Müller truncation condition or first-order ABC, considering free space.

Equation (2.18), in its variational form, can be expressed as

$$\int_{\Omega} \boldsymbol{w} \cdot \left[\nabla \times \bar{\bar{\mu}}^{-1}\nabla \times \boldsymbol{E} + \bar{\bar{\varepsilon}}\frac{\partial^2 \boldsymbol{E}}{\partial t^2} + \frac{\partial \boldsymbol{J}_{imp}}{\partial t}\right] d\Omega = 0 \tag{2.20}$$

$\forall \, \boldsymbol{w} \in \mathcal{W}$, being $\mathcal{W}$ the test space, and with the usual dot product for $\left(\mathcal{L}^2\left(\Omega\right)\right)^2$.

The Galerkin procedure is the most common approach to obtain the numerical scheme, when the same set of basis functions are used to expand the unknown vector field $\boldsymbol{E}$ and test the equation.

Assuming that Ω is divided into a set of non-overlapping elements, a continuity requirement is imposed between adjacent elements. This condition is applied in a strong way, such that the following relations need to be satisfied,

$$\hat{\mathbf{n}} \times \boldsymbol{E}^+ = \hat{\mathbf{n}} \times \boldsymbol{E}^- \tag{2.21a}$$

$$\hat{\mathbf{n}} \times \left(\bar{\bar{\mu}}^{-1}\nabla \times \boldsymbol{E}\right)^+ = \hat{\mathbf{n}} \times \left(\bar{\bar{\mu}}^{-1}\nabla \times \boldsymbol{E}\right)^- \tag{2.21b}$$

where the superscript $+$ and $-$ refer to adjacent elements.

This is normally fulfilled by choosing vector curl-conforming basis functions, where the mapping is performed using covariant projection, and relating unknowns between adjacent elements.

The solution of the problem is a linear combination of the unknowns and the expansion functions as

$$\tilde{\boldsymbol{E}} = \sum_{m=1}^{M} e_m(t)\, \boldsymbol{\phi}_m(\boldsymbol{r}) = E^T\, \Phi \tag{2.22}$$

where e_m are the unknowns and $\boldsymbol{\phi}_m$ the vector-basis functions. E and Φ are column vectors containing the M unknowns and basis functions, respectively.

Inserting (2.22) into (2.20) and using Φ as test functions, we find a semi-discrete system of ordinary differential equations (ODE) as

$$\mathbb{M}\frac{d^2}{dt^2}E + \mathbb{S}E + J = 0 \tag{2.23}$$

where

$$\mathbb{M}_{ij} = \int_{\Omega} \boldsymbol{\phi}_i \cdot \bar{\bar{\varepsilon}} \boldsymbol{\phi}_j\, d\Omega \tag{2.24a}$$

$$\mathbb{S}_{ij} = \int_{\Omega} \nabla \times \boldsymbol{\phi}_i \cdot \bar{\bar{\mu}}^{-1} \nabla \times \boldsymbol{\phi}_j\, d\Omega \tag{2.24b}$$

$$J_i = \int_{\Omega} \boldsymbol{\phi}_i \cdot \frac{\partial}{\partial t} \boldsymbol{J}_{imp}\, d\Omega \tag{2.24c}$$

The main advantage of the scheme (2.23), compared to dual-field schemes, is that only one field has to be computed, which reduces the number of unknowns. This scheme has two major drawbacks, time-discretization of the second-order time derivative requires storage of previous time-step values, and the spatial semi-discrete scheme is implicit in space. The basis functions force continuity between elements, because of (2.21), and thus a complete banded linear system of equations has to be solved in each time step. A solution to find a explicit scheme is to invert the mass matrix $\mathbb{M}$. However, this can be very costly and the inverse mass matrix is, in general, full. This makes the scheme non-applicable for electrically large problems.

2.3.2 Dual-Field Schemes

Two main different approaches can be found in the literature. Both solve two equations, the Ampere's and Faraday's Laws, also referred as the first-order coupled Maxwell curl equations. In one case, the electric-field intensity ($\boldsymbol{E}$) and the magnetic-flux density ($\boldsymbol{B}$) are computed [24, 25, 26, 27, 133] but, in the other case, are the electric-field intensity ($\boldsymbol{E}$) and the magnetic-field intensity ($\boldsymbol{H}$). In the latter case, the Continuous Galerkin

approach can be used [134], or the Discontinuous Galerkin approach, proposed in this work.

2.3.2.1   E-B Finite-Element Time-Domain Method

Again, let a material region Ω be characterized by the electric permittivity tensor $\bar{\bar{\varepsilon}}$ and the magnetic permeability tensor $\bar{\bar{\mu}}$. It is considered lossless, electric and magnetic conductivity equal to zero, for simplicity. The electric field $\boldsymbol{E}$ and the magnetic flux $\boldsymbol{B}$ within the domain obey the first-order coupled Maxwell curl equations given by

$$\bar{\bar{\varepsilon}}\,\frac{\partial \boldsymbol{E}}{\partial t} = \bar{\mu}^{-1}\,\nabla \times \boldsymbol{B} - \boldsymbol{J}_{imp} \tag{2.25a}$$

$$\frac{\partial \boldsymbol{B}}{\partial t} = -\nabla \times \boldsymbol{E} \tag{2.25b}$$

where $\boldsymbol{J}_{imp}$ is the impressed current, the source of our problem. Let us formulate the most common boundary conditions, PEC, PMC, and ABC:

$$\hat{\mathbf{n}} \times \boldsymbol{E} = 0 \qquad\qquad \text{on } \partial_{PEC}\Omega \tag{2.26a}$$

$$\hat{\mathbf{n}} \times \boldsymbol{B} = 0 \qquad\qquad \text{on } \partial_{PMC}\Omega \tag{2.26b}$$

$$\hat{\mathbf{n}} \times (\hat{\mathbf{n}} \times \boldsymbol{E}) = c\,\hat{\mathbf{n}} \times \boldsymbol{B} \qquad \text{on } \partial_{\infty}\Omega \tag{2.26c}$$

Again, we have adopted the Silver-Müller truncation condition or first-order ABC, considering free space.

The electric field $\boldsymbol{E}$ is expanded in terms of Whitney edge basis functions $\boldsymbol{w}_i^1$, $i = 1, 2, ...N_e$, and the magnetic flux $\boldsymbol{B}$ is expanded in terms of Whitney face basis functions $\boldsymbol{w}_i^2$, $i = 1, 2, ...N_f$. Thus, the expression for the unknown fields are

$$\tilde{\boldsymbol{E}} = \sum_{m=1}^{N_e} e_m\,(t)\,\boldsymbol{w}_m^1\,(\boldsymbol{r}) = E^T\,W^1 \tag{2.27a}$$

$$\tilde{\boldsymbol{B}} = \sum_{m=1}^{N_f} b_m\,(t)\,\boldsymbol{w}_m^2\,(\boldsymbol{r}) = B^T\,W^2 \tag{2.27b}$$

where e_m and b_m are the unknowns, and N_e and N_f are the number of edges and faces, respectively.

We denote column vectors containing the unknowns as, $E = [e_1, e_2, ..., e_{N_e}]^T$ and $B = [b_1, b_2, ..., b_{N_f}]^T$ and the sets of basis functions as, $W^1 = [w_1^1, w_2^1, ..., w_{N_e}^1]^T$ and $W^2 = [w_1^2, w_2^2, ..., w_{N_f}^2]^T$.

Inserting (2.27) into (2.25), we see that the second equation (2.25b) does not need to be tested, since naturally becomes an identity. After testing the first equation (2.25a), according to the Galerkin procedure, the results is a semi-discrete system of two ordinary differential equations (ODE's).

$$[\star_\varepsilon] \frac{d}{dt} E = [d^*_{\mathrm{curl}}] [\star_{\mu^{-1}}] B - J \tag{2.28a}$$

$$\frac{d}{dt} B = -[d_{\mathrm{curl}}] E \tag{2.28b}$$

where the $N_f \times N_e$ matrix $[d_{\mathrm{curl}}]$ and the $N_e \times N_f$ $[d^*_{\mathrm{curl}}]$ are (metric free) sparse curl incidence matrices on the primal and dual grids, respectively, the elements of which assume only $\{-1, 0, 1\}$ values. The identity $[d_{\mathrm{curl}}]^T = [d^*_{\mathrm{curl}}]$ holds, in general, up to boundary terms. The incidence matrices fulfill the following expression:

$$\nabla \times W^1 = [d^*_{\mathrm{curl}}] W^2 \tag{2.29}$$

J column vector corresponds with the source term

$$J_i = \int_\Omega \boldsymbol{w}_i^1 \cdot \boldsymbol{J}_{imp} \, d\Omega \tag{2.30}$$

The discrete Hodge matrices $[\star_\varepsilon]$ (size $N_e \times N_e$) and $[\star_{\mu^{-1}}]$ (size $N_f \times N_f$) in (2.28) are given by the following integrals,

$$[\star_\varepsilon]_{ij} = \int_\Omega \boldsymbol{w}_i^1 \cdot \bar{\bar{\varepsilon}} \boldsymbol{w}_j^1 \, d\Omega \tag{2.31a}$$

$$[\star_{\mu^{-1}}]_{ij} = \int_\Omega \boldsymbol{w}_i^2 \cdot \bar{\bar{\mu}}^{-1} \boldsymbol{w}_j^2 \, d\Omega \tag{2.31b}$$

In summary, the scheme employs edge basis functions (Whitney 1-form) to expand $\boldsymbol{E}$, and face basis functions (Whitney 2-form) to expand $\boldsymbol{B}$. It is important to notice that this strategy retains conformality to the discrete de Rham diagram [135], this being the reason to choose $\boldsymbol{B}$, instead of $\boldsymbol{H}$ as other schemes. This fact avoids spurious solutions of the form $t\nabla\phi$, which are present in the single-field FETD [15, 136, 137], particularly restrictive for the use of PML.

The result is a scheme composed by two ODE's with two fields as unknowns. Its computational cost is comparable to the single-field scheme. The Hodge (mass) matrices are sparse, but not diagonal, and the solution of the associated linear system is the most

computationally intensive part of the scheme. The sparse linear-system solution is required only for the electric-field update in (2.28a), with (2.28b) being explicit. Therefore, the size of the linear system to be solved is as large as the single-field scheme.

It is important to note that this scheme involves only first-order time derivatives instead of the second-order ones of the single-field case. This allows the use of conventional Leap-Frog time discretization which avoids to keep in memory previous states.

The main drawback of this scheme, as for the single-field case, is that is very costly for electrically large problems and becomes non-applicable in real problems.

2.3.2.2 E-H Finite-Element Time-Domain Method

Again, let a material region Ω be characterized by the electric permittivity tensor $\bar{\bar{\varepsilon}}$ and the magnetic permeability tensor $\bar{\bar{\mu}}$. It is considered lossless, electric and magnetic conductivity equal to zero, for simplicity. The electric field $\boldsymbol{E}$ and the magnetic field $\boldsymbol{H}$ within the domain obey the first-order coupled Maxwell curl equations given by

$$\bar{\bar{\varepsilon}}\,\frac{\partial \boldsymbol{E}}{\partial t} = \nabla \times \boldsymbol{H} - \boldsymbol{J}_{imp} \tag{2.32a}$$

$$\bar{\bar{\mu}}\,\frac{\partial \boldsymbol{H}}{\partial t} = -\nabla \times \boldsymbol{E} \tag{2.32b}$$

where $\boldsymbol{J}_{imp}$ is the impressed current, source of our problem. Now the boundary conditions, PEC, PMC, and Silver-Müller ABC are:

$$\hat{\mathbf{n}} \times \boldsymbol{E} = 0 \qquad \text{on } \partial_{PEC}\Omega \tag{2.33a}$$

$$\hat{\mathbf{n}} \times \boldsymbol{H} = 0 \qquad \text{on } \partial_{PMC}\Omega \tag{2.33b}$$

$$\hat{\mathbf{n}} \times (\hat{\mathbf{n}} \times \boldsymbol{E}) = \eta_0\,\hat{\mathbf{n}} \times \boldsymbol{H} \qquad \text{on } \partial_{\infty}\Omega \tag{2.33c}$$

In the same way as in the E-B scheme, the electric and magnetic fields are expanded, and equations (2.32) are tested. In this case, the basis function sets for electric and magnetic fields are the same. Thus, the expressions for the unknown fields, considering vector-basis functions, take the following form

$$\tilde{\boldsymbol{E}} = \sum_{m=1}^{N} e_m\,(t)\,\boldsymbol{\phi}_m\,(\boldsymbol{r}) = E^T\,\Phi \tag{2.34a}$$

$$\tilde{\boldsymbol{H}} = \sum_{m=1}^{N} h_m\,(t)\,\boldsymbol{\phi}_m\,(\boldsymbol{r}) = H^T\,\Phi \tag{2.34b}$$

where e_m and h_m are the unknowns, $\boldsymbol{\phi}_m$ represents the vector-basis functions, and N is the number of dofs or expansion/testing functions. We denote column vectors containing

the unknowns as, $E = [e_1, e_2, ..., e_N]^T$ and $H = [h_1, h_2, ..., h_N]^T$, and the basis functions set as, $\Phi = [\phi_1, \phi_2, ..., \phi_N]^T$.

There are two different approaches depending on how the continuity between adjacent elements is considered. It can be applied in a strong way, as it is in the single-field scheme, or, otherwise, discontinuity can be allowed across the boundaries, forcing the flux to be continuous.

In the first case, where field continuity is forced, an equivalent requirement for the basis functions such as (2.21) has to be established,

$$\hat{\mathbf{n}} \times \boldsymbol{E}^+ = \hat{\mathbf{n}} \times \boldsymbol{E}^- \tag{2.35a}$$

$$\hat{\mathbf{n}} \times \boldsymbol{H}^+ = \hat{\mathbf{n}} \times \boldsymbol{H}^- \tag{2.35b}$$

Inserting (2.34) into (2.32), and testing these two equations according to the Galerkin procedure, we obtain the following semi-discrete system of ODE's,

$$\mathbb{M}_{\bar{\bar{\varepsilon}}} \frac{d}{dt} E = \mathbb{S} \, H - J \tag{2.36a}$$

$$\mathbb{M}_{\bar{\bar{\mu}}} \frac{d}{dt} H = -\mathbb{S} \, E \tag{2.36b}$$

where

$$\mathbb{M}_{\bar{\bar{\alpha}} \, ij} = \int_{\Omega} \phi_i \cdot \bar{\bar{\alpha}} \phi_j \, d\Omega, \quad \text{with } \bar{\bar{\alpha}} = \{\bar{\bar{\varepsilon}}, \bar{\bar{\mu}}\} \tag{2.37a}$$

$$\mathbb{S}_{ij} = \int_{\Omega} \phi_i \cdot \nabla \times \phi_j \, d\Omega \tag{2.37b}$$

$$J_i = \int_{\Omega} \phi_i \cdot \frac{\partial}{\partial t} \boldsymbol{J}_{imp} \, d\Omega \tag{2.37c}$$

The mass matrices $\mathbb{M}_{\bar{\bar{\alpha}}}$ are sparse and not diagonal, due to the (2.35) requirement for the basis functions, which makes it necessary to share the same unknown in adjacent elements. Thus, the scheme (2.36) is implicit in space and requires the resolution of two linear systems each time-step, making this approach computationally prohibitive for electrically large problems.

In the case that field discontinuity between elements were allowed, basis functions do not have the (2.35) requirement. Electrical and magnetic fields are expanded element by element and the solution is not forced to be continuous at the boundaries between adjacent elements. Instead, continuous numerical fluxes are defined at the interface in order to connect the solution between them in the manner used in Finite Volume

Time Domain (FVTD) methods, which is the main idea of Discontinuous Galerkin Time Domain (DGTD) methods. Two common flux conditions are found in the literature: the centered flux [52], and the upwind flux [84]. The latter is the one actually employed in FVTD, and in fact, FVTD can be regarded as a special case of DGTD with this flux, and 0th order (constant) scalar basis functions [75]. Apart from these two flux conditions, a generalized flux can be expressed [53, 63] with a parameter that penalizes the jump of the vector tangential components between the elements.

The main advantage of DGTD over FVTD is its higher order in space, while over Continuous FETD, the advantage resides in the fact that the mass matrices ($\mathbb{M}_{\bar{\bar{\alpha}}}$) become diagonal and DGTD needs only the inversion of M square matrices of $Q \times Q$ elements (with M the number of elements and Q the number of basis functions per element), while larger matrices ($\simeq MQ \times MQ$) are involved in Continuous FETD.

Chapter 3

Spatial Discontinuous Galerkin Method to Solve Maxwell's Equations

The Discontinuous Galerkin Time Domain method (DGTD) is a numerical technique which is attracting a lot of attention in computational electromagnetics (CEM)[69]. DGTD starts from a variational formulation to integrate the spatial part of time-domain (TD) Maxwell's curl equations, with some differential integration scheme for the time part. Like in Finite Element Methods (FEM), the space is divided into M non-overlapping elements, in each of which the solution is expanded in a set of local basis functions of arbitrary order. A weak form of Maxwell's curl equations is found element by element by employing a Galerkin test procedure. Unlike in FEM, the solution is allowed to be fully discontinuous across the boundaries between adjacent elements. Thus local mass and stiffness matrices do not require the assembly of adjacent element terms, with the subsequent computational advantage over classical FEM.

In this chapter, the Discontinuous Galerkin formulation, in its semi-discrete form, is developed in a general framework which unifies different fluxes evaluation schemes successfully applied to this method. The problem of dealing with anisotropic materials in DGTD is addressed, in a 3-D general form. The conformal uniaxial perfect matching layer (C-UPML) truncation condition is formulated in the Discontinuous Galerkin context. Finally, the proposed spatial discretization scheme is studied, analyzing numerical dispersion and dissipation, spurious and convergence topics.

3.1 Discontinuous Galerkin Formulation

The Maxwell's curl equations in three space dimension ($\mathbb{R}^3$) for heterogeneous isotropic linear media without sources can be given in a unified form as follows. The electric field $\boldsymbol{E} = (E_x, E_y, E_z)$ and the magnetic field $\boldsymbol{H} = (H_x, H_y, H_z)$ must satisfy following equations:

$$\mu\frac{\partial \boldsymbol{H}}{\partial t} = -\nabla \times \boldsymbol{E} - \sigma_m \boldsymbol{H} \tag{3.1a}$$

$$\varepsilon\frac{\partial \boldsymbol{E}}{\partial t} = \nabla \times \boldsymbol{H} - \sigma_e \boldsymbol{E} \tag{3.1b}$$

The electric isotropic permittivity $\varepsilon\left(\boldsymbol{r}\right)$, the electric isotropic conductivity $\sigma_e\left(\boldsymbol{r}\right)$, the magnetic isotropic permeability $\mu\left(\boldsymbol{r}\right)$ and the magnetic isotropic conductivity $\sigma_m\left(\boldsymbol{r}\right)$ are varying in space. Equations (3.1) do not include terms for impressed electric and/or magnetic currents. The reason is that sources will be considered surface current densities and will be included in the formulation through the flux terms.

Let Ω be a bounded finite region of $\mathbb{R}^3$ whose boundary is $\partial\Omega$, where a numerical solution of equations (3.1) is intended to be computed. The domain Ω is subdivided into M non-overlapping and conformal elements, tetrahedra as described previously in section 2.1, which conform the computational domain, Ω_M. The mth element is defined by the volume $\mathcal{T}_m$, the boundaries $\partial\mathcal{T}_m$ and the electric and magnetic parameters ($\varepsilon\left(\boldsymbol{r}\right)$, $\sigma_e\left(\boldsymbol{r}\right)$, $\mu\left(\boldsymbol{r}\right)$ and $\sigma_m\left(\boldsymbol{r}\right)$).

$$\Omega \simeq \; \Omega_M = \bigcup_M \mathcal{T}_m \tag{3.2}$$

Local inner product and norm are defined in the finite elements $\mathcal{T}_m$ as,

$$\langle \boldsymbol{u}, \boldsymbol{v}\rangle_{\mathcal{T}_m} = \int_{\mathcal{T}_m} \boldsymbol{u} \cdot \boldsymbol{v} \; dv, \quad \|\boldsymbol{u}\|^2_{\mathcal{T}_m} = \langle \boldsymbol{u}, \boldsymbol{u}\rangle \tag{3.3}$$

and also the local inner product over the boundaries $\partial\mathcal{T}_m$,

$$\langle \boldsymbol{u}, \boldsymbol{v}\rangle_{\partial\mathcal{T}_m} = \oint_{\partial\mathcal{T}_m} \boldsymbol{u} \cdot \boldsymbol{v} \; ds, \tag{3.4}$$

In this section, a semi-discrete scheme, based upon Discontinuous Galerkin technique and vector-basis functions, is developed. Firstly, the basic semi-discrete scheme is formulated. Then, the implementation of the most common boundary conditions is described, which makes use of the flux terms to apply them in a weak way.

3.1.1 Semi-Discrete Scheme Formulation

Let us define the sets of local vector-basis functions, described previously in section 2.2, which are, in general, different in each element $\mathcal{T}_m$, as,

$$\mathcal{B}^m = \{\phi_1^m, \phi_2^m, ..., \phi_Q^m\} \ , \ m = 1, ..., M \tag{3.5}$$

This basis functions are used to expand the unknown vector fields quantities ($\boldsymbol{E}$ and $\boldsymbol{H}$) and test equation (3.1), which gives rise to the Galerkin method. Thus, the weak form of Maxwell's equations set (3.1) is found by using the inner product.

$$\int_{\mathcal{T}_m} \left[\mu \frac{\partial \boldsymbol{H}}{\partial t} + \nabla \times \boldsymbol{E} + \sigma_m \boldsymbol{H} \right] \cdot \boldsymbol{\phi}_{q'}^m \ dv = 0 \tag{3.6a}$$

$$\int_{\mathcal{T}_m} \left[\varepsilon \frac{\partial \boldsymbol{E}}{\partial t} - \nabla \times \boldsymbol{H} + \sigma_e \boldsymbol{E} \right] \cdot \boldsymbol{\phi}_{q'}^m \ dv = 0 \tag{3.6b}$$

Applying some algebra to the curl terms, we obtain,

$$\int_{\mathcal{T}_m} (\nabla \times \boldsymbol{U}) \cdot \boldsymbol{\phi}_{q'}^m \ dv = \int_{\mathcal{T}_m} \nabla \cdot (\boldsymbol{U} \times \boldsymbol{\phi}_{q'}^m) \ dv + \int_{\mathcal{T}_m} (\nabla \times \boldsymbol{\phi}_{q'}^m) \cdot \boldsymbol{U} \ dv =$$
$$= \oint_{\partial \mathcal{T}_m} (\hat{\mathbf{n}}^m \times \boldsymbol{U}) \cdot \boldsymbol{\phi}_{q'}^m \ ds + \int_{\mathcal{T}_m} (\nabla \times \boldsymbol{\phi}_{q'}^m) \cdot \boldsymbol{U} \ dv \tag{3.7}$$

with $\boldsymbol{U} = \{\boldsymbol{E}, \boldsymbol{H}\}$, and $\hat{\mathbf{n}}^m$ the outward unit vector normal to the element m.

Introducing (3.7) into (3.6) together with a tangential field continuity condition between adjacent elements leads to a continuous FETD method [11]. Namely, adding the superscript + to the fields at $\partial \mathcal{T}_m$ calculated in the element adjacent to m, the continuity on the tangential field components on the common face $\partial \mathcal{T}_m$ of two adjacent elements requires for continuous FETD that

$$\hat{\mathbf{n}}^m \times \boldsymbol{E}^{m+} = \hat{\mathbf{n}}^m \times \boldsymbol{E}^m \ , \ \hat{\mathbf{n}}^m \times \boldsymbol{H}^{m+} = \hat{\mathbf{n}}^m \times \boldsymbol{H}^m \tag{3.8}$$

The main drawback of the resulting algorithm resides in its implicit nature, which requires the solution of large systems of linear equations [118]. The core idea of DGTD is to relax the continuity conditions to yield a quasi-explicit algorithm. Namely, instead of plugging (3.8) into (3.7) and (3.6), DGTD defines numerical values of the tangential fields on $\partial \mathcal{T}_m$, henceforth called numerical fluxes ($\hat{\mathbf{n}}^m \times \boldsymbol{H}^{m*}$ and $\hat{\mathbf{n}}^m \times \boldsymbol{E}^{m*}$), which do not coincide with any of the values of the tangential fields at any side of $\partial \mathcal{T}_m$ but

depend linearly on them,

$$\hat{\mathbf{n}}^m \times \boldsymbol{E}^{m*} = \hat{\mathbf{n}}^m \times \left(\boldsymbol{f}_E^- \left(\boldsymbol{E}^m, \boldsymbol{H}^m \right) + \boldsymbol{f}_E^+ \left(\boldsymbol{E}^{m+}, \boldsymbol{H}^{m+} \right) \right) \tag{3.9a}$$

$$\hat{\mathbf{n}}^m \times \boldsymbol{H}^{m*} = \hat{\mathbf{n}}^m \times \left(\boldsymbol{f}_H^- \left(\boldsymbol{H}^m, \boldsymbol{E}^m \right) + \boldsymbol{f}_H^+ \left(\boldsymbol{H}^{m+}, \boldsymbol{E}^{m+} \right) \right) \tag{3.9b}$$

This numerical flux is the one actually employed by any pair of adjacent elements to calculate the surface (flux) integrals in (3.7), instead of $\hat{\mathbf{n}}^m \times \boldsymbol{E}^m$ and $\hat{\mathbf{n}}^m \times \boldsymbol{H}^m$.

Three common choices of the numerical flux are reported in the literature and are widely described in section 3.2. A general form for these numerical fluxes is

$$\hat{\mathbf{n}}^m \times \boldsymbol{E}^{m*} = \hat{\mathbf{n}}^m \times \boldsymbol{E}^m + \kappa_e^m \left[\hat{\mathbf{n}}^m \times (\boldsymbol{E}^{m+} - \boldsymbol{E}^m) + \boldsymbol{M}_s \right] +$$
$$\nu_h^m \left[\hat{\mathbf{n}}^m \times (\hat{\mathbf{n}}^m \times (\boldsymbol{H}^{m+} - \boldsymbol{H}^m) - \boldsymbol{J}_s) \right] \tag{3.10a}$$

$$\hat{\mathbf{n}}^m \times \boldsymbol{H}^{m*} = \hat{\mathbf{n}}^m \times \boldsymbol{H}^m + \kappa_h^m \left[\hat{\mathbf{n}}^m \times (\boldsymbol{H}^{m+} - \boldsymbol{H}^m) - \boldsymbol{J}_s \right] -$$
$$\nu_e^m \left[\hat{\mathbf{n}}^m \times (\hat{\mathbf{n}}^m \times (\boldsymbol{E}^{m+} - \boldsymbol{E}^m) + \boldsymbol{M}_s) \right] \tag{3.10b}$$

where we have also included possible surface currents, to be used, for instance, in the implementation of Huygen's sources [138]. Table 3.1 shows the expressions for the κ and ν factors for centered, upwind and partial penalized numerical fluxes. The terms which are multiplied by ν factors are known as dissipative terms. These terms introduce some dissipation to the scheme [59], but are essential to avoid the propagation of non-physical or spurious modes in the computational domain. In section 3.5.1, dissipation rates are numerically evaluated in the eigenvalue problem, finding that the dissipation rates for the spurious modes are much higher than for the physical modes [53]. In case of $\nu = 0$ (centered flux), there is no dissipation for both, physical and spurious modes, what introduces spectral pollution to the method. In [63], Montseny et al. took advantage of this fact and introduced, in a centered scheme, dissipation terms which improves accuracy, referred here as partial penalized.

TABLE 3.1: Parameters in equation (3.10) to yield centered, upwind and penalized numerical fluxes. $Z^m = \sqrt{\frac{\mu^m}{\varepsilon^m}} = \frac{1}{Y^m}$ is the intrinsic impedance of the element m, and $Z^{m+} = \frac{1}{Y^{m+}}$ is that of the adjacent one.

	κ_e^m	κ_h^m	ν_h^m	ν_e^m
centered	$\frac{1}{2}$	$\frac{1}{2}$	0	0
upwind	$\frac{Y^{m+}}{Y^m + Y^{m+}}$	$\frac{Z^{m+}}{Z^m + Z^{m+}}$	$\frac{1}{Y^m + Y^{m+}}$	$\frac{1}{Z^m + Z^{m+}}$
penalized	$\frac{Y^{m+}}{Y^m + Y^{m+}}$	$\frac{Z^{m+}}{Z^m + Z^{m+}}$	$\frac{\tau}{Y^m + Y^{m+}}$	$\frac{\tau}{Z^m + Z^{m+}}$

Introducing (3.10) into (3.7), the curl terms can be written as,

$$
\int\limits_{\mathcal{T}_m} (\nabla \times \boldsymbol{E}^{m*}) \cdot \boldsymbol{\phi}_{q'}^m \, dv = \int\limits_{\mathcal{T}_m} (\nabla \times \boldsymbol{E}^{m}) \cdot \boldsymbol{\phi}_{q'}^m \, dv -
$$

$$
\oint\limits_{\partial \mathcal{T}_m} \kappa_e^m \left[\hat{\mathbf{n}}^m \times \left(\boldsymbol{E}^m - \boldsymbol{E}^{m+} \right) - \boldsymbol{M}_s \right] \cdot \boldsymbol{\phi}_{q'}^m \, ds -
$$

$$
\oint\limits_{\partial \mathcal{T}_m} \nu_h^m \left[\hat{\mathbf{n}}^m \times \left(\hat{\mathbf{n}}^m \times \left(\boldsymbol{H}^m - \boldsymbol{H}^{m+} \right) + \boldsymbol{J}_s \right) \right] \cdot \boldsymbol{\phi}_{q'}^m \, ds \quad (3.11\text{a})
$$

$$
\int\limits_{\mathcal{T}_m} (\nabla \times \boldsymbol{H}^{m*}) \cdot \boldsymbol{\phi}_{q'}^m \, dv = \int\limits_{\mathcal{T}_m} (\nabla \times \boldsymbol{H}^{m}) \cdot \boldsymbol{\phi}_{q'}^m \, dv -
$$

$$
\oint\limits_{\partial \mathcal{T}_m} \kappa_h^m \left[\hat{\mathbf{n}}^m \times \left(\boldsymbol{H}^m - \boldsymbol{H}^{m+} \right) + \boldsymbol{J}_s \right] \cdot \boldsymbol{\phi}_{q'}^m \, ds +
$$

$$
\oint\limits_{\partial \mathcal{T}_m} \nu_e^m \left[\hat{\mathbf{n}}^m \times \left(\hat{\mathbf{n}}^m \times \left(\boldsymbol{E}^m - \boldsymbol{E}^{m+} \right) - \boldsymbol{M}_s \right) \right] \cdot \boldsymbol{\phi}_{q'}^m \, ds \quad (3.11\text{b})
$$

The semi-discrete algorithm is found by assuming that the space and time dependencies of the fields can be separated. Thus, the spatial part is expanded, as it was said before, within each element in the sets of vector-basis functions equal to the sets of test functions (Galerkin method).

$$
\boldsymbol{H} \simeq \tilde{\boldsymbol{H}} = \sum_{q=1}^{Q} h_q^m(t) \, \boldsymbol{\phi}_q^m(\boldsymbol{r}) \tag{3.12a}
$$

$$
\boldsymbol{E} \simeq \tilde{\boldsymbol{E}} = \sum_{q=1}^{Q} e_q^m(t) \, \boldsymbol{\phi}_q^m(\boldsymbol{r}) \tag{3.12b}
$$

Finally, after expanding the vector magnitudes, $\boldsymbol{H}$ and $\boldsymbol{E}$ as (3.12), and introducing the proposed evaluation expression of the curl terms (3.11) in (3.6), the final form of the semi-discrete algorithm at the element m appears bellow. It has been assumed that the material properties are constant inside each element.

$$
\mu \mathbb{M} d_t H^m + (\sigma_m \mathbb{M} - \mathbb{F}_{\nu h}) H^m + \mathbb{F}_{\nu h}^+ H^{m+} = -(\mathbb{S} - \mathbb{F}_{\kappa e}) E^m - \mathbb{F}_{\kappa e}^+ E^{m+} - M_{s\kappa} + J_{s\nu} \tag{3.13a}
$$

$$
\varepsilon \mathbb{M} d_t E^m + (\sigma_e \mathbb{M} - \mathbb{F}_{\nu e}) E^m + \mathbb{F}_{\nu e}^+ E^{m+} = (\mathbb{S} - \mathbb{F}_{\kappa h}) H^m + \mathbb{F}_{\kappa h}^+ H^{m+} - J_{s\kappa} - M_{s\nu} \tag{3.13b}
$$

where

- H^m and E^m are column vector varying in time with the field coefficients (dofs) in the element m, and H^{m+} and E^{m+} with the field coefficients (dofs) of the adjacent

elements,

$$H^m = \left(h_1^m(t), \ldots, h_Q^m(t)\right)^T \tag{3.14a}$$

$$E^m = \left(e_1^m(t), \ldots, e_Q^m(t)\right)^T \tag{3.14b}$$

- $M_{s\kappa}$, $M_{s\nu}$, $J_{s\kappa}$ and $J_{s\nu}$ are column vector varying in time with the weak form of the surface source terms in the element m,

$$M_{s\kappa} = \left(\left\langle \boldsymbol{\phi}_1^m, \kappa_e^m \boldsymbol{M}_s(\boldsymbol{r},t)\right\rangle_{\partial \mathcal{T}_m}, \ldots, \left\langle \boldsymbol{\phi}_Q^m, \kappa_e^m \boldsymbol{M}_s(\boldsymbol{r},t)\right\rangle_{\partial \mathcal{T}_m}\right)^T \tag{3.15a}$$

$$M_{s\nu} = \left(\left\langle \boldsymbol{\phi}_1^m, \nu_e^m \hat{\mathbf{n}}^m \times \boldsymbol{M}_s(\boldsymbol{r},t)\right\rangle_{\partial \mathcal{T}_m}, \ldots, \left\langle \boldsymbol{\phi}_Q^m, \nu_e^m \hat{\mathbf{n}}^m \times \boldsymbol{M}_s(\boldsymbol{r},t)\right\rangle_{\partial \mathcal{T}_m}\right)^T \tag{3.15b}$$

$$J_{s\kappa} = \left(\left\langle \boldsymbol{\phi}_1^m, \kappa_h^m \boldsymbol{J}_s(\boldsymbol{r},t)\right\rangle_{\partial \mathcal{T}_m}, \ldots, \left\langle \boldsymbol{\phi}_Q^m, \kappa_h^m \boldsymbol{J}_s(\boldsymbol{r},t)\right\rangle_{\partial \mathcal{T}_m}\right)^T \tag{3.15c}$$

$$J_{s\nu} = \left(\left\langle \boldsymbol{\phi}_1^m, \nu_h^m \hat{\mathbf{n}}^m \times \boldsymbol{J}_s(\boldsymbol{r},t)\right\rangle_{\partial \mathcal{T}_m}, \ldots, \left\langle \boldsymbol{\phi}_Q^m, \nu_h^m \hat{\mathbf{n}}^m \times \boldsymbol{J}_s(\boldsymbol{r},t)\right\rangle_{\partial \mathcal{T}_m}\right)^T \tag{3.15d}$$

- $\mathbb{M}$ is the mass matrix,

$$[\mathbb{M}]_{q'q} = \left\langle \boldsymbol{\phi}_{q'}^m, \boldsymbol{\phi}_q^m\right\rangle_{\mathcal{T}_m} \tag{3.16}$$

- $\mathbb{S}$ is the stiffness matrix

$$[\mathbb{S}]_{q'q} = \left\langle \boldsymbol{\phi}_{q'}^m, \nabla \times \boldsymbol{\phi}_{qm}\right\rangle_{\mathcal{T}_m} \tag{3.17}$$

- $\mathbb{F}$ are the flux matrices

$$[\mathbb{F}_{\kappa h}]_{q'q} = \left\langle \boldsymbol{\phi}_{q'}^m, \hat{\mathbf{n}}^m \times \kappa_h^m \boldsymbol{\phi}_q^m\right\rangle_{\partial \mathcal{T}_m}, \quad [\mathbb{F}_{\kappa e}]_{q'q} = \left\langle \boldsymbol{\phi}_{q'}^m, \hat{\mathbf{n}}^m \times \kappa_e^m \boldsymbol{\phi}_q^m\right\rangle_{\partial \mathcal{T}_m} \tag{3.18a}$$

$$[\mathbb{F}_{\nu h}]_{q'q} = \left\langle \boldsymbol{\phi}_{q'}^m, \hat{\mathbf{n}}^m \times \hat{\mathbf{n}}^m \times \nu_h^m \boldsymbol{\phi}_q^m\right\rangle_{\partial \mathcal{T}_m}, \quad [\mathbb{F}_{\nu e}]_{q'q} = \left\langle \boldsymbol{\phi}_{q'}^m, \hat{\mathbf{n}}^m \times \hat{\mathbf{n}}^m \times \nu_e^m \boldsymbol{\phi}_q^m\right\rangle_{\partial \mathcal{T}_m} \tag{3.18b}$$

$$\left[\mathbb{F}_{\kappa h}^+\right]_{q'q} = \left\langle \boldsymbol{\phi}_{q'}^m, \hat{\mathbf{n}}^m \times \kappa_h^m \boldsymbol{\phi}_q^{m+}\right\rangle_{\partial \mathcal{T}_m}, \quad \left[\mathbb{F}_{\kappa e}^+\right]_{q'q} = \left\langle \boldsymbol{\phi}_{q'}^m, \hat{\mathbf{n}}^m \times \kappa_e^m \boldsymbol{\phi}_q^{m+}\right\rangle_{\partial \mathcal{T}_m} \tag{3.18c}$$

$$\left[\mathbb{F}_{\nu h}^+\right]_{q'q} = \left\langle \boldsymbol{\phi}_{q'}^m, \hat{\mathbf{n}}^m \times \hat{\mathbf{n}}^m \times \nu_h^m \boldsymbol{\phi}_q^{m+}\right\rangle_{\partial \mathcal{T}_m}, \quad \left[\mathbb{F}_{\nu e}^+\right]_{q'q} = \left\langle \boldsymbol{\phi}_{q'}^m, \hat{\mathbf{n}}^m \times \hat{\mathbf{n}}^m \times \nu_e^m \boldsymbol{\phi}_q^{m+}\right\rangle_{\partial \mathcal{T}_m} \tag{3.18d}$$

Notice that κ and ν factors, when the upwind flux is employed, are function of the electric and magnetic parameters of the material of m element and all adjacent elements, $m+$, so it is not a constant value for all $[\mathbb{F}]_{q'q}$ coefficients. In case of centered flux is straightforward employed, κ factors are constant $\left(\frac{1}{2}\right)$ and ν factors are equal to 0, so $\mathbb{F}_{\kappa h} = \mathbb{F}_{\kappa e}$, $\mathbb{F}_{\kappa h}^+ = \mathbb{F}_{\kappa e}^+$ and $\mathbb{F}_{\nu h} = \mathbb{F}_{\nu e}^+ = \mathbb{F}_{\nu h}^+ = \mathbb{F}_{\nu e} = 0$.

It is important to note that, if the space discretization, described in section 2.1, and the vector-basis functions, introduced in section 2.2, are used in the semi-discrete system (3.13), some matrices can be shared between the elements, since are independent of geometrical data, resulting in a very significant memory saving. These matrices are: $\mathbb{S}$, $\mathbb{F}_{\kappa e}$, $\mathbb{F}_{\kappa h}$, $\mathbb{F}_{\kappa e}^+$ and $\mathbb{F}_{\kappa h}^+$. Following, this fact is proved for the $\mathbb{S}$ matrix.

The expression for a ϕ vector expansion function, in the 3-D reference cell, can be written as,

$$\phi = f_1(L_1, L_2, L_3)\nabla L_1 + f_2(L_1, L_2, L_3)\nabla L_2 + f_3(L_1, L_2, L_3)\nabla L_3 \qquad (3.19)$$

where L_1, L_2, L_3 are local coordinates. Following notation is used,

$$\phi = \phi_{\nabla L_1}\nabla L_1 + \phi_{\nabla L_2}\nabla L_2 + \phi_{\nabla L_2}\nabla L_1 = \phi_x\hat{\mathbf{x}} + \phi_y\hat{\mathbf{y}} + \phi_z\hat{\mathbf{z}} \qquad (3.20)$$

where $\phi_{\nabla L_i} = f_i(L_1, L_2, L_3)$, $i = 1, 2, 3$ are just polynomial functions.

We use curl-conforming basis functions on curvilinear cells, so the appropriate mapping is given by the contravariant transformation (2.15), here rewritten for convenience with the introduced notation,

$$\begin{bmatrix} \phi_x \\ \phi_y \\ \phi_z \end{bmatrix} = J^{-1} \begin{bmatrix} \phi_{\nabla L_1} \\ \phi_{\nabla L_2} \\ \phi_{\nabla L_3} \end{bmatrix} \qquad (3.21)$$

J refers to Jacobian matrix. The curl operation can be evaluated making use of the expressions (2.16) and (2.17), which can be written in a compact form as follows,

$$\begin{bmatrix} (\nabla \times \phi)_x \\ (\nabla \times \phi)_y \\ (\nabla \times \phi)_z \end{bmatrix} = \frac{J^T}{|J|} \begin{bmatrix} \frac{\partial \phi_{\nabla L_3}}{\partial L_2} - \frac{\partial \phi_{\nabla L_2}}{\partial L_3} \\ \frac{\partial \phi_{\nabla L_1}}{\partial L_3} - \frac{\partial \phi_{\nabla L_3}}{\partial L_1} \\ \frac{\partial \phi_{\nabla L_2}}{\partial L_1} - \frac{\partial \phi_{\nabla L_1}}{\partial L_2} \end{bmatrix} \qquad (3.22)$$

Therefore, $\mathbb{S}$ matrix does not depend on geometrical information as evidenced bellow,

$$[\mathbb{S}]_{q'q} = \int_{V^m} \phi_{q'} \cdot (\nabla \times \phi_q)\, dV =$$

$$\iiint_{L_1\, L_2\, L_3} \left(J^{-1} \begin{bmatrix} \phi_{\nabla L_1} \\ \phi_{\nabla L_2} \\ \phi_{\nabla L_3} \end{bmatrix}_{q'} \right)^T \frac{J^T}{|J|} \begin{bmatrix} \frac{\partial \phi_{\nabla L_3}}{\partial L_2} - \frac{\partial \phi_{\nabla L_2}}{\partial L_3} \\ \frac{\partial \phi_{\nabla L_1}}{\partial L_3} - \frac{\partial \phi_{\nabla L_3}}{\partial L_1} \\ \frac{\partial \phi_{\nabla L_2}}{\partial L_1} - \frac{\partial \phi_{\nabla L_1}}{\partial L_2} \end{bmatrix}_q |J|\, dL_1 dL_2 dL_3 =$$

$$\iiint_{L_1\, L_2\, L_3} \begin{bmatrix} \phi_{\nabla L_1} & \phi_{\nabla L_2} & \phi_{\nabla L_3} \end{bmatrix}_{q'} \begin{bmatrix} \frac{\partial \phi_{\nabla L_3}}{\partial L_2} - \frac{\partial \phi_{\nabla L_2}}{\partial L_3} \\ \frac{\partial \phi_{\nabla L_1}}{\partial L_3} - \frac{\partial \phi_{\nabla L_3}}{\partial L_1} \\ \frac{\partial \phi_{\nabla L_2}}{\partial L_1} - \frac{\partial \phi_{\nabla L_1}}{\partial L_2} \end{bmatrix}_q dL_1 dL_2 dL_3 \qquad (3.23)$$

since the kernels of these integrals are a combination of polynomial functions that depend only on local coordinates. For $\mathbb{F}_{\kappa e}$, $\mathbb{F}_{\kappa h}$, $\mathbb{F}_{\kappa e}^+$ and $\mathbb{F}_{\kappa h}^+$ matrices similar results can be obtained.

3.1.2   Boundary Conditions

The flux conditions which serve to connect adjacent fields, also serve to implement the most common boundary conditions. Following this approach, the implementation of the most useful boundary conditions is described below.

1. The interface of two elements with different ε and μ is handled in an indirect manner in the DGTD formulation, thanks to taking the same tangential components of the fields $\hat{\mathbf{n}}^m \times \boldsymbol{E}^{m*}$ and $\hat{\mathbf{n}}^m \times \boldsymbol{H}^{m*}$ in the flux integrals for two adjacent elements.

2. PEC boundary conditions on a face of an element m, require the tangential component of the electric field employed in the flux integrals to be null, and the tangential magnetic field to be continuous,

$$\hat{\mathbf{n}}^m \times \boldsymbol{E}^{m+} = -\hat{\mathbf{n}}^m \times \boldsymbol{E}^m \tag{3.24a}$$

$$\hat{\mathbf{n}}^m \times \boldsymbol{H}^{m+} = \hat{\mathbf{n}}^m \times \boldsymbol{H}^m \tag{3.24b}$$

   This is easily fulfilled, in a weak form, considering different κ and ν factors in the face of the m element in which PEC boundary condition is intended to be applied.

$$\kappa_{e\,\mathrm{PEC}}^m = 2\,\kappa_e^m, \quad \nu_{e\,\mathrm{PEC}}^m = 2\,\nu_e^m \tag{3.25a}$$

$$\kappa_{h\,\mathrm{PEC}}^m = 0, \qquad \nu_{h\,\mathrm{PEC}}^m = 0 \tag{3.25b}$$

3. PMC conditions are reciprocal of PEC,

$$\hat{\mathbf{n}}^m \times \boldsymbol{H}^{m+} = -\hat{\mathbf{n}}^m \times \boldsymbol{H}^m \tag{3.26a}$$

$$\hat{\mathbf{n}}^m \times \boldsymbol{E}^{m+} = \hat{\mathbf{n}}^m \times \boldsymbol{E}^m \tag{3.26b}$$

   and the expressions for the κ and ν factors,

$$\kappa_{h\,\mathrm{PMC}}^m = 2\,\kappa_h^m, \quad \nu_{h\,\mathrm{PMC}}^m = 2\,\nu_h^m \tag{3.27a}$$

$$\kappa_{e\,\mathrm{PMC}}^m = 0, \qquad \nu_{e\,\mathrm{PMC}}^m = 0 \tag{3.27b}$$

   Note that for the upwind flux, both for PEC and PMC, we must also assume $Y^{m+} = Y^m$ and $Z^{m+} = Z^m$.

4. Regarding the absorbing boundary conditions (ABC), the straightest ones are the so-called first-order Silver-Müller (SM-ABC) [139], which are based on considering that outside the computation domain the fields propagate as plane waves normally

to the interface, $\hat{\mathbf{n}} \times \hat{\mathbf{n}} \times \boldsymbol{E} = Z\left(\hat{\mathbf{n}} \times \boldsymbol{H}\right)$, $\hat{\mathbf{n}} \times \hat{\mathbf{n}} \times \boldsymbol{H} = -Y\left(\hat{\mathbf{n}} \times \boldsymbol{E}\right)$. For the upwind flux, this is directly implemented since it is equivalent to assuming that there is no contribution to the flux from outside the region of solution, only remaining $\boldsymbol{f}_{E,H}^{-}$ in (3.9).

$$Y^m \left(\hat{\mathbf{n}}^m \times \boldsymbol{E}^{m+}\right) = -\hat{\mathbf{n}}^m \times \hat{\mathbf{n}}^m \times \boldsymbol{H}^{m+} \Rightarrow \hat{\mathbf{n}}^m \times \boldsymbol{f}_E^+ = \hat{\mathbf{n}}^m \times \frac{Y^m \boldsymbol{E}^{m+} + \hat{\mathbf{n}}^m \times \boldsymbol{H}^{m+}}{Y^m + Y^{m+}} = 0 \tag{3.28a}$$

$$Z^m \left(\hat{\mathbf{n}}^m \times \boldsymbol{H}^{m+}\right) = \hat{\mathbf{n}}^m \times \hat{\mathbf{n}}^m \times \boldsymbol{E}^{m+} \Rightarrow \hat{\mathbf{n}}^m \times \boldsymbol{f}_H^+ = \hat{\mathbf{n}}^m \times \frac{Z^m \boldsymbol{H}^{m+} - \hat{\mathbf{n}}^m \times \boldsymbol{E}^{m+}}{Z^m + Z^{m+}} = 0 \tag{3.28b}$$

In case of the centered flux, the SM-ABC is implemented with a slightly different expression,

$$\hat{\mathbf{n}}^m \times \boldsymbol{E}^{m+} = -\frac{1}{Y^m}\left(\hat{\mathbf{n}}^m \times \hat{\mathbf{n}}^m \times \boldsymbol{H}^m\right) \tag{3.29a}$$

$$\hat{\mathbf{n}}^m \times \boldsymbol{H}^{m+} = \frac{1}{Z^m}\left(\hat{\mathbf{n}}^m \times \hat{\mathbf{n}}^m \times \boldsymbol{E}^m\right) \tag{3.29b}$$

In both cases the final formulation is the same. The SM-ABC, as the other boundary conditions previously shown, is easily implemented just modifying the values of the κ and ν factors,

$$\kappa_{e\,\text{SM-ABC}}^m = \kappa_{h\,\text{SM-ABC}}^m = \frac{1}{2} \tag{3.30a}$$

$$\nu_{h\,\text{SM-ABC}}^m = \frac{1}{2\,Y^m}, \quad \nu_{e\,\text{SM-ABC}}^m = \frac{1}{2\,Z^m} \tag{3.30b}$$

SM-ABC provides perfect analytically reflection coefficient for normal incidence, numerically reduced by the accuracy of the method, so depends on the order of the expansion functions p and the size of the elements h. This figure rapidly degrades when the angle of incidence changes from normal incidence [140]. In section 3.4.1, conformal uniaxial perfect matched layer (C-UPML) is developed and integrated in the scheme to overcome that limitation of the SM-ABC. It is important to note that both ABC (SM-ABC and C-UPML) can be used together [91, 92, 141, 142], improving the overall performance. This can be done with no cost in the DG framework, sice SM-ABC is just removing outside flux terms.

3.2   Numerical Fluxes Evaluation

The flux concept appears in CEM in finite volume time domain (FVTD) methods, [83, 84]. In FVTD, upwind flux evaluation is the mechanics to interchange information

between elements. Centered flux has been considered in DGTD due to its simplicity, versatility and efficiency, but raises the issues of spurious. In between of these two flux conditions, a generalized flux can be expressed [53, 63] with a parameter that penalized the jump of the vector tangential components between the elements.

Figure 3.1(a) shows the general case, without superficial sources, of the interface of two elements containing different materials. The objective is to evaluate $\hat{\mathbf{n}} \times \boldsymbol{E}^*$ and $\hat{\mathbf{n}} \times \boldsymbol{H}^*$, known as flux functions, for all point P located in $\partial \mathcal{T}_m$ needed to compute the flux coming from $\mathcal{T}_m+$ to $\mathcal{T}_m$ element, across the face $\partial \mathcal{T}_m$. The $\hat{\mathbf{n}} \times \boldsymbol{E}^{*+}$ and $\hat{\mathbf{n}} \times \boldsymbol{H}^{*+}$ flux functions refer to the reciprocal flux to $\mathcal{T}_m+$ coming from $\mathcal{T}_m$.

The flux functions are defined by solving exactly, as upwind does, or approximately, as centered or partial penalized, a one-dimensional Riemann problem in the direction $\hat{\mathbf{n}}$ to the face $\partial \mathcal{T}_m$, where $\hat{\mathbf{n}} \times \boldsymbol{E}^m$ and $\hat{\mathbf{n}} \times \boldsymbol{E}^{m+}$, and $\hat{\mathbf{n}} \times \boldsymbol{H}^m$ and $\hat{\mathbf{n}} \times \boldsymbol{H}^{m+}$, will be discontinuous.

Let us define a local coordinates, t_1, t_2 and n, and the associated orthonormal local vector base $(\hat{\mathbf{t}}_1, \hat{\mathbf{t}}_2, \hat{\mathbf{n}})$ as,

$$\hat{\mathbf{t}}_1 = \frac{\partial \boldsymbol{r}}{\partial t_1} \left| \frac{\partial \boldsymbol{r}}{\partial t_1} \right|^{-1} \tag{3.31a}$$

$$\hat{\mathbf{t}}_2 = \frac{\partial \boldsymbol{r}}{\partial t_2} \left| \frac{\partial \boldsymbol{r}}{\partial t_2} \right|^{-1} \tag{3.31b}$$

$$\hat{\mathbf{n}} = \hat{\mathbf{t}}_1 \times \hat{\mathbf{t}}_2 \tag{3.31c}$$

Note that infinite local vector bases could be found, the idea is to decompose into normal $(\hat{\mathbf{n}})$ and tangential $(\hat{\mathbf{t}}_1, \hat{\mathbf{t}}_2)$ components along the face $\partial \mathcal{T}_m$, so any of the infinite local vector bases could be considered. The transformation matrices, $\bar{\bar{R}}$ and $\bar{\bar{R}}^{-1}$, between the local vectorial base of (3.31) and the Cartesian vectorial base can be defined as,

$$\begin{pmatrix} \hat{\mathbf{x}} \\ \hat{\mathbf{y}} \\ \hat{\mathbf{z}} \end{pmatrix} = \bar{\bar{R}} \begin{pmatrix} \hat{\mathbf{t}}_1 \\ \hat{\mathbf{t}}_2 \\ \hat{\mathbf{n}} \end{pmatrix}, \qquad \begin{pmatrix} \hat{\mathbf{t}}_1 \\ \hat{\mathbf{t}}_2 \\ \hat{\mathbf{n}} \end{pmatrix} = \bar{\bar{R}}^{-1} \begin{pmatrix} \hat{\mathbf{x}} \\ \hat{\mathbf{y}} \\ \hat{\mathbf{z}} \end{pmatrix} \tag{3.32}$$

In figure 3.1(b), impressed electric and magnetic surface current densities ($\boldsymbol{J}_s$ and $\boldsymbol{M}_s$) along the face $\partial \mathcal{T}_m$, have been included in the setup. These current sources must be considered in the flux evaluation, and the discontinuity in the tangential components of

(a) Flux evaluation setup, without sources.   (b) Flux evaluation setup, with sources.
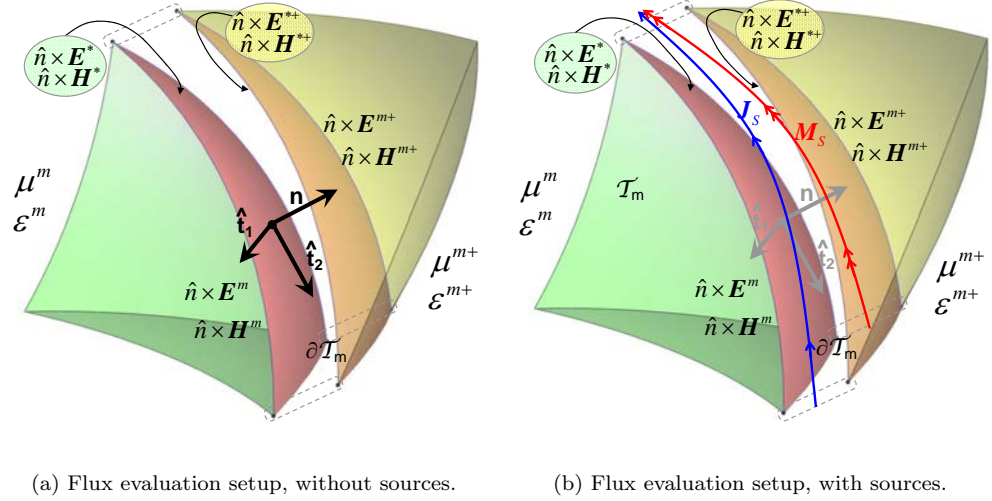
FIGURE 3.1: Flux evaluation setups

Both tetrahedra are physically in contact, have been represented separated just for clarification. The subscript ^{m} in the local vectors $\hat{\mathbf{t}}_1, \hat{\mathbf{t}}_2$ and $\hat{\mathbf{n}}$ has been removed for the same purpose.

the fields shall be introduced, fulfilling the well-known boundary conditions,

$$\hat{\mathbf{n}} \times (\boldsymbol{E}_2 - \boldsymbol{E}_1) = -\boldsymbol{M}_s \tag{3.33a}$$

$$\hat{\mathbf{n}} \times (\boldsymbol{H}_2 - \boldsymbol{H}_1) = \boldsymbol{J}_s \tag{3.33b}$$

The subindexes 1 and 2 correspond to the semi-spaces at one side and the other of the surface where the currents are flowing. $\boldsymbol{J}_s$ will produce a discontinuity in the vector $\hat{\mathbf{n}} \times \boldsymbol{H}$, and $\boldsymbol{M}_s$ will produce a discontinuity in the vector $\hat{\mathbf{n}} \times \boldsymbol{E}$.

In this section, numerical flux evaluation expressions are formulated for isotropic mediums, including superficial current sources.

3.2.1 Centered Flux Evaluation

The centered flux [107] can be evaluated just by averaging the solutions of the fields at both sides of the interface.

The expressions for the centered fluxes on the outer boundary face of the problem of figure 3.1(a) are the following,

$$\hat{\mathbf{n}} \times \boldsymbol{E}^* = \hat{\mathbf{n}} \times \boldsymbol{E}^{*+} = \hat{\mathbf{n}} \times \frac{\boldsymbol{E}^m + \boldsymbol{E}^{m+}}{2} \tag{3.34a}$$

$$\hat{\mathbf{n}} \times \boldsymbol{H}^* = \hat{\mathbf{n}} \times \boldsymbol{E}^{*+} = \hat{\mathbf{n}} \times \frac{\boldsymbol{H}^m + \boldsymbol{H}^{m+}}{2} \tag{3.34b}$$

Figure 3.1(b) shows the general case with surface current sources on the interface of the two elements. The flux expressions must fulfilled with the boundary conditions (3.33) as follows,

$$\hat{\mathbf{n}} \times \left(\boldsymbol{E}^* - \boldsymbol{E}^{*+} \right) = \boldsymbol{M}_s \tag{3.35a}$$

$$\hat{\mathbf{n}} \times \left(\boldsymbol{H}^* - \boldsymbol{H}^{*+} \right) = -\boldsymbol{J}_s \tag{3.35b}$$

Averaging again the solutions at both sides of the interface results,

$$\hat{\mathbf{n}} \times \boldsymbol{E}^* = \frac{\hat{\mathbf{n}} \times \boldsymbol{E}^m}{2} + \frac{\hat{\mathbf{n}} \times \boldsymbol{E}^{m+} + \boldsymbol{M}_s}{2} = \frac{\hat{\mathbf{n}} \times \left(\boldsymbol{E}^m + \boldsymbol{E}^{m+} \right) + \boldsymbol{M}_s}{2} \tag{3.36a}$$

$$\hat{\mathbf{n}} \times \boldsymbol{H}^* = \frac{\hat{\mathbf{n}} \times \boldsymbol{H}^m}{2} + \frac{\hat{\mathbf{n}} \times \boldsymbol{H}^{m+} - \boldsymbol{J}_s}{2} = \frac{\hat{\mathbf{n}} \times \left(\boldsymbol{H}^m + \boldsymbol{H}^{m+} \right) - \boldsymbol{J}_s}{2} \tag{3.36b}$$

The reciprocal flux expression can be written as,

$$\hat{\mathbf{n}} \times \boldsymbol{E}^{*+} = \frac{\hat{\mathbf{n}} \times \left(\boldsymbol{E}^m + \boldsymbol{E}^{m+} \right) - \boldsymbol{M}_s}{2} \tag{3.37a}$$

$$\hat{\mathbf{n}} \times \boldsymbol{H}^{*+} = \frac{\hat{\mathbf{n}} \times \left(\boldsymbol{H}^m + \boldsymbol{H}^{m+} \right) + \boldsymbol{J}_s}{2} \tag{3.37b}$$

It is important to note that all the centered flux functions expressed above do not depend on material parameters, so these expressions are valid for any kind of materials; dispersive, anisotropic, ...

3.2.2   Upwind Flux Evaluation

One standard approach for the development of numerical schemes to deal with multidimensional and/or hyperbolic problems with source terms [1], is to use a fractional-step or operation-splitting method [143]. In this approach simpler problems are somehow solved, and the combination of them drives to a global scheme that approximates the solution of the full problem.

Let us consider the time-domain Maxwell's curl equations, assuming there is net electric charge or current ($\sigma_e \neq 0$), considering heterogeneous isotropic materials, with μ and ε

---

[1]Referred to source terms as those included in the formulation apart from the ones belonging to the hyperbolic conservative problem. For instance, dissipative terms due to electric or magnetic conductivity, or new terms included in the formulation for the treatment of special materials as dispersive or PML mediums.

depending on space, where a electromagnetic wave is propagating.

$$\mu\frac{\partial \boldsymbol{H}}{\partial t} + \nabla \times \boldsymbol{E} = 0 \tag{3.38a}$$

$$\varepsilon\frac{\partial \boldsymbol{E}}{\partial t} - \nabla \times \boldsymbol{H} + \sigma_e \boldsymbol{E} = 0 \tag{3.38b}$$

The electric and magnetic field vectors are expressed in the local vectorial base described in figures 3.1, $\boldsymbol{E} = (E_{t_1}, E_{t_2}, E_n)$ and $\boldsymbol{H} = (H_{t_1}, H_{t_2}, H_n)$. The ∇ operator can be decomposed into two terms,

$$\nabla = \frac{\partial}{\partial n}\hat{\mathbf{n}} + \nabla_S \tag{3.39}$$

where $\frac{\partial}{\partial n} = \nabla \cdot \hat{\mathbf{n}}$ and ∇_S denote the normal and surface derivatives with respect to the local coordinates, respectively. The decomposition of the term $\nabla \times \boldsymbol{E}$ results (a dual expression holds for the $\nabla \times \boldsymbol{H}$ term),

$$
\begin{aligned}
\nabla \times \boldsymbol{E} &= \frac{\partial}{\partial n}\hat{\mathbf{n}} \times \boldsymbol{E} + \nabla_S \times \boldsymbol{E} \\
\frac{\partial}{\partial n}\hat{\mathbf{n}} \times \boldsymbol{E} &= -\partial_n E_{t_2}\,\hat{\mathbf{t}}_1 + \partial_n E_{t_1}\,\hat{\mathbf{t}}_2 \\
\nabla_S \times \boldsymbol{E} &= \partial_{t_2} E_n\,\hat{\mathbf{t}}_1 - \partial_{t_1} E_n\,\hat{\mathbf{t}}_2 + (\partial_{t_1} E_{t_2} - \partial_{t_2} E_{t_1})\,\hat{\mathbf{n}}
\end{aligned}
\tag{3.40}
$$

Time-domain Maxwell's curl equations of (3.38) can be rewritten as,

$$\frac{\partial \boldsymbol{H}}{\partial t} + \frac{1}{\mu}\frac{\partial}{\partial n}\hat{\mathbf{n}} \times \boldsymbol{E} + \frac{1}{\mu}\nabla_S \times \boldsymbol{E} = 0 \tag{3.41a}$$

$$\frac{\partial \boldsymbol{E}}{\partial t} - \frac{1}{\varepsilon}\frac{\partial}{\partial n}\hat{\mathbf{n}} \times \boldsymbol{H} - \frac{1}{\varepsilon}\nabla_S \times \boldsymbol{H} + \frac{\sigma_e}{\varepsilon}\boldsymbol{E} = 0 \tag{3.41b}$$

A operation-splitting method for (3.41) is applied by first splitting the equations system into two subproblems that can be solved independently. In this case we take these to be:

Problem A:
$$\frac{\partial \boldsymbol{H}}{\partial t} + \frac{1}{\mu}\frac{\partial}{\partial n}\hat{\mathbf{n}} \times \boldsymbol{E} = 0 \tag{3.42a}$$

$$\frac{\partial \boldsymbol{E}}{\partial t} - \frac{1}{\varepsilon}\frac{\partial}{\partial n}\hat{\mathbf{n}} \times \boldsymbol{H} = 0 \tag{3.42b}$$

Problem B:
$$\frac{\partial \boldsymbol{H}}{\partial t} + \frac{1}{\mu}\nabla_S \times \boldsymbol{E} = 0 \tag{3.43a}$$

$$\frac{\partial \boldsymbol{E}}{\partial t} - \frac{1}{\varepsilon}\nabla_S \times \boldsymbol{H} + \frac{\sigma_e}{\varepsilon}\boldsymbol{E} = 0 \tag{3.43b}$$

The idea of the operation-splitting method is that different methods can be used for each subproblem and combined to obtain a global scheme. Hence, we split the general problem

(3.38) into a homogeneous conservation law, that includes the Riemann problem, and the rest, then we can use standard methods for each.

With this approach, we isolate the discontinuous problem from the rest, which is fully continuous. It is important to remark that this separation can always be done, although other source terms were considered in the formulation. The expressions derived bellow, therefore, are valid in a wide sense for any isotropic medium (dissipative, dispersive, PML and so on), as soon as Problems A is identified. Notice also that different subproblems could have been defined, for instance the source terms can be extracted in a new subproblem from Problem B. However, the proposed separation of problems is enough for our purpose, since only Problem A is required to derive upwind flux evaluation expressions.

We intend to solve Problem A in the scenario shown in figure 3.1, allowing discontinuities of the fields. This makes that some singularities arise in the derivative terms $\frac{\partial}{\partial n}$. This fact drives to the Riemann problem. Problem A can be rewritten as a first-order hyperbolic multidimensional system of four PDE,

$$\partial_t H_{t_1} - \frac{1}{\mu}\partial_n E_{t_2} = 0 \tag{3.44a}$$

$$\partial_t H_{t_2} + \frac{1}{\mu}\partial_n E_{t_1} = 0 \tag{3.44b}$$

$$\partial_t E_{t_1} + \frac{1}{\varepsilon}\partial_n H_{t_2} = 0 \tag{3.44c}$$

$$\partial_t E_{t_2} - \frac{1}{\varepsilon}\partial_n H_{t_1} = 0 \tag{3.44d}$$

where normal components have been removed, since are not part of Problem A. The one-dimensional Riemann problem can be expressed in a compact manner as,

$$\partial_t \bar{q} + \bar{\mathbb{A}}_n \partial_n \bar{q} = 0 \tag{3.45}$$

with $\bar{q} = (H_{t_1}, H_{t_2}, E_{t_1}, E_{t_2})^T$ and $\bar{\mathbb{A}}_n$ matrix,

$$\bar{\mathbb{A}}_n = \begin{pmatrix} 0 & 0 & 0 & -\frac{1}{\mu} \\ 0 & 0 & \frac{1}{\mu} & 0 \\ 0 & \frac{1}{\varepsilon} & 0 & 0 \\ -\frac{1}{\varepsilon} & 0 & 0 & 0 \end{pmatrix} \tag{3.46}$$

The equation system (3.45) is hyperbolic because the matrix $\bar{\mathbb{A}}_n$ has 4 real eigenvalues (λ_p). We refer to the corresponding set of 4 linearly independent right eigenvectors as (r_p). Any vector $\bar{q}$ or ($\hat{\mathbf{n}} \times \boldsymbol{H}$ and $\hat{\mathbf{n}} \times \boldsymbol{E}$) can be uniquely decomposed as linear combination of these eigenvectors, what provides a decomposition into distinct waves.

The corresponding eigenvalues of $\bar{\mathbb{A}}_n$ give the wave speeds at which each wave propagates in the medium. There are two eigenvalues $\frac{-1}{\sqrt{\mu\varepsilon}}$ and two eigenvalues $\frac{+1}{\sqrt{\mu\varepsilon}}$. The minus sign means that the wave is coming into the element and the plus sign the wave is going out.

$$
\begin{aligned}
\lambda_1 = \lambda_2 = \frac{-1}{\sqrt{\mu\varepsilon}}; \qquad & r_1 = (0, -Y, 1, 0)^T; \qquad r_2 = (Y, 0, 0, 1)^T \\
\lambda_3 = \lambda_4 = \frac{1}{\sqrt{\mu\varepsilon}}; \qquad & r_3 = (0, Y, 1, 0)^T; \qquad r_4 = (-Y, 0, 0, 1)^T
\end{aligned}
\tag{3.47}
$$

where $Z = \sqrt{\frac{\mu}{\varepsilon}} = \frac{1}{Y}$.

It important to note that (3.45) corresponds to a variable-coefficient linear system. We can identified a matrix $\bar{\mathbb{A}}_n^m$ in $\mathcal{T}_m$ and a possible different matrix $\bar{\mathbb{A}}_n^{m+}$ in $\mathcal{T}_{m+}$. Solving the Riemann problem consists of fulfilling the Rankine-Hugoniot jump condition [143] at both sides of $\partial\mathcal{T}_m$, which is easily solved in terms of the eigenvalues and eigenvectors of the matrices $\bar{\mathbb{A}}_n^m$ and $\bar{\mathbb{A}}_n^{m+}$. The Rankine-Hugoniot condition means decomposing the jumps or discontinuities into a linear combinations of the eigenvectors.

The solution of the Riemann problem are the intermediate states ($\bar{q}^*$ and $\bar{q}^{*+}$). Figure 3.2 shows the domains for these solutions. The jumps between the intermediate states and the values at both sides of $\partial\mathcal{T}_m$, must be a linear combination of the eigenvectors associated to the negative eigenvalues for the element $\mathcal{T}_m$, and the eigenvectors associated to the positive eigenvalues for the element $\mathcal{T}_{m+}$. Hence we must have,

$$
\bar{q}^* - \bar{q}^m = \alpha_1^m r_1^m + \alpha_2^m r_2^m \tag{3.48a}
$$

$$
\bar{q}^{m+} - \bar{q}^{*+} = \alpha_3^{m+} r_3^{m+} + \alpha_4^{m+} r_4^{m+} \tag{3.48b}
$$

for some scalar coefficients α_1^m, α_2^m, α_3^{m+} and α_4^{m+}. In order to solve the equation system (3.48), we need a relation between $\bar{q}^*$ and $\bar{q}^{*+}$. If no surface current sources are present, as in figure 3.1(a), then $\bar{q}^* = \bar{q}^{*+}$, otherwise, if there is surface current sources, as in figure 3.1(b), the jumps introduced by the boundary conditions of (3.35), must be considered.

The results for the scalar coefficients without surface current sources are the following,

$$
\begin{aligned}
\alpha_1^m &= \frac{\left(H_{t_2}^m - H_{t_2}^{m+}\right) - Y^{m+}\left(E_{t_1}^m - E_{t_1}^{m+}\right)}{Y^m + Y^{m+}} & \alpha_2^m &= -\frac{\left(H_{t_1}^m - H_{t_1}^{m+}\right) + Y^{m+}\left(E_{t_2}^m - E_{t_2}^{m+}\right)}{Y^m + Y^{m+}} \\
\alpha_3^{m+} &= -\frac{\left(H_{t_2}^m - H_{t_2}^{m+}\right) + Y^m\left(E_{t_1}^m - E_{t_1}^{m+}\right)}{Y^m + Y^{m+}} & \alpha_4^{m+} &= \frac{\left(H_{t_1}^m - H_{t_1}^{m+}\right) - Y^m\left(E_{t_2}^m - E_{t_2}^{m+}\right)}{Y^m + Y^{m+}}
\end{aligned}
\tag{3.49}
$$
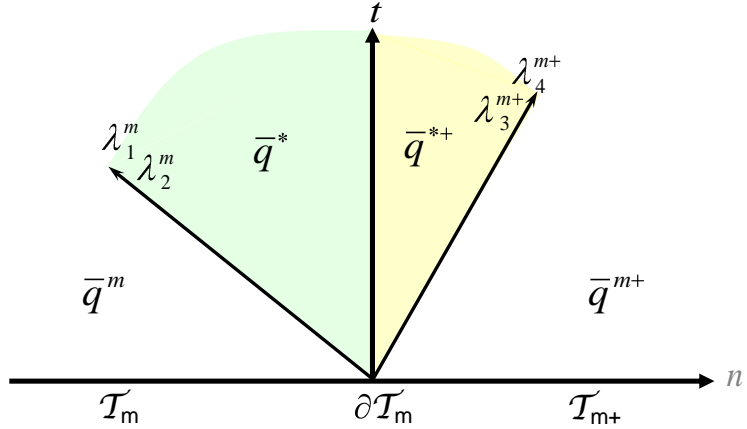
FIGURE 3.2: Structure of the solution to the Riemann problem for homogeneous materials (variable-coefficient), in the space-time plane (n-t plane). $\partial \mathcal{T}_m$ shows the interface between the two different elements. The waves propagate at its speed in each material. Between the waves are two states $\bar{q}^*$, $\bar{q}^{*+}$.

Using equations (3.48), the solutions for each tangential field component are,

$$H_{t_1}^* = H_{t_1}^{*+} = \frac{Z^m H_{t_1}^m + Z^{m+} H_{t_1}^{m+} - \left(E_{t_2}^m - E_{t_2}^{m+}\right)}{Z^m + Z^{m+}} \tag{3.50a}$$

$$H_{t_2}^* = H_{t_2}^{*+} = \frac{Z^m H_{t_2}^m + Z^{m+} H_{t_2}^{m+} + \left(E_{t_1}^m - E_{t_1}^{m+}\right)}{Z^m + Z^{m+}} \tag{3.50b}$$

$$E_{t_1}^* = E_{t_1}^{*+} = \frac{Y^m E_{t_1}^m + Y^{m+} E_{t_1}^{m+} + \left(H_{t_2}^m - H_{t_2}^{m+}\right)}{Y^m + Y^{m+}} \tag{3.50c}$$

$$E_{t_2}^* = E_{t_2}^{*+} = \frac{Y^m E_{t_2}^m + Y^{m+} E_{t_2}^{m+} - \left(H_{t_1}^m - H_{t_1}^{m+}\right)}{Y^m + Y^{m+}} \tag{3.50d}$$

which can be expressed in electric and magnetic fields format as,

$$\hat{\mathbf{n}} \times \boldsymbol{E}^* = \hat{\mathbf{n}} \times \boldsymbol{E}^{*+} = \hat{\mathbf{n}} \times \frac{Y^m \boldsymbol{E}^m + Y^{m+} \boldsymbol{E}^{m+} + \hat{\mathbf{n}} \times \left(\boldsymbol{H}^{m+} - \boldsymbol{H}^m\right)}{Y^m + Y^{m+}} \tag{3.51a}$$

$$\hat{\mathbf{n}} \times \boldsymbol{H}^* = \hat{\mathbf{n}} \times \boldsymbol{H}^{*+} = \hat{\mathbf{n}} \times \frac{Z^m \boldsymbol{H}^m + Z^{m+} \boldsymbol{H}^{m+} - \hat{\mathbf{n}} \times \left(\boldsymbol{E}^{m+} - \boldsymbol{E}^m\right)}{Z^m + Z^{m+}} \tag{3.51b}$$

Finally, a general form of the solution of the Riemann problem, with surface electric and magnetic current densities, appears bellow.

$$\hat{\mathbf{n}} \times \boldsymbol{E}^* = \frac{\hat{\mathbf{n}} \times \left(Y^m \boldsymbol{E}^m + Y^{m+} \boldsymbol{E}^{m+}\right) + Y^{m+} \boldsymbol{M}_s + \hat{\mathbf{n}} \times \left[\hat{\mathbf{n}} \times \left(\boldsymbol{H}^{m+} - \boldsymbol{H}^m\right) - \boldsymbol{J}_s\right]}{Y^m + Y^{m+}}$$
$$\text{(3.52a)}$$

$$\hat{\mathbf{n}} \times \boldsymbol{H}^* = \frac{\hat{\mathbf{n}} \times \left(Z^m \boldsymbol{H}^m + Z^{m+} \boldsymbol{H}^{m+}\right) - Z^{m+} \boldsymbol{J}_s - \hat{\mathbf{n}} \times \left[\hat{\mathbf{n}} \times \left(\boldsymbol{E}^{m+} - \boldsymbol{E}^m\right) + \boldsymbol{M}_s\right]}{Z^m + Z^{m+}}$$
$$\text{(3.52b)}$$

$$\hat{\mathbf{n}} \times \boldsymbol{E}^{*+} = \frac{\hat{\mathbf{n}} \times \left(Y^m \boldsymbol{E}^m + Y^{m+} \boldsymbol{E}^{m+}\right) - Y^{m+} \boldsymbol{M}_s + \hat{\mathbf{n}} \times \left[\hat{\mathbf{n}} \times \left(\boldsymbol{H}^{m+} - \boldsymbol{H}^m\right) - \boldsymbol{J}_s\right]}{Y^m + Y^{m+}}$$
$$\text{(3.52c)}$$

$$\hat{\mathbf{n}} \times \boldsymbol{H}^{*+} = \frac{\hat{\mathbf{n}} \times \left(Z^m \boldsymbol{H}^m + Z^{m+} \boldsymbol{H}^{m+}\right) + Z^{m+} \boldsymbol{J}_s - \hat{\mathbf{n}} \times \left[\hat{\mathbf{n}} \times \left(\boldsymbol{E}^{m+} - \boldsymbol{E}^m\right) + \boldsymbol{M}_s\right]}{Z^m + Z^{m+}}$$
$$\text{(3.52d)}$$

3.2.3 Partial Penalized Flux Evaluation

The partial penalized flux [53, 63, 69, 70] generalizes both previous schemes. Two different terms can be clearly identified in all upwind flux expressions. Considering (3.52), the same holds for (3.51), and introducing the penalty parameter, τ, may be written the general flux evaluation expressions as,

$$\hat{\mathbf{n}} \times \boldsymbol{E}^* = \frac{\hat{\mathbf{n}} \times \left(Y^m \boldsymbol{E}^m + Y^{m+} \boldsymbol{E}^{m+}\right) + Y^{m+} \boldsymbol{M}_s}{Y^m + Y^{m+}} - \tau \frac{\hat{\mathbf{n}} \times \left[\hat{\mathbf{n}} \times \left(\boldsymbol{H}^m - \boldsymbol{H}^{m+}\right) + \boldsymbol{J}_s\right]}{Y^m + Y^{m+}}$$
$$\text{(3.53a)}$$

$$\hat{\mathbf{n}} \times \boldsymbol{H}^* = \frac{\hat{\mathbf{n}} \times \left(Z^m \boldsymbol{H}^m + Z^{m+} \boldsymbol{H}^{m+}\right) - Z^{m+} \boldsymbol{J}_s}{Z^m + Z^{m+}} + \tau \frac{\hat{\mathbf{n}} \times \left[\hat{\mathbf{n}} \times \left(\boldsymbol{E}^m - \boldsymbol{E}^{m+}\right) - \boldsymbol{M}_s\right]}{Z^m + Z^{m+}}$$
$$\text{(3.53b)}$$

$$\hat{\mathbf{n}} \times \boldsymbol{E}^{*+} = \frac{\hat{\mathbf{n}} \times \left(Y^m \boldsymbol{E}^m + Y^{m+} \boldsymbol{E}^{m+}\right) - Y^{m+} \boldsymbol{M}_s}{Y^m + Y^{m+}} - \tau \frac{\hat{\mathbf{n}} \times \left[\hat{\mathbf{n}} \times \left(\boldsymbol{H}^m - \boldsymbol{H}^{m+}\right) + \boldsymbol{J}_s\right]}{Y^m + Y^{m+}}$$
$$\text{(3.53c)}$$

$$\hat{\mathbf{n}} \times \boldsymbol{H}^{*+} = \frac{\hat{\mathbf{n}} \times \left(Z^m \boldsymbol{H}^m + Z^{m+} \boldsymbol{H}^{m+}\right) + Z^{m+} \boldsymbol{J}_s}{Y^m + Y^{m+}} + \tau \frac{\hat{\mathbf{n}} \times \left[\hat{\mathbf{n}} \times \left(\boldsymbol{E}^m - \boldsymbol{E}^{m+}\right) - \boldsymbol{M}_s\right]}{Z^m + Z^{m+}}$$
$$\text{(3.53d)}$$

where $\tau = 1$ reflects the upwind flux, while $\tau = 0$ can be considered a central flux evaluation expression. Note that (3.53) with $\tau = 0$ is not rigourously (3.36) and (3.37), some differences appear in the media interfaces, but both expressions are equivalent in practice.

The penalty parameter plays the role of penalize the jump terms ($\hat{\mathbf{n}} \times \left(\boldsymbol{E}^m - \boldsymbol{E}^{m+}\right)$ and $\hat{\mathbf{n}} \times \left(\boldsymbol{H}^m - \boldsymbol{H}^{m+}\right)$). This terms stabilize the solution, and eliminate spurious modes that

appear with centered flux introducing some dissipation, much higher for the spurious modes than for the physical ones. A complete analysis of this topic appears in section 3.5.1.

3.3 Discontinuous Galerkin for Anisotropic Materials

Up to now, most formulations of the DGTD method are restricted to isotropic and, in some cases, dispersive materials [95, 113]. The treatment of anisotropic materials within a DGTD approach was discussed in [103], where the authors employed central flux as has been deduced in section 3.2.1. But, central flux limitations are very well-known and recently, in [101], upwind flux for 2-D systems was derived. Here, a generalized upwind flux expressions in 3-D are derived, and the scheme reported in [101] could be seen as a special case.

Let us consider in this case, the time-domain Maxwell's curl equations, where we introduce the electric permittivity and the magnetic permeability tensors, which are varying in space and both defined symmetric positive ($\bar{\bar{\varepsilon}}$ and $\bar{\bar{\mu}}$).

$$\bar{\bar{\mu}}\frac{\partial \boldsymbol{H}}{\partial t} + \nabla \times \boldsymbol{E} = 0 \tag{3.54a}$$

$$\bar{\bar{\varepsilon}}\frac{\partial \boldsymbol{E}}{\partial t} - \nabla \times \boldsymbol{H} = 0 \tag{3.54b}$$

the medium is considered lossless, electric and magnetic conductivity equal to zero, for simplicity.

In this section, flux evaluation expressions for DG with anisotropic materials will be developed first, and then, the complete semi-discrete scheme will be formulated.

3.3.1 Flux Evaluation in Anisotropic Materials

In order to extend the application of DG method to anisotropic materials in 3-D, it is necessary to develop the expressions for the upwind flux case. The expressions for the centered flux shown in section 3.2.1 are also valid for anisotropic materials, and the partial penalized flux expressions are easily obtained from upwind flux ones, just including the factor τ in the dissipative terms.

Considering the setup of the figures 3.1, we can define the $\bar{\bar{\varepsilon}}$ and $\bar{\bar{\mu}}$, also the inverse of the tensors, in the local vectorial base described in figure 3.1 as,

$$\bar{\bar{\varepsilon}} = \begin{pmatrix} \epsilon_{11} & \epsilon_{12} & \epsilon_{1n} \\ \epsilon_{21} & \epsilon_{22} & \epsilon_{2n} \\ \epsilon_{n1} & \epsilon_{n2} & \epsilon_{nn} \end{pmatrix} \qquad \bar{\bar{\varepsilon}}^{-1} = \begin{pmatrix} \epsilon'_{11} & \epsilon'_{12} & \epsilon'_{1n} \\ \epsilon'_{21} & \epsilon'_{22} & \epsilon'_{2n} \\ \epsilon'_{n1} & \epsilon'_{n2} & \epsilon'_{nn} \end{pmatrix} \tag{3.55a}$$

$$\bar{\bar{\mu}} = \begin{pmatrix} \mu_{11} & \mu_{12} & \mu_{1n} \\ \mu_{21} & \mu_{22} & \mu_{2n} \\ \mu_{n1} & \mu_{n2} & \mu_{nn} \end{pmatrix} \qquad \bar{\bar{\mu}}^{-1} = \begin{pmatrix} \mu'_{11} & \mu'_{12} & \mu'_{1n} \\ \mu'_{21} & \mu'_{22} & \mu'_{2n} \\ \mu'_{n1} & \mu'_{n2} & \mu'_{nn} \end{pmatrix} \tag{3.55b}$$

Following the same approach that in the isotropic materials case, a operation-splitting method for (3.54) is applied by first splitting the equations system into two subproblems. For this propose, we decompose the rotational terms with (3.40), and split (3.54) in the following problems:

Problem A:
$$\frac{\partial \boldsymbol{H}}{\partial t} + \bar{\bar{\mu}}^{-1}\frac{\partial}{\partial n}\hat{\mathbf{n}} \times \boldsymbol{E} = 0 \tag{3.56a}$$

$$\frac{\partial \boldsymbol{E}}{\partial t} - \bar{\bar{\varepsilon}}^{-1}\frac{\partial}{\partial n}\hat{\mathbf{n}} \times \boldsymbol{H} = 0 \tag{3.56b}$$

Problem B:
$$\frac{\partial \boldsymbol{H}}{\partial t} + \bar{\bar{\mu}}^{-1}\nabla_S \times \boldsymbol{E} = 0 \tag{3.57a}$$

$$\frac{\partial \boldsymbol{E}}{\partial t} - \bar{\bar{\varepsilon}}^{-1}\nabla_S \times \boldsymbol{H} = 0 \tag{3.57b}$$

Following exactly the same procedure that has been applied in the case of isotropic materials, we can derive the one-dimension Riemann problem of (3.45), where in this case the $\bar{\mathbb{A}}_n$ matrix looks like,

$$\bar{\mathbb{A}}_n = \begin{pmatrix} 0 & 0 & \mu'_{12} & -\mu'_{11} \\ 0 & 0 & \mu'_{22} & -\mu'_{21} \\ -\epsilon'_{12} & \epsilon'_{11} & 0 & 0 \\ -\epsilon'_{22} & \epsilon'_{21} & 0 & 0 \end{pmatrix} \tag{3.58}$$

and the expression for the four PDEs are,

$$\partial_t H_{t_1} + \mu'_{12}\partial_n E_{t_1} - \mu'_{11}\partial_n E_{t_2} = 0 \tag{3.59a}$$

$$\partial_t H_{t_2} + \mu'_{22}\partial_n E_{t_1} - \mu'_{21}\partial_n E_{t_2} = 0 \tag{3.59b}$$

$$\partial_t E_{t_1} - \epsilon'_{12}\partial_n H_{t_1} + \epsilon'_{11}\partial_n H_{t_2} = 0 \tag{3.59c}$$

$$\partial_t E_{t_2} - \epsilon'_{22}\partial_n H_{t_1} + \epsilon'_{21}\partial_n H_{t_2} = 0 \tag{3.59d}$$

Let us define some 2×2 matrices to clarify the expressions.

$$\bar{\bar{\epsilon}}_2^{-1} = \begin{pmatrix} \epsilon'_{11} & \epsilon'_{12} \\ \epsilon'_{21} & \epsilon'_{22} \end{pmatrix}, \qquad \bar{\bar{\mu}}_2^{-1} = \begin{pmatrix} \mu'_{11} & \mu'_{12} \\ \mu'_{21} & \mu'_{22} \end{pmatrix} \tag{3.60a}$$

$$\mathbb{D}_2 = \begin{pmatrix} 0 & -1 \\ 1 & 0 \end{pmatrix}, \qquad \mathbb{D}_2^{-1} = \mathbb{D}_2^T = -\mathbb{D}_2 = \begin{pmatrix} 0 & 1 \\ -1 & 0 \end{pmatrix} \tag{3.60b}$$

We can now express $\bar{\mathbb{A}}_n$ in a compact manner as,

$$\bar{\mathbb{A}}_n = \begin{pmatrix} \mathbb{O}_2 & \bar{\bar{\mu}}_2^{-1}\mathbb{D}_2 \\ \bar{\bar{\epsilon}}_2^{-1}\mathbb{D}_2^{-1} & \mathbb{O}_2 \end{pmatrix} \tag{3.61}$$

where $\mathbb{O}_2$ is a 2×2 matrix with all elements equal to 0.

As it has been previously explained, to solve the Riemann problem it is necessary to know the 4 real eigenvalues (λ_p) and the corresponding set of 4 linearly independent right eigenvectors (r_p) of the matrix $\bar{\mathbb{A}}_n$. This is the same that diagonalize the matrix $\bar{\mathbb{A}}_n$ in the following way,

$$\bar{\mathbb{A}}_n = \mathbb{R}_{\bar{\mathbb{A}}_n} \Lambda_{\bar{\mathbb{A}}_n} \mathbb{R}_{\bar{\mathbb{A}}_n}^{-1} \tag{3.62}$$

where each column of the $\mathbb{R}_{\bar{\mathbb{A}}_n}$ corresponds to one right eigenvector, and each element of the diagonal of the matrix $\Lambda_{\bar{\mathbb{A}}_n}$ is the associated eigenvalue.

The eigenvalues of $\bar{\mathbb{A}}_n$ are precisely the solutions λ to the equation

$$\det\left(\bar{\mathbb{A}}_n - \lambda\mathbb{I}_4\right) = 0 \tag{3.63}$$

Here det is the determinant operation and $\mathbb{I}_n$ are $n \times n$ identity matrices.

Operating with the blocks matrices defined above we find,

$$\det\left(\bar{\mathbb{A}}_n - \lambda\mathbb{I}_4\right) = -\det\left(\bar{\bar{\epsilon}}_2^{-1}\mathbb{D}_2^{-1}\bar{\bar{\mu}}_2^{-1}\mathbb{D}_2 - \lambda^2\mathbb{I}_2\right) = -\det\left(\mathbb{M}_2 - \lambda^2\mathbb{I}_2\right) = 0 \tag{3.64}$$

where we have defined a new matrix $\mathbb{M}_2$, whose eigenvalues $(c_1^2$ and $c_2^2)$ are the square of the eigenvalues of $\bar{\mathbb{A}}_n$ matrix $(-c_1, -c_2, c_1$ and $c_2)$. Thus, we can made following definitions,

$$\mathbb{C}_2 = \begin{pmatrix} c_1 & 0 \\ 0 & c_2 \end{pmatrix}, \qquad \mathbb{M}_2 = \bar{\bar{\epsilon}}_2^{-1}\mathbb{D}_2^{-1}\bar{\bar{\mu}}_2^{-1}\mathbb{D}_2 \tag{3.65}$$

and also need to diagonalize the matrix $\mathbb{M}_2$ which can be expressed as,

$$\mathbb{M}_2 = \mathbb{R}_{\mathbb{M}_2}\mathbb{C}_2\mathbb{C}_2\mathbb{R}_{\mathbb{M}_2}^{-1} \tag{3.66}$$
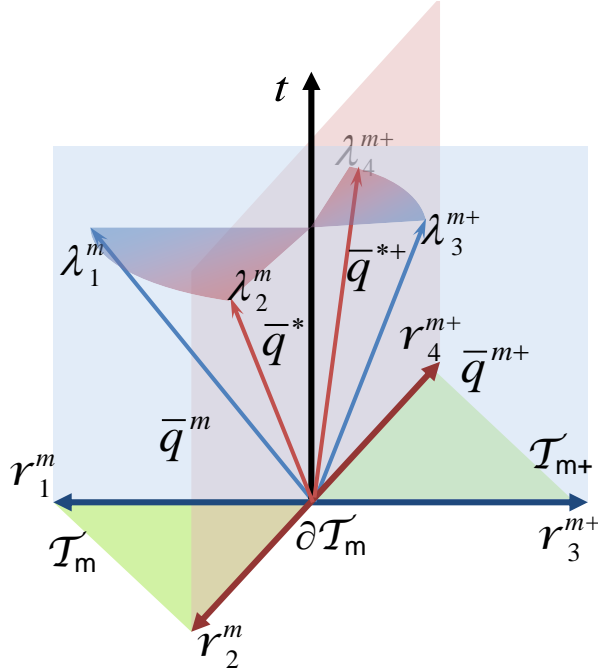
FIGURE 3.3: Structure of the solution to the Riemann problem for anisotropic materials (variable-coefficient), in a 3-D representation of the space(2-D)-time(1-D) independent variables. $\partial \mathcal{T}_m$ shows the interface between the two different elements. The waves propagate at its speed in each material. Between the waves are two states $\bar{q}^*$, $\bar{q}^{*+}$, linear combination of the right eigenvectors r_p.

Now, we are ready to diagonalize $\bar{\mathbb{A}}_n$, as stated in (3.62), choosing the following expression for the matrix with the 4 eigenvectors as columns, which must fulfill with the identity,

$$\bar{\mathbb{A}}_n = \begin{pmatrix} \mathbb{O}_2 & \bar{\bar{\mu}}_2^{-1}\mathbb{D}_2 \\ \bar{\bar{\varepsilon}}_2^{-1}\mathbb{D}_2^{-1} & \mathbb{O}_2 \end{pmatrix} = \begin{pmatrix} -\mathbb{Y}_2\mathbb{D}_2\mathbb{R}_{\mathbb{M}_2} & \mathbb{Y}_2\mathbb{D}_2\mathbb{R}_{\mathbb{M}_2} \\ \mathbb{R}_{\mathbb{M}_2} & \mathbb{R}_{\mathbb{M}_2} \end{pmatrix} \begin{pmatrix} -\mathbb{C}_2 & \mathbb{O}_2 \\ \mathbb{O}_2 & \mathbb{C}_2 \end{pmatrix} \frac{1}{2} \begin{pmatrix} -\mathbb{R}_{\mathbb{M}_2}^{-1}\mathbb{Z}_2\mathbb{D}_2^{-1} & \mathbb{R}_{\mathbb{M}_2}^{-1} \\ \mathbb{R}_{\mathbb{M}_2}^{-1}\mathbb{Z}_2\mathbb{D}_2^{-1} & \mathbb{R}_{\mathbb{M}_2}^{-1} \end{pmatrix} \tag{3.67}$$

Operating with expression (3.67), we can easily find the expressions for two matrices, refer here as "impedance" ($\mathbb{Z}_2$) and "admittance" ($\mathbb{Y}_2$), which play a role equivalent to the impedance (Z) and admittance (Y) magnitudes defined for the isotropic case,

$$\mathbb{Y}_2 = \bar{\bar{\mu}}_2^{-1}\mathbb{D}_2\mathbb{R}_{\mathbb{M}_2}\mathbb{C}_2^{-1}\mathbb{R}_{\mathbb{M}_2}^{-1}\mathbb{D}_2^{-1} \tag{3.68a}$$

$$\mathbb{Z}_2 = \mathbb{R}_{\mathbb{M}_2}\mathbb{C}_2^{-1}\mathbb{R}_{\mathbb{M}_2}^{-1}\bar{\bar{\varepsilon}}_2^{-1} \tag{3.68b}$$

Notice that (3.67) condition is fulfilled and also the following, $\mathbb{Z}_2\mathbb{D}_2^{-1}\mathbb{Y}_2\mathbb{D}_2 = \mathbb{I}_2$.

We can identified a matrix $\bar{\mathbb{A}}_n^m$ in $\mathcal{T}_m$ and, in general, a different matrix $\bar{\mathbb{A}}_n^{m+}$ in $\mathcal{T}_{m+}$. Solving the Riemann problem consists of fulfilling the Rankine-Hugoniot jump condition

[143] at both sides of $\partial \mathcal{T}_m$ which is easily solved in terms of the eigenvalues and eigenvectors of the matrices $\mathbb{A}_n^m$ and $\mathbb{A}_n^{m+}$. The Rankine-Hugoniot condition means decomposing the jumps or discontinuities into a linear combinations of the eigenvectors. The solution of the Riemann problem are the intermediate states ($\bar{q}^*$ and $\bar{q}^{*+}$). Figure 3.3 shows the domains for these solutions. The jumps between the intermediate states and the values at both sides of $\partial \mathcal{T}_m$ must be a linear combination of the eigenvectors associated to the negative eigenvalues for the element $\mathcal{T}_m$ and the eigenvectors associated to the positive eigenvalues for the element $\mathcal{T}_{m+}$. Hence, the decomposition of the discontinuity into a linear combination of the eigenvectors is the following,

$$\bar{q}^{m+} - \bar{q}^m = \begin{pmatrix} -\mathbb{Y}_2^m \mathbb{D}_2 \mathbb{R}_{\mathbb{M}_2^m} & \mathbb{Y}_2^{m+} \mathbb{D}_2 \mathbb{R}_{\mathbb{M}_2^{m+}} \\ \mathbb{R}_{\mathbb{M}_2^m} & \mathbb{R}_{\mathbb{M}_2^{m+}} \end{pmatrix} \begin{pmatrix} \alpha_1^m \\ \alpha_2^m \\ \alpha_3^{m+} \\ \alpha_4^{m+} \end{pmatrix} \tag{3.69}$$

obtaining, for the anisotropic medium, the following expressions for the scalar coefficients considering there are not surface currents,

$$\begin{pmatrix} \alpha_1^m \\ \alpha_2^m \\ \alpha_3^{m+} \\ \alpha_4^{m+} \end{pmatrix} = \begin{pmatrix} -\mathbb{R}_{\mathbb{M}_2^m}^{-1} \mathbb{D}_2^{-1} \left(\mathbb{Y}_2^m + \mathbb{Y}_2^{m+} \right)^{-1} & \mathbb{R}_{\mathbb{M}_2^m}^{-1} \mathbb{D}_2^{-1} \left(\mathbb{Y}_2^m + \mathbb{Y}_2^{m+} \right)^{-1} \mathbb{Y}_2^{m+} \mathbb{D}_2 \\ \mathbb{R}_{\mathbb{M}_2^{m+}}^{-1} \mathbb{D}_2^{-1} \left(\mathbb{Y}_2^m + \mathbb{Y}_2^{m+} \right)^{-1} & \mathbb{R}_{\mathbb{M}_2^{m+}}^{-1} \mathbb{D}_2^{-1} \left(\mathbb{Y}_2^m + \mathbb{Y}_2^{m+} \right)^{-1} \mathbb{Y}_2^m \mathbb{D}_2 \end{pmatrix} \begin{pmatrix} H_{t_1}^{m+} - H_{t_1}^m \\ H_{t_2}^{m+} - H_{t_2}^m \\ E_{t_1}^{m+} - E_{t_1}^m \\ E_{t_2}^{m+} - E_{t_2}^m \end{pmatrix} \tag{3.70}$$

Finally, substituting the scalar coefficients α into equations (3.48), the solutions for the tangential components of the electric and magnetic fields are,

$$\begin{pmatrix} H_{t_1}^* \\ H_{t_2}^* \end{pmatrix} = \mathbb{D}_2 \left(\mathbb{Z}_2^m + \mathbb{Z}_2^{m+} \right)^{-1} \left[\mathbb{Z}_2^m \mathbb{D}_2^{-1} \begin{pmatrix} H_{t_1}^m \\ H_{t_2}^m \end{pmatrix} + \mathbb{Z}_2^{m+} \mathbb{D}_2^{-1} \begin{pmatrix} H_{t_1}^{m+} \\ H_{t_2}^{m+} \end{pmatrix} - \begin{pmatrix} E_{t_1}^{m+} - E_{t_1}^m \\ E_{t_2}^{m+} - E_{t_2}^m \end{pmatrix} \right] \tag{3.71a}$$

$$\begin{pmatrix} E_{t_1}^* \\ E_{t_2}^* \end{pmatrix} = \mathbb{D}_2^{-1} \left(\mathbb{Y}_2^m + \mathbb{Y}_2^{m+} \right)^{-1} \left[\mathbb{Y}_2^m \mathbb{D}_2 \begin{pmatrix} E_{t_1}^m \\ E_{t_2}^m \end{pmatrix} + \mathbb{Y}_2^{m+} \mathbb{D}_2 \begin{pmatrix} E_{t_1}^{m+} \\ E_{t_2}^{m+} \end{pmatrix} - \begin{pmatrix} H_{t_1}^{m+} - H_{t_1}^m \\ H_{t_2}^{m+} - H_{t_2}^m \end{pmatrix} \right] \tag{3.71b}$$

or in electric and magnetic fields format can be written as,

$$\hat{\mathbf{n}} \times \boldsymbol{E}^* = \left(\bar{\bar{Y}}^m + \bar{\bar{Y}}^{m+} \right)^{-1} \left[\bar{\bar{Y}}^m \hat{\mathbf{n}} \times \boldsymbol{E}^m + \bar{\bar{Y}}^{m+} \hat{\mathbf{n}} \times \boldsymbol{E}^{m+} + \hat{\mathbf{n}} \times \hat{\mathbf{n}} \times \left(\boldsymbol{H}^{m+} - \boldsymbol{H}^m \right) \right] \tag{3.72a}$$

$$\hat{\mathbf{n}} \times \boldsymbol{H}^* = \left(\bar{\bar{Z}}^m + \bar{\bar{Z}}^{m+} \right)^{-1} \left[\bar{\bar{Z}}^m \hat{\mathbf{n}} \times \boldsymbol{H}^m + \bar{\bar{Z}}^{m+} \hat{\mathbf{n}} \times \boldsymbol{H}^{m+} - \hat{\mathbf{n}} \times \hat{\mathbf{n}} \times \left(\boldsymbol{E}^{m+} - \boldsymbol{E}^m \right) \right] \tag{3.72b}$$

the tensors are built from matrices defined by subindex 2 but completed to dimension 3 as follows,

$$
\bar{\bar{A}} = \begin{pmatrix} & & 0 \\ & \mathbb{A}_2 & 0 \\ 0 & 0 & 1 \end{pmatrix} \quad \text{with } \bar{\bar{A}} = \left\{ \bar{\bar{Z}}, \bar{\bar{Y}} \right\} \tag{3.73}
$$

3.3.2   Semi-Discrete Scheme Formulation

Following the DG procedure, described in section 3.1.1, with (3.54), we can find the general semi-discrete algorithm at the element m applicable also to anisotropic materials. Sources and medium losses, which could be also anisotropic, have been omitted for simplicity.

$$
\mathbb{M}_{\bar{\bar{\mu}}} d_t H^m - \mathbb{F}_{\nu h} H^m + \mathbb{F}_{\nu h}^+ H^{m+} = -\left(\mathbb{S} - \mathbb{F}_{\kappa e} \right) E^m - \mathbb{F}_{\kappa e}^+ E^{m+} \tag{3.74a}
$$

$$
\mathbb{M}_{\bar{\bar{\varepsilon}}} d_t E^m - \mathbb{F}_{\nu e} E^m + \mathbb{F}_{\nu e}^+ E^{m+} = \left(\mathbb{S} - \mathbb{F}_{\kappa h} \right) H^m + \mathbb{F}_{\kappa h}^+ H^{m+} \tag{3.74b}
$$

where

- H^m, H^{m+}, E^m and E^{m+} are column vector with the dofs varying in time defined in (3.14).

- $\mathbb{M}_{\bar{\bar{\mu}}}$ and $\mathbb{M}_{\bar{\bar{\varepsilon}}}$ are the mass matrices,

$$
\left[\mathbb{M}_{\bar{\bar{\mu}}} \right]_{q'q} = \left\langle \phi_{q'}^m, \bar{\bar{\mu}} \phi_q^m \right\rangle_{\mathcal{T}_m} \tag{3.75a}
$$

$$
\left[\mathbb{M}_{\bar{\bar{\varepsilon}}} \right]_{q'q} = \left\langle \phi_{q'}^m, \bar{\bar{\varepsilon}} \phi_q^m \right\rangle_{\mathcal{T}_m} \tag{3.75b}
$$

- $\mathbb{S}$ is the stiffness matrix, which does not change from the homogeneous case, (3.17).

- $\mathbb{F}$ are the flux matrices

$$[\mathbb{F}_{\kappa h}]_{q'q} = \left\langle \phi_{q'}^m, \bar{\bar{R}} \left(\bar{\bar{Z}}^m + \bar{\bar{Z}}^{m+} \right)^{-1} \bar{\bar{Z}}^{m+} \bar{\bar{R}}^{-1} \left(\hat{\mathbf{n}}^m \times \phi_q^m \right) \right\rangle_{\partial \mathcal{T}_m} \tag{3.76a}$$

$$[\mathbb{F}_{\kappa e}]_{q'q} = \left\langle \phi_{q'}^m, \bar{\bar{R}} \left(\bar{\bar{Y}}^m + \bar{\bar{Y}}^{m+} \right)^{-1} \bar{\bar{Y}}^{m+} \bar{\bar{R}}^{-1} \left(\hat{\mathbf{n}}^m \times \phi_q^m \right) \right\rangle_{\partial \mathcal{T}_m} \tag{3.76b}$$

$$[\mathbb{F}_{\nu h}]_{q'q} = \left\langle \phi_{q'}^m, \bar{\bar{R}} \left(\bar{\bar{Y}}^m + \bar{\bar{Y}}^{m+} \right)^{-1} \bar{\bar{R}}^{-1} \left(\hat{\mathbf{n}}^m \times \hat{\mathbf{n}}^m \times \phi_q^m \right) \right\rangle_{\partial \mathcal{T}_m} \tag{3.76c}$$

$$[\mathbb{F}_{\nu e}]_{q'q} = \left\langle \phi_{q'}^m, \bar{\bar{R}} \left(\bar{\bar{Z}}^m + \bar{\bar{Z}}^{m+} \right)^{-1} \bar{\bar{R}}^{-1} \left(\hat{\mathbf{n}}^m \times \hat{\mathbf{n}}^m \times \phi_q^m \right) \right\rangle_{\partial \mathcal{T}_m} \tag{3.76d}$$

$$\left[\mathbb{F}_{\kappa h}^+\right]_{q'q} = \left\langle \phi_{q'}^m, \bar{\bar{R}} \left(\bar{\bar{Z}}^m + \bar{\bar{Z}}^{m+} \right)^{-1} \bar{\bar{Z}}^{m+} \bar{\bar{R}}^{-1} \left(\hat{\mathbf{n}}^m \times \phi_q^{m+} \right) \right\rangle_{\partial \mathcal{T}_m} \tag{3.76e}$$

$$\left[\mathbb{F}_{\kappa e}^+\right]_{q'q} = \left\langle \phi_{q'}^m, \bar{\bar{R}} \left(\bar{\bar{Y}}^m + \bar{\bar{Y}}^{m+} \right)^{-1} \bar{\bar{Y}}^{m+} \bar{\bar{R}}^{-1} \left(\hat{\mathbf{n}}^m \times \phi_q^{m+} \right) \right\rangle_{\partial \mathcal{T}_m} \tag{3.76f}$$

$$\left[\mathbb{F}_{\nu h}^+\right]_{q'q} = \left\langle \phi_{q'}^m, \bar{\bar{R}} \left(\bar{\bar{Y}}^m + \bar{\bar{Y}}^{m+} \right)^{-1} \bar{\bar{R}}^{-1} \left(\hat{\mathbf{n}}^m \times \hat{\mathbf{n}}^m \times \phi_q^{m+} \right) \right\rangle_{\partial \mathcal{T}_m} \tag{3.76g}$$

$$\left[\mathbb{F}_{\nu e}^+\right]_{q'q} = \left\langle \phi_{q'}^m, \bar{\bar{R}} \left(\bar{\bar{Z}}^m + \bar{\bar{Z}}^{m+} \right)^{-1} \bar{\bar{R}}^{-1} \left(\hat{\mathbf{n}}^m \times \hat{\mathbf{n}}^m \times \phi_q^{m+} \right) \right\rangle_{\partial \mathcal{T}_m} \tag{3.76h}$$

$\bar{\bar{R}}$ and $\bar{\bar{R}}^{-1}$ are the transformation matrices from the local vectorial base to Cartesian vectorial base defined in (3.32).

This semi-discrete scheme corresponds to the upwind flux evaluation case. In case of partial penalized flux, the factor τ should be included in the terms $\mathbb{F}_{\nu h}$, $\mathbb{F}_{\nu h}^+$, $\mathbb{F}_{\nu e}$ and $\mathbb{F}_{\nu e}^+$. For centered flux scheme, the simpler expression (3.18) for the flux matrices can be used, keeping (3.75) for the mass matrices.

3.4 Absorbing Boundary Conditions

Most of the problems appearing in this study are posed on unbounded domains. To compute a numerical solution to such problems, it is necessary to truncate the space. This is done by introducing artificial boundaries and/or regions what defines a finite domain Ω. This boundary are named as Absorbing Boundary Conditions (ABC) which simulate the extension of the domain to infinity. The main objectives concerned in the design of ABC are, easy and efficient implementation, with respect to both memory and computational time, and ideally non-reflecting boundary condition. Many ABCs types have been reported during last three decades, all these ABCs are designed to have good performance for one particular case. Moreover, the computational cost depends on the order of the truncation in terms of their Taylor series approximation. If accuracy is required, higher-order ABCs should be used [144, 145, 146, 147].

Two ABC types have been addressed in this study, the so-called Silver-Müller (SM-ABC) and Conformal Uniaxial Perfectly Matched Layer (C-UPML). It is important to note that both ABC (SM-ABC and C-UPML) can be used together [91, 92, 141, 142], improving the overall performance. Due to its simplicity in DG context, SM-ABC has been previously described in section 3.1.2. Following, the implementation of the conformal UPML is described in detail.

3.4.1   Conformal Uniaxial Perfectly Matched Layer Formulation

Since Bérenger [148] introduction in 1994, of the PML method applied to FDTD method, many different implementation and types of PMLs have been reported, but two kind of formulations are prevalent. The first, known as non-Maxwellian PML or split-field PML, Bérenguer's PML belongs to this class, are derived by splitting the curl operator in the different Cartesian components creating new nonphysical electric and magnetic pseudo-fields in the PML region. The right combination of them recovers the original Maxwell equations. Once this new components have been introduced, different electric and magnetic conductivities can be applied to attenuate the energy inside the PML but keeping impedance continuity with the Maxwellian medium. In the second kind formulations, Maxwellian PML or uniaxial PML (UPML) which was proposed later [87], the PML region is described as an artificial anisotropic absorbing material which is introduced in the Maxwell equations fulfilling the same objectives, the energy inside the PML will be attenuated and this energy get into the PML without reflection.

Both formulations, split-field and UPML, were derived independently trying to avoid reflection of the incident field on the PML. However, both formulation were shown to be equivalent using the general approach of stretched spatial coordinates [88, 89, 90]. In both cases the same thing is done, but the information inside the degrees of freedom is different in each case. Following, the formulation for UPML is reviewed, which has been implemented in DGTD context in this work.

Let us consider the setup of figure 3.4 used for the conformal UPML problem. There, the interface of the PML region with the homogeneous medium is the surface S, and S' is a surface conformal to S containing the PML internal point P', where we intend to formulate the UPML. Considering the projected point P of P' on S, we can define local coordinates as ξ_1, ξ_2 and ξ_3, and both surfaces S and S' can be expressed as a functions of these local coordinates,

$$S \equiv f\left(\xi_1, \xi_2\right), \quad \xi_3 = 0 \tag{3.77a}$$

$$S' \equiv f\left(\xi_1, \xi_2\right) + \xi_3 \tag{3.77b}$$
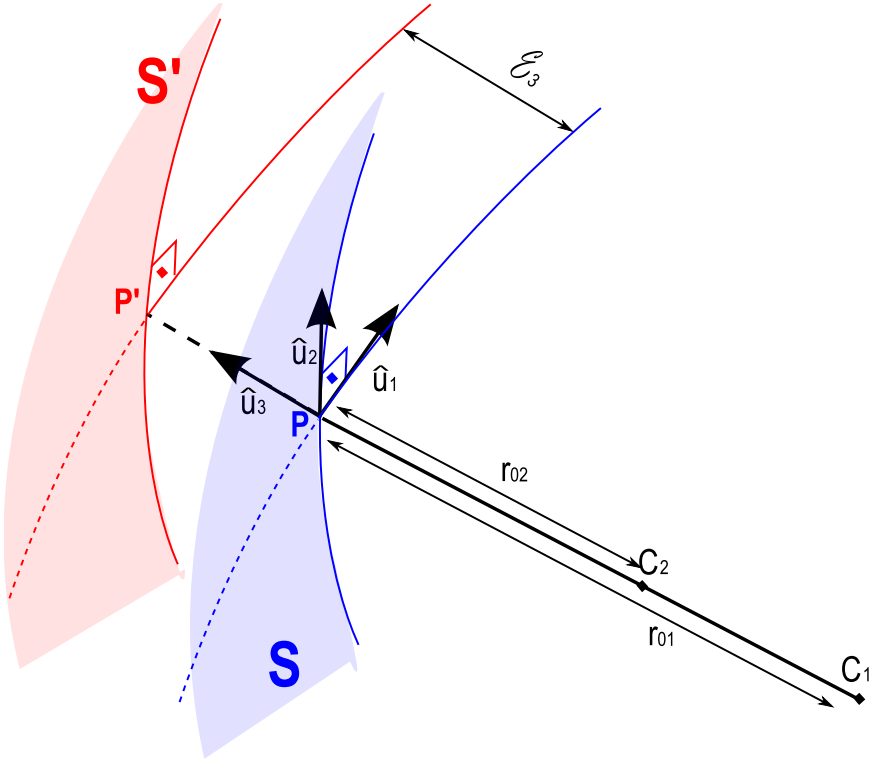
FIGURE 3.4: Conformal UPML setup.

The locus of points of constant ξ_3 correspond to parallel surfaces at a distance of ξ_3 to S.

An orthonormal local vectorial base can be defined as,

$$\hat{\mathbf{u}}_1 = u_1\left(\xi_1, \xi_2\right) = \frac{\partial \boldsymbol{r}}{\partial \xi_1} \left| \frac{\partial \boldsymbol{r}}{\partial \xi_1} \right|^{-1} \tag{3.78a}$$

$$\hat{\mathbf{u}}_2 = u_2\left(\xi_1, \xi_2\right) = \frac{\partial \boldsymbol{r}}{\partial \xi_2} \left| \frac{\partial \boldsymbol{r}}{\partial \xi_2} \right|^{-1} \tag{3.78b}$$

$$\hat{\mathbf{u}}_3 = \hat{\mathbf{u}}_1 \times \hat{\mathbf{u}}_2 \tag{3.78c}$$

related to the Cartesian base through the basis-change matrix $\bar{\bar{R}}$, and the principal radii of curvature of the doubly curved surface S and S' are function of the local coordinates,

$$r_01 = r_01\left(\xi_1, \xi_2\right), \quad r_02 = r_02\left(\xi_1, \xi_2\right) \tag{3.79a}$$

$$r_1 = r_01 + \xi_3, \quad r_2 = r_02 + \xi_3 \tag{3.79b}$$

The UPML consists of a change on the metric of the space to the complex space in the vectorial base $(\hat{\mathbf{u}}_1, \hat{\mathbf{u}}_2, \hat{\mathbf{u}}_3)$ of the local coordinate ξ_3. The spatial coordinates inside the

PML are mapped to the complex variables domain as:

$$\xi_3 \longrightarrow \tilde{\xi}_3 = \int_0^{\xi_3} s(\tau)\, d\tau \tag{3.80}$$

where $s(\tau)$ is the complex stretching variable, which can take different expressions [92, 149]. In this work, the following expression has been used,

$$s(\tau) = 1 + \frac{1}{j\omega}\sigma_{max}\left(\frac{\tau}{\Delta\xi_3}\right)^2 \tag{3.81}$$

where $\Delta\xi_3$ is the PML thick and σ_{max} the maximum conductivity in the PML. These two parameters characterize the PML layer and determine the rate of decay of the energy of the transmitter wave into the PML. Notice that we have chosen a parabolic dependence of the stretching variable, this means the conductivity inside the PML medium will grow in a parabolic profile. This growing rate can be tuned to minimize the reflexion of the PML [148], but optimum value is usually problem dependent. Parabolic profile is a typical choice.

The ideally reflected wave coefficient depends on the incident angle (θ) and can be evaluated with the expression,

$$R_0(\theta) = e^{-\frac{2}{3}\frac{\sigma_{max}\Delta\xi_3}{c}\cos(\theta)} \tag{3.82}$$

where $c = \frac{1}{\sqrt{\mu\varepsilon}}$ is the speed with which the wave travels along the direction of $\hat{\mathbf{u}}_3$.

The resulting update expression of the spatial coordinate is given by,

$$\tilde{\xi}_3 = \xi_3 + \frac{1}{j\omega}\sigma_{max}\frac{\xi_3}{3}\left(\frac{\xi_3}{\Delta\xi_3}\right)^2 \tag{3.83}$$

and the stretching curvature radios by,

$$\tilde{r}_1 = r_01 + \tilde{\xi}_3 = r_1 + \frac{1}{j\omega}\sigma_{max}\frac{\xi_3}{3}\left(\frac{\xi_3}{\Delta\xi_3}\right)^2 \tag{3.84a}$$

$$\tilde{r}_2 = r_02 + \tilde{\xi}_3 = r_2 + \frac{1}{j\omega}\sigma_{max}\frac{\xi_3}{3}\left(\frac{\xi_3}{\Delta\xi_3}\right)^2 \tag{3.84b}$$

Next expressions defined the metric coefficients,

$$\begin{aligned}
h_1 &= \frac{r_1}{r_01}, & \tilde{h}_1 &= \frac{\tilde{r}_1}{r_01} \\
h_2 &= \frac{r_2}{r_02}, & \tilde{h}_2 &= \frac{\tilde{r}_2}{r_02} \\
h_3 &= 1, & \tilde{h}_3 &= s
\end{aligned} \tag{3.85}$$

The change of the space metric of (3.80) and (3.81) can be easily implemented as an artificial anisotropic material [88, 89, 90], whose general metric tensor, in local coordinates, can be expressed in terms of the metric coefficients as,

$$
\bar{\bar{\Lambda}} = \hat{\mathbf{u}}_1\hat{\mathbf{u}}_1\left(s\frac{h_1}{\tilde{h}_1}\frac{\tilde{h}_2}{h_2}\right) + \hat{\mathbf{u}}_2\hat{\mathbf{u}}_2\left(s\frac{h_2}{\tilde{h}_2}\frac{\tilde{h}_1}{h_1}\right) + \hat{\mathbf{u}}_3\hat{\mathbf{u}}_3\left(\frac{1}{s}\frac{\tilde{h}_1}{h_1}\frac{\tilde{h}_2}{h_2}\right) = \begin{pmatrix} s\frac{h_1}{\tilde{h}_1}\frac{\tilde{h}_2}{h_2} & 0 & 0 \\ 0 & s\frac{h_2}{\tilde{h}_2}\frac{\tilde{h}_1}{h_1} & 0 \\ 0 & 0 & \frac{1}{s}\frac{\tilde{h}_1}{h_1}\frac{\tilde{h}_2}{h_2} \end{pmatrix}
$$
(3.86)

Inserting (3.79), (3.84) and (3.85) in (3.86), three different conductivities can be defined, corresponding to each space direction, depending on the curvature radio and the distance to the S surface.

$$
\sigma_3\left(\xi_3\right) = \sigma_{max}\left(\frac{\xi_3}{\Delta\xi_3}\right)^2
$$
(3.87a)

$$
\sigma_1\left(\xi_3\right) = \sigma_3\frac{\xi_3}{3r_1}
$$
(3.87b)

$$
\sigma_2\left(\xi_3\right) = \sigma_3\frac{\xi_3}{3r_2}
$$
(3.87c)

Finally the expression of the metric tensor is,

$$
\bar{\bar{\Lambda}} = \begin{pmatrix} \frac{\left(1+\frac{\sigma_3}{j\omega}\right)\left(1+\frac{\sigma_2}{j\omega}\right)}{\left(1+\frac{\sigma_1}{j\omega}\right)} & 0 & 0 \\ 0 & \frac{\left(1+\frac{\sigma_3}{j\omega}\right)\left(1+\frac{\sigma_1}{j\omega}\right)}{\left(1+\frac{\sigma_2}{j\omega}\right)} & 0 \\ 0 & 0 & \frac{\left(1+\frac{\sigma_1}{j\omega}\right)\left(1+\frac{\sigma_2}{j\omega}\right)}{\left(1+\frac{\sigma_3}{j\omega}\right)} \end{pmatrix}
$$
(3.88)

The UPML can be expressed in the frequency domain in a Maxwellian form, and in the local vectorial base as,

$$
\nabla \times \boldsymbol{E} = -j\omega\mu\bar{\bar{\Lambda}}\boldsymbol{H}
$$
(3.89a)

$$
\nabla \times \boldsymbol{H} = j\omega\varepsilon\bar{\bar{\Lambda}}\boldsymbol{E}
$$
(3.89b)

For simplicity, only one component of (3.89a) is written, similar results can be found for the other components and (3.89b),

$$
\begin{aligned}
(\nabla \times \boldsymbol{E})\,|_{\hat{\mathbf{u}}_1} &= -j\omega\mu\frac{\left(1+\frac{\sigma_3}{j\omega}\right)\left(1+\frac{\sigma_2}{j\omega}\right)}{\left(1+\frac{\sigma_1}{j\omega}\right)}\boldsymbol{H}|_{\hat{\mathbf{u}}_1} \\
&= -j\omega\mu\boldsymbol{H}|_{\hat{\mathbf{u}}_1} - \mu\left(\sigma_3+\sigma_2-\sigma_1\right)\boldsymbol{H}|_{\hat{\mathbf{u}}_1} - \mu\frac{\left(\sigma_3-\sigma_1\right)\left(\sigma_2-\sigma_1\right)}{j\omega+\sigma_1}\boldsymbol{H}|_{\hat{\mathbf{u}}_1}
\end{aligned}
$$
(3.90)

Equation ([3.90]) can be solved introducing an auxiliary field and an auxiliary partial differential equation. Fourier transform, using identity $j\omega f(\omega) \rightarrow (\partial/\partial t) f(t)$, is applied to formulate the equivalent differential equations in time-domain,

$$\left.\frac{\partial \boldsymbol{M}}{\partial t}\right|_{\hat{\mathbf{u}}_1} = -\sigma_1 \boldsymbol{M}|_{\hat{\mathbf{u}}_1} + \mu(\sigma_3 - \sigma_1)(\sigma_2 - \sigma_1)\boldsymbol{H}|_{\hat{\mathbf{u}}_1} \tag{3.91a}$$

$$\mu\left.\frac{\partial \boldsymbol{H}}{\partial t}\right|_{\hat{\mathbf{u}}_1} = -(\nabla \times \boldsymbol{E})|_{\hat{\mathbf{u}}_1} - \mu(\sigma_3 + \sigma_2 - \sigma_1)\boldsymbol{H}|_{\hat{\mathbf{u}}_1} - \boldsymbol{M}|_{\hat{\mathbf{u}}_1} \tag{3.91b}$$

Finally, the set of equations for the PML layer for the fields magnitudes $\boldsymbol{E}$, $\boldsymbol{H}$ and the auxiliary fields (polarization currents) $\boldsymbol{M}$ and $\boldsymbol{J}$, can be written as,

$$\frac{\partial \boldsymbol{M}}{\partial t} = -\bar{\bar{A}}_2 \boldsymbol{M} + \mu\bar{\bar{A}}_3 \boldsymbol{H} \tag{3.92a}$$

$$\mu\frac{\partial \boldsymbol{H}}{\partial t} = -\nabla \times \boldsymbol{E} - \boldsymbol{M} - \mu\bar{\bar{A}}_1 \boldsymbol{H} \tag{3.92b}$$

$$\frac{\partial \boldsymbol{J}}{\partial t} = -\bar{\bar{A}}_2 \boldsymbol{J} + \varepsilon\bar{\bar{A}}_3 \boldsymbol{E} \tag{3.92c}$$

$$\varepsilon\frac{\partial \boldsymbol{E}}{\partial t} = \nabla \times \boldsymbol{H} - \boldsymbol{J} - \varepsilon\bar{\bar{A}}_1 \boldsymbol{E} \tag{3.92d}$$

where all vectorial magnitudes are expressed in the Cartesian vectorial base $(\hat{\mathbf{x}}, \hat{\mathbf{y}}, \hat{\mathbf{z}})$. The tensors $\bar{\bar{A}}_1$, $\bar{\bar{A}}_2$ and $\bar{\bar{A}}_3$ have the form,

$$\bar{\bar{A}}_1 = \bar{\bar{R}} \begin{pmatrix} \sigma_3 + \sigma_2 - \sigma_1 & 0 & 0 \\ 0 & \sigma_1 + \sigma_3 - \sigma_2 & 0 \\ 0 & 0 & \sigma_2 + \sigma_1 - \sigma_3 \end{pmatrix} \bar{\bar{R}}^{-1} \tag{3.93a}$$

$$\bar{\bar{A}}_2 = \bar{\bar{R}} \begin{pmatrix} \sigma_1 & 0 & 0 \\ 0 & \sigma_2 & 0 \\ 0 & 0 & \sigma_3 \end{pmatrix} \bar{\bar{R}}^{-1} \tag{3.93b}$$

$$\bar{\bar{A}}_3 = \bar{\bar{R}} \begin{pmatrix} (\sigma_2 - \sigma_1)(\sigma_3 - \sigma_1) & 0 & 0 \\ 0 & (\sigma_3 - \sigma_2)(\sigma_1 - \sigma_2) & 0 \\ 0 & 0 & (\sigma_1 - \sigma_3)(\sigma_2 - \sigma_3) \end{pmatrix} \bar{\bar{R}}^{-1} \tag{3.93c}$$

being $\bar{\bar{R}}$ and $\bar{\bar{R}}^{-1}$ the transformation matrices from the local vectorial base, defined in ([3.78]), and the Cartesian vectorial base,

$$\begin{pmatrix} \hat{\mathbf{x}} \\ \hat{\mathbf{y}} \\ \hat{\mathbf{z}} \end{pmatrix} = \bar{\bar{R}} \begin{pmatrix} \hat{\mathbf{u}}_1 \\ \hat{\mathbf{u}}_2 \\ \hat{\mathbf{u}}_3 \end{pmatrix}, \qquad \begin{pmatrix} \hat{\mathbf{u}}_1 \\ \hat{\mathbf{u}}_2 \\ \hat{\mathbf{u}}_3 \end{pmatrix} = \bar{\bar{R}}^{-1} \begin{pmatrix} \hat{\mathbf{x}} \\ \hat{\mathbf{y}} \\ \hat{\mathbf{z}} \end{pmatrix} \tag{3.94}$$

In order to solve ([3.92]) it is necessary to evaluate σ_1, σ_2 and σ_3 in every point inside the
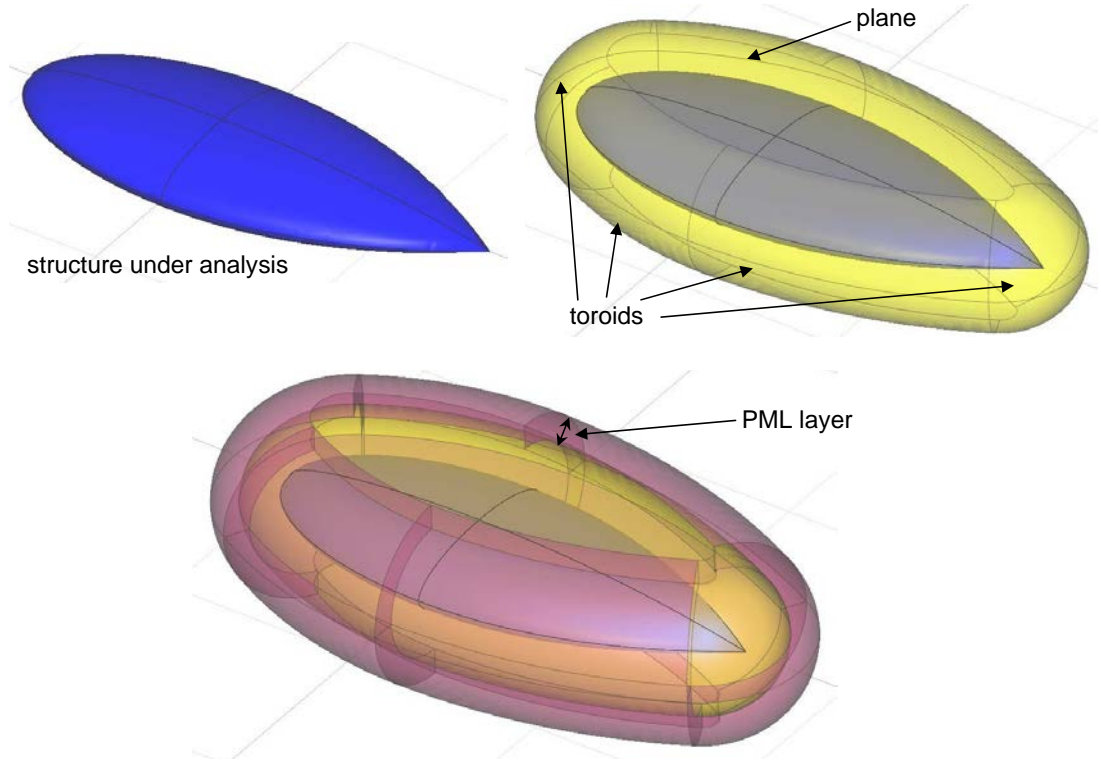
FIGURE 3.5: Definition of a conformal UPML making use of canonical geometries.

PML region. According to (3.87), these conductivities values depend on the two principal radii of curvature r_1, r_2 of a general (doubly-curved) surface and the distance to the PML frontier, ξ_3. Finding these variables in a general problem is not an easy task, some solution have been proposed in 2-D [26, 88, 150]. In this work, solutions for canonical geometries have been implemented, so in a particular problem one or a combination of different canonical geometries can be applied to truncate the computational domain as is depicted in figure 3.5. In this case, the space, which encloses the structure under analysis, is truncated by a closed surface composed of pieces of toroids and plane surfaces. Once this frontier is established, the PML region is defined with the required thickness.

3.4.2 Discontinuous Galerkin Semi-Discrete Scheme Formulation

The Galerkin procedure jointly with the DG spatial technique, of section 3.1.1, can be straightforwardly applied to (3.92), since curl terms in equations (3.92a) and (3.92c) do not change from regular Maxwell's equations. Hence, considering that the auxiliary fields are expanded with the same set of basis functions, and auxiliary differential equations are tested following Galerkin procedure, we find the following spatial semi-discrete scheme

for the element m located in a PML region,

$$\mathbb{M}d_t M^m + \mathbb{M}_{A_2} M^m = \mu\mathbb{M}_{A_3} H^m \tag{3.95a}$$

$$\mu\mathbb{M}d_t H^m + (\mu\mathbb{M}_{A_1} - \mathbb{F}_{\nu h})H^m + \mathbb{F}_{\nu h}^+ H^{m+} = -(\mathbb{S} - \mathbb{F}_{\kappa e})E^m - \mathbb{F}_{\kappa e}^+ E^{m+} - \mathbb{M}M^m \tag{3.95b}$$

$$\mathbb{M}d_t J^m + \mathbb{M}_{A_2} J^m = \varepsilon\mathbb{M}_{A_3} E^m \tag{3.95c}$$

$$\varepsilon\mathbb{M}d_t E^m + (\varepsilon\mathbb{M}_{A_1} - \mathbb{F}_{\nu e})E^m + \mathbb{F}_{\nu e}^+ E^{m+} = (\mathbb{S} - \mathbb{F}_{\kappa h})H^m + \mathbb{F}_{\kappa h}^+ H^{m+} - \mathbb{M}J^m \tag{3.95d}$$

where

- H^m, H^{m+}, E^m, E^{m+}, M^m and J^m are column vector with the dofs varying in time as (3.14).

- $\mathbb{M}$ is the mass matrix defined in (3.16) and $\mathbb{M}_{A_1}$, $\mathbb{M}_{A_2}$ and $\mathbb{M}_{A_3}$ are mass matrices but affected by the tensors defined previously in (3.93),

$$[\mathbb{M}_{A_i}]_{q'q} = \left\langle \phi_{q'}^m, \bar{\bar{A}}_i \phi_q^m \right\rangle_{\mathcal{T}_m} \qquad \text{with } i = \{1, 2, 3\} \tag{3.96}$$

- $\mathbb{S}$ is the stiffness matrix defined in (3.17).

- $\mathbb{F}$ are the flux matrices defined in (3.18)

It is important to note that in DG methods, the simplest absorbing boundary condition, equivalent to a first-order Silver-Müller (SM-ABC), can be applied with no cost, just setting the incoming flux to zero (see section 3.1.2). Hence, both (SM-ABC and C-UPML) can be used together, improving the overall performance [92].

3.5 Analysis of the DG Semi-Discrete Scheme

The traditional approach to analyze the spatially/temporally propagating accuracy, dispersion and dissipation errors, of Discontinuous Galerkin Methods is based upon the eigenvalue problem. Hu et al. in 2002 [47], presented a detailed study of the eigensolution of the DG Method with uniform and nonuniform grids applied to a system of hyperbolic equations in one-dimension (1-D) space. In CEM, some studies appear in 2004, Hesthaven and Warburton [53], where the presence and behavior of spurious modes in the DG operator are described, and Ainsworth [55, 56] who studied the dispersive and dissipative properties of the DG methods in the Helmholtz equation. In 2006, Warburton and Embree [54] described the role of the penalty in DG methods. Cohen and Duruflé, in 2007 [62] showed the need of dissipation terms to avoid spurious modes

in the DG schemes. Sármány et al., also in 2007, in [59], studied the dispersion and dissipation errors, but considering the time integration scheme as well.

Classical continuous FEM methods, both in curl-curl and in the mixed formulation, are well known for supporting spurious modes, which are non-physical solutions arising in the numerical approximation not present in the analytical problem. Specially harmful are non-divergent spurious modes (for divergence-free analytical problems) excited at not null frequencies, since they severely corrupt near-field solutions. Lots of strategies to reduce them are found in the literature. For nodal (scalar basis) FEM, regularization techniques including conditions on the divergence of the solution, have been successfully employed [151]. For vector FEM, it is possible to use curl-conforming elements for which the basis vectors respect the natural (dis)continuity of the electromagnetic fields[2], only supporting spurious modes at null-frequency [27]. Higher-order hierarchal basis functions were introduced in [132] with this purpose.

DGTD also exhibit the appearance of spurious modes [47, 53, 54, 55, 56, 59, 62]. However an added advantage of DGTD over FETD resides in its discontinuous nature that permits to remove them due to the use upwind/penalized fluxes [54, 55, 56, 59, 62]. As stated above, these fluxes are characterized by the addition to Maxwell equations of dissipative terms, and are proven to attenuate spurious modes in space more strongly than physical modes. The suppression of spurious modes becomes a critical issue for DGTD formulations of the Perfectly Matched Layer (PML) truncation condition, since instabilities appear otherwise [70]. Both DGTD for vector and scalar basis are spurious-free for penalized fluxes, and have been successfully developed by several authors [28, 52, 58, 60, 69, 86, 95, 97, 102, 108, 138], finding comparable levels of accuracy. Of course, there are advantages and disadvantages of vector and nodal formulations, basically in terms of computational implementations, also depending on the time integration scheme.

In this section we revisit the topic of spurious modes for simple 1-D and 3-D problems in DGTD. Convergence of the dispersion and dissipation relationships of the method is also analyzed for the semi-discrete DG space operator.

3.5.1   Numerical Dispersion and Dissipation of the DG Semi-Discrete Scheme

The dispersion and dissipation of the numerical method will be studied by searching for plane-wave solutions of frequency ω and wavevector $\mathbf{k}$, in general complex. These

---

[2]Continuity on the tangential components, and discontinuity in the normal ones.

functions, replaced in the original equations, lead to an eigenproblem, with eigenvalues providing the numerical dispersion and dissipation relationships $\omega = f(\mathbf{k})$, and with eigenvectors providing the numerical-structure relationships between the dofs (field components). For instance, the analytical Maxwell's equations support planewaves in free-space with the well-known dispersion relationship $\omega^2 = k^2/c^2$, and eigenvectors related by $\eta_0 \mathbf{H} = \hat{\mathbf{k}} \times \mathbf{E}$, with c and η_0 being the free-space speed of light and impedance, respectively.

A practical way to study the dispersion of a numerical scheme approaching Maxwell's equations consists of restricting the space of solution to a bounded region with periodic boundary conditions (PBC), since they can be numerically enforced in an easy way. Let us assume for simplicity a 1-D-domain $x \in [0, \Delta]$ and let us search for modes fulfilling PBCs in space

$$\boldsymbol{\Psi}(x = \Delta, t) = e^{-j\alpha}\boldsymbol{\Psi}(x = 0, t) \ , \forall t \ , \ \ \boldsymbol{\Psi} = \{\boldsymbol{E}, \boldsymbol{H}\} \tag{3.97}$$

for arbitrary $\alpha \in [0, 2\pi)$. Plane-wave solutions of the form $e^{j(\omega t - kx)}$ (leftwards $k > 0$ and rightwards $k < 0$) comply with the PBC condition (3.97) for a infinite numerable spectrum of real wavenumbers k_n (each oscillating at a complex frequency ω_n)

$$k_n = \pm\left(\frac{\alpha}{\Delta} + \frac{\pi}{\Delta}2n\right) \ , \ n = 0, -1, +1, -2, +2, \ldots$$
$$\omega_n = f(k_n) \tag{3.98}$$

where we will refer to $k_0 = \frac{\alpha}{\Delta}$ as a fundamental mode, and to all other k_n as harmonic modes.

Let us apply this technique to the DG method in a semi-discrete form in space,

$$d_t H^m = \frac{1}{\mu}\mathbb{M}^{-1}\left[-\left(\mathbb{S} - \mathbb{F}_{\kappa e}\right)E^m - \mathbb{F}_{\kappa e}^+ E^{m+} + \mathbb{F}_{\nu h}H^m - \mathbb{F}_{\nu h}^+ H^{m+}\right] \tag{3.99a}$$

$$d_t E^m = \frac{1}{\varepsilon}\mathbb{M}^{-1}\left[\left(\mathbb{S} - \mathbb{F}_{\kappa h}\right)H^m + \mathbb{F}_{\kappa h}^+ H^{m+} + \mathbb{F}_{\nu e}E^m - \mathbb{F}_{\nu e}^+ E^{m+}\right] \tag{3.99b}$$

which is a simplified version of (3.13) for the m element, formulated in free-space without sources.

We define a column vector $\mathbf{U} = \left[\left(h_1^1, ..., h_Q^1\right), ..., \left(h_1^M, ..., h_Q^M\right), \left(e_1^1, ..., e_Q^1\right), ..., \left(e_1^M, ..., e_Q^M\right)\right]^T$ with all the dofs of a given problem and express the homogeneous semi-discrete DG equations (3.99),

$$j\omega \mathbf{U} = \mathcal{A}_{DG}\mathbf{U} \tag{3.100}$$

with $\mathcal{A}_{DG}$ the semi-discrete DG operator. PBCs are easily enforced in DG through the flux conditions by setting

$$
\begin{aligned}
\hat{\mathbf{n}}^m \times \boldsymbol{\Psi}^{m+}|_{x=\Delta} &= e^{-j\alpha}(\hat{\mathbf{n}}^m \times \boldsymbol{\Psi}^m|_{x=0})\,, \\
\hat{\mathbf{n}}^m \times \boldsymbol{\Psi}^{m+}|_{x=0} &= e^{j\alpha}(\hat{\mathbf{n}}^m \times \boldsymbol{\Psi}^m|_{x=\Delta})\,, \qquad \boldsymbol{\Psi} = \{\boldsymbol{E}, \boldsymbol{H}\}
\end{aligned}
\tag{3.101}
$$

Plugging (3.101) into (3.100), we find a homogeneous algebraic system of equations, with a number of unknowns equal to the number of dofs. Nontrivial solutions correspond to the eigenvectors of the semi-discrete space operator. Under the assumption that the space operator is diagonalizable, there will exist a basis of eigenvectors $\mathbf{U}_m$, $m = (0, 1, \ldots, \text{dofs} - 1)$, each propagating with a complex frequency $\omega = \tilde{k}_m$, with $\tilde{k}_m$ its corresponding eigenvalue.

It should be noted that the Shannon sampling theorem [152] establishes an upper limit to the maximum wavenumber which can be sampled in a spatial domain discretized with dofs samples. For instance, let us assume a one-element domain in 1-D-DGTD, solved with p^{th}-order polynomials ((p+1) electric dofs plus (p+1) magnetic dofs). The analytical bandwidth (3.98) which can be represented numerically is restricted to

$$
|k_n| = \left| k_0 + \frac{\pi}{\Delta} 2n \right| \leq \frac{\pi}{\Delta}(p+1)\,,\ n = (0, -1, +1, \ldots)
\tag{3.102}
$$

That is, for each $k_0 \neq \pi/\Delta$ there[3] exist $(p+1)$ leftwards analytical modes $+|k_n|$ plus $(p+1)$ rightwards ones $-|k_n|$, which can be numerically approximated. Of course, numerical eigenvalues $\tilde{k}$ fulfilling the Shannon sampling theorem are not necessarily proper approximation of the analytical ones k. In a broad sense, we will refer to these numerical modes which do not *properly* approximate any analytical one, as *spurious* or *nonphysical* modes.

Let us illustrate this for our simple 1-D 1-element case solved by nodal-DGTD and Lagrange polynomial p^{th}-order basis. Figures 3.6, 3.7 show the dispersion and dissipation relation for 1st- and 2nd-order basis (with centered and upwind fluxes). We note that, for $p = 1$, there appear one rightwards and one leftwards solution which approximate the fundamental mode for well-resolved problems ($L \equiv k_0\Delta/(p+1) \to 0$). Another two modes (one leftwards plus rightwards) solutions are found, which should correspond to the first harmonics ($|k_{-1}| = \frac{2\pi}{\Delta} - k_0$). Due to the coarse discretization of these modes, close to their own Shannon limit for $L \to 0$, the numerical phase speed is far from the analytical one. These poorly sampled modes (for a well-resolved fundamental one) with an undesired behavior are the spurious or nonphysical modes. It bears noticing that, in

---

[3]See figures 3.6, 3.7 to see the case $k_0 = \pi/\Delta$

case of ($L \to \pi$), when $|k_{-1}| \approx 0$ and $|k_0| \approx \frac{2\pi}{\Delta}$, the situation is the opposite: the fundamental modes numerically propagate in a wrong way, providing a good approximation of what has been defined as harmonics.

For $p = 2$, a similar analysis can be made. Apart from the two fundamental modes, another four modes (two leftward plus two rightward) appear. In case of $L \to 0$, the first harmonics ($\pm k_{-1}$) can be distinguished in the numerical dispersion functions, but the second harmonics $\pm k_{+1}$ present wrong behavior on the phase speed. For different intervals of L, the different solutions, fundamental or harmonics modes, ($\pm \tilde{k}_0, \pm \tilde{k}_{-1}, \pm \tilde{k}_{+1}$) offer a better or worse approximation to the analytical solutions ($\pm k_0, \pm k_{-1}, \pm k_{+1}$). In case of upwind flux, much better approximation over more bandwidth is achieved than for centered flux.

A noteworthy point here is to analyze the dissipation relationship of the upwind flux. All modes propagate with an attenuation that is larger for poorly resolved modes than for well-resolved ones. Clearly, for the fundamental mode, dissipation is minimum for $L \to 0$. In case of the harmonics, this situation takes place for different intervals of L, where they are properly resolved. Furthermore, in all cases, good phase dispersion corresponds to low dissipation, and poor phase dispersion corresponds to a high dissipation relationship. However, for the centered flux, the numerical modes do not attenuate in any case, and poorly sampled analytical modes with wrong behavior (spurious) may appear together with the well-resolved ones in a simulation.

The definition we use here of spurious solutions is broad in the sense that it provides information for the whole spectrum of the semi-discrete space operator (which constitute a basis for all possible solutions or diagonalizable operators): it provides criteria to distinguish physical from nonphysical behavior, just in terms of the correct approximation between the analytical and numerical solutions. However, the qualification of spurious mode actually depends on the analytical problem under study. For instance, if we excite the PBC-analytical problem with the fundamental mode as initial values, we might not expect the appearance of any of the higher harmonics in its numerical counterpart. In this narrow sense, any solution apart from that corresponding to the fundamental mode might also be considered spurious (see [53]), even if it is well resolved in space. To illustrate this, we have projected the fundamental (rightward) analytical mode k_0, expanded in a $p = 10$ polynomial basis, into the basis of numerical eigenvectors. Since these are not orthogonal, we cannot assume a modal separation of the energy, but we still find that for a good resolution $L = 0.005$, the numerical mode propagates with $\tilde{k}_0 \approx k_0$ with an amplitude ~ 572 times higher that of the next mode, whereas this ratio lowers to ~ 28 for a resolution of $L = 0.11$.
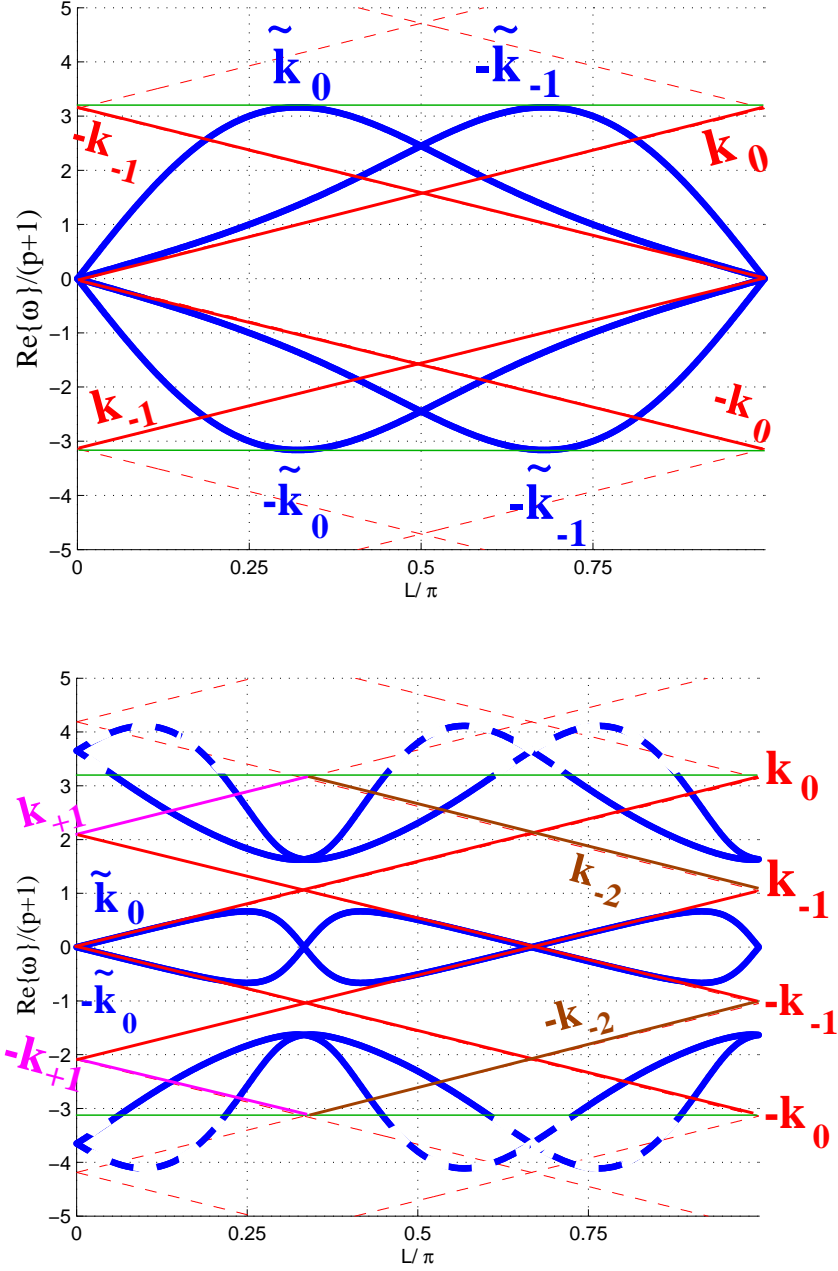
FIGURE 3.6: Numerical dispersion and dissipation $\omega = f(\tilde{k}_n)$ as a function of $L = k_0\Delta/(p+1)$, for scalar 1-D-DGTD. Analytical dispersion in red $\omega = k_n = ((p+1)L + 2n\pi)/\Delta$. Sub-index in $\tilde{k}_m$ has been added *a posteriori* according to the analytical mode matched for some L region (no identification for $\tilde{k}_m$ has been guessed for $p = 2$ in the centered case). Up: Centered p=1, Down: Centered p=2. The bandwidth allowed by Shannon theorem is delimited with green lines, while dashed lines indicate modes outside this band. Blue is used for numerical modes and red (magenta & brown) for the analytical ones. ($\Delta = 1$, $\mu_0 = 1$, $\varepsilon_0 = 1$)
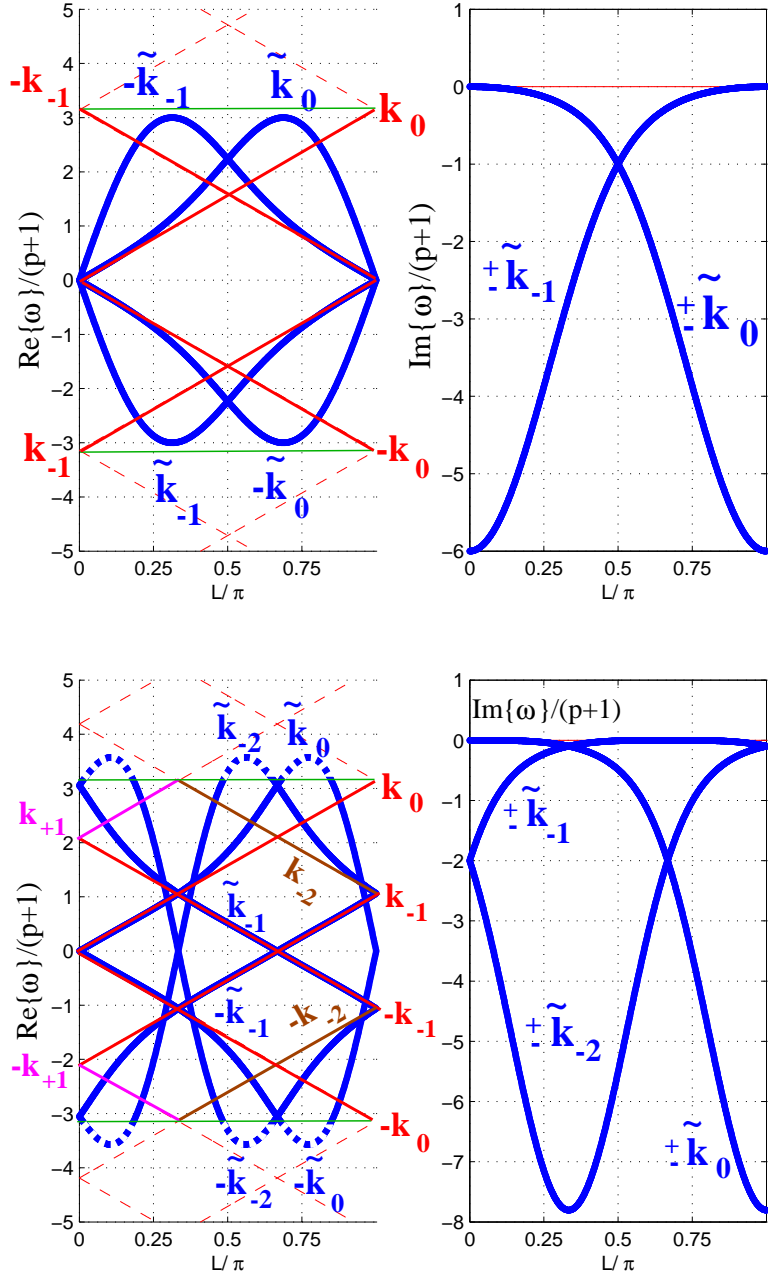
FIGURE 3.7: Numerical dispersion and dissipation $\omega = f(\tilde{k}_n)$ as a function of $L = k_0\Delta/(p+1)$, for scalar 1-D-DGTD. Analytical dispersion in red $\omega = k_n = ((p+1)L + 2n\pi)/\Delta$. Sub-index in $\tilde{k}_m$ has been added *a posteriori* according to the analytical mode matched for some L region (no identification for $\tilde{k}_m$ has been guessed for $p = 2$ in the centered case) . Up: Upwind p=1, Bottom: Upwind p=2. The bandwidth allowed by Shannon theorem is delimited with green lines, while dashed lines indicate modes outside this band. Blue is used for numerical modes and red (magenta & brown) for the analytical ones. ($\Delta = 1, \mu_0 = 1, \varepsilon_0 = 1$)
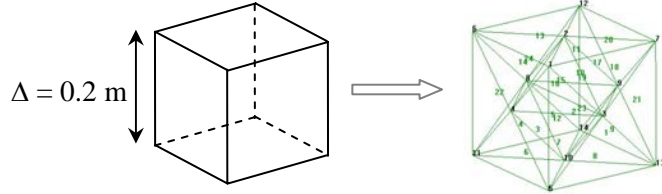
FIGURE 3.8: Geometry under analysis for the 3-D eigen-problem.
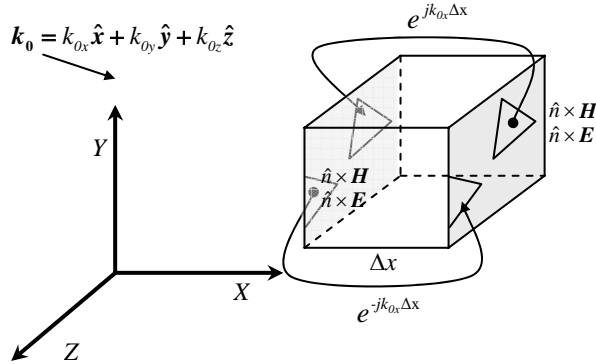
FIGURE 3.9: Examples of the application of the 3-D-PBC between contour faces from elements located at opposite sides.

3.5.2 Extension to Three Dimension

Let us move to a 3-D case solved with hierarchal vector basis that is complete up to order $p = 2$, both for the gradient and the rotational spaces. We have meshed a cubic domain in a symmetrical way composed of 24 tetrahedra, as is depicted in figure 3.8.

The 3-D-PBC in space can be expressed as,

$$
\begin{aligned}
\hat{\mathbf{n}} \times \boldsymbol{H}|_{i+\Delta i} &= \hat{\mathbf{n}} \times \boldsymbol{H}|_i \, e^{-j\alpha_i}, \\
\hat{\mathbf{n}} \times \boldsymbol{E}|_{i+\Delta i} &= \hat{\mathbf{n}} \times \boldsymbol{E}|_i \, e^{-j\alpha_i} \qquad \text{with } i = \{x, y, z\}
\end{aligned}
\tag{3.103}
$$

where α_i is the phase shift in each direction of the space. Considering that $\mathbf{k}_0 = k_{0x}\hat{\mathbf{x}} + k_{0y}\hat{\mathbf{y}} + k_{0z}\hat{\mathbf{z}}$ is the fundamental mode, the phase shift can be evaluated by $\alpha_i = k_{0i}\Delta_i$. In our case, we enforced PBC in the x-direction with $\alpha_x = 2\pi\Delta$, being $\Delta = 0.2$, and PBC conditions at the YZ and ZX-planes with $\alpha_y = \alpha_z = 0$ (no delay). An example of the application of the 3-D-PBC is depicted in figure 3.9.

The numerical eigenvalue $\tilde{k}$ is plotted in figure 3.10. There are $2MQ = 1440$ modes corresponding to the number of dofs of the problem ($M = 24$ tetrahedra and $Q = 30$ dofs per element). Again, we find that the spectrum of the DG operator depends heavily on the flux-evaluation scheme. It can be seen that, for the centered scheme, none of

the modes supported by the numerical method has dissipation $\tilde{k}_{imag} = 0$. Therefore, all numerical modes, both well-resolved physical and poorly resolved spurious solutions, could be present in a numerical simulation and propagate on the computational domain. On the contrary, for the upwind case, we can clearly distinguish between well-resolved physical modes [4] and poorly resolved spurious modes by looking at their attenuation $\tilde{k}_{imag} \approx 0$. Hence, poorly resolved spurious modes decrease exponentially with spatial position and do not propagate along the computational domain. It is important to note that some undesirable dissipation also affects the well-resolved physical modes, depending on their spatial resolution.

For the penalized flux with $\tau = 0.1$, similar conclusions are drawn. The main difference is that the dissipation of the spurious modes decreases compared to the upwind case. However, the choice of the τ parameter also has an impact on the stability conditions of the final numerical scheme, as appears following (section 4.3) for the Leap-Frog (LF) scheme and in [70] for Runge-Kutta (RK). In general, the stability upper limit in Δt becomes more restrictive when τ increases. The use of partial penalized flux with small values of the τ parameter has negligible effects on the stability of the scheme while keeping enough practical attenuation in the poorly resolved spurious modes.

Finally, let us consider a more realistic case: a 1m-side cubic 3-D PEC cavity meshed with 5025 tetrahedra (see figure 3.11). The fields in the cavity are then excited via a electric-current source with a Gaussian pulse time signal, with 10dB bandwidth of approximately 400 MHz. The problem has been simulated up to a physical time of 0.5 μs by means of a fourth-order Runge-Kutta (RK4) time-integration scheme. This problem was computed with centered, upwind and partial penalized flux, with very low $\tau = 0.025$ with hierarchal vector-basis functions of complete order $p = 2$.

The electric field is sampled at one point and the Fourier transform performed for the vertical component (see figure 3.12). The power spectrum computed with centered flux is noisy and shows spectral pollution due to the presence of nonphysical spurious modes. In case of upwind or partial penalized flux (even for such a low value of τ), we can clearly distinguish the different resonant frequencies.

A similar analysis appears in [53] with nodal functions, where the presence of spurious modes, in case of centered flux, were reported as well. In case of upwind or penalized schemes, the spurious modes are also present but having a significant dissipation associated only with them (very little dissipation for the physical models depending on the level of discretization) avoiding spectral pollution and the contamination of the solutions. This fact, as has been proved above, does not depend on the kind of basis functions used

---

[4]Four fundamental rightward/leftward planewaves (two polarizations) and their corresponding harmonics.
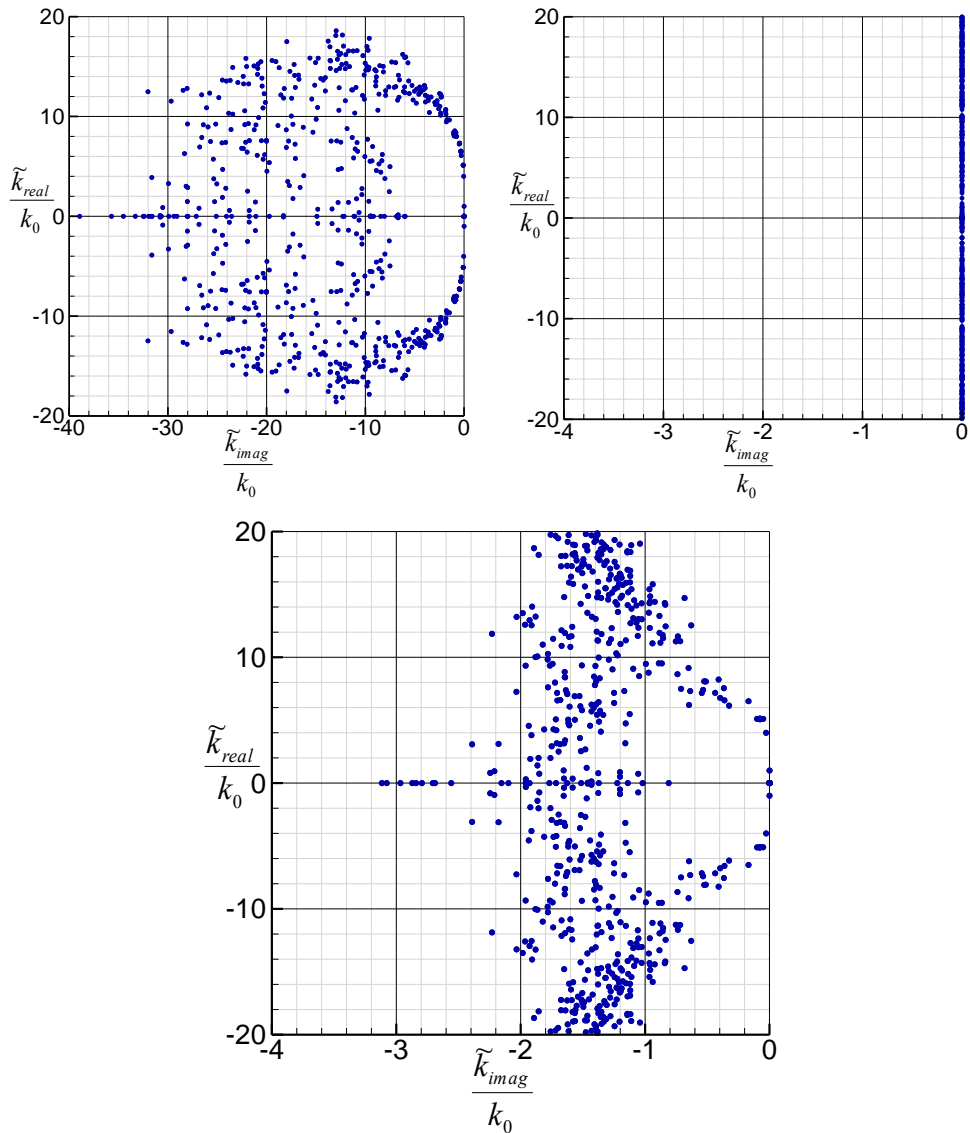
FIGURE 3.10: Spectrum of the DG operator for a cubic domain (meshed with 24 tetrahedra) with PBC ($\mathbf{k}_0 = 2\pi\hat{\mathbf{x}}$, $\Delta = 0.2$ and $p = 2$). Upwind flux (upper left), Centered flux (upper right), Partially penalized flux $\tau = 0.1$ (lower).
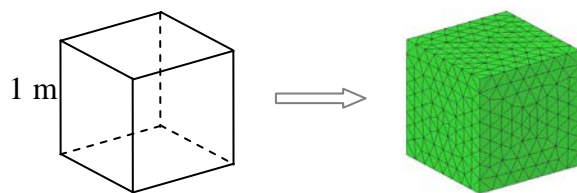

FIGURE 3.11: Cubic PEC cavity.
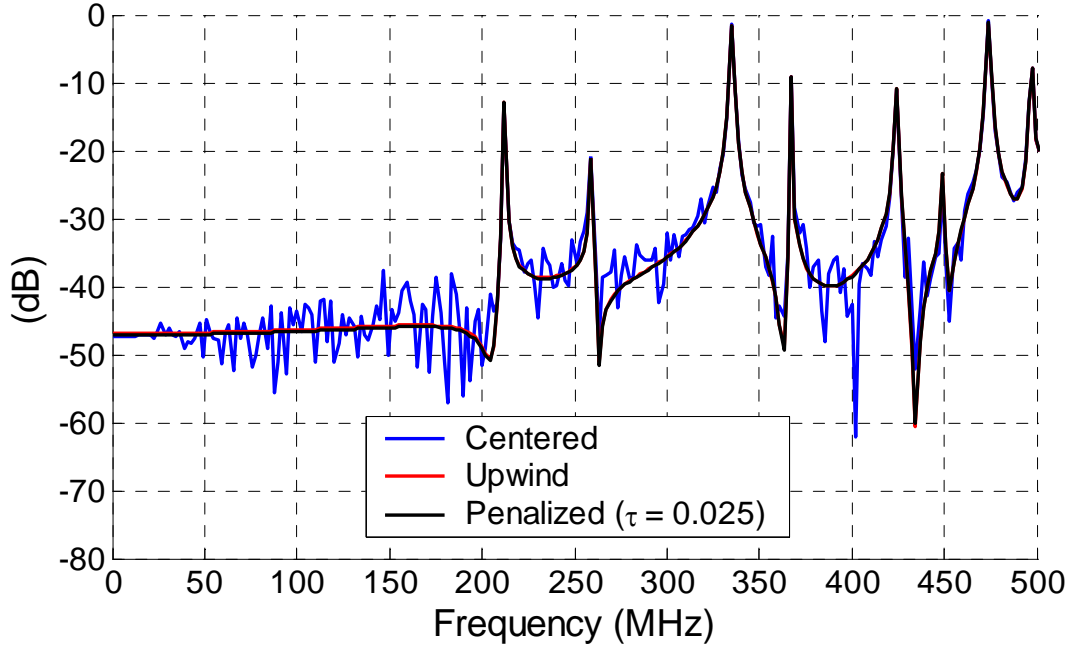
FIGURE 3.12: Power spectrum of the vertical component of electric field sampled at a point inside the cavity, computed using centered, upwind and partial penalized ($\tau = 0.025$) fluxes, 4th-order 2N-storage Runge-Kutta and $p = 2$.

by the scheme, as has been widely investigated in FEM in frequency domain, and it is a remarkable difference in Discontinuous Galerkin time domain methods, compare to the continuous formulation.

3.5.3   Convergence of the DG Semi-Discrete Scheme

The objective of this analysis is to understand the nature of the errors of the DG operator, estimate the convergence rates and analyze the influence of the τ parameter. Some convergence rates of Discontinuous Galerkin methods has been conjectured and/or proven in other works, [47, 55, 56]. In our case the convergence rates of the DG operator have been numerically evaluated with the 3-D problem described in the previous section (see figure 3.8) with $\mathbf{k}_0 = 2\pi\hat{\mathbf{x}}$. The eigenvalue problem is numerically solved for different Δ values. In all cases, the closest eigenvalue $\widetilde{k}_m$ to $k_0 = |\mathbf{k}_0|$ is chosen as the valid one, referred here as $\widetilde{k}_0 = \widetilde{k}_{real} + j\widetilde{k}_{imag}$. Numerical-dispersion, numerical-dissipation and global errors can be computed as a function of $\widetilde{k}_0$ and k_0.

Two different sources of error can be identified, one due to dispersion or phase delay, which is in the real part ($\widetilde{k}_{real}$) related to the numerical velocity phase as $\frac{\omega}{\widetilde{k}_{real}}$, and the other is dissipation or amplitude decreasing of the wave, which is related to the imaginary part ($\widetilde{k}_{imag}$). Following expressions has been used to evaluate the different

errors per wavelength (λ),

L^2-norm error per wavelength due to phase delay: $\quad \left| e^{-jk_0\lambda} - e^{-j\widetilde{k}_{real}\lambda} \right| \qquad$ (3.104a)

L^2-norm error per wavelength due to dissipation: $\quad \left| 1 - e^{\widetilde{k}_{imag}\lambda} \right| \qquad$ (3.104b)

L^2-norm error per wavelength: $\quad \left| e^{-jk_0\lambda} - e^{-j\widetilde{k}_0\lambda} \right| \qquad$ (3.104c)
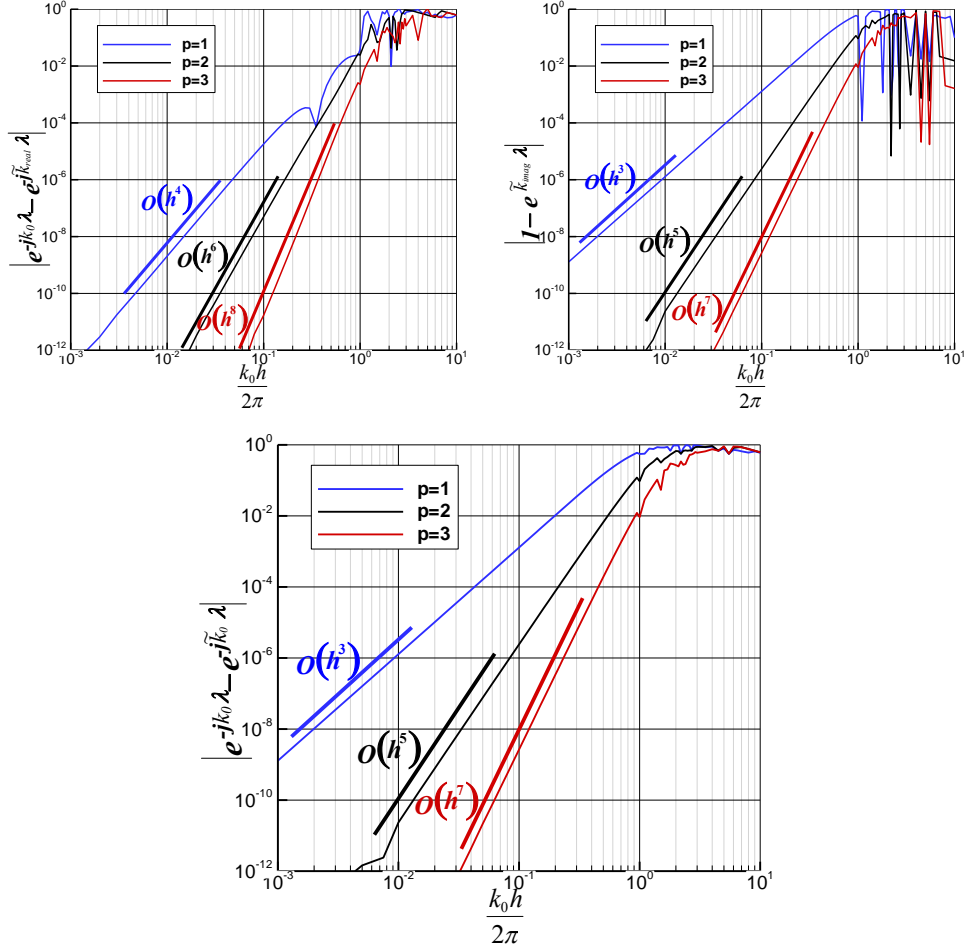

FIGURE 3.13: Convergence of the dispersion (upper left), dissipation (upper right) and L^2-norm (lower) errors of the physical mode for the DG operator with upwind flux.

The results for upwind flux appear in figure 3.13, where super-convergence property of the DG operator is proved. The convergence rate for the phase error agrees with $O\left(h^{2p+2}\right)$ and the amplitude error follows $O\left(h^{2p+1}\right)$, being p the order of the polynomial space for the vector-basis functions, and h a measure for the size of elements, $h = \Delta$ has been chosen in our case. These convergence rates are similar to those obtained by Hu et al. [47] or Ainsworth [55, 56].

Figure 3.14 shows the influence of the τ parameter in the dispersion, dissipation and L^2-norm errors for different p orders. In general, most of the practical and real applications need an error of about 10^{-2}, so this zone of the curves are of particular interest.


(a.1) Dispersion error.   (a.2) Dissipation error.   (a.3) L^2-norm error.

(b.1) Dispersion error.   (b.2) Dissipation error.   (b.3) L^2-norm error.

(c.1) Dispersion error.   (c.2) Dissipation error.   (c.3) L^2-norm error.
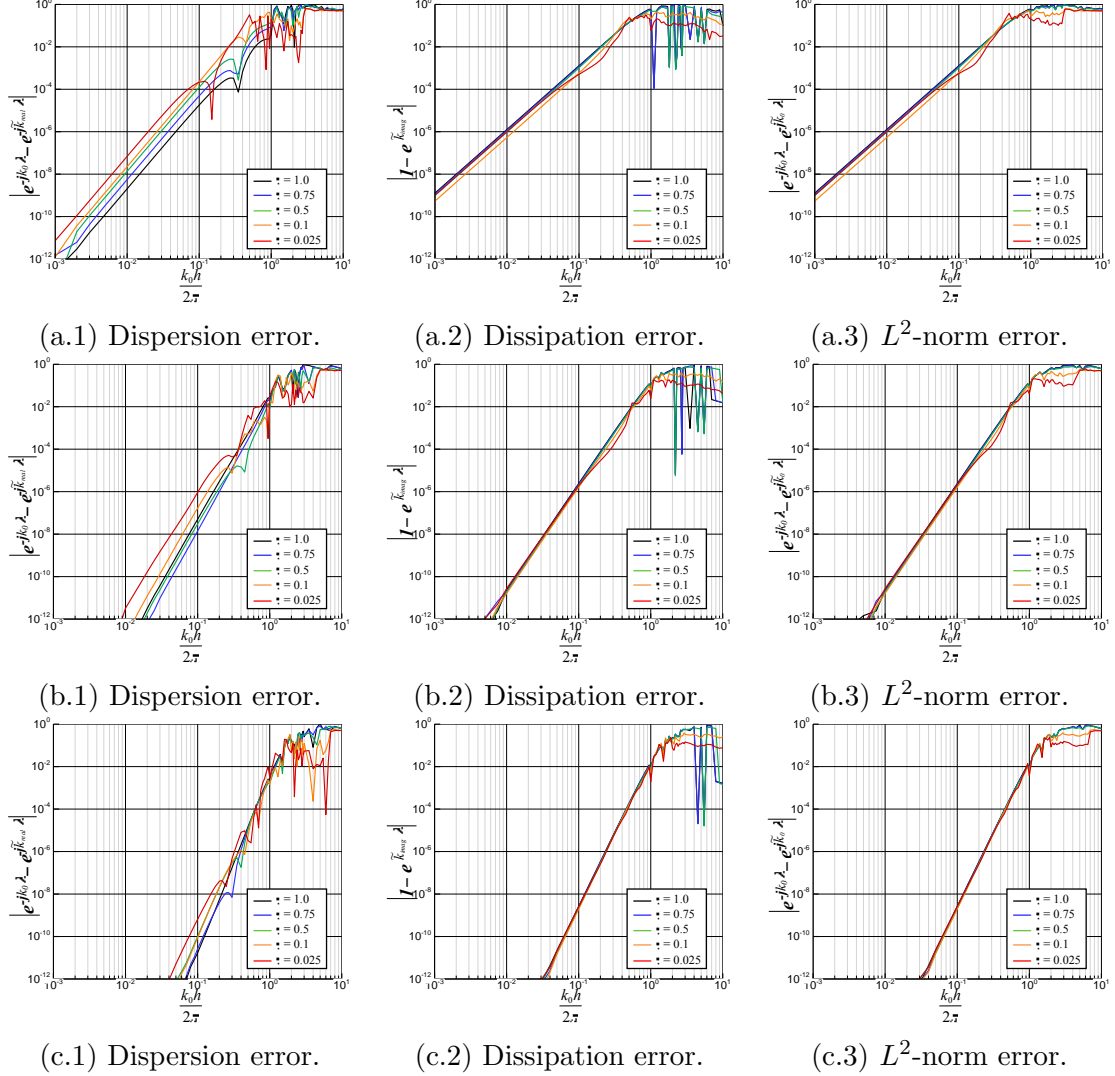
FIGURE 3.14: Influence of the τ parameter in the error of the DG operator for different p orders. (a) $p = 1$, (b) $p = 2$ and (c) $p = 3$.

Figures 3.13 and 3.14 call for the following remarks:

- The error and the convergence rate for the dissipation error is worse than for the dispersion error. Thus, the dissipation error places a higher requirement on the resolution of the scheme than the dispersion error in the DG operator. This is an important change from other methods like FDTD, which are not dissipative and there is only dispersion error.

- Super-convergence of the error is found in all cases.

- Despite of the fact that the dissipation of the spurious modes is only function of τ parameter and very sensible to its value, dissipation error of the physical mode is not noticeably reduced decreasing τ.

- However, τ has an influence in the dispersion error, but it is negligible from a practical point of view.

- The typical error where real problems are solved, which is about 10^{-2}, is in the zone where the convergence rate becomes exponential.

- This analysis has been performed considering a plane wave traveling in an homogenous medium. The extension of all these conclusions to any general problem must be done with care. In case of geometrical singularities, as corners or vertex, the convergence rate considerably decreases. It is very well-know that these problems shall be dealt by increasing the resolution of the mesh, giving rise to h-p refinement strategies.

This analysis do not take into account the time integration method. From spatial DG discretization point of view, the main limitation is in the dissipation error, and the dispersion error is bellow dissipation error. This fact should be considered in the design of time integration schemes to avoid the introduction of more dissipation and keep under control the dispersion error. It is important to notice that, the general approach for the design of Runge-Kutta schemes optimizes the time step necessary for stable solutions, while holding dispersion and dissipation fixed. It is found that maximizing dispersion minimizes dissipation, and *viceversa*. In case of Leap-Frog, there is not dissipation and the dispersion error depends on Δt being a second-order accurate scheme. Some limitations are, therefore, expected in case of LF because of dispersion error. Leap-Frog with DG method is analyzed in detail in section 4.5. Higher order Leap-Frog (LF_N) schemes have been proposed with DG method which can relax that limitation, [67]

3.6   Summary of the Proposed Semi-Discrete Scheme

In this chapter a semi-discrete scheme for the Maxwell's equation has been formulated. The spatial discretization scheme is based on the Discontinuous Galerkin methodology, and expressions for the flux evaluation, capable of easily dealing with the most common boundary conditions (dielectrics, PEC, PMC, SM-ABC) and anisotropic materials, has been developed. The formulation of the conformal UPML truncation condition has been reviewed and integrated in the DG semi-discrete scheme. Finally, the numerical dispersion and dissipation of the spatial DG scheme have been analyzed, and the convergence

rates of the different kinds of errors (dispersion and dissipation) have been numerical estimated.

Three different schemes has been proposed for the evaluation of the flux between elements. Following the three are listed and a short rationale has been included.

- The centered flux, which is the simplest method, drives to numerical methods that has problems with non-physical solutions or spurious modes.

- The upwind flux, which is the typically used in FVTD and it is the solutions to the Riemann problem in the discontinuity of the tangential field components, drives to a quasi-explicit semi-discrete scheme in space, not being fully explicit. In this case, efficient time integration schemes, as the Leap-Frog can not be applied without important restriction in the time-step. Respect to the spurious modes, they are affected by the dissipation terms much more than the physical solutions, obtaining a spurious-free method.

- The partial penalized flux is based upon the upwind scheme but the dissipative terms are reduced by a factor. These terms are the ones that make upwind flux scheme implicit in space. Making these terms smaller permits to use Leap-Frog time integration scheme more efficiently and in an explicit way. The dissipation of the spurious modes is smaller than in case of upwind flux, due to the reduction of the dissipation terms, but are again much higher than for the physical solutions. The result is a method where Leap-Frog can be used, and spurious-free, if the dissipative terms are high enough.

Chapter 4

Discontinuous Galerkin Time Domain Methods

Since the FDTD method was firstly proposed by Yee in 1966 [1] for solving Maxwell's equations, it has become undoubtedly the most widespread method among physicists and engineers, due to its simplicity and flexibility to deal with real problems. However, their inability to effectively handle complex geometries, due to stair-casing error, and the limitations in the accuracy (second order in space and time $O\left(h^2, \Delta t^2\right)$), prompted some scientists to search for alternatives long ago, being Finite Element (FE) the obvious alternative. Considering all the schemes based on FE in the literature, Discontinuous Galerkin Time Domain (DGTD) approaches gather most of the advantages of FDTD; spatial explicit algorithm, simplicity, easy parallelization, and memory and computational cost growing linearly with the number of elements. Besides, DGTD schemes retain most of the goods of FE, adaptability of the unstructured meshes and spatial super-convergence what allows to deal with problems where the required precision varies over the entire domain, or when the solution lacks smoothness.

With the spatial semi-discrete system at hand, the choice of the time integration scheme is a crucial step for the global efficiency and viability of a numerical method. There are two major families: implicit and explicit methods. Implicit schemes, as Crank-Nicolson [75], require to solve a banded system of linear equations each time-step, which becomes impractical in electrically large problems. Implicit methods usually are unconditionally stable, and the time-step can be chosen as long as possible, considering only the highest frequency under analysis, reducing to the minimum the number of required time-steps in a complete simulation. Explicit schemes, however, are conditionally stable depending on the spatial discretization, which results in a large number of iteration per analysis, but the computational effort is very low for each time-step.

It is important to remark here that the core idea of DGTD is to relax the continuity conditions to yield a quasi-explicit algorithm. Hence, in this study, we focus on explicit time integration schemes. Our objective is to design an arbitrary high-order DGTD method, which combines the spatial discretization features of the method, discussed in Chapter 3, with a efficient explicit time integration scheme.

There are two main explicit temporal integration schemes usually employed in DGTD methods; (i) the well-proven and versatile Runge-Kutta (RK) schemes and (ii) the efficient Leap-Frog (LF) classically used for Maxwell's equations. Both schemes are reviewed in this dissertation, but the main effort is put on LF, where a algorithm named as Leap-Frog Discontinuous Galerkin (LFDG), is formulated, and, a fully explicit Local Time Stepping (LTS) strategy is developed.

The overall accuracy of a time domain (TD) method is function of the convergence of the spatial scheme with the element size (h), and the convergence of the temporal integration scheme with the time-step (Δt). To characterize, therefore, the accuracy limits of a TD method, not only does the spatial semi-discrete scheme have to be considered in the analysis, but also the time integration method.

In this chapter, the Leap-Frog Discontinuous Galerkin (LFDG) algorithm, based upon partial penalized flux evaluation, second-order Leap-Frog time integration scheme and hierarchal vector-basis functions, is introduced. A Local Time Stepping algorithm is also developed to make the method efficient enough to deal with real problems. The LFDG method is analyzed, considering topics like stability, spurious and global convergence of the method. Finally, a computational cost versus accuracy analysis of the LFDG method is performed and compared to the well-known FDTD method.

4.1 Temporal Integration

The general DG spatial semi-discrete formulation introduced in Chapter 3, results in a quasi-explicit scheme, in space, which permits efficiently the use of explicit time integration methods.

In this section, the more common schemes applied in DGTD methods are reviewed and apply to the ODE system of (3.13). Firstly, the Low-Storage Runge-Kutta (LSRK) scheme, which has been extensively used in DGTD methods [52]. Then, the well-know Leap-Frog (LF), for which a local time stepping (LTS) technique has been developed.

4.1.1 Runge-Kutta Scheme

Explicit Runge-Kutta (RK) methods are particularly popular due to their robustness, flexibility and good performance. The main advantage of RK schemes, compared to Leap-Frog (LF), is that these schemes easily allow to adjust the order of time integration m to the order p of the spatial discretization. The used of fixed-order time-integration schemes may spoil the high-order convergence of the global scheme. Thus, Cockburn, Shu and collaborators in a series of papers [35, 36, 37, 38, 39], have proposed to use RK methods for the time-marching of DGTD methods. In particular, they have employed a special variation, where the number of stages s is equal to the order m of the method. However, two problems are associated with these schemes. First, during a time-step the results of all stages must be kept in memory, this leads to memory requirements proportional to sN, being N number of the dofs. Increasing the order m in time, increases memory requirements being prohibitively for electrically large problems. The second problem is that the maximum allowed time-step in each element for these schemes is quite restricted and becomes even more severe for higher orders of m.

In order to overcome these problems when order m grows, increasing of memory requirements and decreasing of efficiency due to more restricted stability condition, Hesthaven and Warburton, [52], and other authors, as Chen [58], have explored the use of Low-Storage Runge-Kutta (LSRK) methods. The required memory in these methods is proportional to $2N$, independently of the number of stages, Williamson [153]. Furthermore, by using a larger number of stages $s > m$, it becomes possible to relax stability condition. The disadvantage is that such methods are only known up to order $m = 4$. However, for most real problems this suffices (recall that LF at best operates with second-order accuracy, $m = 2$). Some particularly popular LSRK schemes with $m = 4$ and $s = 5$ have been derived by Carpenter and Kennedy [154]. One of this schemes is the actually used in this work and described bellow. A very interesting comparison of the different available RK methods applied to DGTD method in Maxwell's equations was performed by Diehl, Busch and Niegemann in [70].

Let us consider the matrix form of the semi-discrete system within each element m without sources expressed as,

$$d_t H^m = \frac{1}{\mu} \mathbb{M}^{-1} \left[-\left(\mathbb{S} - \mathbb{F}_{\kappa e}\right) E^m - \mathbb{F}_{\kappa e}^+ E^{m+} + \mathbb{F}_{\nu h} H^m - \mathbb{F}_{\nu h}^+ H^{m+} - \sigma_m \mathbb{M} H^m \right] \quad (4.1a)$$

$$d_t E^m = \frac{1}{\varepsilon} \mathbb{M}^{-1} \left[\left(\mathbb{S} - \mathbb{F}_{\kappa h}\right) H^m + \mathbb{F}_{\kappa h}^+ H^{m+} + \mathbb{F}_{\nu e} E^m - \mathbb{F}_{\nu e}^+ E^{m+} - \sigma_e \mathbb{M} E^m \right] \quad (4.1b)$$

where we have left, in the left hand side, the time derivatives of the electric and magnetic fields. We can identified (4.1) as a first order coupled ordinary differential equations

(ODE's) of the form,

$$d_t U = F\left[t, U\left(t\right)\right].$$ (4.2)

being $U = [H, E]$, all the dofs of the problem.

The discrete approximation is made with an 5-stage explicit RK scheme. The general implementation over a time-step Δt, from t_n to $t_n + \Delta t$, is accomplished by,

$$k_1 = F\left(t_n, U^n\right)$$ (4.3a)

$$k_i = F\left(t_n + c_i \Delta t, U^n + \Delta t \sum_{j=1}^{i-1} a_{i,j} k_j\right) \quad i = 2, 3, 4, 5$$ (4.3b)

$$U_{n+1} = U^n + \Delta t \sum_{j=1}^{5} b_j k_j$$ (4.3c)

where $U^n = U(t_n)$ and $U_{n+1} = U(t_n + \Delta t)$ and the fixed scalars $a_{i,j}$, b_j and c_i are the coefficients of the RK formula.

This algorithm can be reworked, where each successive stage depends only on the previous one which gives rise to the Low-Storage Runge-Kutta (LSRK) method. Thus, the 5-stage equivalent algorithm becomes,

$$dU_j^n = A_j dU_{j-1} + \Delta t F\left(t_n + c_j \Delta t, U_j^n\right)$$ (4.4a)

$$U_j^n = U_{j-1} + B_j dU_j^n \quad j = 1, 2, 3, 4, 5$$ (4.4b)

So that the algorithm is self-starting, $(A_1 = 0)$ and only dU^n and U^n must be kept in memory, which results in a 2N-storage algorithm.

In [154] appear precise values of A_j, B_j and c_j that are required to yield a 4th order scheme. Table 4.1 shows those used in this work.

4.1.2 Leap-Frog Scheme

In this section the Leap-Frog Discontinuous Galerkin (LFDG) algorithm is formulated. It is based on the spatial DG scheme described in Chapter 3, where the explicit Leap-Frog time integration scheme is applied.

An important limitation of any explicit time-integration scheme is the stability condition, which imposes a maximum time step (Δt_{MAX}^m) in each element. The time step is found to be dependent on its electrical size, and on the order of the basis functions employed in that particular element. The material of adjacent elements, boundary conditions on its faces, aspect-ratio, and curvature (in case quadratic elements) also influence the

TABLE 4.1: Coefficients for optimal 5-stage, 4th order, 2N-Storage RK Scheme.

COEFFICIENT	VALUE
A_1	0.0
A_2	$-\frac{567301805773}{1357537059087}$
A_3	$-\frac{2404267990393}{2016746695238}$
A_4	$-\frac{3550918686646}{2091501179385}$
A_5	$-\frac{1275806237668}{842570457699}$
B_1	$\frac{1432997174477}{9575080441755}$
B_2	$\frac{5161836677717}{13612068292357}$
B_3	$\frac{1720146321549}{2090206949498}$
B_4	$\frac{3134564353537}{44814673103381}$
B_5	$\frac{2277821191437}{14882151754819}$
c_1	0.0
c_2	$\frac{1432997174477}{9575080441755}$
c_3	$\frac{2526269341429}{6820363962896}$
c_4	$\frac{2006345519317}{32243100637761}$
c_5	$\frac{2802321613138}{2924317926251}$

stability condition [63]. This fact, when we are dealing with unstructured meshes, results in strong disparities in the required time step among elements, leading to a global time-step constrained by the smallest one, in order to ensure global stability. This leads to a major waste of computational time in updating elements at a rate much slower than its own maximum time step. To avoid this problem, a fully explicit local time stepping (LTS) strategy has been developed based upon a leap-frog integration scheme. Similar schemes appear in [63, 79, 80].

Finally, we extend the LFDG algorithm to the semi-discrete system of (3.95), which considers a UMPL medium with DG spatial discretization.

4.1.2.1 LFDG Algorithm

Let us consider the matrix form of the DG semi-discrete system of Chapter 3, within each element m without sources expressed as,

$$\mu \mathbb{M} d_t H^m + \sigma_m \mathbb{M} H^m - \mathbb{F}_{\nu h} H^m + \mathbb{F}_{\nu h}^+ H^{m+} = -\left(\mathbb{S} - \mathbb{F}_{\kappa e}\right) E^m - \mathbb{F}_{\kappa e}^+ E^{m+} \qquad (4.5a)$$

$$\varepsilon \mathbb{M} d_t E^m + \sigma_e \mathbb{M} E^m - \mathbb{F}_{\nu e} E^m + \mathbb{F}_{\nu e}^+ E^{m+} = \left(\mathbb{S} - \mathbb{F}_{\kappa h}\right) H^m + \mathbb{F}_{\kappa h}^+ H^{m+} \qquad (4.5b)$$

The basis of leap-frog (LF) scheme is to sample the unknown fields in a staggered way. Thus, the electric field is evaluated at $t_n = n\Delta t$, and the magnetic field, at $t_{n+\frac{1}{2}} = \left(n + \frac{1}{2}\right)\Delta t$. In the same way, equation (4.5a) is evaluated (or tested in time, if we consider a point matching testing procedure), at t_n and the equation (4.5b) at $t_{n+\frac{1}{2}}$.

The first-order time derivatives will be approximated by central difference method, which is second-order accurate.

$$(d_t H^m)_n = \frac{H^m_{n+\frac{1}{2}} - H^m_{n-\frac{1}{2}}}{\Delta t} + O\left(\Delta t^2\right); \quad (d_t E^m)_{n+\frac{1}{2}} = \frac{E^m_{n+1} - E^m_n}{\Delta t} + O\left(\Delta t^2\right) \quad (4.6)$$

For the terms with the electric and magnetic conductivity, we use an average approximation which is also a second order approximation of the identity operation.

$$H^m_n = \frac{H^m_{n+\frac{1}{2}} + H^m_{n-\frac{1}{2}}}{2} + O\left(\Delta t^2\right); \quad E^m_{n+\frac{1}{2}} = \frac{E^m_{n+1} + E^m_n}{2} + O\left(\Delta t^2\right) \quad (4.7)$$

For the two extra dissipative terms arising from the upwind flux formulation, we use the backward approximation ($H^m_n \simeq H^m_{n-\frac{1}{2}}$ and $E^m_{n+\frac{1}{2}} \simeq E^m_n$), since an average approximation (4.7) would yield a globally implicit scheme, due to the coupling terms from the adjacent elements [94]. This fact introduces a slightly penalization in the stability condition, and considering that purely upwind flux evaluation requires an also smaller time step, the alternative is the use of partially penalized flux evaluation [63]. When we choose an appropriate value of the τ parameter, the effect in the stability of the scheme is very low (analyzed in detail in section 4.3). In case of centered flux evaluation, these terms are null, but problems arise in relation to spurious modes (see section 3.5.1). When the temporal approximation for the dofs is inserted in (4.5), the resulting fully explicit LFDG algorithm is the following,

$$H^m_{n+\frac{1}{2}} = \alpha_m H^m_{n-\frac{1}{2}} + \beta_m \mathbb{M}^{-1} \left[-\left(\mathbb{S} - \mathbb{F}_{\kappa e}\right) E^m_n - \mathbb{F}^+_{\kappa e} E^{m+}_n + \mathbb{F}_{\nu h} H^m_{n-\frac{1}{2}} - \mathbb{F}^+_{\nu h} H^{m+}_{n-\frac{1}{2}} \right] \quad (4.8a)$$

$$E^m_{n+1} = \alpha_e E^m_n + \beta_e \mathbb{M}^{-1} \left[\left(\mathbb{S} - \mathbb{F}_{\kappa h}\right) H^m_{n+\frac{1}{2}} + \mathbb{F}^+_{\kappa h} H^{m+}_{n+\frac{1}{2}} + \mathbb{F}_{\nu e} E^m_n - \mathbb{F}^+_{\nu e} E^{m+}_n \right] \quad (4.8b)$$

where the expressions for the constants are,

$$\alpha_m = \frac{1 - \frac{\Delta t \sigma_m}{2\mu}}{1 + \frac{\Delta t \sigma_m}{2\mu}}, \quad \beta_m = \frac{\Delta t}{\mu \left(1 + \frac{\Delta t \sigma_m}{2\mu}\right)} \quad (4.9a)$$

$$\alpha_e = \frac{1 - \frac{\Delta t \sigma_e}{2\varepsilon}}{1 + \frac{\Delta t \sigma_e}{2\varepsilon}}, \quad \beta_e = \frac{\Delta t}{\varepsilon \left(1 + \frac{\Delta t \sigma_e}{2\varepsilon}\right)} \quad (4.9b)$$

4.1.2.2 Local Time Stepping

The basis of the proposed LTS strategy is to arrange all the elements of the complete mesh into L levels, considering each its own maximum time step and making use of average approximations (or linear interpolations) when needed. The time step for the level l is $\Delta t_l = (2k+1)^{l-1} \Delta t_1$, k being a positive real integer and Δt_1 the effective time

step for the first level ($l = 1$). All the elements of the l level must fulfill the condition $\Delta t_l < \Delta t^m_{MAX}$ (being Δt^m_{MAX} the maximum Δt for stability at the element m). For instance, $k = 2$ means that there is a factor 3 between the time steps of consecutive levels.

First of all, at the pre-process stage, we classify all the mesh elements into $2*L-1$ possible sets requiring a special treatment: L different levels plus the $L - 1$ interfaces. Figure 4.1 shows an example in 2-D, where two levels and the interface have been identified.
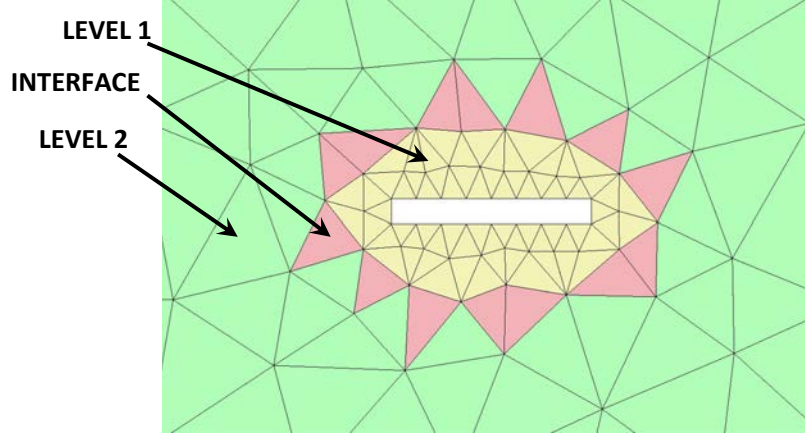

FIGURE 4.1: 2-D classification example of two LTS levels and the interface.

For simplicity, let us describe the LTS algorithm for this particular case ($L = 2$). The procedure can be easily generalized to any problem with L levels. Let us define two updating expressions, one for the electric field and other for the magnetic field, from the LFDG algorithm of (4.8).

$$H^m_{n+\frac{p}{2}} = f_H \left(p\Delta t_1, H^m_{n-\frac{p}{2}}, H^{m+}_{n-\frac{p}{2}}, E^m_n, E^{m+}_n \right) \tag{4.10a}$$

$$E^m_{n+p} = f_E \left(p\Delta t_1, E^m_n, E^{m+}_n, H^m_{n+\frac{p}{2}}, H^{m+}_{n+\frac{p}{2}} \right) \tag{4.10b}$$

where p is an integer value, which allows us to use the updating functions to compute samples of the fields to any multiple of Δt_1.

The starting state 0 for the full sequence is shown in figure 4.2. The sequence of the proposed local time-stepping algorithm continues as (see also figure 4.3):

- *Step 1. Update magnetic field, f_H, for the level 1 ($H_{n+\frac{1}{2}}$), interface and level 2 ($H_{n+\frac{3}{2}}$).*
  In case of level 1, $p = 1$ must be used, and for the level 2 and the interface, $p = 3$. We need E_n dofs, which are all available.

time	LEVEL 1		INTERFACE		LEVEL 2	
$(n-3/2)\Delta t_1$		H		H		H
$(n-1)\Delta t_1$	E					
$(n-1/2)\Delta t_1$		H		H		
$(n)\Delta t_1$	E		E		E	
$(n+1/2)\Delta t_1$						
$(n+1)\Delta t_1$						
$(n+3/2)\Delta t_1$						
$(n+2)\Delta t_1$						
$(n+5/2)\Delta t_1$						
$(n+3)\Delta t_1$						

FIGURE 4.2: Initial state, previously to the sequence of the LTS, for the three different sets of the scenario of figure 4.1, (L=2).

- *Step 2. Update electric field, f_E, for the level 1 and interface (E_{n+1}).*
  In both cases $p = 1$ must be used. We need $H_{n+\frac{1}{2}}$ dofs. This information is available in level 1, but has to be evaluated in the interface, by averaging $H_{n+\frac{3}{2}}$ and $H_{n-\frac{1}{2}}$, and in level 2, by interpolating $H_{n+\frac{1}{2}} = \frac{2}{3}H_{n+\frac{3}{2}} + \frac{1}{3}H_{n-\frac{3}{2}}$.

- *Step 3. Update magnetic field, f_H, for the level 1 ($H_{n+\frac{3}{2}}$).*
  Clearly, $p = 1$ must be used. E_{n+1} is needed, in level 1 and interface, and available.

- *Step 4. Update electric field, f_E, for the level 1 (E_{n+2}), interface and level 2 (E_{n+3}).*
  In case of level 1, $p = 1$ must be used, and for the level 2 and the interface, $p = 3$. We need $H_{n+\frac{3}{2}}$ dofs, which are available.

- *Step 5. Update magnetic field, f_H, for the level 1 and interface ($H_{n+\frac{5}{2}}$).*
  In both cases $p = 1$ must be used. We need E_{n+2} dofs. This information is available in level 1, but has to be evaluated in the interface, averaging E_{n+1} and E_{n+3}, and in level 2, interpolating $E_{n+2} = \frac{2}{3}E_{n+3} + \frac{1}{3}E_n$.

- *Step 6. Update electric field, f_E, for the level 1 (E_{n+3}).*
  Obviously, $p = 1$ must be used. $H_{n+\frac{5}{2}}$ is needed, in level 1 and interface, and available.

  After this step, we are again in the state 0 for the next sequence. It should be noted that we will need to bear in mind some previous steps of the dofs for interpolation proposes.

(a) Step 1.

time	LEVEL 1		INTERFACE		LEVEL 2	
$(n-3/2)\Delta t_1$		H		H		H
$(n-1)\Delta t_1$	E					
$(n-1/2)\Delta t_1$		H		H		
$(n)\Delta t_1$	Ⓔ	Δt_1	Ⓔ	$3\Delta t_1$	Ⓔ	$3\Delta t_1$
$(n+1/2)\Delta t_1$		**H**				
$(n+1)\Delta t_1$						
$(n+3/2)\Delta t_1$				**H**		**H**
$(n+2)\Delta t_1$						
$(n+5/2)\Delta t_1$						
$(n+3)\Delta t_1$						

(b) Step 2.

time	LEVEL 1		INTERFACE		LEVEL 2	
$(n-3/2)\Delta t_1$		H		H		Ⓗ
$(n-1)\Delta t_1$	E					
$(n-1/2)\Delta t_1$		*H*		Ⓗ		*1/3*
$(n)\Delta t_1$		*E*		*E*	*1/2*	*E*
$(n+1/2)\Delta t_1$	Δt_1	Ⓗ	Δt_1	○		○
$(n+1)\Delta t_1$		**E**		**E**	*1/2*	*2/3*
$(n+3/2)\Delta t_1$				Ⓗ		Ⓗ
$(n+2)\Delta t_1$						
$(n+5/2)\Delta t_1$						
$(n+3)\Delta t_1$						

(c) Step 3.

time	LEVEL 1		INTERFACE		LEVEL 2	
$(n-3/2)\Delta t_1$		H		H		H
$(n-1)\Delta t_1$	E					
$(n-1/2)\Delta t_1$		H		H		
$(n)\Delta t_1$	E			E		E
$(n+1/2)\Delta t_1$		H				
$(n+1)\Delta t_1$	Ⓔ	Δt_1	Ⓔ			
$(n+3/2)\Delta t_1$		**H**		H		H
$(n+2)\Delta t_1$						
$(n+5/2)\Delta t_1$						
$(n+3)\Delta t_1$						

(d) Step 4.

time	LEVEL 1		INTERFACE		LEVEL 2	
$(n-3/2)\Delta t_1$		H		H		H
$(n-1)\Delta t_1$	E					
$(n-1/2)\Delta t_1$		H		H		
$(n)\Delta t_1$	E			E		E
$(n+1/2)\Delta t_1$		H				
$(n+1)\Delta t_1$		E		E		
$(n+3/2)\Delta t_1$	Δt_1	Ⓗ	$3\Delta t_1$	Ⓗ	$3\Delta t_1$	Ⓗ
$(n+2)\Delta t_1$		**E**				
$(n+5/2)\Delta t_1$						
$(n+3)\Delta t_1$				**E**		**E**

(e) Step 5.

time	LEVEL 1		INTERFACE		LEVEL 2	
$(n-3/2)\Delta t_1$		H		H		H
$(n-1)\Delta t_1$	E					
$(n-1/2)\Delta t_1$		H		H		
$(n)\Delta t_1$	E			E		Ⓔ
$(n+1/2)\Delta t_1$		H				
$(n+1)\Delta t_1$	E			Ⓔ		*1/3*
$(n+3/2)\Delta t_1$		H	*1/2*	H		H
$(n+2)\Delta t_1$	Ⓔ	Δt_1	○	Δt_1	○	
$(n+5/2)\Delta t_1$		**H**	*1/2*	**H**	*2/3*	
$(n+3)\Delta t_1$				Ⓔ		Ⓔ

(f) Step 6.

time	LEVEL 1		INTERFACE		LEVEL 2	
$(n-3/2)\Delta t_1$		H		H		H
$(n-1)\Delta t_1$	E					
$(n-1/2)\Delta t_1$		H		H		
$(n)\Delta t_1$	E			E		E
$(n+1/2)\Delta t_1$		H				
$(n+1)\Delta t_1$	E			E		
$(n+3/2)\Delta t_1$		H		H		H
$(n+2)\Delta t_1$		E				
$(n+5/2)\Delta t_1$	Δt_1	Ⓗ		Ⓗ		
$(n+3)\Delta t_1$		**E**		E		E

FIGURE 4.3: Sequence of the LTS algorithm for the scenario of figure 4.1, (L=2). Leap Frog steps are drawn in solid lines, and interpolation in dashed format. The required samples for an updating step appear inside a circle, and the computed samples in bold.

4.1.2.3 The LFDG algorithm in PML regions

The extension of the leap-frog temporal integration scheme to the semi-discrete system of (3.95) is perfectly straightforward. The auxiliary unknown field M must be evaluated at $t_n = n\Delta t$, as the electric field, and the auxiliary unknown field J, at $t_{n+\frac{1}{2}} = \left(n + \frac{1}{2}\right)\Delta t$, as the magnetic field. In the same way, equation (3.95c) is tested at t_n, as equation (3.95b), and the equation (3.95a) at $t_{n+\frac{1}{2}}$, as (3.95d).

Making the approximations, the first-order time derivatives by central difference method, the identity operation by the average approximation, and the dissipative terms of the flux evaluation by the backward approximation, we can formulate the following fully explicit algorithm for the PML medium,

$$M_n^m = \mathbb{A}_2 M_{n-1}^m + \mu \Delta t \mathbb{A}_3 H_{n-\frac{1}{2}}^m \tag{4.11a}$$

$$H_{n+\frac{1}{2}}^m = \mathbb{A}_{11} H_{n-\frac{1}{2}}^m +$$
$$\beta_m \mathbb{A}_{12} \left[-\left(\mathbb{S} - \mathbb{F}_{\kappa e}\right) E_n^m - \mathbb{F}_{\kappa e}^+ E_n^{m+} + \mathbb{F}_{\nu h} H_{n-\frac{1}{2}}^m - \mathbb{F}_{\nu h}^+ H_{n-\frac{1}{2}}^{m+} - \mathbb{M} M_n^m \right] \tag{4.11b}$$

$$J_{n+\frac{1}{2}}^m = \mathbb{A}_2 J_{n-\frac{1}{2}}^m + \varepsilon \Delta t \mathbb{A}_3 E_n^m \tag{4.11c}$$

$$E_{n+1}^m = \mathbb{A}_{11} E_n^m +$$
$$\beta_e \mathbb{A}_{12} \left[\left(\mathbb{S} - \mathbb{F}_{\kappa h}\right) H_{n+\frac{1}{2}}^m + \mathbb{F}_{\kappa h}^+ H_{n+\frac{1}{2}}^{m+} + \mathbb{F}_{\nu e} E_{n-1}^m - \mathbb{F}_{\nu e}^+ E_{n-1}^{m+} - \mathbb{M} J_{n+\frac{1}{2}}^m \right] \tag{4.11d}$$

where,

$$\mathbb{A}_2 = \left(\mathbb{M} + \frac{\Delta t}{2}\mathbb{M}_{A_2}\right)^{-1} \left(\mathbb{M} - \frac{\Delta t}{2}\mathbb{M}_{A_2}\right) \tag{4.12a}$$

$$\mathbb{A}_3 = \left(\mathbb{M} + \frac{\Delta t}{2}\mathbb{M}_{A_2}\right)^{-1} \mathbb{M}_{A_3} \tag{4.12b}$$

$$\mathbb{A}_{11} = \left(\mathbb{M} + \frac{\Delta t}{2}\mathbb{M}_{A_1}\right)^{-1} \left(\mathbb{M} - \frac{\Delta t}{2}\mathbb{M}_{A_1}\right) \tag{4.12c}$$

$$\mathbb{A}_{12} = \left(\mathbb{M} + \frac{\Delta t}{2}\mathbb{M}_{A_1}\right)^{-1} \tag{4.12d}$$

The LTS procedure, described in the previous section, can be straightforwardly extended to the PML updating equations (4.11). Notice that the unknown auxiliary fields are completely explicit, and no information from adjacent elements is required, as far as the M is updated after the electric field, and J after the magnetic field.

4.2 Eigenvalue Problem Setup of LFDG Algorithm

The Leap-Frog Discontinuous Galerkin (LFDG) algorithm is based on the system equation of (4.8), which has been rewritten bellow without sources and considering lossless medium,

$$H^m_{n+\frac{1}{2}} = H^m_{n-\frac{1}{2}} + \frac{\Delta t}{\mu} \mathbb{M}^{-1} \left[-\left(\mathbb{S} - \mathbb{F}_{\kappa e}\right) E^m_n - \mathbb{F}^+_{\kappa e} E^{m+}_n + \mathbb{F}_{\nu h} H^m_{n-\frac{1}{2}} - \mathbb{F}^+_{\nu h} H^{m+}_{n-\frac{1}{2}} \right] \quad (4.13\text{a})$$

$$E^m_{n+1} = E^m_n + \frac{\Delta t}{\varepsilon} \mathbb{M}^{-1} \left[\left(\mathbb{S} - \mathbb{F}_{\kappa h}\right) H^m_{n+\frac{1}{2}} + \mathbb{F}^+_{\kappa h} H^{m+}_{n+\frac{1}{2}} + \mathbb{F}_{\nu e} E^m_n - \mathbb{F}^+_{\nu e} E^{m+}_n \right] \quad (4.13\text{b})$$

Let us defined three column vectors, one with magnetic degrees of freedom (dofs) at the instant time $\left(n - \frac{1}{2}\right) \Delta t$, $\boldsymbol{H}_{n-\frac{1}{2}} = \left[\left(H^1_{n-\frac{1}{2}}\right)^T, ..., \left(H^M_{n-\frac{1}{2}}\right)^T \right]^T$, other with the electric dofs at the instant time $n\Delta t$, $\boldsymbol{E}_n = \left[\left(E^1_n\right)^T, ..., \left(E^M_n\right)^T \right]^T$, and the last one with both, magnetic and electric dofs, $\boldsymbol{U}_n = \left[\left(\boldsymbol{H}_{n-\frac{1}{2}}\right)^T, \left(\boldsymbol{E}_n\right)^T \right]^T$. Equations (4.13) can be expressed in a compact manner, for the complete computational domain as,

$$\boldsymbol{H}_{n+\frac{1}{2}} = \left(\mathbb{I}_{MQ} + \frac{\Delta t}{\mu} \mathbb{M}_{\nu h} \right) \boldsymbol{H}_{n-\frac{1}{2}} + \frac{\Delta t}{\mu} \mathbb{M}_{S\kappa e} \boldsymbol{E}_n \quad (4.14\text{a})$$

$$\boldsymbol{E}_{n+1} = \left(\mathbb{I}_{MQ} + \frac{\Delta t}{\varepsilon} \mathbb{M}_{\nu e} \right) \boldsymbol{E}_n + \frac{\Delta t}{\varepsilon} \mathbb{M}_{S\kappa h} \boldsymbol{H}_{n+\frac{1}{2}} \quad (4.14\text{b})$$

where $\mathbb{I}_{MQ}$ is the $MQ \times MQ$ identity matrix, and $\mathbb{M}_{\nu h}$, $\mathbb{M}_{S\kappa e}$, $\mathbb{M}_{\nu e}$ and $\mathbb{M}_{S\kappa h}$ are $MQ \times MQ$ matrices, which are the result of assembling the element-matrices of (4.13).

Inserting (4.14a) into (4.14b), the following fully explicit system is obtained,

$$\boldsymbol{H}_{n+\frac{1}{2}} = \left(\mathbb{I}_{MQ} + \frac{\Delta t}{\mu} \mathbb{M}_{\nu h} \right) \boldsymbol{H}_{n-\frac{1}{2}} + \frac{\Delta t}{\mu} \mathbb{M}_{S\kappa e} \boldsymbol{E}_n \quad (4.15\text{a})$$

$$\boldsymbol{E}_{n+1} = \left(\mathbb{I}_{MQ} + \frac{\Delta t}{\varepsilon} \mathbb{M}_{\nu e} + \frac{(\Delta t)^2}{\mu \varepsilon} \mathbb{M}_{S\kappa h} \mathbb{M}_{S\kappa e} \right) \boldsymbol{E}_n + \frac{\Delta t}{\varepsilon} \left(\mathbb{M}_{S\kappa h} + \frac{\Delta t}{\mu} \mathbb{M}_{S\kappa h} \mathbb{M}_{\nu h} \right) \boldsymbol{H}_{n-\frac{1}{2}} \quad (4.15\text{b})$$

which can be written in a compact manner as,

$$\boldsymbol{U}_{n+1} = \mathcal{A}_{LFDG} \boldsymbol{U}_n \quad (4.16)$$

where the matrix $\mathcal{A}_{LFDG}$ is the Discontinuous Galerkin operator with the Leap-Frog algorithm. It is the result of assembling all the element-matrices of (4.14) in a $2MQ \times 2MQ$ matrix, following (4.15) form. Matrix $\mathcal{A}_{LFDG}$ depends on DG spatial discretization features such as mesh size, order of the basis functions p and τ, and also on LF time integration scheme and time-step Δt.

Considering time-harmonic plane wave of the form $e^{j(\omega t - \mathbf{k}_0 \hat{\mathbf{r}})}$, where ω is the angular frequency and $\mathbf{k}_0$ is the physical wavevector, the analytical relation between $\boldsymbol{U}_{n+1}$ and $\boldsymbol{U}_n$ is,

$$\boldsymbol{U}_{n+1} = e^{j\omega\Delta t}\boldsymbol{U}_n \tag{4.17}$$

with the amplification factor $e^{j\omega\Delta t}$.

In the same manner as in section 3.5.1 for the DG semi-discrete operator, periodic boundary conditions (PBC) of equation (3.101) and figure 3.9, can be applied in order to find a self-dependent linear system.

The exact wavenumber k_0 is given by the well-know dispersion relation $k_0 = \frac{w}{c}$, with $c = \frac{1}{\sqrt{\mu\varepsilon}}$ the speed of the wave. For the numerical scheme of (4.16), the amplification factor can be evaluated solving the following eigenvalue problem,

$$e^{j\widetilde{\omega}\Delta t}\boldsymbol{U}_n = \mathcal{A}_{LFDG}\boldsymbol{U} \tag{4.18}$$

where we can find $2MQ$ eigenvalues ($\lambda_{\mathcal{A}_{LFDG}}^m, m = 1, ..., 2MQ$). From the relation to the analytical (ideal) solution for a physical plane wave propagating in a homogeneous lossless medium (4.17), we can obtain the possibly complex-valued wavenumbers ($\widetilde{k}^m = \widetilde{k}_{real}^m + j\widetilde{k}_{imag}^m, m = 1, ..., 2MQ$) of the numerical operator as,

$$\widetilde{k}^m = j\frac{\ln\left(\lambda_{\mathcal{A}_{LFDG}}^m\right)}{c\Delta t}, \quad m = 1, ..., 2MQ \tag{4.19}$$

4.3 Stability Analysis of the LFDG Algorithm

The LFDG algorithm is a explicit and conditionally stable scheme. Some stability appear in [60, 61, 63], where some stability conditions were derived. These analyses establish a stability condition based on the maximum eigenvalue that can be supported by the scheme. In order to avoid solving an eigenvalue problem for every element in a specific problem, a maximum limit for the highest eigenvalue can be estimated to assure stability. Thus, a Δt_{max} can be chosen 'a priori' based on geometrical properties of the elements. Following this procedure, larger Δt does not mean an unstable scheme, but shorter Δt assures stability of the scheme. For the first-order $p = 1$, DGTD with $\tau = 0$ or centered flux, in an homogeneous medium, following condition must be satisfied by all the m elements to assure stability,

$$c\Delta t\frac{8 + \sqrt{40}}{3} < \frac{4V_m}{\partial V_m} \tag{4.20}$$

being V_m the element volume, and ∂V_m the element perimeter or the sum of the surface of all faces of the element.

In case of $\tau \neq 0$, that expressions are not valid and the stability condition becomes more restricted and more difficult for a 'a priori' estimation, [63].

A numerical stability analysis has been performed on the geometry of figure 3.8, where PBCs have been applied on the contour. The maximum Δt is numerically found for different p orders and τ values. The strategy to find Δt_{max} is to solve the eigenvalue problem of (4.18) for different Δt until a maximum value of Δt is found that keeps all the complex-valued $\widetilde{k}^m$ with imaginary part negative, $\widetilde{k}_{imag}^m < 0, m = 1, ..., 2MQ$.
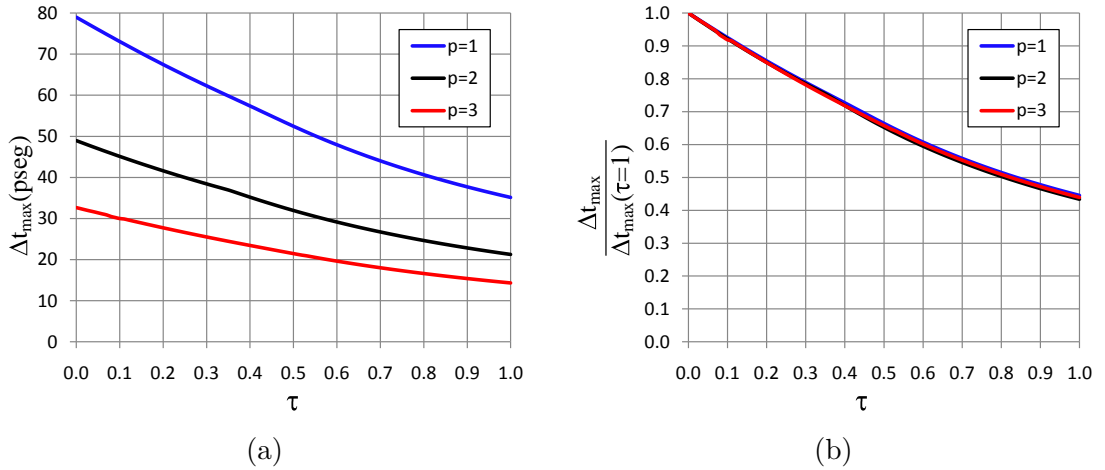
FIGURE 4.4: Numerical stability analysis of the LFDG algorithm for the geometry of figure 3.8 with $\mathbf{k}_0 = 2\pi\hat{\mathbf{x}}$ and $\Delta = 0.2$. (a) Dependence of Δt_{max} with τ parameter. (b) Relative penalization of Δt_{max} with τ parameter.

Figure 4.4 shows the results. It can be seen almost a linear dependence between the Δt_{max} and the τ parameter. This relative relation does not depend on the order of the basis functions p. Higher values of τ parameter require shorter Δt values to keep stability. For this reason, it is desirable to keep τ parameter as low as possible to not penalize the stability condition, and high enough to eliminate spurious modes.

Table 4.2 shows some interesting values extracted from the results. The penalization for using $\tau = 0.1$ is about 9% in the Δt. In case of $\tau = 1.0$, upwind flux, the computation cost would be increased by a factor of 2.25. The third column shows a estimation of the increment in the number of time-steps due to the reduction of time-step when order p is increased. This factor is about 1.6 from $p = 1$ to $p = 2$, and 2.5 from $p = 1$ to $p = 3$. It is important to notice that the computational cost for different orders does not depend only on Δt. If higher order are used, the number of dofs also increases and so

the computational cost per iteration. On the other hand, accuracy is better for higher order p, so the number of elements can be reduced, what means increase h. For all these reasons, a tradeoff is needed between the size of mesh, accuracy and order p. This analysis, from computational cost point of view, appears in section 4.6.

TABLE 4.2: Results of the numerical stability analysis of the LFDG algorithm

	$\frac{\Delta t_{max}(p,\tau=0)}{\Delta t_{max}(p,\tau=0.1)}$	$\frac{\Delta t_{max}(p,\tau=0)}{\Delta t_{max}(p,\tau=1)}$	$\frac{\Delta t_{max}(p=1,\tau=0.1)}{\Delta t_{max}(p,\tau=0.1)}$
$p=1$	1.08	2.25	1.00
$p=2$	1.09	2.30	1.62
$p=3$	1.09	2.28	2.44

4.4 Numerical Results of the LFDG Eigenproblem

Figures 4.5 and 4.6 show the spectrum of the LFDG, for the geometry of figure 3.8 with PBCs, and for different fluxes evaluation schemes and Δt, respectively. In all cases, following parameters have be used: $\mathbf{k}_0 = 2\pi\hat{\mathbf{x}}$, $p = 2$ and $\Delta = 0.2$.

The analysed cases that appear in figure 4.5 are similar to those of figure 3.10 solved with the DG operator. It can be seen that the time integration scheme has impact in the eigenvalue problem, which is slightly distorted, but the nature of the spectrum of the LFDG algorithm is similar to the DG semi-discrete problem. Thus, same conclusions related to non-physical solutions or spurious modes made for semi-discrete scheme in section 3.5.2, can be extended for the LFDG algorithm.

Figure 4.6 shows the spectrum of the LFDG algorithm for Δt close to Δt_{max}. It can be seen that the spectrum of LFDG is not symmetrical respect to the real part. In the DG operator, for all the numerical wavenumbers i, defined as $\widetilde{k}^i = \widetilde{k}^i_{real} + j\widetilde{k}^i_{imag}$, another j wavenumber can be found which fulfilled the following condition, $\widetilde{k}^j = -\widetilde{k}^i_{real} + j\widetilde{k}^i_{imag}$. In the LFDG case, this condition is not exactly fulfilled, and it is more clear if Δt is close to Δt_{max} and in the wavenumbers close to the instability (big value of $\left|\widetilde{k}^m_{real}\right|$ and $\widetilde{k}^m_{imag}$ close to zero, even positive in case of an unstable situation). The reason to this phenomenon is that we are using backward approximation of the penalization terms, instead of central difference, to avoid that the scheme becomes implicit. Hence, we are using delayed samples of the fields instead of updated samples, which drives to a non-symmetrical eigenvalues. This fact makes the stability condition slightly more restrictive.

Another feature of the spectrum is explained following. When Δt increases, there are a maximum and a minimum limits for the real part of the numerical wavenumbers. These limits, together with negative imaginary part, define the stability region of the temporal
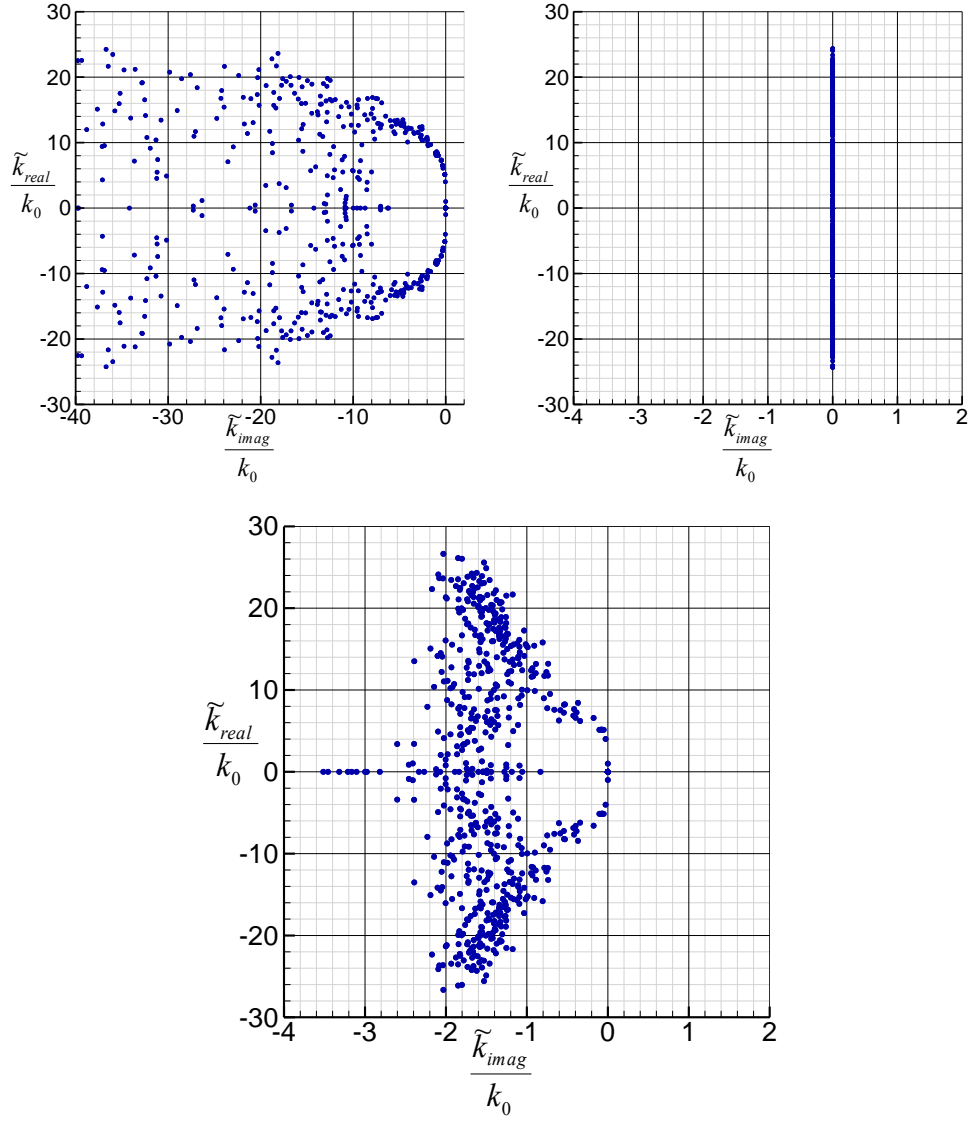
FIGURE 4.5: Spectrum of the LFDG operator for a cubic domain (meshed with 24 tetrahedra) with PBC ($\mathbf{k}_0 = 2\pi\hat{\mathbf{x}}$, $\Delta = 0.2$ and $p = 2$). Upwind flux (upper left), Centered flux (upper right), Partially penalized flux $\tau = 0.1$ (lower).

scheme in the complex plane of $\widetilde{k}$. If Δt is larger than Δt_{max}, are those wavenumbers that produce the instability. The reason for this is similar that for the FDTD case, and is intrinsic to the Leap-Frog scheme.

Let us consider the general equation,

$$d_t \boldsymbol{U} = c \,\mathfrak{F}_s [\boldsymbol{U}] \tag{4.21}$$

(a) $\Delta t = 0.99 \Delta t_{max}$.

(b) $\Delta t = 1.01 \Delta t_{max}$.
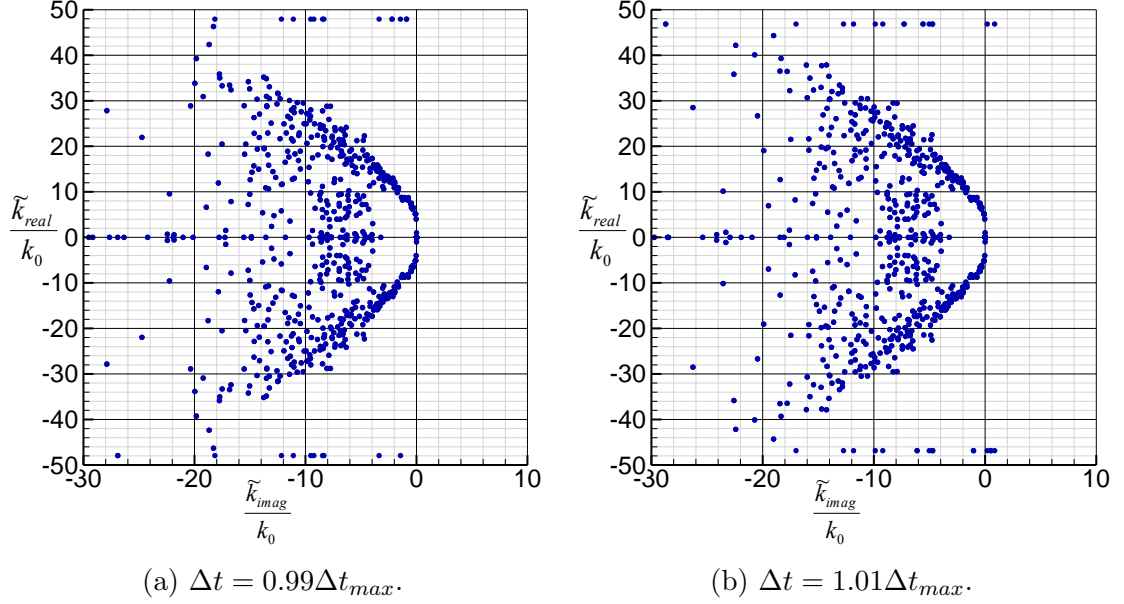
FIGURE 4.6: Results of the eigenvalue problem (spectrum of the LFDG operator) for Δt close to Δt_{max}, of the problem of figure 3.8 with PBCs, with $\tau = 0.4$, $\mathbf{k}_0 = 2\pi\hat{\mathbf{x}}$, $p = 2$ and $\Delta = 0.2$.

where we are looking for a solution to $\boldsymbol{U}$, and $\mathfrak{F}_s$ is a spatial operator. If we apply Leap-Frog to the temporal derivative we obtain,

$$\frac{\boldsymbol{U}\left(\left(n+\frac{1}{2}\right)\Delta t\right) - \boldsymbol{U}\left(\left(n-\frac{1}{2}\right)\Delta t\right)}{\Delta t} = c\,\mathfrak{F}_s\left[\boldsymbol{U}\left(n\Delta t\right)\right] \tag{4.22}$$

Now we consider the monochromatic problem ($e^{j(\omega t - \mathbf{k}_0\hat{\mathbf{r}})}$), obtaining the following result,

$$\frac{e^{j\omega\frac{\Delta t}{2}} - e^{-j\omega\frac{\Delta t}{2}}}{\Delta t}\boldsymbol{U}\left(n\Delta t\right) = c\,\mathfrak{F}_s\left[\boldsymbol{U}\left(n\Delta t\right)\right] \tag{4.23}$$

which can be reduced to the expression,

$$\sin\left(\omega\frac{\Delta t}{2}\right)e^{-j\mathbf{k}_0\hat{\mathbf{r}}} = \frac{c\,\Delta t}{2j}\mathfrak{F}_s\left[e^{-j\mathbf{k}_0\hat{\mathbf{r}}}\right] \tag{4.24}$$

The result is that all the modes supported by $\mathfrak{F}_s$, ($\widetilde{k}^m$), must be under the stability condition imposed by (4.24). Obtaining $\widetilde{\omega}^m$ complex-values with imaginary part greater or equal to zero to keep stability,

$$\widetilde{\omega}^m = \frac{2}{\Delta t}\arcsin\left(-\frac{c\,\Delta t}{2}\widetilde{k}^m\right) \tag{4.25}$$

Notice that the problem of the equation (4.25), is equivalent to the eigenvalue problem of (4.18). The arcsin operation fixes the maximum and minimum limits for the real part

of the numerical wavevectors of figure 4.6, and, for larger Δt, produces the instability.

4.5   Convergence of the LFDG Algorithm

The objective of this analysis is to compare the errors of the complete LFDG algorithm (temporal integration plus spatial discretization), with the spatial DG operator alone, which results appear in section 3.5.3. A comparison with FDTD has also been included.

A numerical convergence analysis has been performed on the problem of figure 3.8, considering PBCs and $\mathbf{k}_0 = 2\pi\hat{\mathbf{x}}$. The eigenvalue problem of (4.18) is numerically solved for different Δ values. In all cases, the closest eigenvalue $\widetilde{k}^m$ to $k_0 = |\mathbf{k}_0|$ is chosen as the valid one, referred here as $\widetilde{k}_0 = \widetilde{k}_{real} + j\widetilde{k}_{imag}$. Numerical-dispersion, numerical-dissipative and global errors can be computed as a function of $\widetilde{k}_0$ and k_0. The expressions (3.104) have been used to evaluate the different errors per wavelength.

The results of the analysis appear in figure 4.7. For the LFDG cases, $\tau = 0.1$ and $\Delta t = 0.7\Delta t_{max}$ have been used. The expression to evaluate $\widetilde{k}_0$ for the FDTD case is the very well-known numerical dispersion relation for this method written bellow [155],

$$\widetilde{k}_0 = \frac{2}{h} \arcsin\left(\frac{h}{c\,\Delta t} \sin(\frac{k_0\,c\,\Delta t}{2})\right) \tag{4.26}$$

and the stability condition,

$$\Delta t_{max} = \frac{h}{c\sqrt{3}} \tag{4.27}$$

The influence of Δt has been considered in figure 4.8, where the analysis have been carried out for different values of Δt and $p = 2$.

Figures 4.7 and 4.8 call for the following remarks:

- The results show that the super-convergence property of the DG spatial operator is kept up to a error limit where the convergence of the error becomes $O\left(h^2\right)$ due to the temporal integration method, which is a second order scheme. This convergence rate does not depend upon order of the basis functions p or Δt, and it is the same convergence rate that is obtained by FDTD method.

- The reason to lose the super-convergence property is because of the dispersion error introduced by the Leap-Frog integration scheme. Leap-Frog method is a non-dissipative scheme so the dissipation error is not affected and it is exactly the same as we obtained with the DG operator.
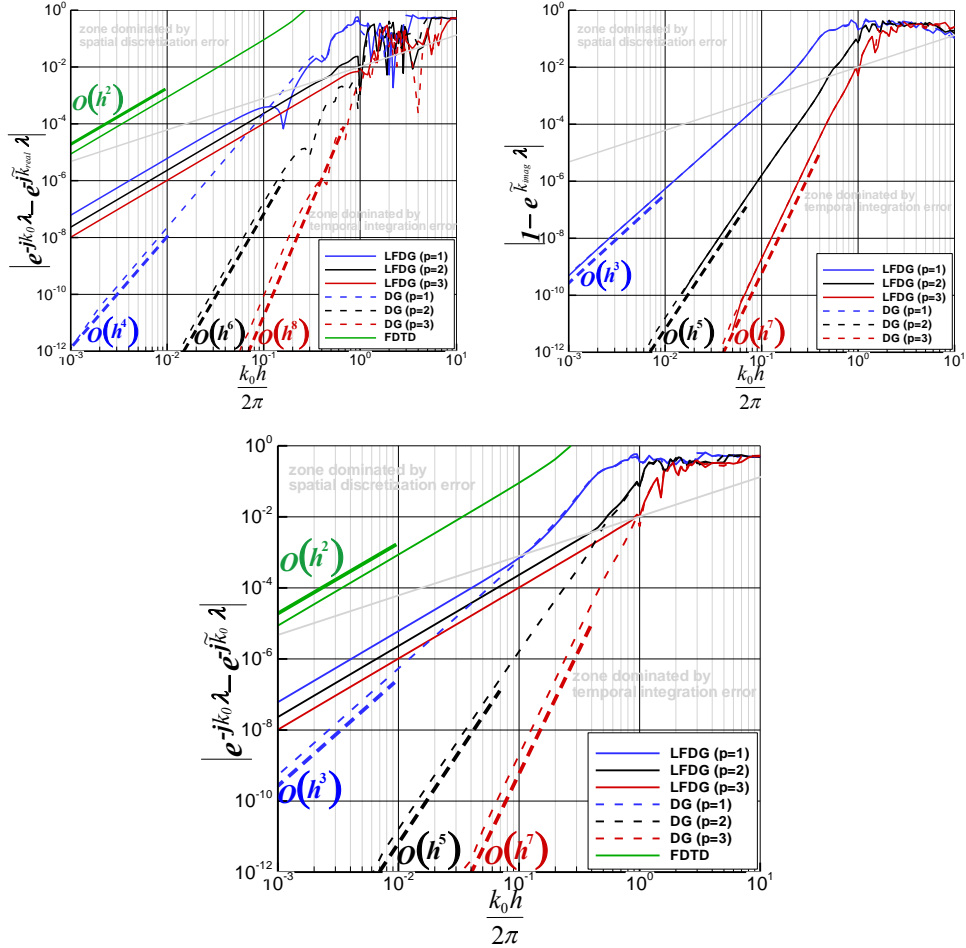
FIGURE 4.7: Convergence of the dispersion (upper left), dissipation (upper right) and L^2-norm (lower) errors of the physical mode for the LFDG algorithm with $\tau = 0.1$ and $\Delta t = 0.7\Delta t_{max}$. Analogous curves for the DG operator and FDTD have been included.

- The limit between the zones where the error is dominated by the spatial discretization and by the temporal integration methods, depends on Δt, as is shown in figure 4.8. This limit can always be improved reducing Δt, but the number of required time-steps in a simulation, and so the computational cost, will grow.

- Although the different in accuracy between LFDG and FDTD looks very high in figure 4.7, it is important to notice that the computational cost of the FDTD is much lower. In section 4.6, FDTD and LFDG, with different order p, methods are compared from computational cost point of view.

- The typical error value where real problems are solved is about 10^{-2}, which corresponds to a resolution of the mesh, in case of the FDTD method, of about $\frac{\lambda}{28}$. It is important to notice that this accuracy value is in the zone dominated by the spatial discretization error for the LFDG method, for $p = 1$, $p = 2$ and $p = 3$ and
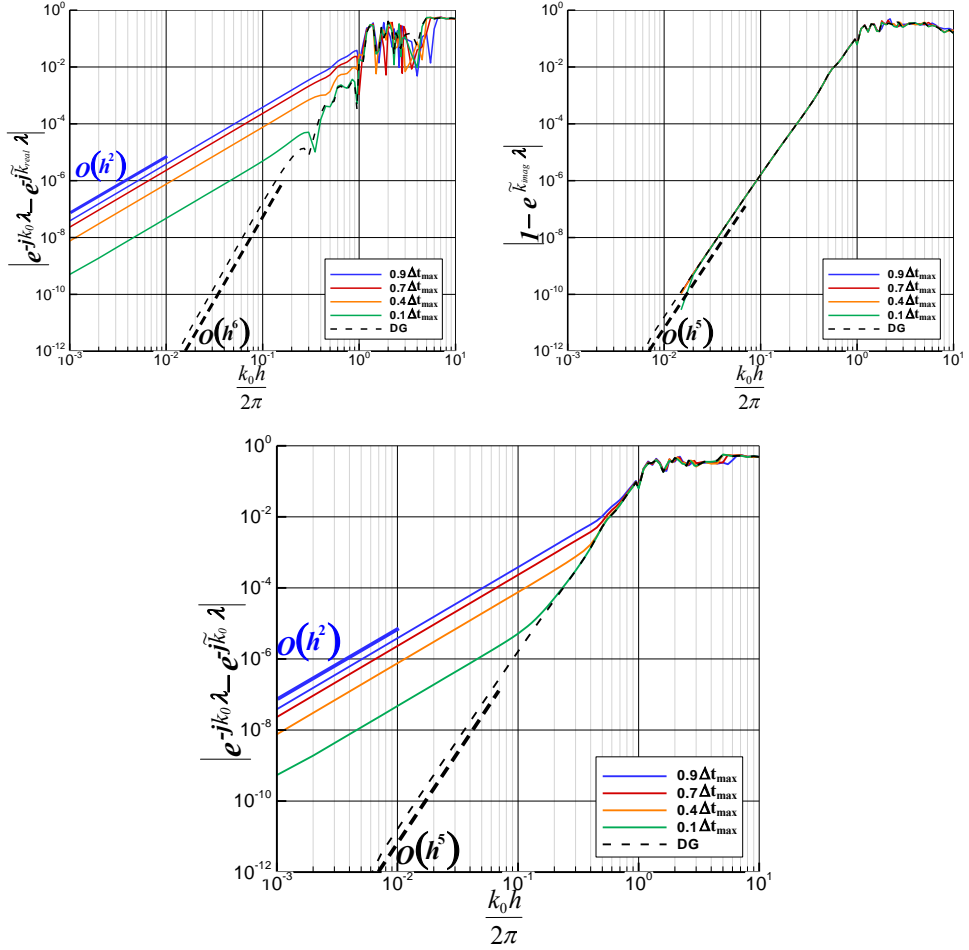
FIGURE 4.8: Influence of Δt in the dispersion (upper left), dissipation (upper right) and L^2-norm (lower) errors of the LFDG algorithm with $\tau = 0.1$ and $p = 2$. Analogous curves for the DG operator have been included.

$\Delta t = 0.7\Delta t_{max}$. This characteristic is not expected to be fulfilled by higher orders that $p = 3$.

- This analysis has been performed considering a plane wave traveling in an homogenous medium. The extension of all these conclusions to any general problem must be done with care. In case of geometrical singularities, as corners or vertex, the convergence rate considerably decreases. These problems must be dealt by h-p techniques. It is important to notice that, in these cases, the temporal integration error loses importance, and is the spatial discretization of the fields which determines the accuracy of the numerical method. LFDG method, as it is a FEM method, is a very efficient method for these cases, if a local time stepping technique is used to permit the use of the very short Δt, in dense regions, and large Δt in the rest.

4.6 Computational Cost vs Accuracy Analysis

In this section we analyse the computational cost versus accuracy, in order to draw an effective application of the proposed algorithm in real problems, and explore the limitations and the efficiency of the method. The main tradeoff takes place between the order of the basis functions p, the mesh resolution h, and accuracy, with the aim of minimizing computational cost.

- Increasing p improves accuracy, but shorter Δt for stability is required, and the computational cost per element is higher.

- Increasing h improves accuracy, but shorter Δt for stability for smaller elements is required, and the number of elements increases.

Following parameters have been fixed in the analysis:

- Geometry and setup of the figure 3.8, considering PBCs and $\mathbf{k}_0 = 2\pi\hat{\mathbf{x}}$.

- $\tau = 0.1$. The influence on the accuracy of the physical mode can be neglected, as has been proven in section 3.5.3. Reducing its value decreases the dissipation of the spurious modes, but increases computational cost (due to more restricted stability condition, figure 4.4). This value has been proven sufficient in real problems.

- $\Delta t = 0.7\Delta t_{max}$. This ratio of 0.7 between the maximum time-step supported by a numerical scheme and the practical one, is a typical choice in time domain simulations. This value avoids instabilities due to non-considered aspects as numerical rounding errors.

In order to be able to compare the different configurations of the method, a computational cost per λ^3 and pseg has been defined. The computational cost for one element m for the LFDG algorithm, is proportional to the square of the number of basis functions Q in that element,

$$C_{element} \propto Q^2 \tag{4.28}$$

The cost for one iteration per λ^3, will be approximately the number of elements per λ^3 multiplied by the cost per element,

$$\frac{C_{1 \text{ iter}}}{\lambda^3} \approx \frac{N_{element}}{\lambda^3} C_{element} \tag{4.29}$$

Finally, the following magnitude (CC) has been defined which will be proportional to the global cost of the method,

$$\frac{\text{Computational Cost}}{\lambda^3 \text{pseg}} \propto K \frac{N_{element}}{\lambda^3} Q^2 \frac{1}{\Delta t \, (\text{pseg})} = CC \qquad (4.30)$$

being K a factor that has been considered equal to 1 for the FDTD case, and equal to 2 for the LFDG method. The reason is that the computational cost for the LFDG method has been considered double of the FDTD due to the additional terms.

The CC magnitude has been computed for the results of the convergence analysis of figure 4.7. FDTD method can be considered as a LFDG of order $p = 0$, where the elements, instead of tetrahedral as is used for LFDG, are cube (Yee cell). The results are shown in figure 4.9, where CC is in the X-axis and, accuracy is in the Y-axis, in the upper side of the plot, and the resolution of the mesh, h, in the lower side.
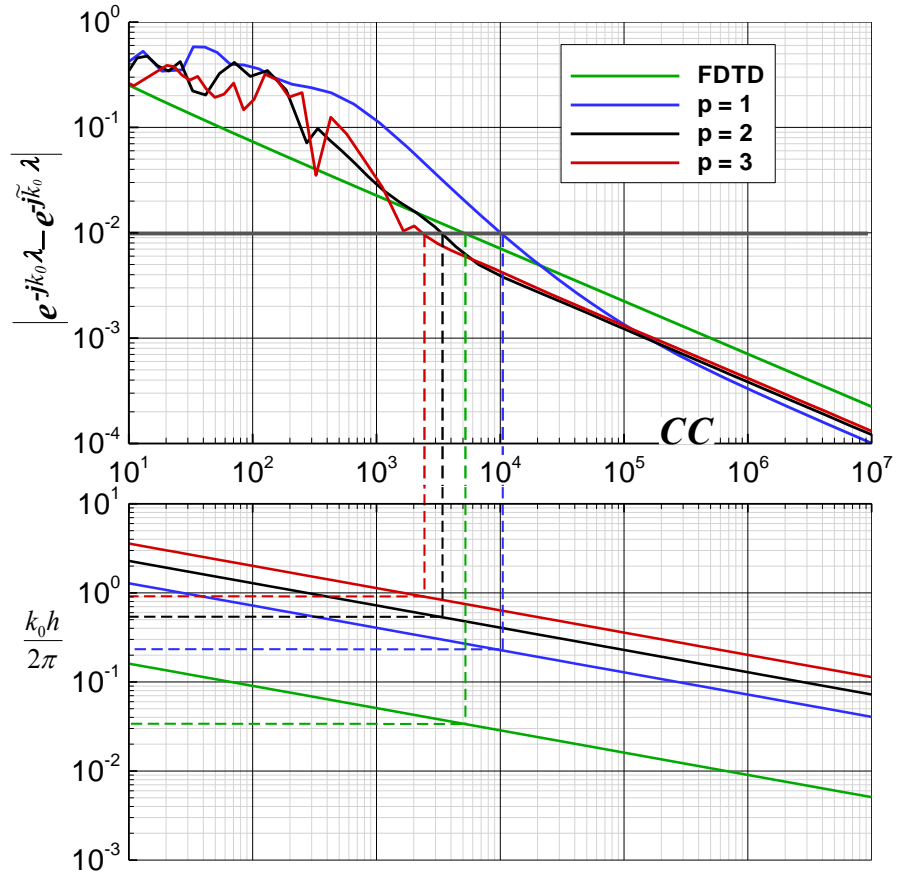
FIGURE 4.9: Computational cost of the LFDG algorithm for $\tau = 0.1$, $\Delta t = 0.7\Delta t_{max}$ and different order of the basis functions p. CC is in the X-axis and, accuracy is in the Y-axis, in the upper side of the plot, and the resolution of the mesh, h, in the lower side. Similar curve of the FDTD method has been included for comparison proposes.

TABLE 4.3: Results of the computational cost analysis for a L^2-norm accuracy of 10^{-2} per wavelength.

	Q	$\frac{\lambda}{h}$	$\frac{N_{element}}{\lambda^3}$	$\frac{N_{functions}}{\lambda^3}$	$c\,\Delta t\,10^3$	$C_{element} \propto$	$\frac{C_{1iter}}{\lambda^3} \propto$	CC	Gain $\left(\frac{CC(p-1)}{CC(p)}\right)$
FDTD	3	28.5	23149	69447	14.1	9	208341	2600	–
$p=1$	12	4.5	2187	26244	17.6	144	314928	9660	–
$p=2$	30	1.9	165	4950	85.3	900	148500	3270	2.95
$p=3$	60	1.1	32	1920	97.1	3600	115200	2260	1.45

The numerical values of the analysis, for the case where the L^2-norm error is about 10^{-2} per wavelength, appear in table 4.3. It can be seen that the size of the elements $(\frac{\lambda}{h})$ for higher values of order p, is bigger. This fact makes that the number of basis functions per λ^3 was lower for higher orders p. Beside, larger Δt are allowed, because of the increment in the size of the elements, even considering that the stability condition is more restrictive for high orders p. Thus, the cost per element increases with p, but the cost for iteration per λ^3 and the overall computational cost decreases with order p. This tendency is not extrapolated to very high accuracy ($< 10^{-3}$), figure 4.9, where the CC figure is practically the same for all orders p. The increment in the computational cost per element is not compensated with a reduction in the number of elements and the time-step. The global error, in the latter case, will be dominated by the temporal integration method, which is just a second-order accurate, and the super-convergence behavior of the error has been lost.

The same reason explains that, the gain for using $p = 3$ instead of $p = 2$ it is not as high as the gain from $p = 1$ to $p = 2$. Thus, due to the lost of super-convergence of the error of LFDG algorithm, using higher p orders that 3 will not be worthy in practical problems. This is one limitation of the method, which avoids to take fully advantage of p refinement techniques. In the other hand, the method has a comparable computational cost to FDTD for practical applications, keeping most of the advantages of finite element methods.

In summary, the results given in figure 4.9 and table 4.3 call for the following conclusions:

- The computational cost of the LFDG method is in the same order of magnitude of the traditional FDTD method. So, it is expected that LFDG has all the advantages of finite element methods as a similar computational cost of the FDTD method.

- Due to the limitations of using a second order accurate time integration scheme, it will not be worthy to use basis functions of order p higher that 3.

- For the typical accuracy required in practical and real electromagnetic problems, from 10^{-2} to 10^{-3} L^2-norm error per wavelength, LFDG method is an efficient algorithm. If very high accuracy would be required, it will be more efficient to

use a time integration method of higher order of accuracy, in order to take more advantage of the super-convergence property of the DG operator.

As a final comment, the information shown in this section is very valuable for the setup of real simulations. Figure 4.9 allows to chose the most efficient, in terms of computational cost, element size h conforming the mesh, establishing a 'a priori' target accuracy. Once the mesh has been generated, again figure 4.9, allows to choose the appropriate 'a priori' p order in each element, depending on its size and required accuracy. The main limitation of this 'a priori' h-p refinement strategy is that figure 4.9 is only valid for a plane wave traveling in an homogenous medium. Keeping accuracy under control when there are geometrical singularities is beyond the scope of this work.

Chapter 5

Validation and Application of Leap Frog Discontinuous Galerkin Method

The Leap-Frog Discontinuous Galerkin (LFDG) method has implemented to solve the 3-D Maxwell's equations. The implementation considers different electromagnetic sources, as ports or plane waves, and simulates different materials and boundary conditions. Capabilities and details of the electromagnetic solver appear in appendix A.

In this chapter, some electromagnetic (EM) problem results, computed with LFDG method, have been collected. Some of the results have been compared with measurements and others with results obtained with other computational methods. Different kind of EM problems have been addressed in order to validate and demonstrate the attractive properties of the LFDG method, which combines all the goods of Time Domain and Finite Element methods. Robustness, accuracy and stability have been proven with very resonant EM problems as microwave filters. Some antenna problems have been used to validate and prove the versatility and efficiency of the method. Accuracy has been demonstrated with the computation of the RADAR cross-section (RCS) of low-observable (LO) targets. Electrically medium and large structures responses under high intensity radiated fields (HIRF) have been computed, including a complete aircraft simulation, showing the efficiency and scalability of the method. Finally, the treatment of anisotropic material is validated.

TABLE 5.1: Number of elements (M) for each set of basis functions for the DMCWF. GxRy stand for x order for the gradient space, y order for the rotational space

	G1R1	G1R2	G2R2	G2R3	G3R3	Total
M	38988	2258	804	2734	15102	59886
dofs	935712	90320	48240	246600	1927320	3248192

TABLE 5.2: Local time stepping level distribution for DMCWF problem.

	L1	L2	L3	L4
M	7	13101	22556	24222
Δt (psg)	$6.96\ 10^{-3}$	$20.88\ 10^{-3}$	$62.64\ 10^{-3}$	$187.92\ 10^{-3}$

5.1 Microwave Filters

Waveguide filters, an especially challenging type of problem for time-domain techniques, are traditionally solved by methods in FD, such as FEM, integral-equation methods, or analytical methods such as the mode matching. Due to the strong resonances that these structures present, two main features are required to deal with them in TD. One is the stability of the method, since very long simulations are necessary. The other is its accuracy, to maintain the coherence of the electromagnetic field throughout the structure. In this work, we use waveguide filters to provide proof of the robustness and accuracy of the LFDG method.

5.1.1 PEC Microwave Filter

A dual-mode circular waveguide filter (DMCWF) is analyzed in this section, which has been analyzed in detail in [156] and measurement are available. The filter is composed of a circular cavity resonator that includes the input and output slots of a DMCWF. Due to the symmetries of the structure, vertical perfect magnetic conductor-wall and horizontal perfect electric conductor-wall symmetry were considered in the numerical simulations, as is depicted in the simulation setup of the figure 5.1.

It is important to note that a dense discretization of the slots is critical for accurate results. This forces to chose small time step in this elements to satisfied stability condition. The used of curvilinear 2nd-order tetrahedral permits to have high geometry discretization accuracy in the cylindrical waveguide, without reducing element size. The basis function used in each tetrahedral element have been selected depending on its size. Table 5.1 gives the number of elements for each set of basis functions, while Table 5.2 gives the number of elements and time step for each level of the LTS algorithm.

Three observables have been considered:
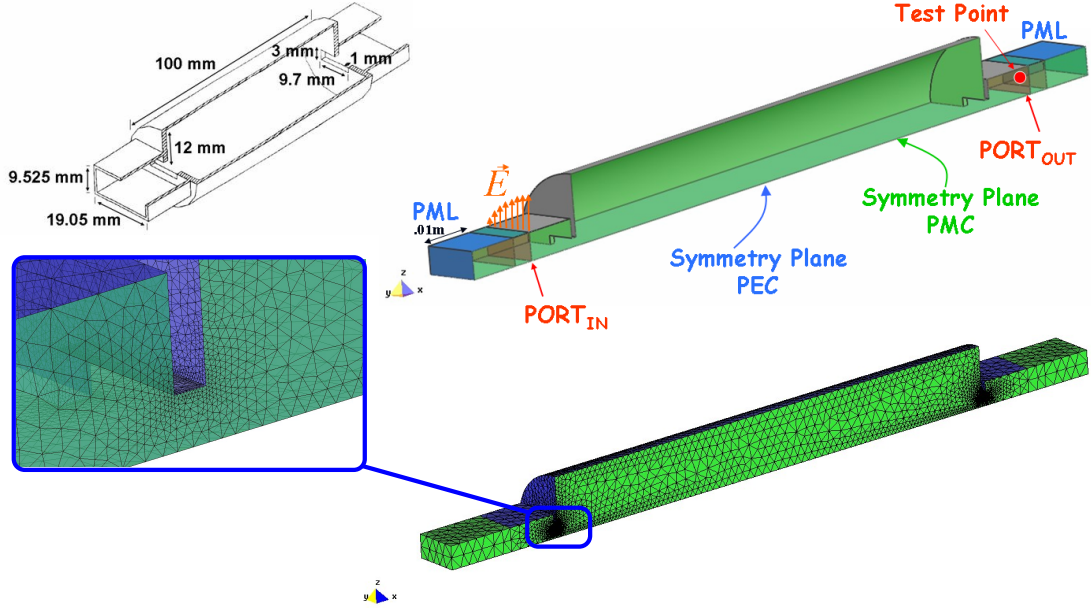
FIGURE 5.1: Dual-mode circular waveguide filter dimensions and problem setup (E_z results overimpose for both fluxes).

1. A field probe inside the rectangular waveguide to record field evolution in TD. Figure 5.2 shows different results for partially penalized ($\tau = 0.025$) and centered flux cases. In the case of centered flux, and due to the spurious modes, Ey and Ex are not null. No noticeable difference is appreciated between centered and penalized for E_z.

2. The filter response in terms of the S_{21} parameter. No remarkable differences were found between centered/upwind or LF/RK4 schemes. For instance, figure 5.3 shows the comparison between measurement, centered, and partial penalized ($\tau = 0.025$) computed with LF and local time stepping, with excellent agreement. No influence on the S_{21} parameter appears to exist due to spurious modes, reaching excellent agreement in all cases.

3. The evolution of the energy inside the structure. Figure 5.4 shows the curves for the two cases referred above. It can be seen that the energy needs considerable time to leave the filter, since the structure is very resonant. This leads to long physical simulation times to achieve accurate results, as are listed in table 5.3. In case of centered, there are more energy inside the structure because of the energy of the spurious modes. However, this does not have influence to find good and accurate results for the S_{21} parameter, the main problem is that some deviations are found in the computed near fields. This is the typical behavior (no problems for far fields computations or average parameter as impedance or S parameters) of spurious modes, not only in DG methods, but in general FEM as well.
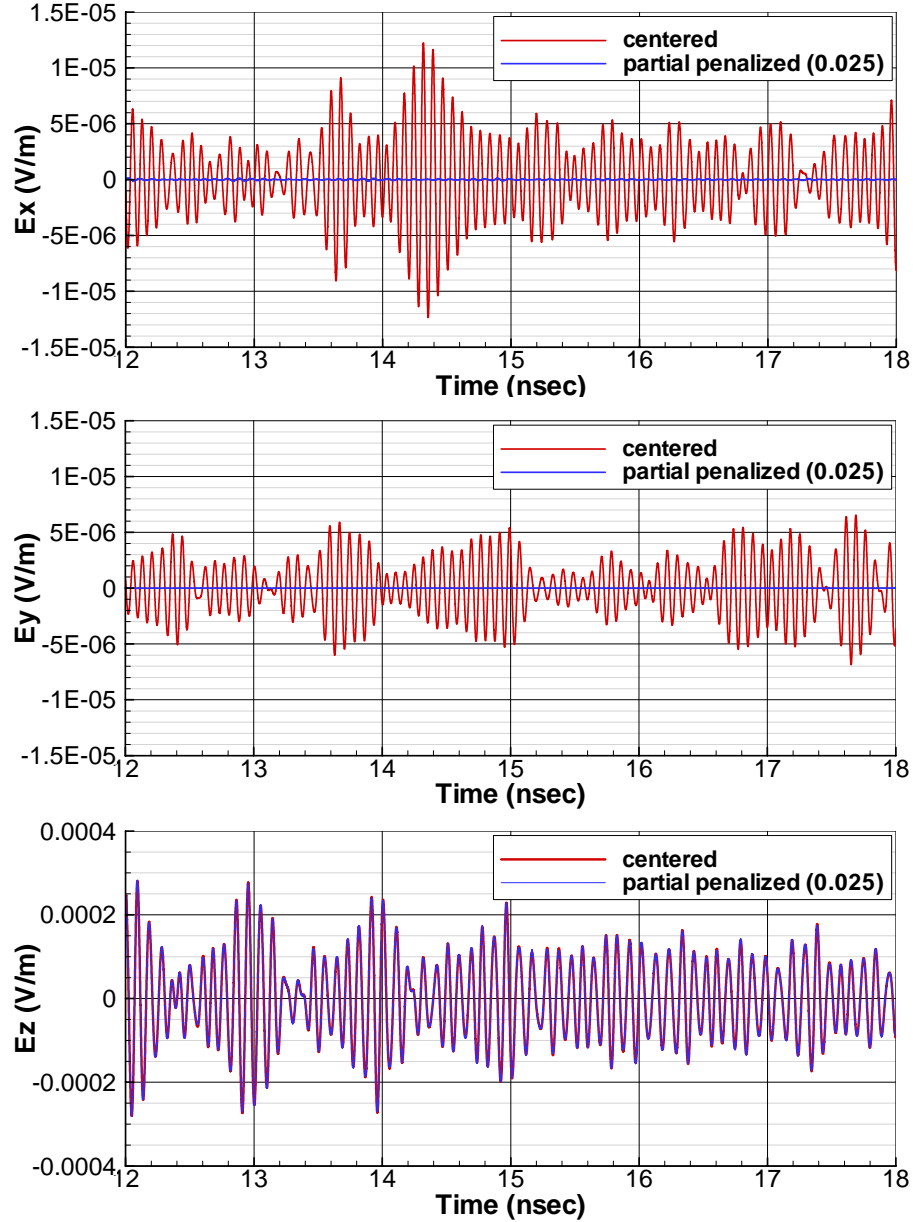
FIGURE 5.2: Dual-mode circular waveguide filter near fields computation.

Table 5.3 summarizes the computational requirements of the different simulations performed. It should be noted that the 2nd-order LF scheme, combined with a 5-level LTS provide the algorithm about 8 times faster than do non-LTS schemes for this numerical case.
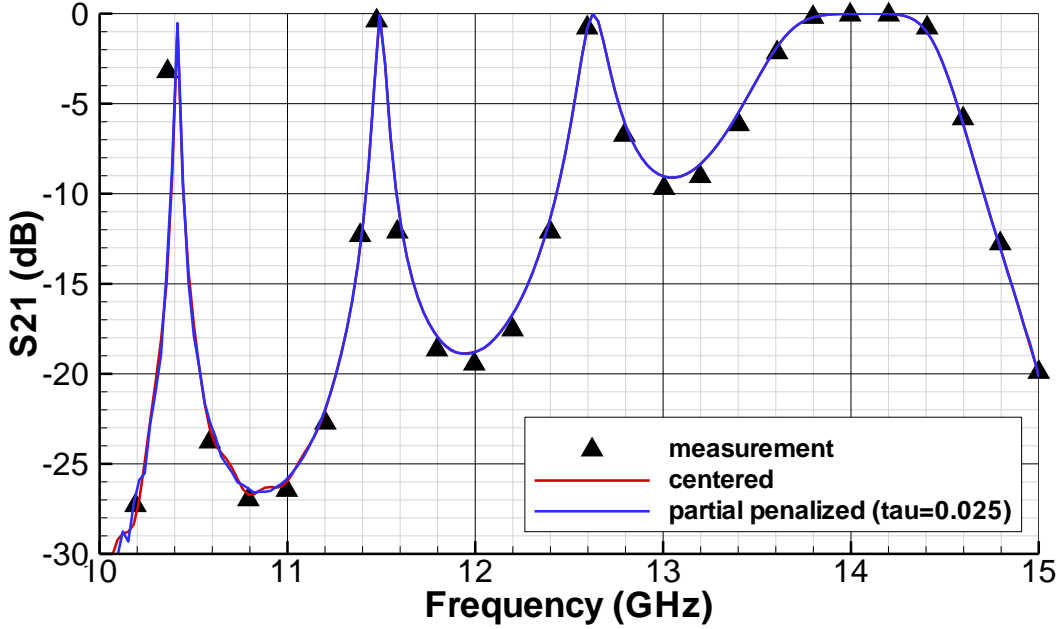
FIGURE 5.3: Dual-mode circular waveguide filter response. Measured and computed data comparison.
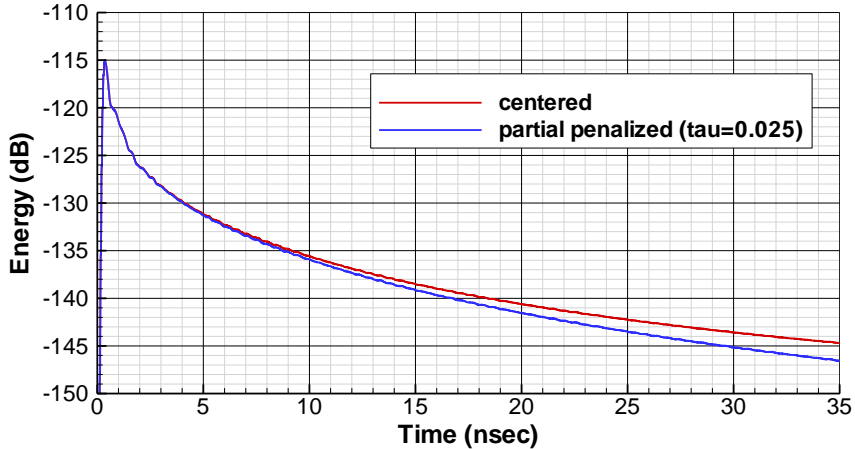
FIGURE 5.4: Evolution of the energy inside the dual-mode circular waveguide filter.

TABLE 5.3: Computational requirements of the different cases (for a 8 processors AMD OPTERON dual core 1.8GHz.). The computed physical time has been 35 nsec. Fluxes: C=centered, U=upwind, P=penalized with $\tau = 0.025$.

Flux	Scheme	Δt ([3])	steps([1])	memory	CPU([2])
C	RK4	24.5 - 24.5	1428572	2.0 GB	121.2 h
U	RK4	24.1 - 24.1	1452282	4.1 GB	213.3 h
C	LF	19.6 - 19.6	1785715	2.0 GB	63.5 h
P	LF	19.2 - 19.2	1822917	4.1 GB	118.5 h
C	LF,5L-LTS	6.96 - 187.9	186250	2.1 GB	8.9 h
P	LF,5L-LTS	6.81 - 183.9	190320	4.3 GB	15.5 h

([1]) Number of steps for the maximum Δt in the problem.
([3]) Minimum-Maximum values in units of 10^{-15} sec.
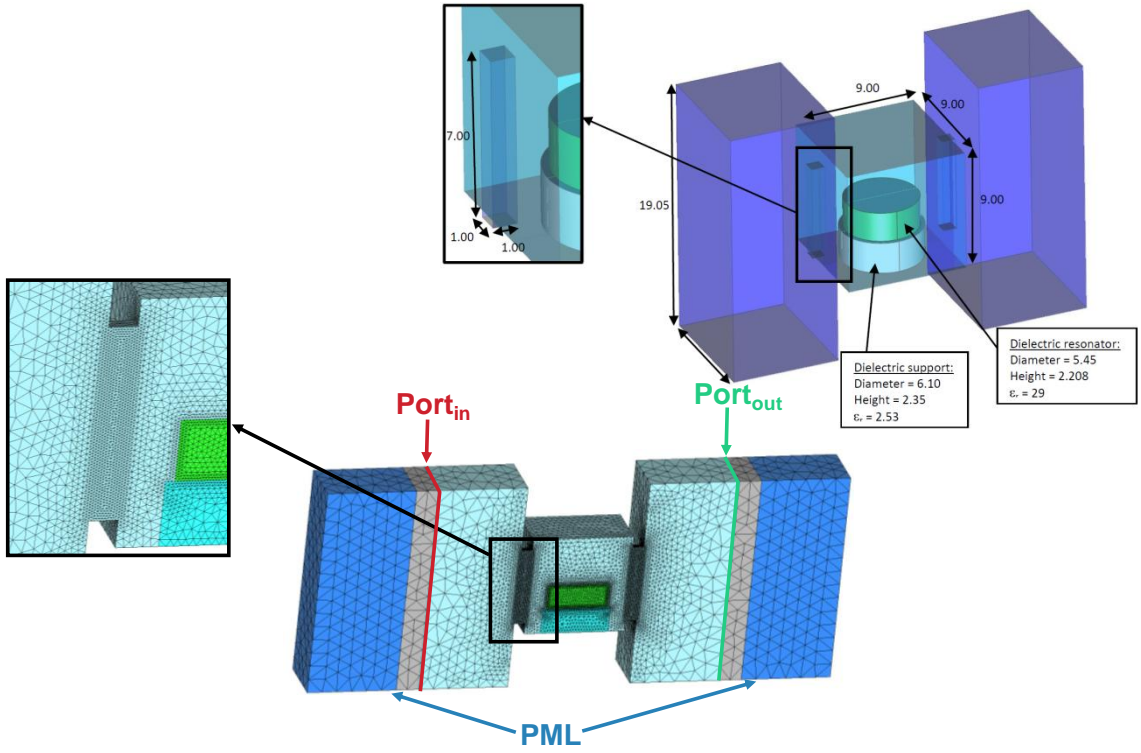
FIGURE 5.5: Single resonator composed of a rectangular cavity loaded by a dielectric cylindrical puck. Simulation setup.

5.1.2 Microwave Filter with Dielectric Material

In this case, we will show is a microwave filter with a dielectric material. The filter is composed of a single resonator based on a rectangular cavity loaded by a dielectric cylindrical puck. This structure has been reported in [157] and measurements are available. Again, the rectangular cavity is excited by two rectangular slots centered on opposite lateral faces. The resonator is chosen with a high permittivity ($\varepsilon_r = 29$) (see setup in figure 5.5). The TE_{10} mode is excited in the input port, by impressing surface magnetic currents with its profile. The backwards propagated mode is absorbed by the PML, and the forward-propagated one is the incident wave used to excite the structure. The reflected wave required to evaluate the S_{21} parameter is computed by projecting the computed electric fields with the TE_{10} profile at the output port. The energy (figure 5.6) takes a long time to leave the cavity due to the presence of the dielectric puck, which makes the structure very resonant. Excellent agreement in the S_{21} parameter between simulation and the measurements is found in figure 5.7. Only the results for a partially penalized ($\tau = 0.025$) flux are shown (similar results can be found with the centered flux, since, as with the previous filter, spurious modes have no noticeable effect on the transmission coefficient).
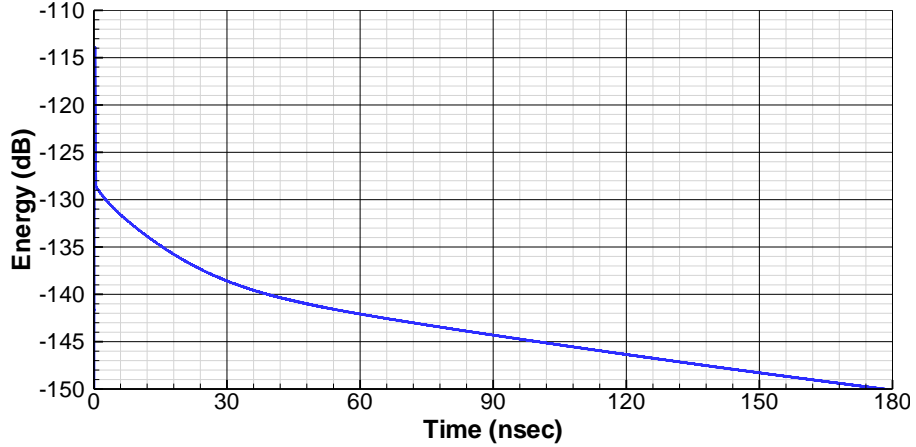
FIGURE 5.6: Evolution of the energy inside the single resonator filter.

The computed physical time, as appears in Table 5.4, was 180 nsec, which corresponds to 1980 cycles of the lowest frequency and 2880 of the highest frequency under analysis. 2nd-order leapfrog with local time stepping has been used with no instability problems. Due to the marked differences in the size of the elements, up to 6 levels in the LTS have been used, and the ratio between the shortest and largest time step was 729. Again, depending on the size of the elements, a different order p of the basis functions has been chosen.

TABLE 5.4: Single resonator simulation description.

flux	partial penalized ($\tau = 0.025$)					
time scheme	2nd-order Leap Frog (6-LTS)					
number of elements	362706					
number of d.o.f.	18505352					
computed physical time	180.0 nsec.					
LTS level	1	2	3	4	5	6
number of elements	2	26	390	177768	94036	90484
number of elements(%)	$5.5 \cdot 10^{-4}$	$7.2 \cdot 10^{-3}$	0.11	49.0	25.9	24.9
Δt (ps)	$6.0 \cdot 10^{-4}$	$1.8 \cdot 10^{-3}$	$5.4 \cdot 10^{-3}$	$1.6 \cdot 10^{-2}$	$4.8 \cdot 10^{-2}$	$1.5 \cdot 10^{-1}$
number of steps	297977292	99325764	33108588	11036196	3678732	1226244
order basis functions	$(\mathcal{G}_0, \mathcal{R}_1)$	$(\mathcal{G}_1, \mathcal{R}_1)$	$(\mathcal{G}_1, \mathcal{R}_2)$	$(\mathcal{G}_2, \mathcal{R}_2)$	$(\mathcal{G}_2, \mathcal{R}_3)$	$(\mathcal{G}_3, \mathcal{R}_3)$
number of elements	0	298113	9302	3535	27577	24177
number of elements(%)	0	82.2	2.6	1.0	7.6	6.7

5.2 Antennas

Time Domain (TD) methods for antenna simulation become very efficient for wideband response computations. Some essential characteristics are required to simulate wideband antennas in TD: modelling of antenna ports for accurately computation of antenna impedance, truncation of the computational domain and efficient treatment
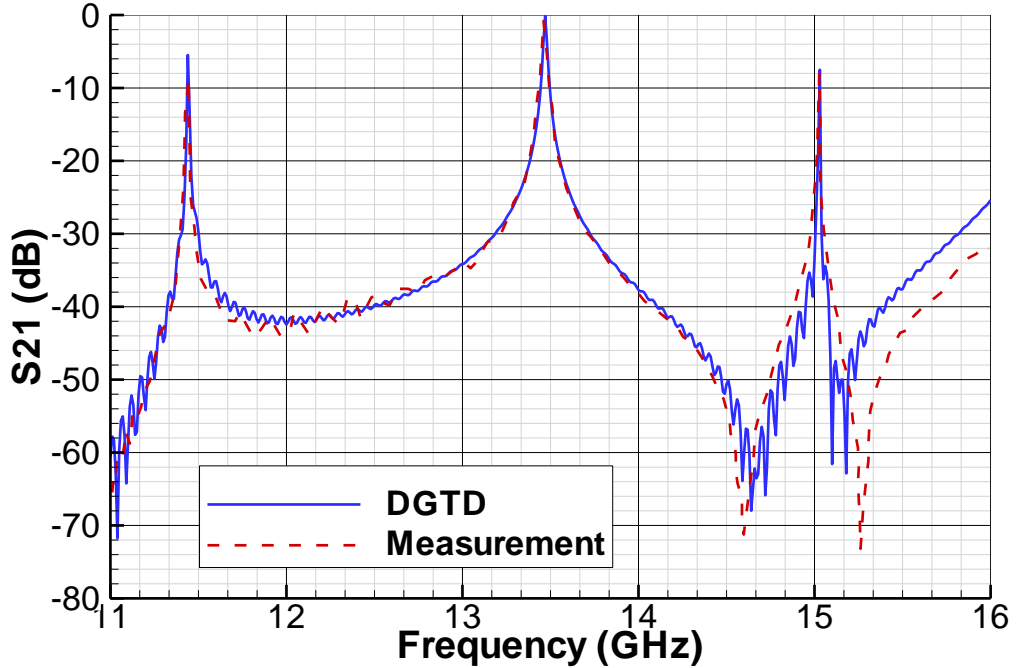
FIGURE 5.7: S_{21} response of the single resonator filter. Measured and computed data comparison.

of high elements size contrast due to geometry details. LFDG method fulfills with these requirements. The traditional methods for antenna excitations, coaxial port and delta-gap, can be easily modeled in Discontinuous Galerkin methods. The Conformal Uniaxial Perfect Matched layer (C-UMPL), formulated in section 3.4, can reduce the computational domains to the minimum. Finally, the application of local time stepping algorithm with the use of arbitrary order p in each element, can efficiently deal with the high contrast in the element size, obtaining a good accuracy level. Two numerical examples are presented to validate, show the applicability, and evaluate the efficiency of the approach.

5.2.1 Wideband Bicone Antenna

A wideband bicone antenna has been designed making used of LFDG method. The antenna has been designed, manufactured and measured, and will be used as a sensor in Low Level Swept Field (LLSF) measurements. The main objective of a LLSF test is to evaluate the transfer function between external and internal fields in a structure. This is a typical test in the aerospace sector, to assess the shielding effectiveness inside the fuselage, in the equipment bays. After the calibration of the external field without the structure, a sample of the field inside the bay have to be taken in order to evaluate the
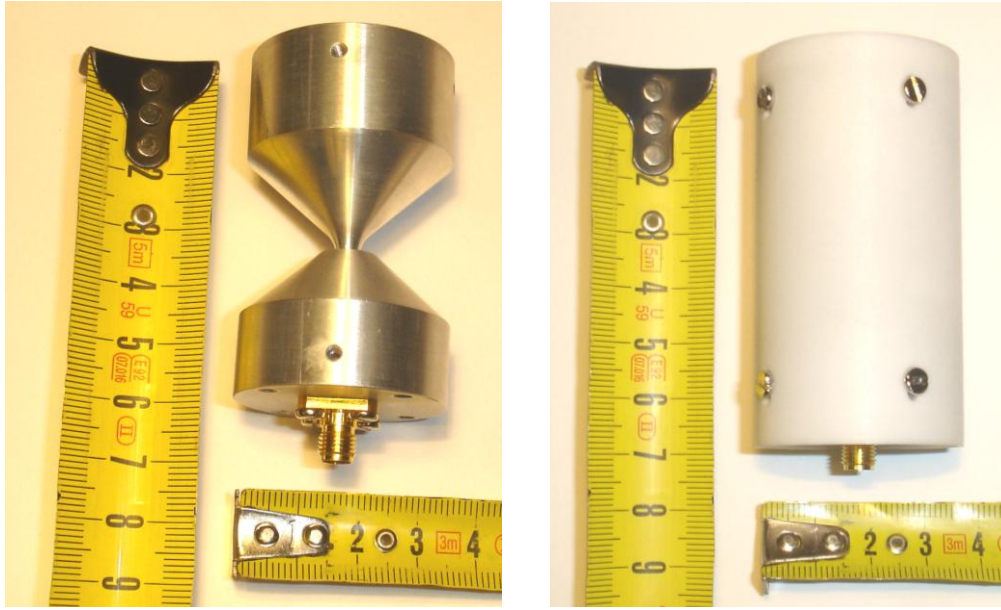
FIGURE 5.8: Wideband bicone antenna.

transfer function. The main requirements for an antenna for this kind of applications are:

- The radiation patterns should be as much omnidirectional as possible, along all the frequency band. The antenna radiation pattern will be significantly modified by the structure itself, omnidirectionality will reduce measurement variations.

- Fuselage attenuation measurements require small antennas in order to fit properly inside any kind of cavity where a final equipment could be installed.

- Good adaptation. VSWR bellow 1.7:1 is the target. This figure is important to have good sensibility and reduce the influence of the structure.

- Wide frequency band. The objective is to cover as much as possible the considered frequency spectrum against the High Intensity Radiated Fields (HIRF) hazard. In our case, the target has been from 1.5 GHz to 18.0 GHz.

The chosen antenna kind to fulfilled with all the above requirements is the bicone antenna. The final mounted design appears in figure 5.8.

Figure 5.9 shows the simulation setup. Following points have been considered in the electromagnetic modelling of the antenna:

- The antenna is meshed with quadratic (2nd) tetrahedral. This is an important point since the geometry has revolution symmetry and all the surface are curved

or doubly-curved. Curvilinear elements significantly improve the spatial discretization.

- The order of basis functions p to expand the electric and magnetic fields has been chosen depending on the element size. The objective is to maintain an appropriate accuracy level along the computational domain with reasonable simulation times.

- Conformal Uniaxial Perfect Matched Layer (C-UPML) has been used to truncate the computation space. This technique is shown to be reflectionless for any angle of incidence, polarization and frequency. The conformity is used to reduce the buffer space minimizing time and memory requirements of each simulation.

- Local Time Stepping technique has been used. Different elements size and different order of the basis functions need different time steps to fulfilled with the stability condition of the time integration scheme. Instead of using the smallest time step, different time step has been chosen which reduces enormously the simulation time.

- The antenna has been excited with a coaxial waveguide where the S11 parameter and input impedance have been computed.

- The radiation patterns for different frequencies has been evaluated computing the near-to-far field transformation of the electric and magnetic fields.

- Two symmetric planes has been used in order to reduce by a factor of four the computational requirements.

The first TEM coaxial mode is weakly injected in the coaxial port, through the flux terms. This is done introducing surface electric and magnetic current density sources of the form,

$$\boldsymbol{M}_s = \hat{\mathbf{n}}_p \times \boldsymbol{E}^{inc} \tag{5.1a}$$

$$\boldsymbol{J}_s = -\,\hat{\mathbf{n}}_p \times \boldsymbol{H}^{inc} \tag{5.1b}$$

where $\hat{\mathbf{n}}_p$ is the unit vector normal to the port, in the direction of propagation of the injected TEM mode. The incidence fields, expressed in cylindrical coordinates ρ and ϕ, take the form of the first TEM mode in a coaxial waveguide,

$$\boldsymbol{E}^{inc} = \frac{V^{inc}\left(t\right)}{\ln\left(b/a\right)} \frac{1}{\rho} \, \hat{\boldsymbol{\rho}} \tag{5.2a}$$

$$\boldsymbol{H}^{inc} = \frac{V^{inc}\left(t\right)}{\eta \ln\left(b/a\right)} \frac{1}{\rho} \, \hat{\boldsymbol{\phi}} \tag{5.2b}$$

being a and b, the inner and outer radii of the concentric conductors, respectively, with the space between them filled with a dielectric of impedance $\eta = \sqrt{\frac{\mu}{\varepsilon}}$. We assume that
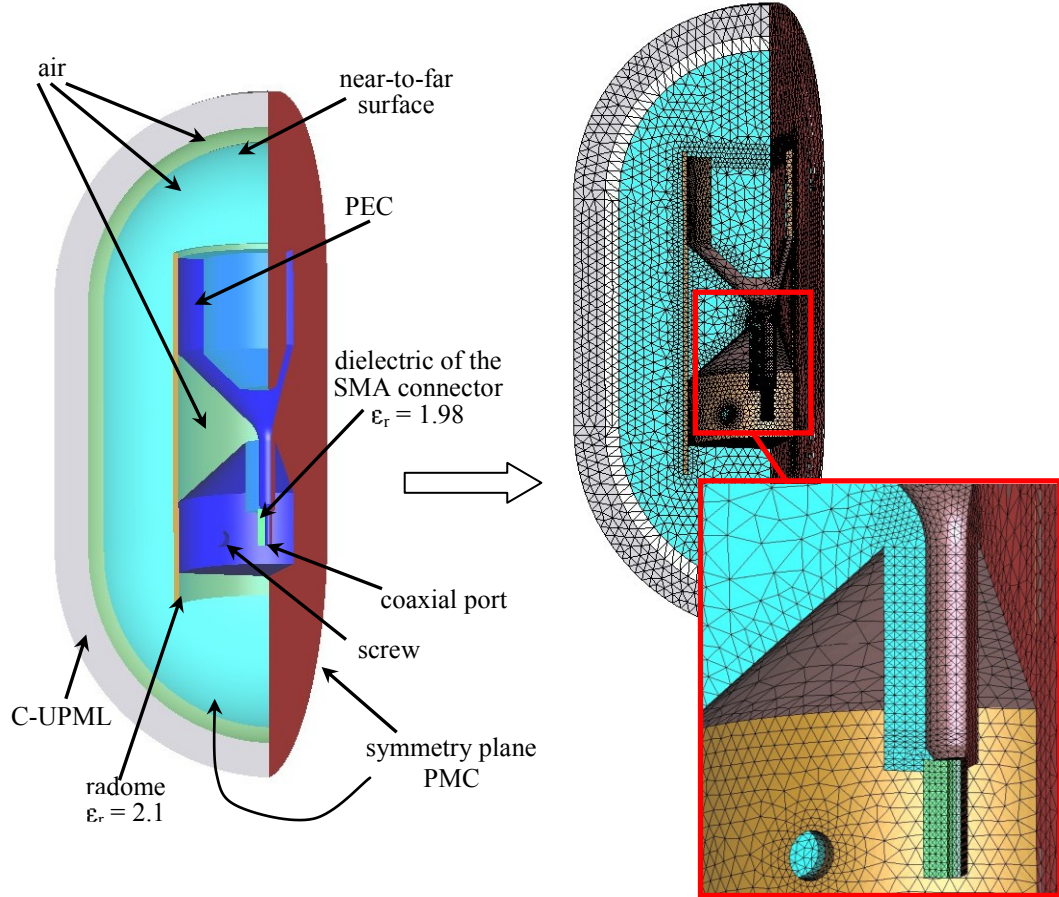
FIGURE 5.9: Simulation setup of the wideband bicone antenna.

the outer conductor is grounded, $V(t) = 0$, and the inner conductor is held at time dependent voltage $V(t) = V^{inc}(t) + V^{scat}(t)$, which includes the incidence (V^{inc}) and the scattered (V^{scat}) waves. Notice that, we can evaluate the antenna impedance and S11 parameter from the computation of V^{scat}.

The coaxial port is truncated with a absorbing boundary condition of first order (or impedance boundary condition), since the coaxial waveguide is operated in the frequency range that ensures that only the lowest mode can propagate (single-mode operation). This fact does not introduce any limitation and avoid the use of PML to truncate the coaxial port.

The coaxial port is excited with a Gaussian pulse time signal (V^{inc}), with 12 dB bandwidth at 20 GHz. The problem has been simulated until a physical time of 2.5 nsec. Some screen shots of the simulation appear in figure 5.10.

The computed and measured S11 and the computed input impedances of the final antenna are shown in figure 5.11, where excellent agreement between both have been found.
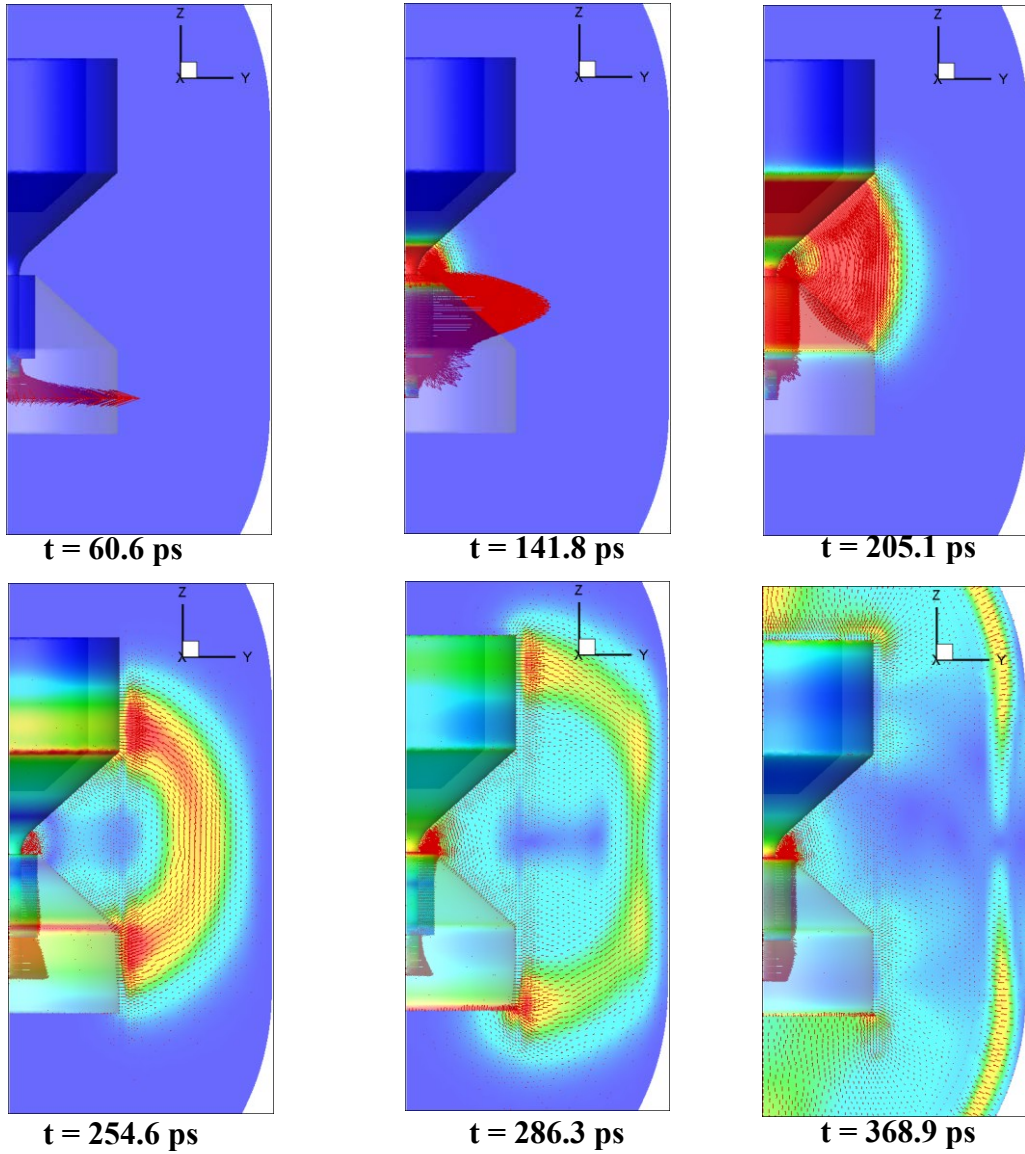
FIGURE 5.10: Screen shots of the simulation of the wideband bicone antenna.

The computed radiation patterns in the symmetrical plane are shown in figure 5.12.

5.2.2 Modelling of Antenna Installation

In this section we use the LFDG method to analyze the expected performance of an antenna installed in the fin leading edge of an aircraft. The proposed geometry is shown figure 5.13, which has been simulated installed on an infinite ground plane.

The structure is excited with a delta-gap. This source model forces an excitation voltage ($V^{inc}(t)$) between two points. The incident electric field takes a time dependent value but constant in space ($\boldsymbol{E}^{inc} = \frac{V^{inc}(t)}{\Delta}\hat{\boldsymbol{l}}_g$ where Δ is the gap width and $\hat{\boldsymbol{l}}_g$ the unit vector
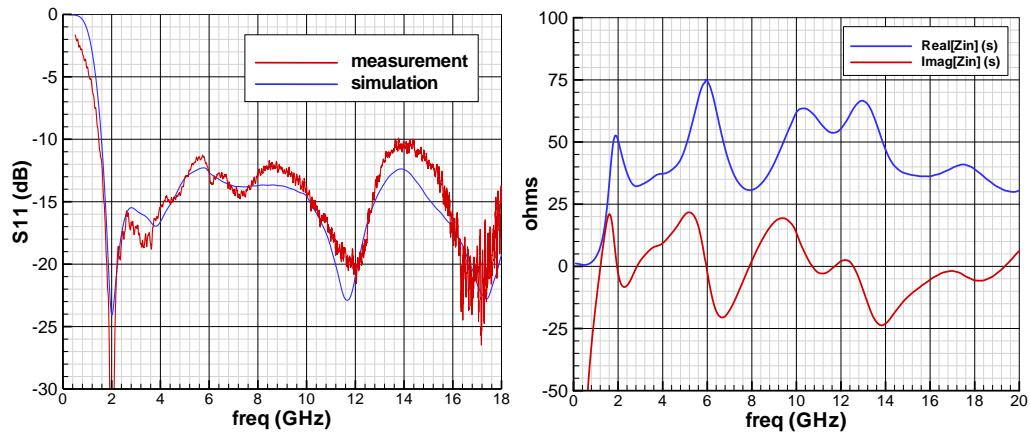
FIGURE 5.11: S11 and input impedance of the wideband bicone antenna. Measurement results of the S11 have been included for validation proposes.
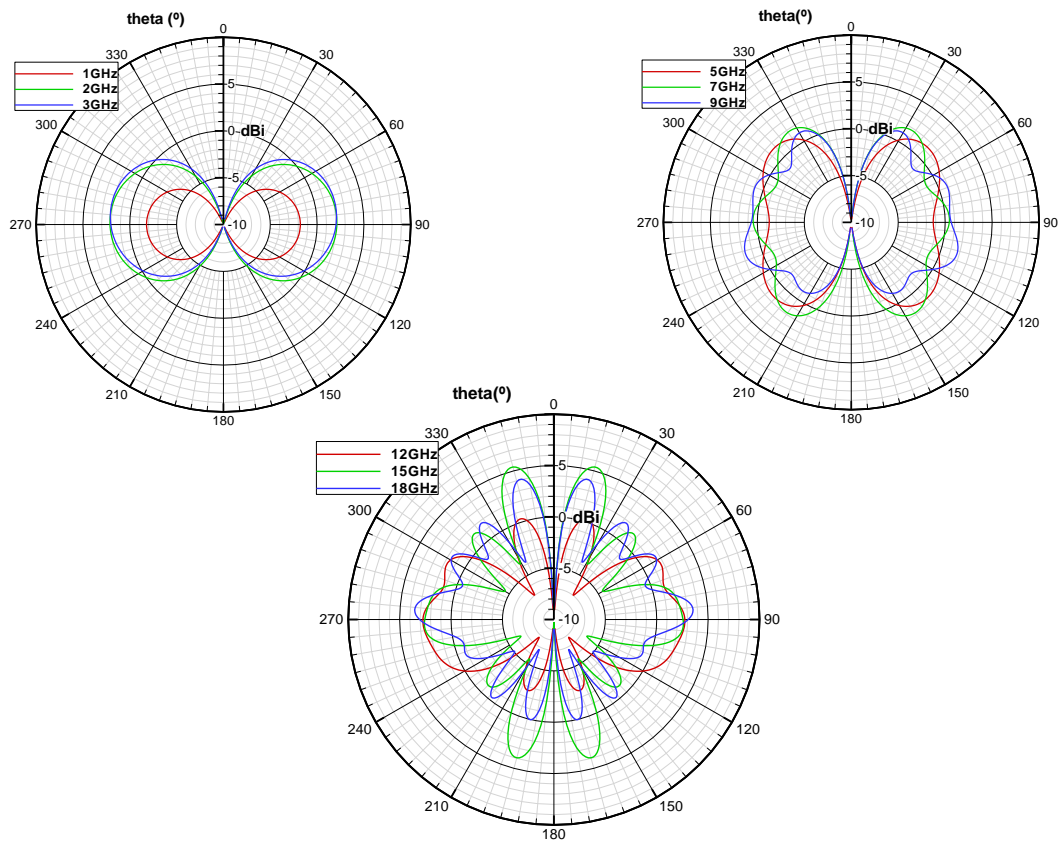
FIGURE 5.12: Radiation patterns of the wideband bicone antenna. The curves show antenna gain for different frequencies in dBi.
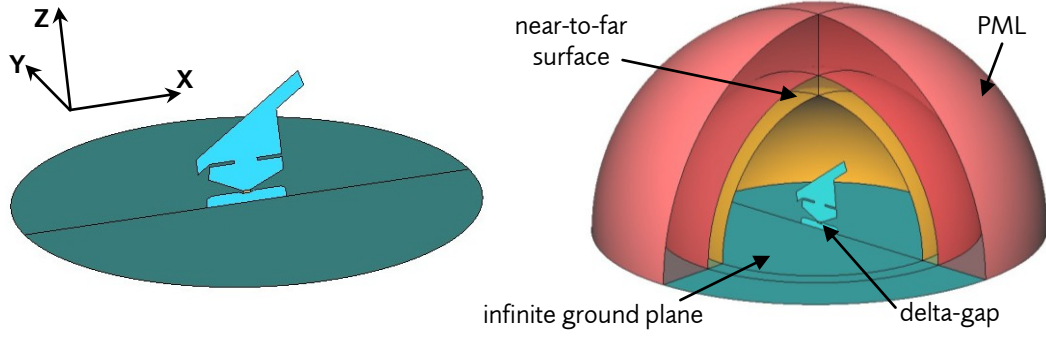
FIGURE 5.13: Antenna installed on an infinite ground plane.
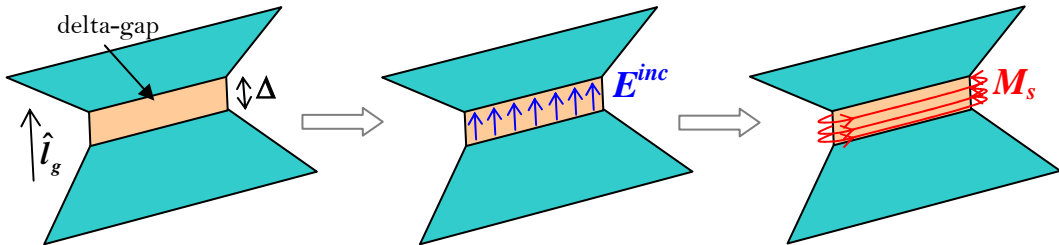
FIGURE 5.14: Delta-gap source model.

following the gap orientation) over the feed gap, and zero elsewhere. The incident magnetic field is zero in the whole computational domain.

The delta-gap source, in DG methods, can be weakly injected introducing a surface magnetic current density in the the flux terms,

$$\boldsymbol{M}_s = \ \hat{\mathbf{n}}_g \times \boldsymbol{E}^{inc} = \ \frac{V^{inc}\left(t\right)}{\Delta} \ \left(\hat{\mathbf{n}}_g \times \hat{\boldsymbol{l}}_g\right) \tag{5.3}$$

where $\hat{\mathbf{n}}_g$ is the unit vector normal to the gap.

Figure 5.14 shows a scheme of the resulting sources, where, for this particular case, we have applied the delta-gap over a PEC surface. This fact makes that the the scattered voltage ($V^{scat}\left(t\right)$) is zero. Thus, we just need to compute the current flowing through the delta-gap to evaluate the the antenna impedance.

The computed input impedance and the radiation patterns (theta vs phi diagrams) for the antenna installed on an infinite ground plane are shown in figures 5.15 and 5.16. This kind of antennas are typically used in VHF and UHF frequency bands. In UHF band the antenna is naturally matched to 50Ω. In case of VHF band, typical VSWR figures could be achieved making used of a matching network. This is the traditional approach to reduce the antenna size for on-board aircraft antennas. Concerning the radiation
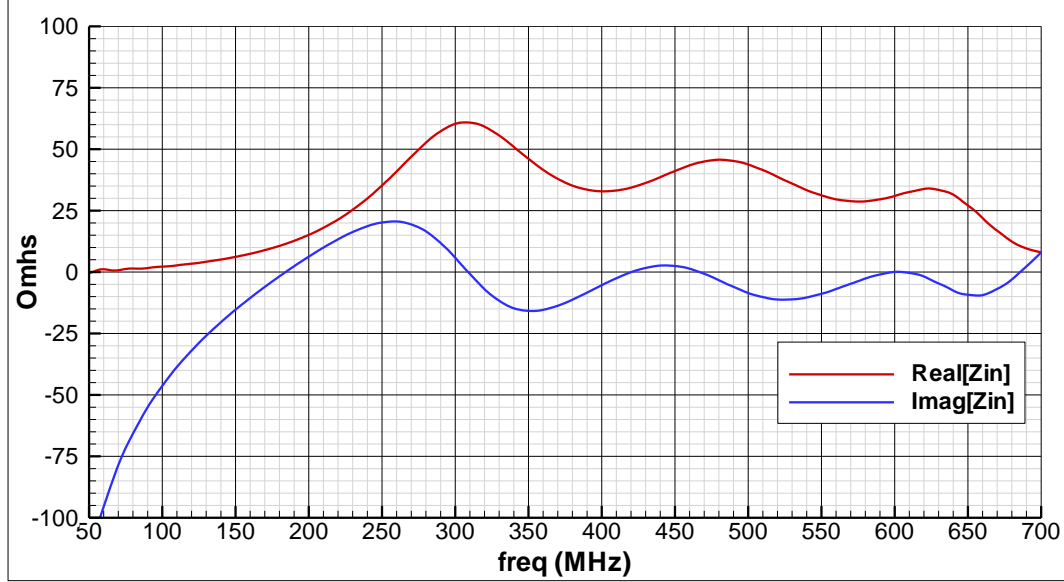
FIGURE 5.15: Input impedance with the antenna installed on an infinite ground plane.

patterns, due to the loading structure on the top of the radiating element, some energy will be radiated in the cross-polar component, which slightly reduces antenna gain in the co-polar component. This effect is more important in UHF band.

The proposed integration concept of this antenna in a fin leading edge of an aircraft is depicted in figure 5.17. The first approach to estimate the antenna performance of the antenna installed in the fin leading edge, is to considered just a piece of tail, as is depicted in simulation setup of figure 5.18. Antenna impedance, and radiation patterns for two frequencies (132 MHz (VHF) and 312 MHz (UHF)) have been computed and the results, theta vs phi radiation patterns, 3-D radiation patterns and impedance, appear in figures 5.19, 5.20 and 5.21.

We find relatively low degradation of the adaptation parameter. However, important differences, due to the masking effect of the fin, are found in the radiation patterns.

5.3 Estimation of the RCS of LO Targets

To validate and test the accuracy of the presented method, we consider a low observable (LO) target in different configurations known as NASA Almond. This is an Electromagnetic Code Consortium benchmark target for validation proposes, defined in [158], where some measurements for a perfect electric conductor (PEC) case, are reported.

(a) VHF (132 MHz) co-polar.

(b) VHF (132 MHz) cross-polar.

(c) UHF (312 MHz) co-polar.

(d) UHF (312 MHz) cross-polar.
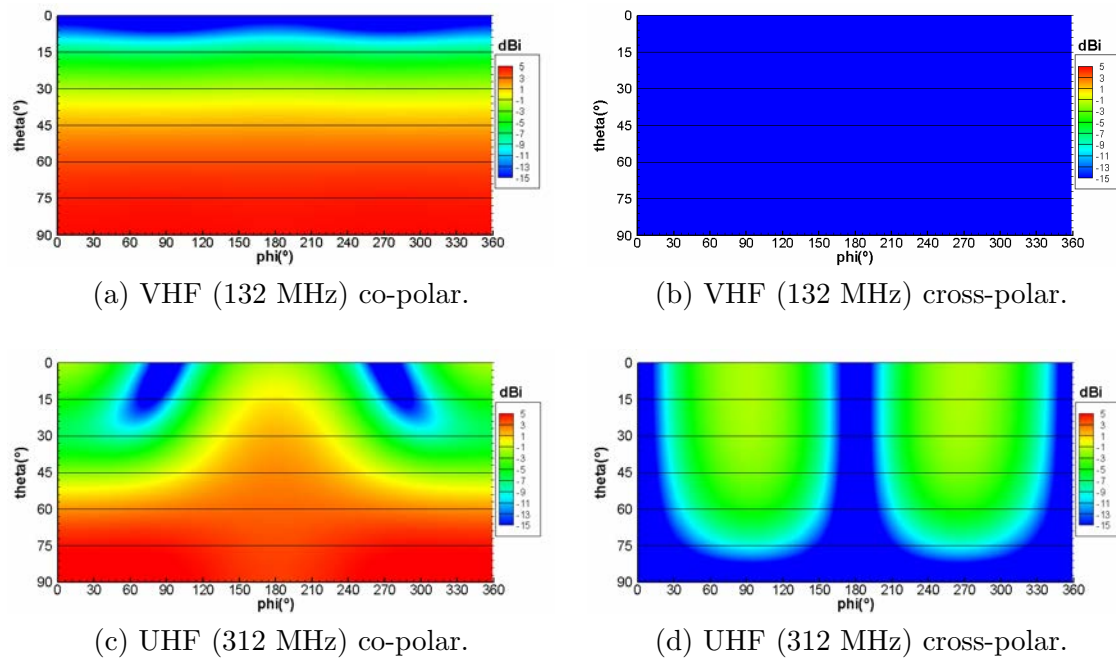
FIGURE 5.16: Theta vs phi radiation patterns with the antenna installed on an infinite ground plane.
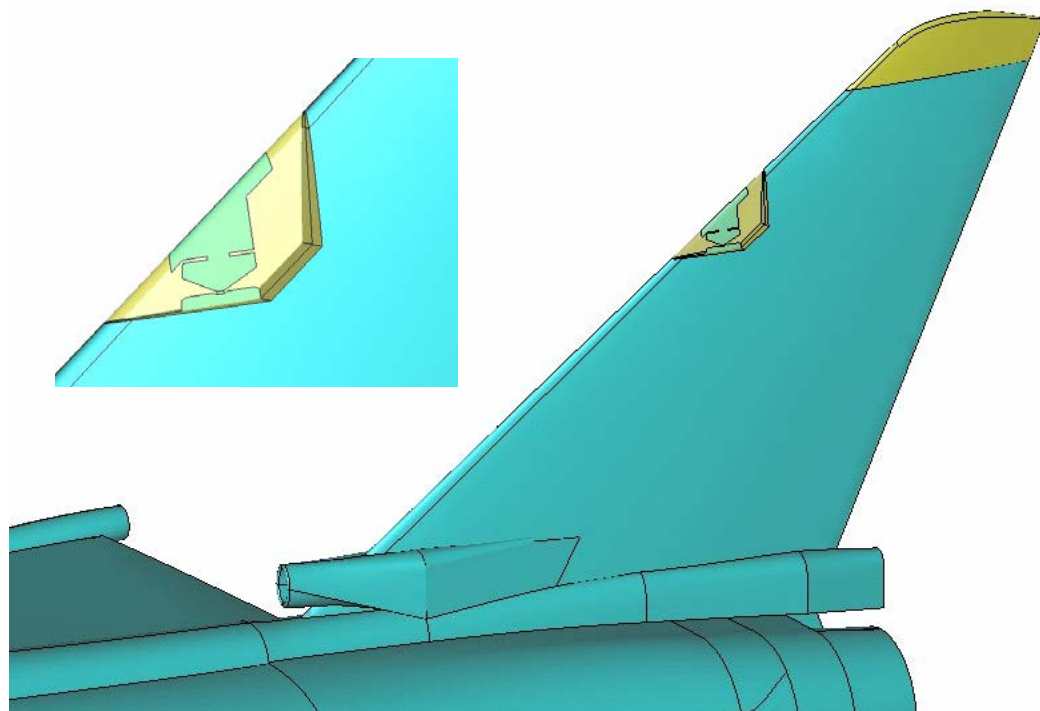
FIGURE 5.17: Antenna integration concept.
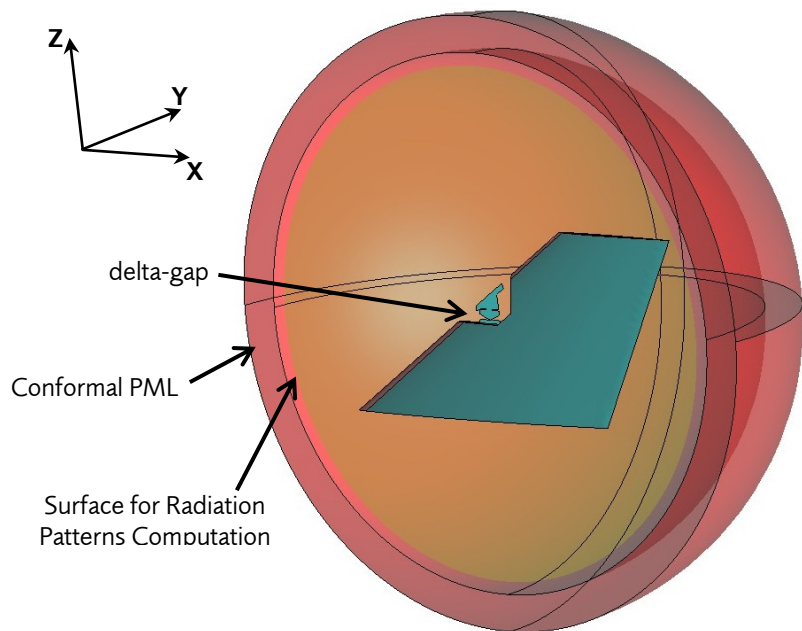
FIGURE 5.18: Installed antenna simulation setup.
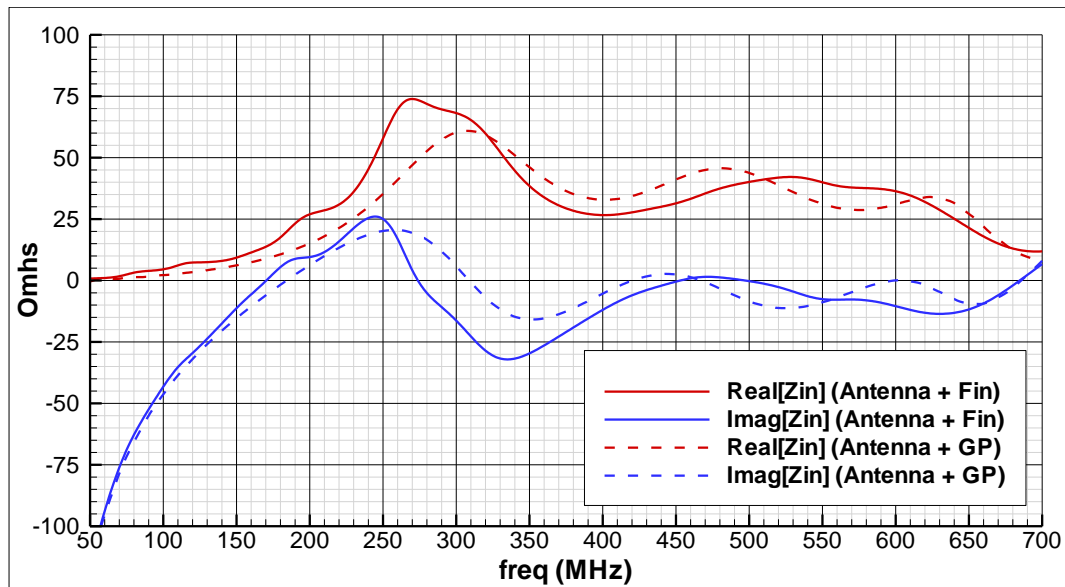
FIGURE 5.19: Input impedance with the antenna installed on the fin leading edge. The results of the antenna installed on an infinite ground plane have been included.

(a) Co-polar.

(b) Cross-polar.

(c) Co-polar 3-D radiation pattern.
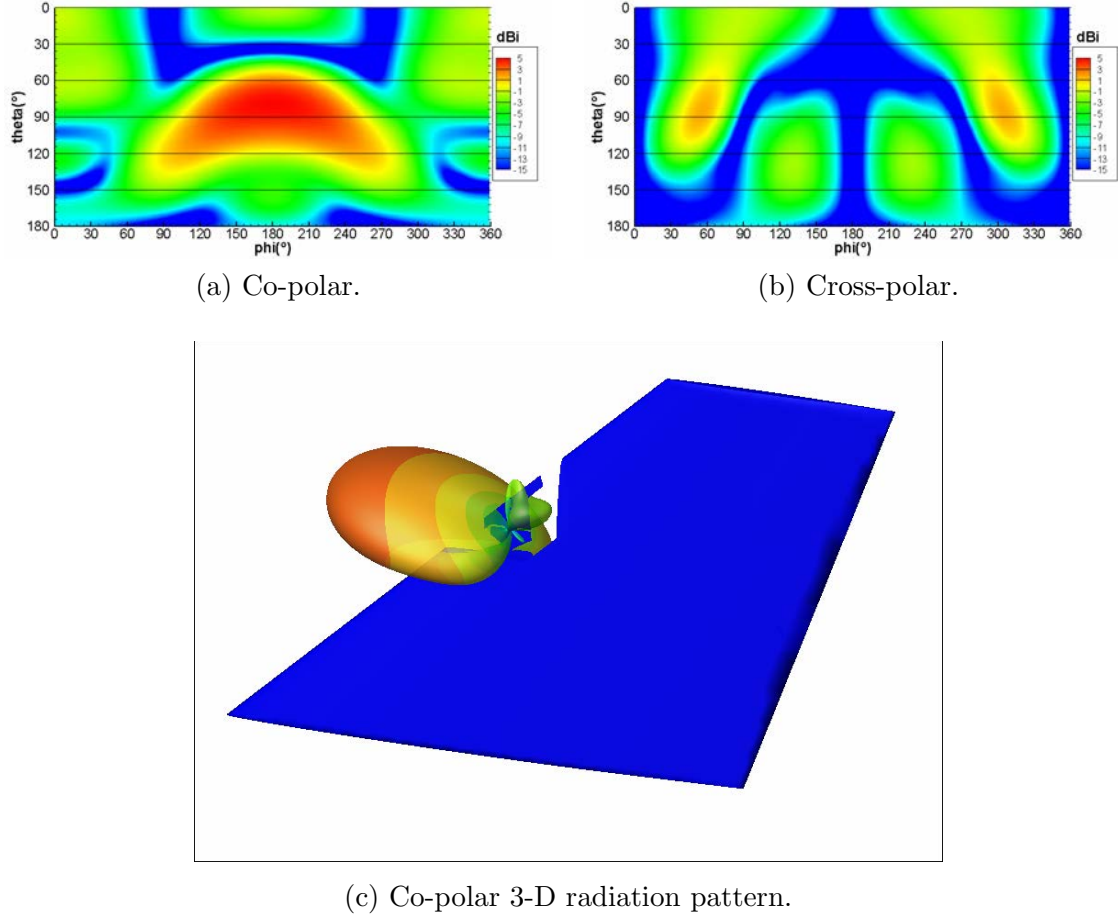
FIGURE 5.20: Radiation patterns for the antenna installed in the fin leading edge at 132 MHz.

Due to the tiny RADAR cross-section (RCS) of this LO target, high accuracy is a must to deal with these kind of EM problems. Thus, this structure are typically solved by Method of Moments (MoM) in FD, which is one of the methods more accurate in CEM.

LFDG algorithm has been used to compute the RCS of the almond and compared to results obtained with MoM Multilevel Fast Multipole Method (MoM-MLFMM). The used MoM-MLFMM code has been HPTESP-MAT, which is a Cassidian Electromagnetic Solver based on MoM-MLFMM on surface integral equations know as Combined Current and Charge Integral Equations (CCCIE) [159, 160], able to deal with composed metallic and homogenous dielectric structures.

(a) Co-polar.

(b) Cross-polar.

(c) Co-polar 3-D radiation pattern.
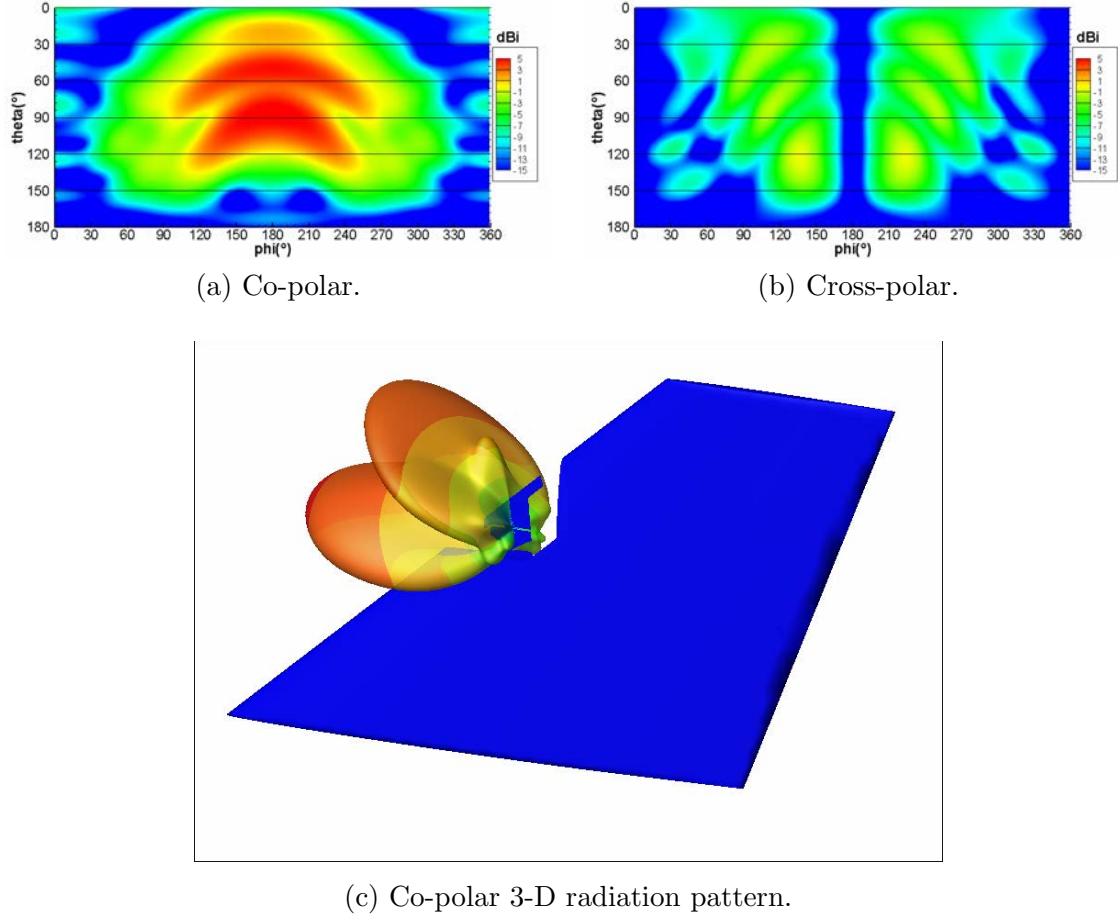
FIGURE 5.21: Radiation patterns for the antenna installed in the fin leading edge at 132 MHz.

The geometrical definition of the PEC structure appears bellow,

Half ellipsoid: for $-0.416667 < t < 0.0$ and $-\pi < \psi < \pi$

$$
\begin{cases}
x = d\,t, \\
y = 0.193333\,d\left(\sqrt{1-\left(\frac{t}{0.416667}\right)^2}\right)\cos\psi, \\
z = 0.06444\,d\left(\sqrt{1-\left(\frac{t}{0.416667}\right)^2}\right)\sin\psi,
\end{cases}
\tag{5.4a}
$$

Half elliptic ogive: for $-0.0 < t < 0.583333$ and $-\pi < \psi < \pi$

$$
\begin{cases}
x = d\,t, \\
y = 4.833450\,d\left(\sqrt{1-\left(\frac{t}{2.083350}\right)^2} - 0.96\right)\cos\psi, \\
z = 1.611148\,d\left(\sqrt{1-\left(\frac{t}{2.083350}\right)^2} - 0.96\right)\sin\psi,
\end{cases}
\tag{5.4b}
$$

where $d = 2.5$ m, is the length of the structure. Notice that this is a complete double curvature geometry, where we can find both, smooth and high curves zones, and also a
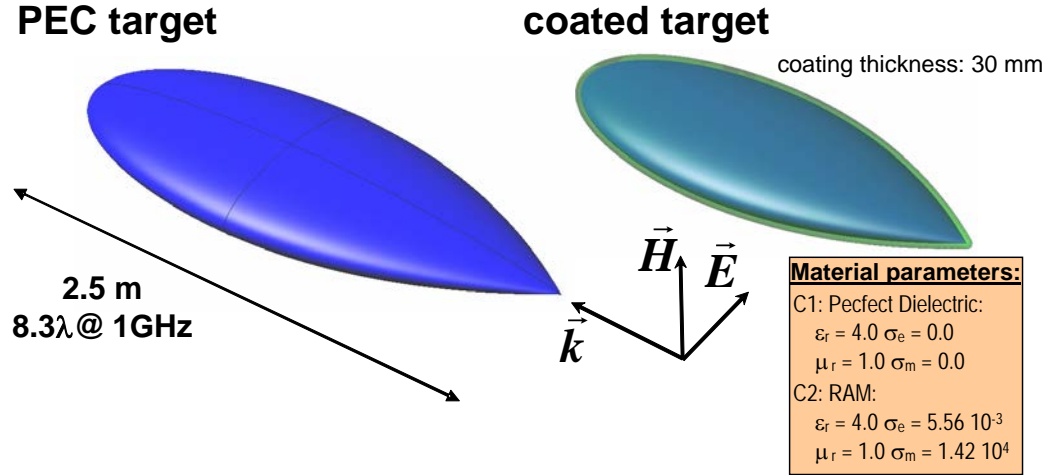
FIGURE 5.22: Geometry under analysis for the NASA Almond.

singular point, the ogive vertex. The right discretization of the curve surfaces (curvilinear 2nd-order tetrahedral), and also a care discretization of the fields close to the vertex (low value of h) are critical to obtain accurate results. Figure 5.22 shows the geometry under analysis. Apart from the PEC case, two different coated material cases has been studied, a perfect dielectric and a RADAR Absorber Material (RAM).

Figure 5.23 gives some details of the simulation setup. Firstly, a total-field region is defined in a way to minimize the size of the computational domain. Secondly, the scattered-field region is created. Finally, the conformal PML layer is defined to close the computational domain. The surface, interface between total-field and scattered-field regions, is used to excited the problem in a weak way, through the flux terms, as a Huygen's source. The same surface is used to compute the near-to-far field transformation and calculate the RCS.

The problem is excited with an horizontal polarized plane wave, impinging on the almond at the vertex. The resulting copolar bi-static RCS at 1 GHz, computed with LFDG and compared the results with MoM, are shown in figure 5.24 for the three cases analyzed. Excellent agreement are found in all cases. The monostatic RCS from 500 MHz to 2 GHz is shown in figure 5.25. Excellent agreement is found for PEC and C2 (RAM material) cases. Minor differences are detected for the C1 (perfect dielectric) case. It is important to notice that this is a challenging case for MoM, where the required number of iterations to solve iteratively the MoM linear system is quite high, and the number of unknowns can not be very high in order to have a solution in a reasonable computation cost. Thus, these minor differences are mainly due to a slightly lack of accuracy in the MoM results.
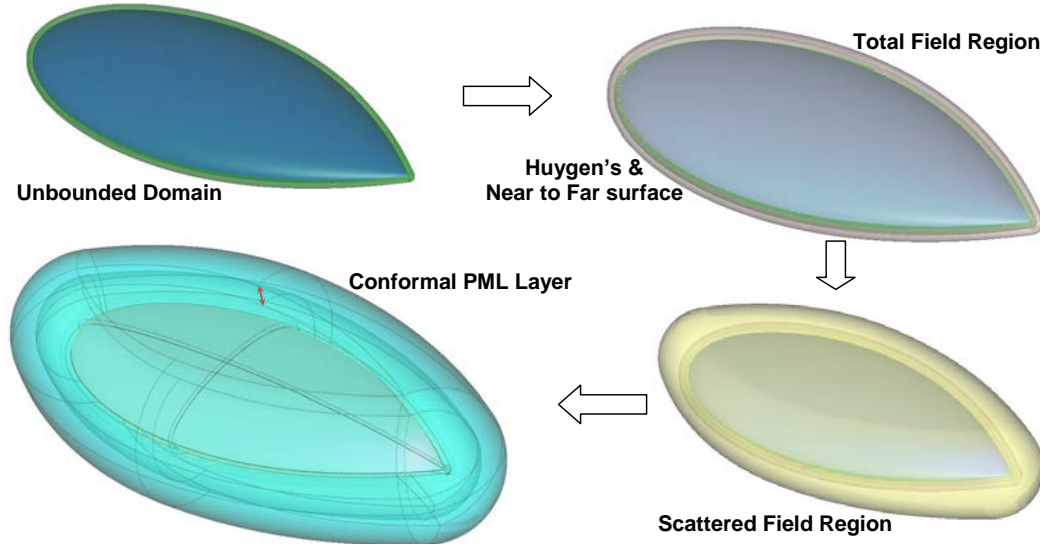
FIGURE 5.23: Simulation setup for the NASA Almond. Starting with the unbounded domain (upper left), a total-field region (with a conformal Huygen's surface) is defined (upper right). This surface is used for the near to far field transformation operation. A scattered-field region is created (lower right) and, finally, the PML layer (lower left).

Concerning computational cost in this EM problem, the CPU time required for the LFDG method, is about 10 times the computational cost of MoM for one frequency. This means that, LFDG is worthy to be used if more than 10 frequency are going to be computed. In our case the monostatic RCS has been computed for 301 frequencies obtaining, obviously, less computational cost for LFDG [1]. In the same way, for the bi-static RCS computation, just for one frequency, MoM requires less CPU time than LFDG.

5.4 High Intensity Radiated Fields

The adverse effects caused by high-intensity radiated fields (HIRF) in any electronic device or in a very complex system, such as an aircraft, is a challenging topic from the standpoint of computational electromagnetics (CEM). The typical approach to tackle this Electromagnetic Compatibility (EMC) problem is based mainly on testing. The development of efficient algorithms, able to deal with electrically large structures, and accurate methods, capable of estimating transfer functions between incident EM fields and internal fields, or induced currents in bundles, has recently been attracting a great deal of interest in the aerospace industry.

---

[1]Because LFDG is a TD method, all frequencies can be solved in just one simulation. MoM requires one simulation (matrix computation and linear system resolution) for each frequency.
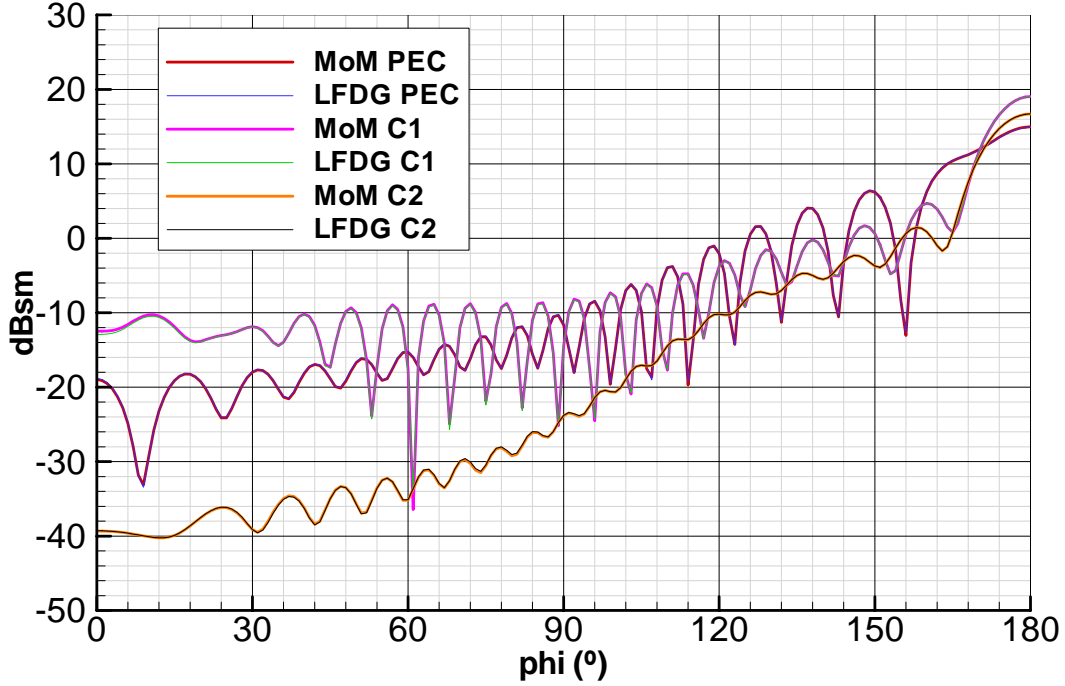
FIGURE 5.24: Bi-static Radar Cross Sections of the NASA almond at 1 GHz. Comparison results between LFDG and MoM.

In this section the capability of the presented method to deal with very complex electromagnetic problems in an accurate way is proved. Firstly in a medium size 3-D object, where a wideband frequency response, considering a plane wave illumination, is computed. Then, a electrically large problem is analyzed in order to assess the scalability of the method.

5.4.1 Medium size 3-D Object

This validation geometry has been taken from a test-case proposed under the HIRF-SE project [161] for cross-validation with measurements of several numerical solvers. It consists on a $600 \times 500 \times 300$ mm brass box, with the front face open (see figure 5.26), with a 30 mm wide flange around the edge. The box has two holes for N-type connectors on the top, labeled A and B in figure 5.26(a). Between these holes, a curved-wire is connected (see figure 5.26(b)), made up of three semi-circles and two vertical straight sections. Its endings are soldered into the N-Type bulkhead connectors A and B.

The box is illuminated perpendicularly to the open face using a linearly polarized plane wave, with electric vertical polarization, in the frequency band 1 to 6 GHz. The power
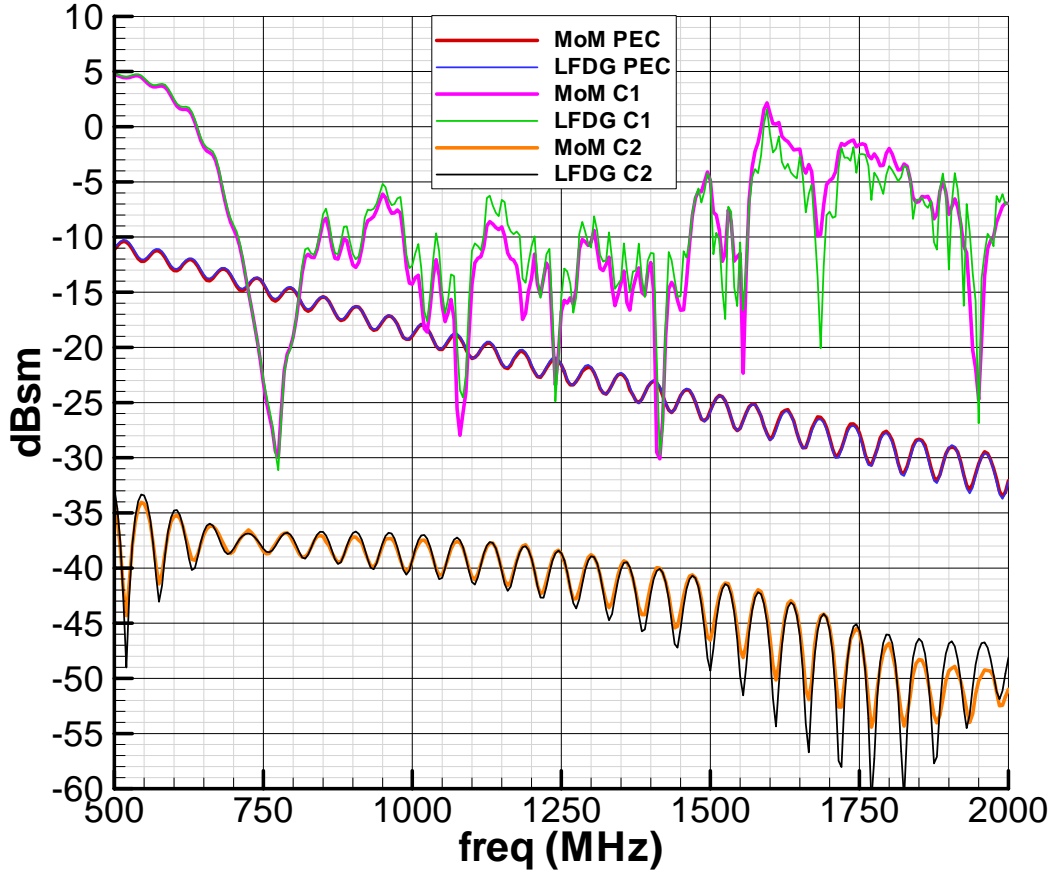
FIGURE 5.25: Monostatic Radar Cross Sections of the NASA Almond. Comparison results between LFDG and MoM.

received in the load of 50Ω at port A is taken for comparison (port B is grounded through a 50Ω load).

The results found with the LFDG algorithm are shown in figure 5.27. They are compared to measurements and FDTD simulations computed with the parallel UGRFDTD package [162]. Excellent agreement is found for LFDG and measurements.

5.4.2 Aircraft Simulation Case

This problem consists of a 3-D numerical test case based on a modified version of Evektor's EV55 metallic aircraft (see figure 5.28), also taken as a workbench for cross-validation of several simulators under the HIRF-SE project [161]. The aircraft model consists on a PEC skin together with a generic part of the cabling. The electrical dimensions at 1 GHz are $53.7 \times 47.4 \times 17.1 \, \lambda$. The PEC shell is considered with zero thickness, and the cable is modeled as a PEC cylinder of radius 3 cm. Some apertures exist in the aircraft shell, cockpit, and fuselage windows, which permit the electromagnetic energy

(a) Metallic box.

(b) Curved-wire geometry.
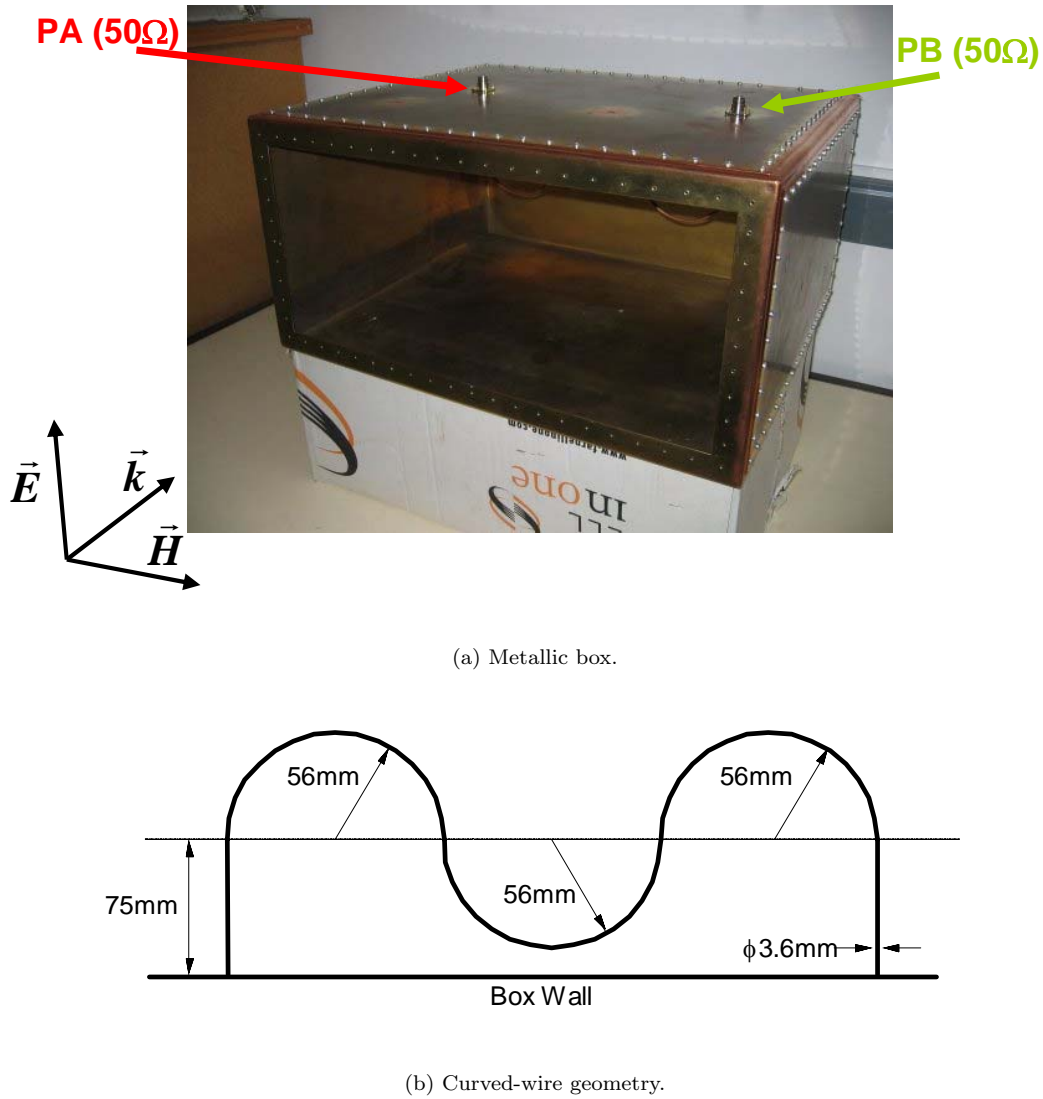
FIGURE 5.26: Setup of the medium size 3-D object.

to couple into the airframe, where there are simplified models for some of the systems and cavities. The aircraft is illuminated with a plane wave coming at 45° below its nose, with the magnetic field in the horizontal plane (see figure 5.28(a)).

Three different kind of probes have been chosen for comparison, for being representative of different coupling scenarios (see figure 5.28(b)):

1. **O1**. The electric field at a surface test-point on top of the cockpit hidden from the illumination coming from underneath.

2. **O2**. The magnetic field in a point inside the airframe more weakly coupled to the illumination, and more susceptible to internal resonances.
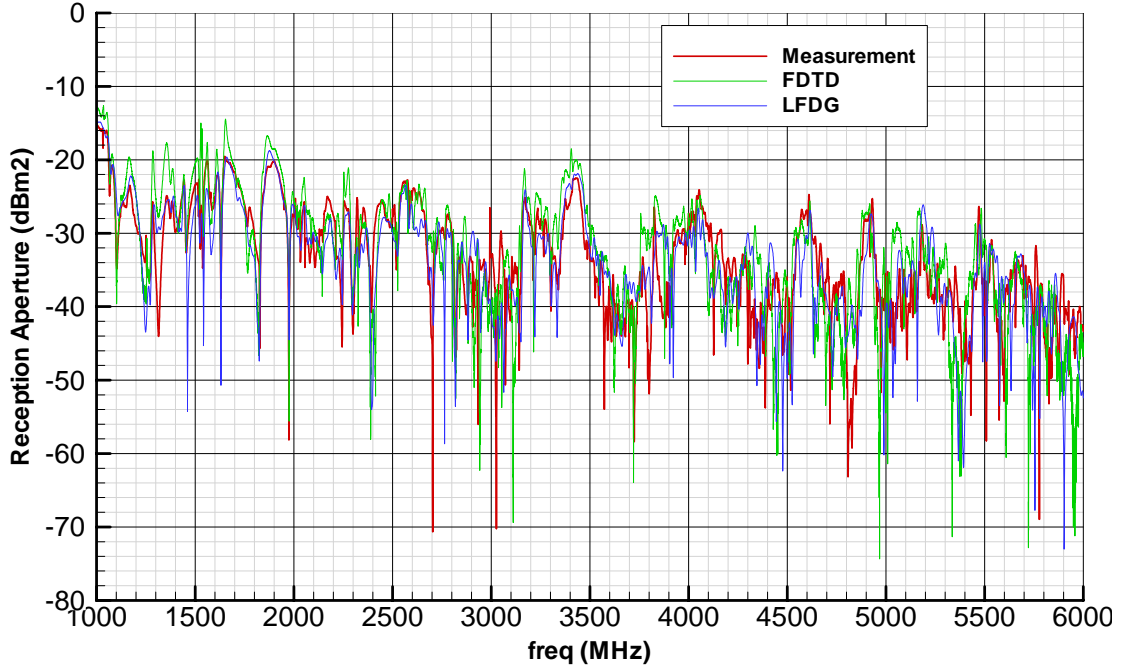
FIGURE 5.27: Reception aperture of the medium size 3D object, the reception aperture being the relation between the power received at port A, and the power density of the plane wave illuminating the box. Measurements are compared with results computed with LFDG and FDTD methods.

3. **O3**. current at the termination of one of the grounded cables.

All these quantities have been found in TD and computed in FD as transfer functions (normalized to the incident field).
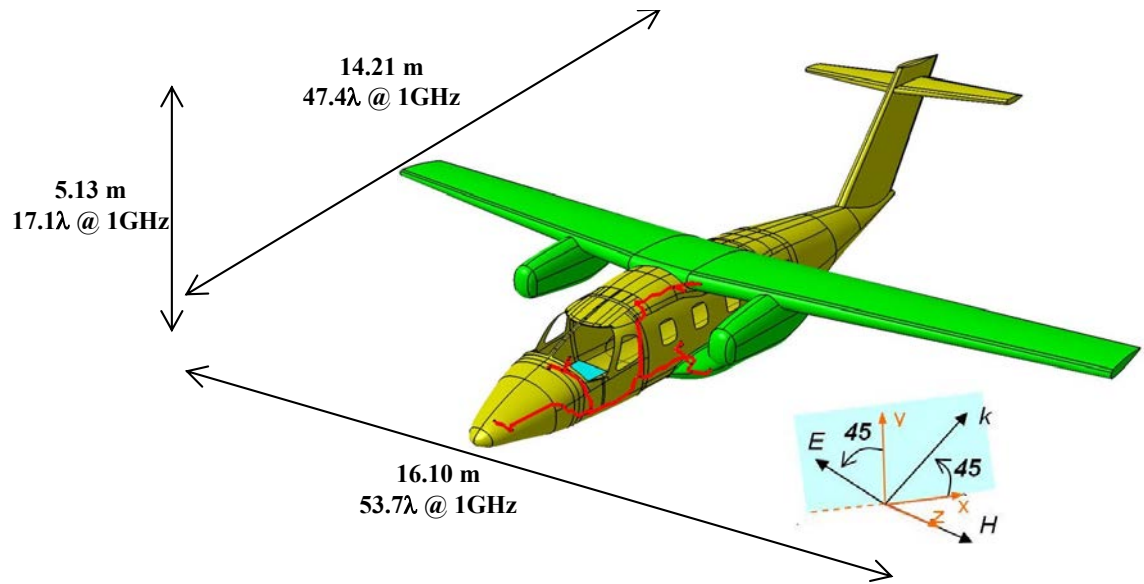
The simulation setup is shown in figure 5.29. A total-field region is defined directly backed by the conformal PML interface. Thus, the scattered-field region is just the PML, with the subsequent computational saving. The surface at the total-field/PML interface layer is used to introduced the excitation as a Huygen's source, through the flux terms, as described in section 3.2.

The plane-wave source uses a Gaussian pulse time signal, with 14 dB bandwidth at 1 GHz. The problem has been simulated up to a physical time of 1.0 μs. Some screen shots of the simulation appear in figure 5.30, and results are shown in figure 5.31, in comparison with those found with FDTD (computed with UGRFDTD package [162]), reflecting very good agreement.
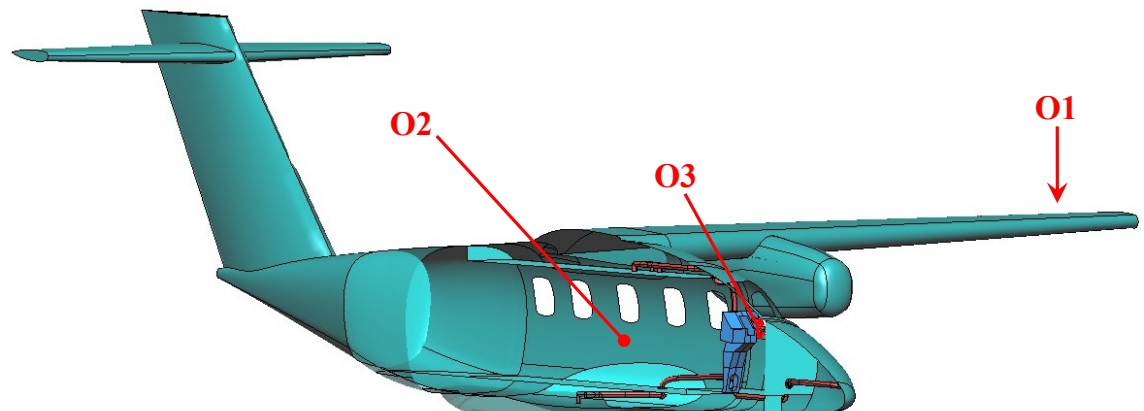
In case of the FDTD simulation, the cell size has been constant of 12 mm ($\frac{\lambda}{25}$ at 1 GHz). In both cases, the expected accuracy [2] is about 10^{-2} per wavelength at 1 GHz.

---

[2]Defining the accuracy as the L^2-norm error per wavelength for a plane wave traveling in free space: $\left| e^{-jk_0\lambda} - e^{-j\widetilde{k}_0\lambda} \right|$, λ being the wavelength, k_0 the analytical wavenumber, and $\widetilde{k}_0$ the numerical one (see sections 3.5.3, 4.5 and 4.6.)

(a) External view and overall dimensions.

(b) Internal view and observation points.

FIGURE 5.28: External and internal geometry of the aircraft-simulation case. There is a cable modeled as a cylinder. There are some apertures in the aircraft shell, cockpit, and fuselage windows, and also different structures and cavities inside the airframe.
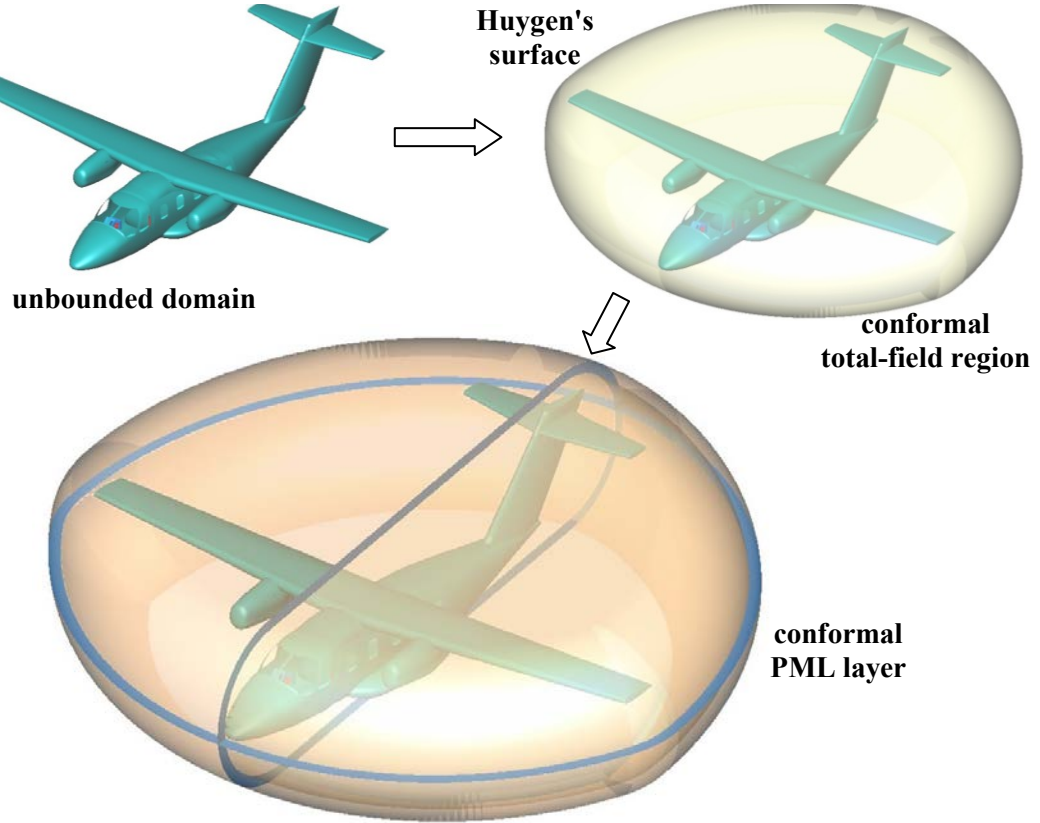
FIGURE 5.29: Simulation setup for the aircraft-simulation case. Starting with the unbounded domain (upper left), a total-field region (with a conformal Huygen's surface) is defined (upper right). Then, from this surface, the conformal PML layer can be created (lower). It should be noted that the scattered-field region is collapsed to the conformal Huygen's surface and is not needed, saving computational space.
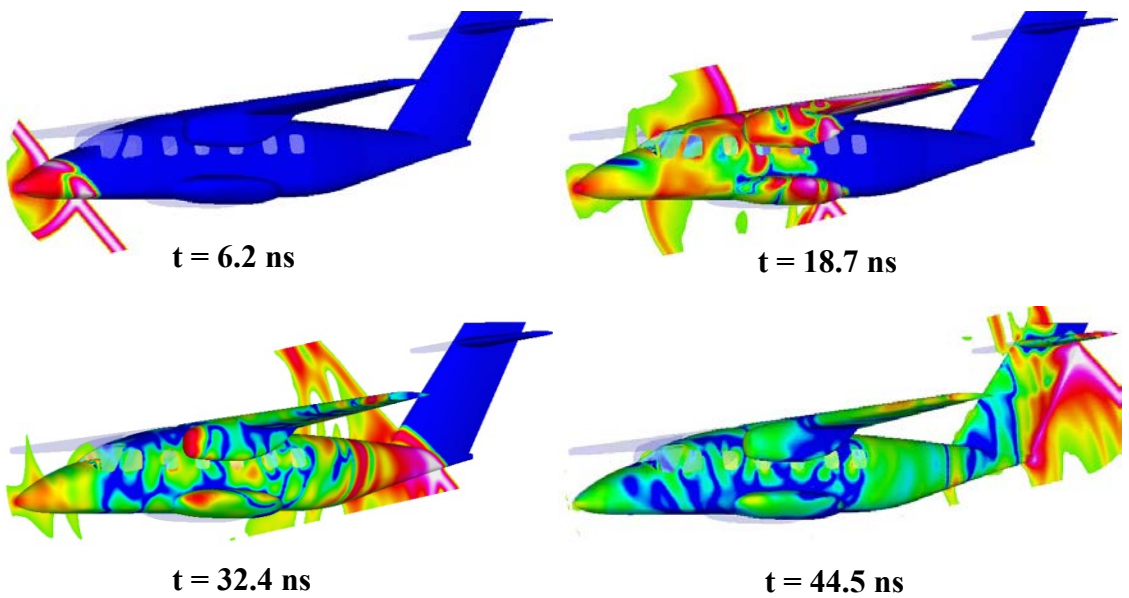

FIGURE 5.30: Screen shots of the aircraft-simulation case.
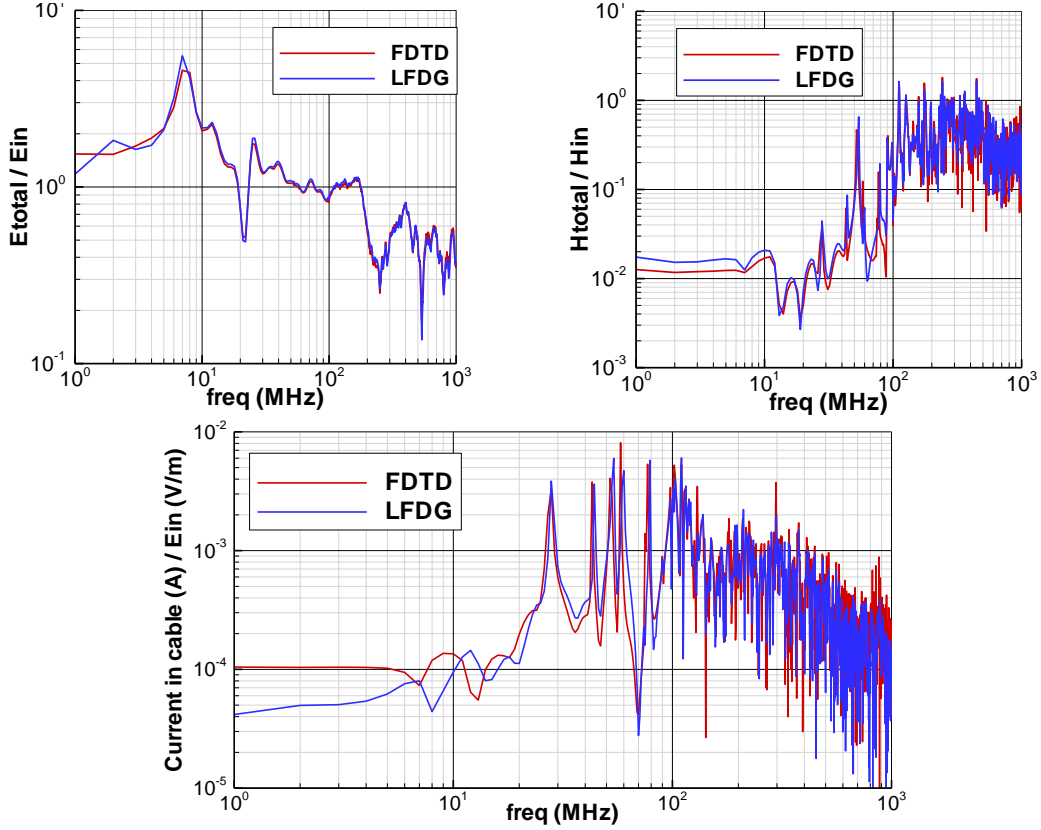
FIGURE 5.31: Computed transfer functions for the aircraft-simulation case. Comparison of results between LFDG and FDTD. Upper left: **O1**, upper right: **O2** and lower: **O3**

Details about the order of the basis functions used in this particular simulation appear in table 5.5, and about the LTS, in table 5.6. A comparison between LFDG and FDTD computational details is made in Table 5.7.

TABLE 5.5: Number of elements (M) for each set of basis functions for the Aircraft Simulation Case. GxRy stand for x order for the gradient space, y order for the rotational space

	G1R1	G1R2	G2R2	G2R3	G3R3	Total
M	96572	6018789	2729857	59	0	8845279
M (%)	1.09	68.05	30.86	0.00	0.00	100.00
dofs	3764112	300664960	204819600	6570	0	509255242
dofs (%)	0.74	59.04	40.22	0.00	0.00	100.00

TABLE 5.6: Local time-stepping level distribution for the Aircraft Simulation Case.

	L1	INTERFACE (L1/L2)	L2	INTERFACE (L1/L2)	L3
M	880	980	125602	217506	8500311
M (%)	0.01	0.01	1.42	2.46	96.10
Δt (ps)	1.59	4.77	4.77	14.32	14.32

For this case, the memory and CPU time is about one order of magnitude larger for LFDG than for FDTD. In case of FDTD, we use single precision variables since it is an

TABLE 5.7: FDTD vs LFDG Comparison.

Method	$M(10^6)^1$	dofs$(10^6)^2$	min. Δt	max. Δt	steps[3]	memory	CPU[4]	$M(10^6)/sg^5$
LFDG	8.845	509.3	1.59 ps	14.32 ps	69837	256.6 GB	114 h	52.2
FDTD	703.704	4394.8	18.00 ps	18.00 ps	55556	36.1 GB	14 h	638.4

[1] Number of elements (M) are 2nd order tetrahedra for LFDG and Yee-cells for FDTD.
[2] Double precision (8 bytes per dof) for LFDG. Single precision (4 bytes per dof) for FDTD.
[3] Number of steps for the max. Δt. The computed physical time has been 1.0 μs.
[4] CPU time corresponds to 10 processors Intel Xeon X5680 6 cores, 3.33Ghz.
   Hybrid Open MP/MPI implementations are used in both cases.
[5] Updated mega-elements per second for the highest LTS level.
   Different orders p have been used for each cell (table 5.5) for LFDG.

advantage of this method, the use of double precision does not usually improve FDTD performance. However, double precision is recommended and used in case of LFDG, where we are using high-order functions, LTS and PML, double-precision variables are required to maintain accuracy and avoid instability due to rounding-off errors. Concerning computational cost, three remarks are due:

- The simplicity of the FDTD algorithm makes it easier for the compilers to obtain faster codes. Techniques such as vectorization and the better use of the cache memory are key for speeding up FDTD algorithm. These techniques are not so effective for DGTD.

- Local time stepping, the presence of PML and the use of different order p elements, make not only the workload prediction more difficult, but the workload balance as well to optimize the parallelization. In one complete iteration of the highest LTS level, the workload is not constant across the mesh in the different steps of the LTS algorithm. In case of FDTD, the workload balance can be made in an almost perfect way.

- The mesh used in the FDTD computation is the simplest one, a uniform structured mesh. Thus, quite high discretization errors are expected because of the staircasing effect. Moreover, the FDTD mesh parses out what is irrelevant compared to cell size, which can be an advantage, if it is also electrically irrelevant, or not. In this case, for instance, a non-uniform mesh had been used, with a smaller cell (2.0 mm), the CPU time would have been very similar to that achieved with LFDG. In the case of LFDG, where curvilinear 2nd-order tetrahedra have been used, the discretization error is very small. Furthermore, the FEM mesh resolved every detail present in the geometrical model. This fact, concerning accuracy, it is clearly shown in the first case presented in the previous test-case, where we compare with measurements.
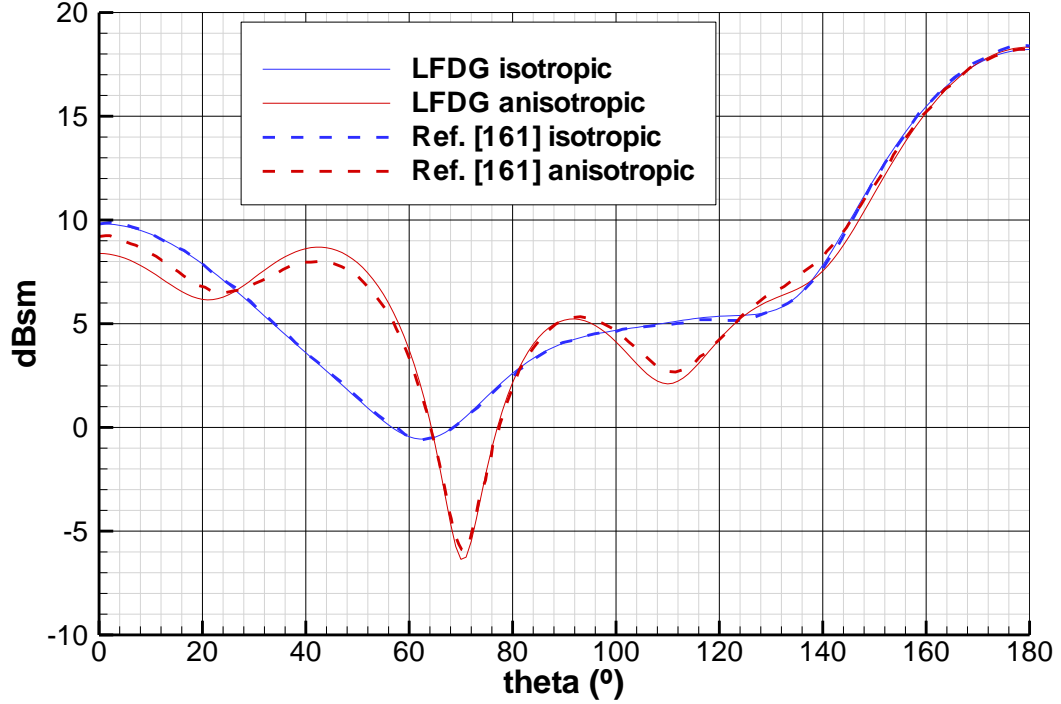
FIGURE 5.32: Bi-static RCS of an isotropic/anisotropic sphere ($D = 1.2\lambda$ and $\lambda = 1.0$ m). LFDG results are compared to those appearing in [163], and computed with Ansoft HFSS.

5.5 Anisotropic Materials

In this section we validate the formulation developed in section 3.3, where the flux terms and the semi-discrete scheme for the anisotropic material case where derived. For comparison, we have used two simple problems of scattering from a non–magnetic dielectric sphere ($\mu_r = 1$): the first one isotropic with $\varepsilon_r = 3.0$, and the second one anisotropic with

$$\bar{\bar{\varepsilon}}_r^{XYZ} = \begin{pmatrix} 3.0 & 0.0 & 0.0 \\ 0.0 & 3.0 & 0.0 \\ 0.0 & 0.0 & 4.0 \end{pmatrix} \tag{5.5}$$

The sphere is illuminated with a x-polarized plane wave, and the bi-static Radar Cross Section (RCS) is computed at a frequency for which the sphere diameter is $D = 1.2\lambda$, with λ being the wavelength. For reference, results from [163], computed with a Finite Element-Boundary Integral-Multilevel Fast Multipole Algorithm, and also computed with Ansoft HFSS commercial software are used. Figure 5.32 shows a good agreement between results found by all methods. The maximum difference found in the anisotropic case compared to HFSS results has been of 0.35 dB.

Chapter 6

Conclusion and Further Work

As a whole, this thesis pursued two global aims. The first one was to explore the potential applicability of the Discontinuous Galerkin spatial discretization to solve Maxwell's equations in Time Domain. The second one, was to propose, implement and apply an promising alternative of this method named Leap-Frog Discontinuous Galerkin (LFDG). To summarise the resulting accomplishments, the scientific contributions of this work are thus highlighted in the following section. Then, a list of future research topics in this area is presented.

6.1 Scientific Contributions

The previous chapters have presented the contributions to science after an in-depth and detailed description of the techniques involved. These achievements are abbreviated next to recapitulate and to give an encompassing view of the research undertaken:

1. **Formulation of the semi-discrete Discontinuous Galerkin spatial discretization scheme.** The formulation has been developed in a general framework which unifies different fluxes evaluation schemes successfully applied to this method. The formulation includes the treatment of the common boundary conditions, anisotropic materials, and absorbing boundary conditions (ABC), the so-called first-order Silver-Müller ABC and the conformal uniaxial perfect matched layer.

2. **Analysis of the Dicontinuous Galerkin seme-discrete scheme.** The dispersion and dissipation of the numerical method have been studied. The topic of the spurious modes has been reviewed. Additionally, the convergence rates of the

dispersion and dissipation relationships of the semi-discrete space operator have been estimated.

3. **Development of the Leap-Frog Dicontinuous Galerkin algorithm.** The well-known Leap-Frog (LF) time integration method have been apply to the DG semi-discrete scheme, obtaining the LFDG algorithm. In this context, a local time stepping strategy has been successfully developed to overcome the critical limitation imposed by the stability condition of the LF explicit temporal discretization scheme.

4. **Analysis of the Leap-Frog Dicontinuous Galerkin algorithm.** Following a similar approach to that used for the semi-discrete scheme, the LFDG algorithm has been studied, considering topics like stability, spurious and global convergence of the method. The convergence rates have been compared to the obtained with the DG space operator alone. The limitations of the LFDG algorithm have been assessed. A final analysis of the computational cost versus accuracy has been performed, and compared to the FDTD method.

5. **Parallel implementation of the Leap-Frog Dicontinuous Galerkin algorithm.** Taking advantage of the parallel nature of LFDG, this algorithm has been implemented on hybrid OMP-MPI programming technique. This two level of parallelization fits perfectly in the modern computers (a number of medium/large shared memory multi-element nodes, interconnected with Infiniband, Myrinet or Gigabit).

6. **Validation and application of the Leap-Frog Dicontinuous Galerkin algorithm.** The LFDG algorithm has been validated with microwave filters, antennas and scattering electromagnetic problems, comparing the results with measurements and other numerical techniques. The method has been applied to real engineering problems, showing some important properties of the method, such as robustness, accuracy, stability, versatility, efficiency, scalability and accuracy.

6.2   Further Work

Although many different computation electromagnetic methods have been deeply and widely developed to deal with most of the practical engineering problems, there is still gaps for which new techniques shall be explored. In this thesis, a method that combines the goods of Finite Element and Time Domain methods is implemented from scratch. To the discretion of the author, the following is a list of the more immediate research topics in this area. However, this list is not exhaustive:

1. **Developing further solver capabilities.** LFDG technique has many similarities to FDTD. In fact, FDTD can be seen as LFDG method of order zero. Hence, most of the capabilities fully assessed and validated in FDTD solvers can be adapted to LFDG. Some of the most useful are, dispersive and/or anisotropic thin layer models, dispersive materials treatment, lumped circuit elements or thin wires.

2. **Improvement the temporal integration convergence rate.** Although LFDG easily permits the selection, in each particular element, of the order of the basis functions for the spatial discretization of electromagnetic fileds, the main limitation of the method is the poor convergence rate of the temporal integration scheme. This fact imposes a limit in the use of p refinement techniques. The temporal integration algorithm should be improved to allow the selection, element-by-element, of the convergence rate of the temporal discretization.

3. **Development of hp-adaptability techniques.** The electromagnetic problems addressed in this work show the importance of the use of hp-adaptability. The development of efficient hp-adaptability techniques, in time domain simulations, will allow the application of the method in a more automatic and blind way. To this aim, a close integration of the mesher in the electromagnetic solver is a critical point.

4. **Multi-physics simulation.** The use of unstructured tetrahedral meshes makes easier multi-physics coupling with other numerical models that also use this kind of meshes.

Appendix A

SEMBA: Numerical Tool for Electromagnetic Fields Computation

A electromagnetic computational tool, based upon the Leap Frog Discontinuos Galerkin (LFDG) algorithm, has been developed. The tool's name is SEMBA. Some implementations details and capabilities are described in this appendix.

A.1 Description of SEMBA

The implementation of the LFDG algorithm explained in chapter 4 is called SEMBA LFDG, hereafter referred as SEMBA. Some high level details about the implementation are listed bellow.

- Self-supporting Fortran 95 code. SEMBA does not make use of any external library, except MPI.

- Hybrid OMP-MPI programming technique, well suited for the new kind of computers: A number of medium/large shared memory multi-element nodes, interconnected with Infiniband, Myrinet or Gigabit.

- Highly optimized code. In algorithm and computing resources (memory & CPU). Matrices which are independent of the element geometry are shared. Incomplete matrices are compressed.

- Most of the code uses double variables. This fact permits to keep under control the accuracy and avoid late-time instabilities.
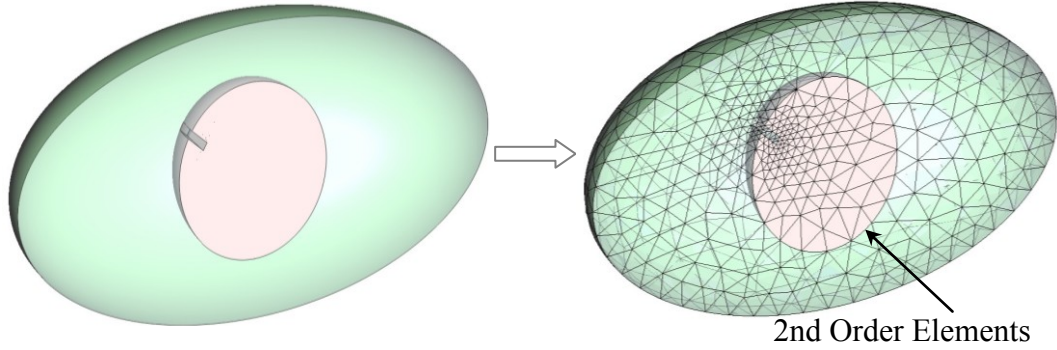
FIGURE A.1: Geometrical discretization.

A.2   Geometrical Discretization.

SEMBA's geometrical discretization is based on first and second order curvilinear tetrahedra. The use of curvilinear elements offers two main advantages. One is the accurate representation of curved boundaries and geometry, what, in many real applications, introduces a dramatic improvement in the accuracy of the numerical approximation. The other is the increment in the efficiency of the method, since curvilinear elements reduce the number of the elements to accurately discretize a geometry, and the obtained mesh has bigger elements, allowing the use of longer time-step in the temporal integration.

Another important point is the capability to generate complex meshes with this kind of elements. This requirement is fulfilled by most of the commercial CAD tools. In our case, GiD [120] is employed for geometrical modelling, meshing and some visualization of the results.

A.3   Mesh Preprocessing.

In order to increase the efficiency of the computations and implement some capabilities, before starting a numerical simulation SEMBA performs some preprocessing tasks. First of all, the mesh is distributed among the different parallel processes. Secondly, the order of the basis functions for each element is chosen, according to the required accuracy. Finally, the elements are organized in different sets, as is required by the Local Time Stepping algorithm.
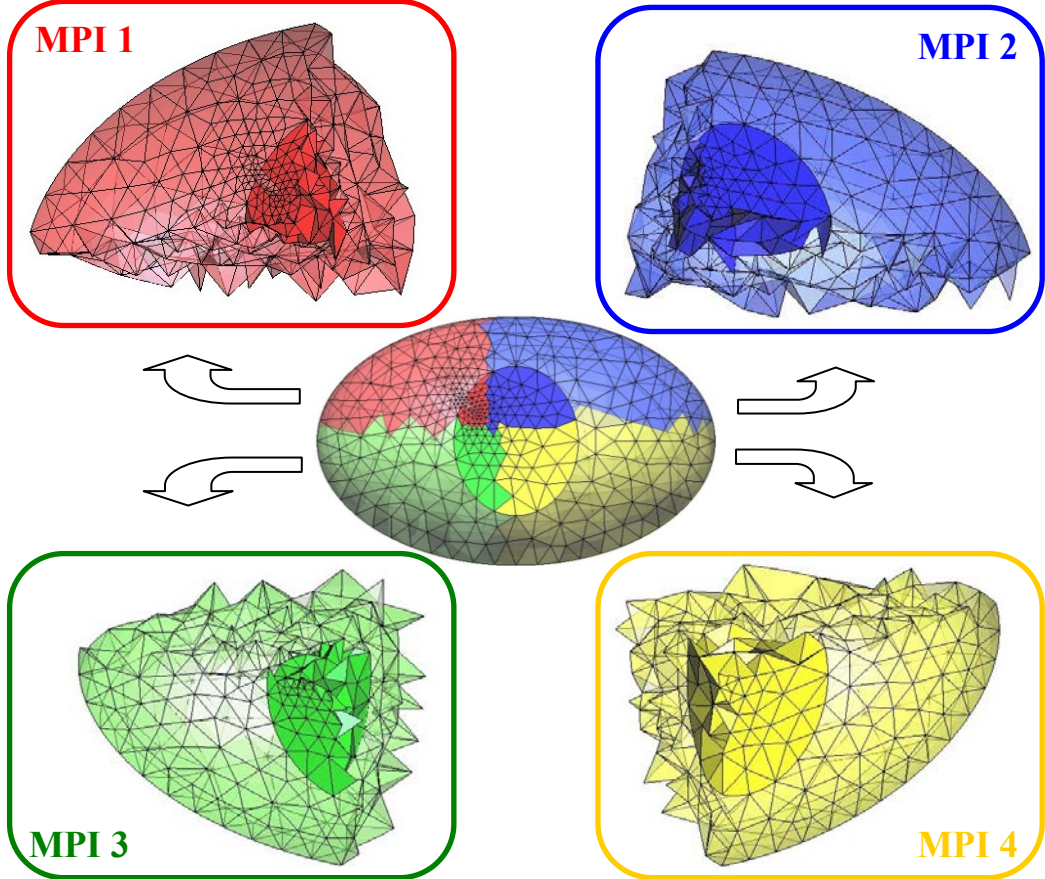
FIGURE A.2: Distribution of the mesh among the MPI processes.

A.3.1   Mesh Distribution.

One of the key advantage of Discontinuous Galerkin methods is its simplicity for the parallelization in memory distributed hardware architecture, making use of the Message Passing Interface (MPI) standard. The mesh is distributed among the M available processes as is depicted in figure A.2. This is the first level of parallelization of the SEMBA solver. Just from the very beginning, in the reading of the mesh, the algorithm is fully parallelized among all MPI processes, obtaining a very high scalability. The required geometrical information for each processes is, obviously, its own geometry, and topological adjacent elements of the neighbor processes. This additional information will be used to computed the flux coming from these adjacent elements to its own computational domain. Obviously, some information will be necessary to be interchanged between neighbor processes in the numerical simulation process.

A.3.2   Selection of the Basis Function.

A h-p refinement heuristic strategy has been developed to choose the size of the mesh, and the order of the basis function in each tetrahedron. The objective is to assure an accuracy level, minimizing the computational cost. The required accuracy could be different across the computational domain, which is an input for the electromagnetic simulation process. The selection of the mesh size has to be made in the mesh generation process, since there are a optimum element size that minimizes computational cost for a required accuracy. The level of accuracy, therefore, defines the optimum element size according to the results shown in sections 4.5 and 4.6. In real meshes, the elements size will vary along the computational domain, and the accuracy is finally adjusted with the selection of the order p. The current implementation of SEMBA uses this 'a priori' approach of the exploitation of h-p refinement techniques mixing different elements sizes (h) and orders (p).

Once the mesh is generated, SEMBA selects element-by-element the order of the basis functions, depending mainly on its size and the required accuracy in the region where the element is located. The aim is to employ higher order basis for bigger tetrahedra, and lower for smaller ones. SEMBA combines gradient spaces of reduced order $p-1$, with rotational spaces of complete order p. The choice is based on similar curves as those appearing in figure 4.9.

It is important to notice that smaller elements need shorter time steps, but if lower orders are used in these elements, the stability condition is relaxed. In the same way, longer time steps can be used in bigger elements combined with higher orders. The combination and mixing different orders of the basis functions depending on element size, makes more homogeneous the time step between all the elements, reducing the number of levels required for the local time stepping algorithm.

This step is carried out in each MPI process, with its own geometry. A graphical example is depicted in figure A.3.

A.3.3   LTS Level Classification.

The local time stepping strategy described in section 4.1.2.2 is implemented in SEMBA. The method requires to classify all the elements, according to its maximum time-step (Δt^m_{max}) for the Leap Frog temporal integration method, in several levels, L. The interfaces between levels shall be identify, since they need a special treatment in the numerical simulation process. In each level l, different time-step will be used in the simulation,
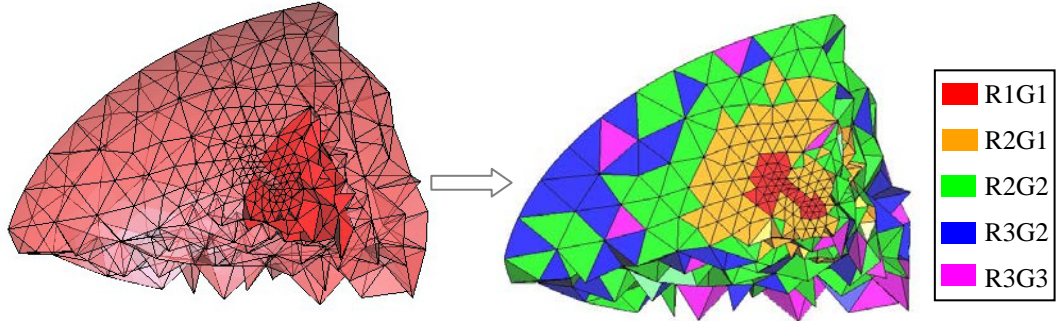
FIGURE A.3: Selection of the expansion function. RxGy stand for x order for the rotational space, y order for the gradient space.
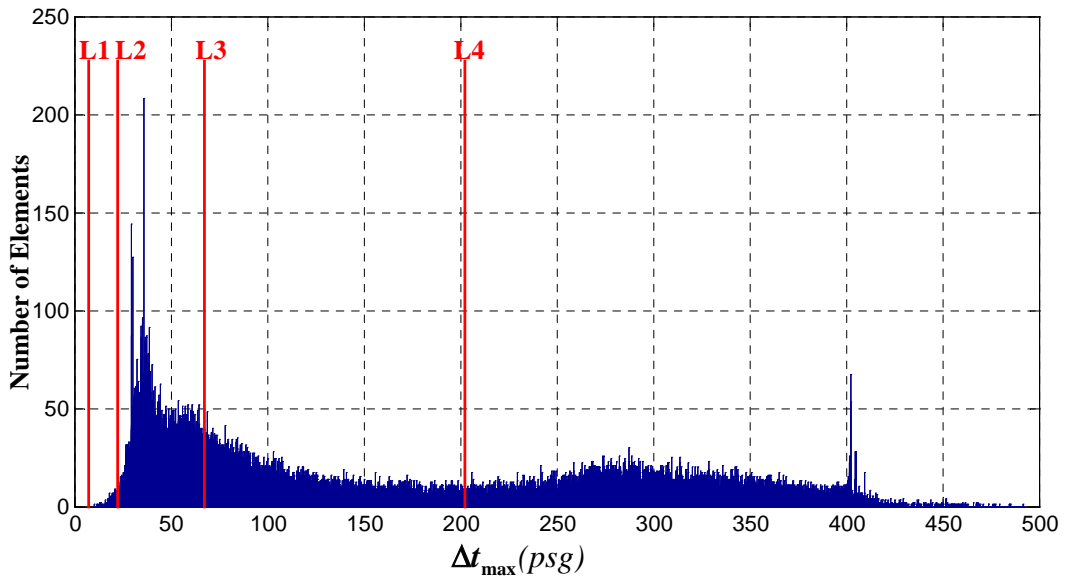

FIGURE A.4: Example of a distribution of Δt_{max}^{m} in a real problem. The choice of Δt_{min} and the time-steps for the different levels ($L = 4$), have been included in the plot. The estimated average time-step has been 88.5 psg, compare to minimum Δt_{max}^{m} (10.5 psg), a gain of about 8 is expected due to the application of LTS.

$3^{(l-1)} \Delta t_1$, being Δt_1 the time-step for the first level. This technique can provide dramatic savings in the CPU-time in real problems, where unstructured meshes contain very small and distorted elements. Figure A.4 shows the distribution of the maximum time-step for all the elements in a real problem. The right choice of Δt_1 is not the minimum Δt_{max}^{m}, this value is tuned to obtain the maximum average time-step.

Finally, let us point out that the proposed LTS strategy requires linear interpolation to find the updated samples in the interfaces between LTS levels. This operation is not exactly an average approximation, and second order accuracy is slightly lost in these zones. This fact has a locally effect in the stability of the scheme. The solution to this
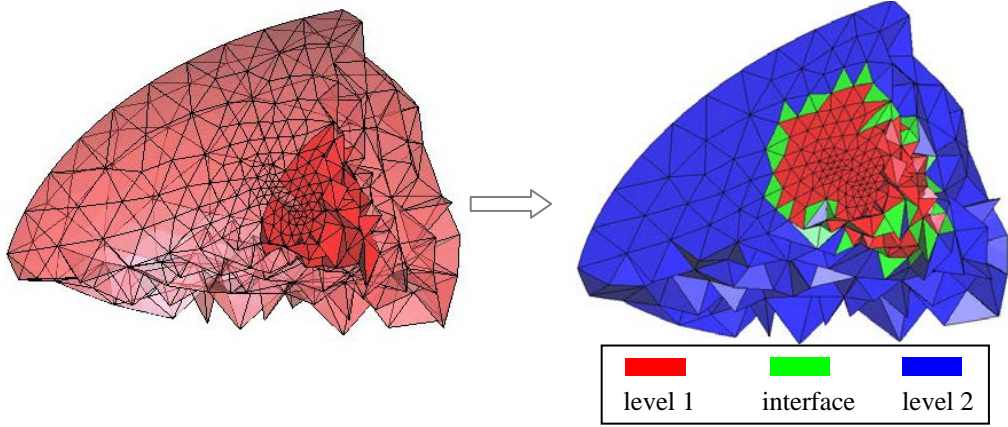
FIGURE A.5: Example of a LTS level classification with $L = 2$.

problem is to penalized the stability condition just for the elements in the interfaces of the LTS levels by a factor (typically 0.8, [63, 94]). This fact introduces some complexity in the right selection of the Δt_1, which is the parameter that fixes the interfaces.

Although, some information, related to the levels assigned to adjacent elements, must be shared between MPI processes, this step can be carried out in each MPI process, with its own geometry. An example with $L = 2$ is shown in figure A.5.

A.4   Numerical Simulation.

Once we have distributed the mesh among the processors, the basis functions in each element has been selected, and the LTS level classification has been established, we can start to prepare the numerical simulation and perform the computation. We following give some details and capabilities of the electromagnetic numerical simulation process.

A.4.1   Materials and Boundary Conditions

Concerning the material modelling capabilities of electromagnetic problems, SEMBA includes the following possibilities:

- Isotropic dielectric and magnetic materials, with the relative electric permittivity (ε_r) and magnetic permeability (μ_r) properties.

- Isotropic lossy electric and magnetic materials, with electric conductivity (σ_e) and magnetic conductivity (σ_m) properties.

- Anisotropic materials. Instead of using the isotropic values, the anisotropic behavior is described with the tensors: $\bar{\bar{\varepsilon}}_r$, $\bar{\bar{\mu}}_r$, $\bar{\bar{\sigma}}_e$ and $\bar{\bar{\sigma}}_m$.

- Perfect electric conductor (PEC) and perfect magnetic conductor (PMC) boundary conditions. This conditions can be used to model geometry, infinite ground planes or symmetric planes.

- Conformal Uniaxial Perfect Match Layer (C-UPML). The conformity of the PML geometry is defined making use of canonical geometries: planes, spheres, cylinders and toroids.

- First-order Impedance Boundary Condition (IBC). This boundary condition can effectively truncate TEM ports as coaxial, avoiding the use of PML. It can also be used to truncate the space, resulting the so-called first-order Silver-Müller absorbing boundary condition.

The treatment of the boundary conditions and material properties are included in the element matrices stored in memory. Following this approach, the time-marching is a very simple algorithm based only on vector-matrices products element-by-element.

A.4.2 Electromagnetic Sources

SEMBA makes use of the flux terms to excite the structures under analysis, following the Huygen's principle. The sources are surface currents distributions which weakly inject the incident fields. This approach can be seen as the traditional incident wave source condition or Total-Field/Scatter-Field technique.

Let us consider that, inside a total-field zone (TFZ), a known wave is propagating, while outside it (scattered-field zone (SFZ)) the field is null. If $\boldsymbol{E}^{inc}$, $\boldsymbol{H}^{inc}$ denote the wave fields at each point of the TFZ/SFZ interface (see figure A.6), the flux across the face of an element m in the TFZ (with this face lying on the TFZ/SFZ interface) needs to consider the equivalent surface currents,

$$\boldsymbol{M}_s = \hat{\mathbf{n}}^m \times \boldsymbol{E}^{inc}$$
$$\boldsymbol{J}_s = -\hat{\mathbf{n}}^m \times \boldsymbol{H}^{inc}$$

and if m is in the scattered field zone

$$\boldsymbol{M}_s = -\hat{\mathbf{n}}^m \times \boldsymbol{E}^{inc}$$
$$\boldsymbol{J}_s = \hat{\mathbf{n}}^m \times \boldsymbol{H}^{inc}$$
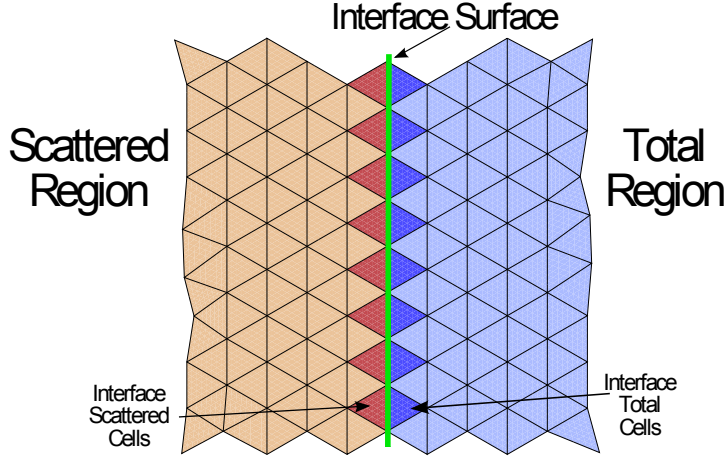
FigURE A.6: Total field/scattered field decomposition. 2-D representation.

This technique can be applied to incorporate any incident field. The different sources implemented in SEMBA are listed bellow:

- Plane wave illumination.

- Coaxial port.

- TE10 rectangular waveguide port.

- Delta-gap port.

A.4.3   General Time-Marching Algorithm

The time-marching algorithm is based on the local time stepping method described in section 4.1.2.2. The different steps are summarized bellow for $L = 2$, completed with the required MPI communications. The algorithm can be easily generalized to any problem with L levels.

- *Step 1.1. MPI Communication of the electric dofs: level 1.*

- *Step 1.2. Update magnetic dofs: level 1, interface and level 2.*

- *Step 2.1. MPI Communication of the electric dofs: level 1, interface and level 2.*

- *Step 2.2. Update electric dofs: level 1 and interface.*

- *Step 3.1. MPI Communication of the electric dofs: level 1 and interface.*

- *Step 3.2. Update magnetic dofs: level 1.*
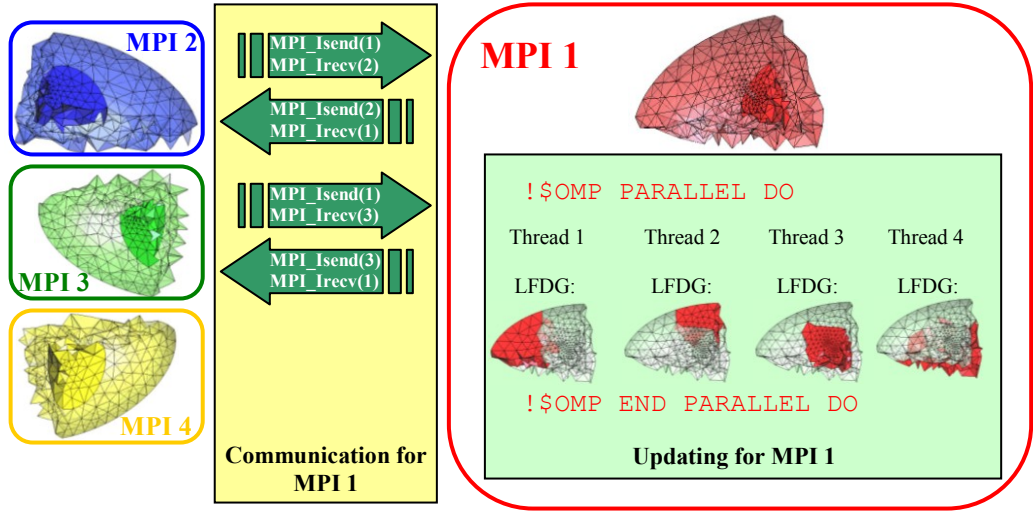
FIGURE A.7: MPI Communication and updating schemes. The communication for the MPI 1 process, takes place between MPI 2 and MPI 3 processes. MPI 1 and MPI 4 are not in contact, so do not require any communication. Inside each MPI processes, different threads update the LFDG algorithm to a group of elements.

- *Step 4.1. MPI Communication of the magnetic dofs: level* 1.

- *Step 4.2. Update electric dofs: level* 1, *interface and level* 2.

- *Step 5.1. MPI Communication of the electric dofs: level* 1, *interface and level* 2.

- *Step 5.2. Update magnetic dofs: level* 1 *and interface.*

- *Step 6.1. MPI Communication of the magnetic dofs: level* 1 *and interface.*

- *Step 6.2. Update electric dofs: level* 1.

Previously to each step of the LTS scheme, a communication (MPI) of the fields (magnetic in case of electric field updating, and *viceversa*), between the adjacent MPI processes, has to be performed. The amount of data to be exchanged will be different for each LTS step (even no data), depending on the required samples, since not all elements are updated in each LTS step. Each updating is computed by N multiple threads (Open MP) having a shared memory parallelization. This point corresponds the second level of parallelization of SEMBA. The Open MP parallelization is made at element level, that means each thread takes care of updating a group of elements. The result is a hybrid MPI/Open MP algorithm. The parallelization strategy, considering both levels, is depicted in figure A.7.

A.5   Postprocessing.

SEMBA implements the following postprocessing capabilities:

- Near-to-far field transformation for radiation patterns and RADAR cross-section (RCS) computation.

- S-parameter computation in ports (coaxial, TE10 rectangular waveguide and Delta gap).

- Impedance computation in ports.

- Current and voltage computation.

- Time domain field probes.

- Frequency domain field probes.

- Surface density fields.

It important to notice that all postprocessing are performed during the simulation stage. The main advantages of doing it in that way are: (i) avoid to save a lot of information in the hard disk and (ii) keeping the parallelization of the algorithm, since none of the process know the whole geometry of the problem, the postprocessing itself is parallelized.

Bibliography

[1] K. S. Yee, "Numerical solution of initial boundary value problems involving maxwells equations in isotropic media," *IEEE Transactions on Antennas and Propagation*, vol. Ap14, no. 3, pp. 302–307, 1966.

[2] P. B. Johns and R. L. Beurle, "Numerical solutions of 2-dimensional scattering problems using a transmission-line matrix," *IEE Proceedings*, vol. 118, no. 9, pp. 1203–1208, 1971.

[3] T. Weiland, "A discretization method for the solution of maxwell's equations for six-component fields," *Archiv fuer Elektronik und Uebertragungstechnik*, vol. 31, no. 3, pp. 116–120, March 1977.

[4] K. K. Mei, "Unimoment method of solving antenna and scattering problems," *IEEE Transactions on Antennas and Propagation*, vol. 22, no. 6, pp. 760–766, November 1974.

[5] Z. J. Cendes, D. N. Shenton, and H. Shahnasser, "Magnetic field computation using delaunay triangulation and complementary finite element methods," *IEEE Transactions on Magnetics*, vol. 19, no. 6, pp. 2551–2554, November 1983.

[6] T. Orikasa, S. Washisu, T. Honma, and I. Fukai, "Finite element method for unbounded field problems and application to two-dimensional taper," *International Journal for Numerical Methods in Engineering*, vol. 19, no. 2, pp. 157–168, February 1983.

[7] S. Salon, "The hybrid finite element-boundary element method in electromagnetics," *IEEE Transactions on Magnetics*, vol. 21, no. 5, pp. 1829–1834, September 1985.

[8] A. Bossavit and J. C. Verite, "A mixed fem-biem method to solve 3-d eddy current problems," *IEEE Transactions on Magnetics*, vol. 18, no. 2, pp. 431–435, March 1982.

[9] D. N. Shenton and Z. J. Cendes, "Three-dimensional finite element mesh generation using delaunay tessellation," *IEEE Transactions on Magnetics*, vol. 21, no. 6, pp. 2535–2538, November 1985.

[10] M. L. Barton and Z. J. Cendes, "New vector finite elements for threedimensional magnetic field computation," *Journal of Applied Physics*, vol. 61, no. 6, pp. 3919–3921, April 1987.

[11] J. F. Lee, R. Lee, and A. Cangellaris, "Time-domain finite-element methods," *IEEE Transactions on Antennas and Propagation*, vol. 45, no. 3, pp. 430–442, March 1997.

[12] D. R. Lynch and K. D. Paulsen, "Time-domain integration of the maxwell equations on finite elements," *IEEE Transactions on Antennas and Propagation*, vol. 38, no. 12, pp. 1933–1942, December 1991.

[13] G. Mur, "The finite-element modeling of three-dimensional time-domain electromagnetic fields in strongly inhomogeneous media," *IEEE Transactions on Magnetics*, vol. 28, no. 2, pp. 1130–1133, March 1992.

[14] J. F. Lee and Z. Sacks, "Whitney elements time domain (wetd) methods," *IEEE Transactions on Magnetics*, vol. 31, no. 3, pp. 1325–1329, May 1995.

[15] J. F. Lee, "Wetd-a finite element time-domain approach for solving maxwell's equations," *IEEE Microwave and Guided Wave Letters*, vol. 4, no. 1, pp. 11–13, January 1994.

[16] S. D. Gedney and U. Navsariwala, "An unconditionally stable finite-element time-domain solution of the vector wave equation," *IEEE Microwave Guided Wave Letters*, vol. 5, no. 10, pp. 332–334, October 1995.

[17] J. M. Jin, M. Zunoubi, K. C. Donepudi, and W. C. Chew, "Frequency-domain and time-domain finite-element solution of maxwell's equations using spectral lanczos decomposition method," *Computation Methods in Applied Mechanics and Engineering*, vol. 169, no. 3–4, pp. 279–296, February 1999.

[18] W. P. C. Jr, L. Pichon, and A. Razek, "A 3d finite element method for the modeling of bounded and unbounded electromagnetic problems in the time domain," *International Journal of Numerical Modelling: Electronic Networks, Devices and Fields*, vol. 13, no. 6, pp. 527–540, 2000.

[19] D. Jiao and J. M. Jin, "A general approach for the stability analysis of the time-domain finite-element method for electromagnetic simulations," *IEEE Transactions on Antennas and Propagation*, vol. 50, no. 11, pp. 1624–1632, November 2002.

[20] ——, "Three-dimensional orthogonal vector basis functions for time-domain finite element solution of vector wave equations," *IEEE Transactions on Antennas and Propagation*, vol. 51, no. 1, pp. 59–65, January 2003.

[21] Z. Lou and J. M. Jin, "Modeling and simulation of broad-band antennas using the time-domain finite element method," *IEEE Transactions on Antennas and Propagation*, vol. 53, no. 12, pp. 4099–4110, December 2005.

[22] R. Wang, H. Wu, A. C. Cangellaris, and J. M. Jin, "Incorporation of a feed network into the time-domain finite-element modeling of antenna arrays," *IEEE Transactions on Antennas and Propagation*, vol. 56, no. 8, pp. 2599–2612, August 2008.

[23] R. N. Rieben, G. H. Rodrigue, and D. A. White, "A high order mixed vector finite element method for solving the time dependent maxwell equations on unstructured grids," *Journal of Computational Physics*, vol. 204, pp. 490–519, 2005.

[24] B. He and F. L. Teixeira, "Sparse and explicit fetd via approximate inverse hodge (mass) matrix," *IEEE Microwave and Wireless Components Letters*, vol. 16, no. 6, pp. 348–350, June 2006.

[25] ——, "Differential forms, galerkin duality, and sparse inverse approximations in finite element solutions of maxwell equations," *IEEE Transactions on Antennas and Propagation*, vol. 55, no. 5, pp. 1359–1368, May 2007.

[26] B. Donderici and F. L. Teixeira, "Conformal perfectly matched layer for the mixed finite element time-domain method," *IEEE Transactions on Antennas and Propagation*, vol. 45, no. 4, pp. 1017–1026, April 2008.

[27] ——, "Mixed finite-element time-domain method for transient maxwell equations in doubly dispersive media," *IEEE Transaction on Microwave Theory and Techniques*, vol. 56, no. 1, pp. 113–120, January 2008.

[28] S. G. Garcia, M. F. Pantoja, C. M. de Jong van Coevorden, A. R. Bretones, and R. G. Martin, "A new hybrid dgtd/fdtd method in 2-d," *IEEE Microwave and Wireless Components Letters*, vol. 18, no. 12, pp. 764–766, December 08.

[29] W. H. Reed and T. R. Hill, "Triangular mesh methods for the neutron transport equation," *Los Alamos Scientific Laboratory*, vol. Technical report LA-UR-73-479, 1973.

[30] P. Lesaint and P. A. Raviart, *On a finite element method for solving the neutron transport equation, in Mathematical Aspects of Finite Elements in Partial Differential Equations*. San Diego: Academic Press, 1974.

[31] C. Johnson and J. Pitkäranta, "An analysis of the discontinuous galerkin method for a scalar hyperbolic equation," *Mathematics of Computation*, vol. 46, no. 173, pp. 1–26, January 1986.

[32] G. R. Richter, "An optimal-order error estimate for the discontinuous galerkin method," *Mathematics of Computation*, vol. 50, no. 181, pp. 75–88, 1988.

[33] T. Peterson, "A note on the convergence of the discontinuous galerkin method for a scalar hyperbolic equation," *SIAM Journal on Numerical Analysis*, vol. 28, no. 1, pp. 133–140, February 1991.

[34] K. S. Bey and J. T. Oden, "hp-version discontinuous galerkin methods for hyperbolic conservation laws," *Computer methods in applied mechanics and engineering*, vol. 133, no. 3–4, pp. 259–286, 1996.

[35] B. Cockburn and C. W. Shu, "Tvb runge-kutta local projection discontinuous galerkin finite element method for conservation laws ii: General framework," *Mathematics of Computation*, vol. 52, pp. 411–435, 1989.

[36] B. Cockburn, S. Hou, and C. W. Shu, "Tvb runge-kutta local projection discontinuous galerkin finite element method for conservation laws iii: One-dimensional systems," *Journal of Computational Physics*, vol. 84, pp. 90–113, 1989.

[37] B. Cockburn, S. Y. Lin, and C. W. Shu, "The runge-kutta local projection discontinuous galerkin finite element method for conservation laws iv: The multidimensional case," *Mathematics of Computation*, vol. 54, pp. 545–581, 1990.

[38] B. Cockburn and C. W. Shu, "The runge-kutta local projection p1-discontinuous galerkin finite element method for scalar conservation laws," *Modélisation Mathématique et Analyse Numérique*, vol. 25, pp. 337–361, 1991.

[39] ——, "The runge-kutta discontinuous galerkin method for conservation laws v: Multidimensional systems," *Journal of Computational Physics*, vol. 141, pp. 199–224, 1998.

[40] F. Bassi and S. Rebay, "A high-order accurate discontinuous finite element method for the numerical solution of the compressible navier-stokes equations," *Journal of Computational Physics*, vol. 131, pp. 267–279, 1997.

[41] B. Cockburn and C. W. Shu, "The local discontinuous galerkin finite element method for convection-diffusion systems," *SIAM Journal on Numerical Analysis*, vol. 35, pp. 2440–2463, 1998.

[42] C. E. Baumann and J. T. Oden, "The local discontinuous galerkin finite element method for convection-diffusion systems," *Computer Methods in Applied Mechanics and Engineering*, vol. 175, no. 3–4, pp. 311–341, July 1999.

[43] R. B. Lowrie, P. L. Roe, and B. V. Leer, "A space-time discontinuous galerkin method for the time-accurate numerical solution of hyperbolic conservation laws," *AIAA Computational Fluid Dynamics Conference, 12th, San Diego, CA; UNITED STATES*, pp. 135–150, June 1995.

[44] R. B. Lowrie, "Compact higher-order numerical methods for hyperbolic conservation laws," Ph.D. dissertation, The University of Michigan, 1996.

[45] F. Q. Hu, M. Y. Hussaini, and J. L. Manthey, "Low dissipation and low dispersion runge-kutta schemes for computational acoustics," *Journal of Computational Physics*, vol. 124, no. 1, pp. 177–191, March 1996.

[46] F. Q. Hu, M. Y. Hussaini, and P. Rasetarinera, "An analysis of the discontinuous galerkin method for wave propagation problems," *Journal of Computational Physics*, vol. 151, no. 2, pp. 921–946, May 1999.

[47] F. Q. Hu and H. L. Atkins, "Eigensolution analysis of the discontinuous galerkin method with nonuniform grids," *Journal of Computational Physics*, vol. 182, no. 2, pp. 516–545, November 1999.

[48] D. A. Kopriva, S. L. Woodruff, L. Stephen, and M. Y. Hussaini, "Computation of electromagnetic scattering with a non-conforming discontinuous spectral element method," *International journal for numerical methods in engineering*, vol. 53, no. 1, pp. 105–122, 2002.

[49] I. Perugia and D. Schötzau, "The hp-local discontinuous galerkin method for low-frequency time-harmonic maxwell equations," *Mathematics of Computation*, vol. 72, no. 243, pp. 1179–1214, July 2003.

[50] P. Houston, I. Perugia, and D. Schötzau, "Mixed discontinuous galerkin approximation of the maxwell operator," *SIAM journal on numerical analysis*, vol. 42, no. 1, pp. 434–459, July 2005.

[51] B. Cockburn, F. Li, and C. W. Shu, "Locally divergence-free discontinuous galerkin methods for the maxwell equations," *Journal of Computational Physics*, vol. 194, pp. 588–610, 2004.

[52] J. S. Hesthaven and T. Warburton, "Nodal high-order methods on unstructured grids - i. time-domain solution of maxwell's equations," *Journal of Computational Physics*, vol. 181, pp. 186–211, 2002.

[53] ——, "High-order nodal discontinuous galerkin methods for the maxwell eigenvalue problem," *Philosophical Transactions: Mathematical, Physical and Engineering Sciences*, vol. 362, no. 1816, pp. 493–524, March 2004.

[54] T. Warburton and M. Embree, "The role of the penalty in the local discontinuous galerkin method for maxwell's eigenvalue problem," *Computer methods in applied mechanics and engineering*, vol. 195, no. 25–28, pp. 3205–3223, July 2006.

[55] M. Ainsworth, "Dispersive and dissipative behaviour of high order discontinuous galerkin finite element methods," *Journal of Computational Physics*, vol. 198, pp. 106–130, 2004.

[56] M. Ainsworth, P. Monk, and W. Muniz, "Dispersive and dissipative properties of discontinuous galerkin finite element methods for the second-order wave equation," *Journal of Scientific Computing*, vol. 27, no. 1–3, pp. 3205–3223, June 2006.

[57] M. J. Grote, A. Schneebeli, and D. Schötzau, "Interior penalty discontinuous galerkin method for maxwell's equations: Energy norm error estimates," *Journal of Computational and Applied Mathematics*, vol. 204, no. 2, pp. 375–386, July 2007.

[58] M. H. Chen, B. Cockburn, and F. Reitich, "High-order RKDG methods for computational electromagnetics," *Journal of Scientific Computing*, vol. 22-23, pp. 205–226, June 2005.

[59] D. Sármány, M. A. Botchev, and J. J. W. van der Vegt, "Dispersion and dissipation error in high-order runge-kutta discontinuous galerkin discretisations of the maxwell equations," *Scientific Computing*, vol. 33, no. 1, pp. 47–74, October 2007.

[60] L. Fezoui, S. Lanteri, S. Lohrengel, and S. Piperno, "Convergence and stability of a discontinuous galerkin time-domain method for the 3d heterogeneous maxwell equations on unstructured meshes," *ESAIM: Mathematical Modelling and Numerical Analysis*, vol. 39, no. 6, pp. 1149–1176, June 2005.

[61] G. Cohen, X. Ferrieres, and S. Pernet, "A spatial high-order hexahedral discontinuous galerkin method to solve maxwell's equations in time domain," *Journal of Computational Physics*, vol. 217, pp. 340–363, 2006.

[62] G. Cohen and M. Duruflé, "Non spurious spectral-like element methods for maxwell's equations," *Journal of Computational Mathematics*, vol. 25, no. 3, pp. 282–304, 2007.

[63] E. Montseny, S. Pernet, X. Ferriéres, and G. Cohen, "Dissipative terms and local time-stepping improvements in a spatial high order discontinuous galerkin scheme

for the time-domain maxwell's equations," *Journal of Computational Physics*, vol. 227, pp. 6795–6820, 2008.

[64] N. Canouet, L. Fezoui, and S. Piperno, "Discontinuous galerkin time-domain solution of maxwell's equations on locally-refined nonconforming cartesian grids," *Compel-the International Journal for Computation and Mathematics in Electrical and Electronic Engineering*, vol. 24, pp. 1381–1401, 2005.

[65] H. Fahs, L. Fezoui, S. Lanteri, and F. Rapetti, "Preliminary investigation of a non-conforming discontinuous galerkin method for solving the time-domain maxwell equations," *IEEE Transactions on Magnetics*, vol. 44, no. 6, pp. 1254–1257, 2008.

[66] H. Fahs, "Development of a hp-like discontinuous galerkin time-domain method on non-conforming simplicial meshes for electromagnetic wave propagation," *Int. J. Numer. Anal. Mod.*, vol. 6, no. 2, pp. 193–216, 2009.

[67] H. Fahs and S. Lanteri, "A high-order non-conforming discontinuous galerkin method for time-domain electromagnetics," *Journal of Computational and Applied Mathematics*, vol. 234, pp. 1088–1096, 2010.

[68] H. Fahs, "Discontinuous galerkin method for time-domain electromagnetic on curvilinear domains," *Applied Mathematical Sciences*, vol. 4, no. 19, pp. 943–958, 2010.

[69] J. S. Hesthaven and T. Warburton, *Nodal Discontinuous Galerkin Methods. Algorithms, Analysis, and Applications.* Springer Science+Business Media, LLC, 233 Spring Street, New York, NY 10013, USA: Springer, 2008.

[70] R. Diehl, K. Busch, and J. Niegemann, "Comparison of low-storage runge-kutta schemes for discontinuous galerkin time-domain simulations of maxwell's equations," *Journal of Computational and Theoretical Nanoscience*, vol. 7, pp. 1–9, 2010.

[71] J. E. Flaherty, R. M. Loy, M. S. Shephard, B. K. Szymanski, J. D. Teresco, and L. H. Ziantz, "Adaptive local refinement with octree load-balancing for the parallel solution of three-dimensional conservation laws," *Journal of Parallel and Distributed Computing*, vol. 47, no. 2, pp. 139–152, 1997.

[72] M. Dumbser, M. Käser, and E. F. Toro, "An arbitrary high order discontinuous galerkin method for elastic waves on unstructured meshes v: Local time stepping and p-adaptivity," *Geophysical Journal International*, vol. 171, no. 23, pp. 695–717, 2007.

[73] A. Taube, M. Dumbser, C. D. Munz, and R. Schneider, "A high-order discontinuous galerkin method with time-accurate local time stepping for the maxwell equations," *International Journal of Numerical Modelling: Electronic Networks, Devices and Fields*, vol. 22, pp. 77–103, 2009.

[74] H. Fahs, "High-order leap-frog based discontinuous galerkin method for the time-domain maxwell equations on non-conforming simplicial meshes," *Numerical Mathematics-Theory Methods and Applications*, vol. 2, no. 3, pp. 275–300, 2009.

[75] A. Catella, V. Dolean, and S. Lanteri, "An unconditionally stable discontinuous galerkin method for solving the 2-D time-domain maxwell equations on unstructured triangular meshes," *IEEE Transactions On Magnetics*, vol. 44, no. 6, pp. 1250–1253, June 2008.

[76] V. Dolean, H. Fahs, L. Fezoui, and S. Lanteri, "Locally implicit discontinuous galerkin method for time domain electromagnetics," *Journal of Computational Physics*, vol. 229, pp. 512–526, 2010.

[77] ——, "Hybrid explicit-implicit time integration for grid-induced stiffness in a dgtd method for time domain electromagnetics," in *Spectral and High Order Methods for Partial Differential Equations*, ser. Lecture Notes in Computational Science and Engineering, J. Hesthaven and E. Rønquist, Eds.   Springer Berlin Heidelberg, 2011, vol. 76, pp. 163–170.

[78] J. M. Sanz-Serna and M. P. Calvo, *Numerical Hamiltonian Problems*.   London, U.K.: Chapman and Hall, 1994.

[79] S. Piperno, "Dgtd methods using modal basis functions and symplectic local time-stepping: Application to wave propagation problems," *Journal of Computational Physics*, vol. 217, pp. 340–363, 2006.

[80] ——, "Symplectic local time-stepping in non-dissipative dgtd methods applied to wave propagation problems," *ESAIM: Mathematical Modelling and Numerical Analysis*, vol. 40, no. 5, pp. 815–841, 2006.

[81] R. W. Davies, K. Morgan, and O. Hassan, "A high order hybrid finite element method applied to the solution of electromagnetic wave scattering problems in the time domain," *Computational Mechanics*, vol. 44, no. 3, pp. 321–331, 2009.

[82] F. Edelvik and G. Ledfelt, "A comparison of time-domain hybrid solvers for complex scattering problems," *International Journal of Numerical Modelling: Electronic Networks, Devices and Fields*, vol. 15, no. 5–6, pp. 475–487, September – December 2002.

[83] V. Shankar, A. H. Mohammadian, and W. F. Hall, "A time-domain finite-volume treatment for the maxwell equations," *Electromagnetics*, vol. 10, no. 1–2, pp. 127–145, 1990.

[84] A. H. Mohammadian, V. Shankar, and W. F. Hall, "Computation of electromagnetic scattering and radiation using a time-domain finite-volume discretization procedure," *Computer Physics Communications*, vol. 68, pp. 175–196, 1991.

[85] A. V. Kabakian, V. Shankar, and W. F. Hall, "Unstructured grid-based discontinuous galerkin method for broadband electromagnetic simulations," *Journal of Scientific Computing*, vol. 20, no. 3, pp. 405–431, June 2004.

[86] T. Xiao and Q. H. Liu, "Three-dimensional unstructured-grid discontinuous galerkin method for maxwell's equations with well-posed perfectly matched layer," *Microwave and Optical Technology Letters*, vol. 46, no. 5, pp. 459–463, September 2005.

[87] S. D. Gedney and J. A. Roden, "The uniaxial perfectly matched layer (upml) truncation of fdtd lattices for generalized media," *URSI Radio Science Meeting , Baltimore MD*, 1996.

[88] F. L. Teixeira and W. C. Chew, "Analytical derivation of a conformal perfectly matched absorber for electromagnetic waves," *Microwave Optical Technology Letters*, vol. 17, no. 4, pp. 231–236, 1998.

[89] ——, "General closed-form pml constitutive tensors to match arbitrary bianisotropic and dispersive linear media," *IEEE Microwave and Guided Wave Letters*, vol. 8, no. 6, pp. 223–225, June 1998.

[90] W. C. Chew and W. H. Weedon, "A 3d perfectly matched medium from modified maxwell's equations with stretched coordinates," *Microwave Optical Tech. Letters*, vol. 7, no. 13, pp. 599–604, 1994.

[91] K. Sankaran, C. Fumeaux, and R. Vahldieck, "Cell-centered finite-volume-based perfectly matched layer for time-domain maxwell system," *IEEE Transaction on Microwave Theory and Techniques*, vol. 54, no. 3, pp. 629–651, March 2006.

[92] ——, "Uniaxial and radial anisotropy models for finite-volume maxwellian absorber," *IEEE Transaction on Microwave Theory and Techniques*, vol. 54, no. 12, pp. 4297–4304, December 2006.

[93] C. Fumeaux, K. Sankaran, and R. Vahldieck, "Spherical perfectly matched absorber for finite-volume 3-d domain truncation," *IEEE Transaction on Microwave Theory and Techniques*, vol. 55, no. 12, pp. 2773–2781, December 2007.

[94] S. Dosopoulos and J. F. Lee, "Interior penalty discontinuous galerkin finite element method for the time-dependent first order maxwell's equations," *IEEE Transactions on Antennas and Propagation*, vol. 58, no. 12, pp. 192–197, December 2010.

[95] T. Lu and P. Z. W. Cai, "Discontinuous galerkin methods for dispersive and lossy maxwell's equations and pml boundary conditions," *Journal of Computational Physics*, vol. 200, no. 2, pp. 549–580, November 2004.

[96] J. Niegemann, M. König, K. Stannigel, and K. Busch, "Higher-order time-domain methods for the analysis of nano-photonic systems," *Photonics and Nanostructures – Fundamentals and Applications*, vol. 7, no. 1, pp. 2–11, February 2009.

[97] S. D. Gedney, C. Luo, J. A. Roden, R. D. Crawford, B. Guernsey, J. A. Miller, T. Kramer, and E. W. Lucas, "The discontinuous galerkin finite-element time-domain method solution of maxwell's equation," *Journal in Applied Computational Electromagnetics Society*, vol. 24, no. 2, pp. 129–142, April 2009.

[98] S. D. Gedney and B. Zhao, "An auxiliary differential equation formulation for the complex-frequency shifted pml," *IEEE Transactions on Antennas and Propagation*, vol. 58, no. 3, pp. 838–847, March 2010.

[99] T. Lu and P. Z. W. Cai, "Discontinuous galerkin time-domain method for gpr simulation in dispersive media," *IEEE Transactions on Geoscience and Remote Sensing*, vol. 43, no. 1, pp. 72–80, January 2005.

[100] K. Stannigel, M. König, J. Niegemann, and K. Busch, "Discontinuous galerkin time-domain computations of metallic nanostructures," *Optics Express*, vol. 17, no. 17, pp. 14 934–14 947, 2009.

[101] M. König, K. Busch, and J. Niegemann, "The discontinuous galerkin time-domain method for maxwell's equations with anisotropic materials," *Photonics and Nanostructures*, vol. 8, no. 4, pp. 303–309, 2010.

[102] L. Pebernet, X. Ferrieres, S. Pernet, B. L. Michielsen, F. Rogier, and P. Degond, "Discontinuous galerkin method applied to electromagnetic compatibility problems: introduction of thin wire and thin resistive material models," *IET Science, Measurement and Technology*, vol. 2, no. 6, pp. 395–401, 2008.

[103] S. Chun and J. Hesthaven, "High-order accurate thin layer approximations for time-domain electromagnetics. part i. general metal backed coatings," *Journal of Computational and Applied Mathematics*, vol. 231, no. 2, pp. 598–611, September 2009.

[104] S. Chun, H. Haddar, and J. S. Hesthaven, "High-order accurate thin layer approximations for time-domain electromagnetics, part ii: Transmission layers," *Journal of Computational and Applied Mathematics*, vol. 234, no. 8, pp. 2587–2608, August 2010.

[105] N. Gödel, T. Warburton, and M. Clemens, "Modeling effects of electromagnetic waves on thin wires with a high-order discontinuous galerkin method," in *Spectral and High Order Methods for Partial Differential Equations*, ser. Lecture Notes in Computational Science and Engineering, E. M. R. J.S. Hesthaven, Ed. Springer Berlin Heidelberg, 2011, vol. 76, pp. 209–218.

[106] S. Dosopoulos and J. F. Lee, "Interconnect and lumped elements modeling in interior penalty discontinuous galerkin time-domain methods," *Journal of Computational Physics*, vol. 229, no. 22, pp. 8521–8536, 2010.

[107] M. Bernacki, L. Fezoui, S. Lanteri, and S. Piperno, "Parallel discontinuous galerkin unstructured mesh solvers for the calculation of three-dimensional wave propagation problems," *Applied Mathematical Modelling*, vol. 30, no. 8, pp. 744–763, August 2006.

[108] M. Bernacki, S. Lanteri, and S. Piperno, "Time-domain parallel simulation of heterogeneous wave propagation on unstructure grids using explicit, non-diffusive, discontinuous galerkin methods," *Journal of Computational Acoustics*, vol. 14, no. 1, pp. 57–81, 2006.

[109] A. Klöckner, T. Warburton, J. Bridge, and J. S. Hesthaven, "Nodal discontinuous galerkin methods on graphics processors," *Journal of Computational Physics*, vol. 228, no. 21, pp. 7863–7882, November 2009.

[110] X. Ji, T. Lu, W. Cai, and P. Zhang, "Discontinuous galerkin time domain (dgtd) methods for the study of 2-d waveguide-coupled microring resonators," *Journal of Lightwave Technology*, vol. 23, no. 11, pp. 3864–3874, November 2005.

[111] C. Chauvière, J. S. Hesthaven, and L. Lurati, "High-order dgtd methods for dispersive maxwell's equations and modelling of silver nanowire coupling," *SIAM Journal on Scientific Computing*, vol. 28, no. 2, pp. 751–775, 2006.

[112] Y. Shi and C. H. Liang, "Simulations of the left-handed medium using discontinuous galerkin method based on the hybrid domains," *Progress In Electromagnetics Research*, vol. 63, pp. 171–191, 2006.

[113] X. Ji, W. Cai, and P. Zhang, "High-order dgtd methods for dispersive maxwell's equations and modelling of silver nanowire coupling," *International Journal for Numerical Methods in Engineering*, vol. 69, no. 2, pp. 308–325, January 2007.

[114] H. Songoro, M. Vogel, and Z. Cendes, "Keeping time with maxwell's equations," *Journal of Computational and Applied Mathematics*, vol. 11, no. 2, pp. 42–49, April 2010.

[115] G. R. Liu and S. S. Quek, *The Finite Element Method. A practical course.* Linacre Haouse, Jordan Hill, Oxford OX2 8DP 200 Wheeler Road, Burlington MA 01803: Elsevier Science, 2003.

[116] O. C. Zienkiewicz and R. L. Taylor, *The Finite Element Method.* London: McGraw-Hill, 1988.

[117] J. E. Akin, *Finite Elements for Analysis and Design.* San Diego: CA: Academic Press, 1994.

[118] P. P. Silvester and R. L. Ferrari, *Finite Elements for Electrical Engineers.* Cambridge: Cambridge University Press, 1990.

[119] D. S. Burnett, *Finite Element Analysis.* Reading: MA: Addison-Wesley, 1987.

[120] GiD, *The personal pre and post processor.* http://www.gidhome.com: International Center for Numerical Methods in Engineering (CIMNE), Barcelona, Spain., 2010.

[121] J. Manges, Y. Xingchao, and Z. Cendes, "Spurious modes in finite-element methods," *IEEE Magazine of Antennas and Propagation*, vol. 37, no. 5, pp. 12–24, October 1995.

[122] A. F. Peterson, *Computational Methods for Electromagnetics.* 445 Hoes Lane, P. O. Box 1331, Piscataway, NJ 08855-1331: IEEE Press, 1998.

[123] A. Bossavit, "A rationale for 'edge-elements' in 3-d fields computations," *IEEE Transactions on Magnetics*, vol. 24, pp. 74–79, 1988.

[124] K. D. Paulsen and D. R. Lynch, "Elimination of vector parasites in finite element maxwell solutions," *IEEE Transactions Microwave Theory and Techniques*, vol. 39, pp. 395–404, 1991.

[125] G. Mur, "The fallacy of edge elements," *IEEE Transactions on Magnetics*, vol. 34, pp. 3244–3247, 1998.

[126] J. C. Nédélec, "Mixed finite elements in r3," *Numerische Mathematik*, vol. 35, pp. 315–341, 1980.

[127] ——, "A new family of mixed finite elements in r3," *Numerische Mathematik*, vol. 50, pp. 57–81, 1986.

[128] J. L. Volakis, A. Chatterjee, and L. Kempel, *Finite element methods for electromagnetics: antennas, microwave circuits and scattering applications.* New York: IEEE Press, 1998.

[129] J. P. Webb, "Edge elements and what they can do for you," *IEEE Transactions on Magnetics*, vol. 29, pp. 1460–1465, 1993.

[130] S. D. Gedney, C. Luo, B. Guernsey, J. A. Roden, R. Crawford, and J. A. Miller, "The discontinuous galerkin finite element time domain method (dgfetd): A high order, globally-explicit method for parallel computation," *2007 IEEE International Symposium on Electromagnetic Compatibility*, pp. 1–3, July 2007.

[131] J. P. Webb and S. McFee, "The use of hierarchal triangles in finite-element analysis of microwave and optical devices," *IEEE Transactions on Magnetics*, vol. 27, no. 5, pp. 4040–4043, September 1991.

[132] J. P. Webb, "Hierarchal vector basis functions of arbitrary order for triangular and tetrahedral finite elements," *IEEE Transactions on Antennas and Propagation*, vol. 47, no. 8, pp. 1244–1253, August 1999.

[133] R. S. Chen, L. Du, Z. Ye, and Y. Yang, "An efficient algorithm for implementing the crank-nicolson scheme in the mixed finite-element time-domain method," *IEEE Transaction on Antennas and Propagation*, vol. 57, no. 10, pp. 3216–3222, October 2009.

[134] P. B. Monk, "A mixed method for approximating maxwell's equations," *SIAM Journal on Numerical Analysis*, vol. 28, no. 6, pp. 1610–1634, December 1991.

[135] J. L. Volakis, K. Sertel, and B. C. Usner, *Frequency Domain Hybrid Finite Element Methods for Electromagnetics.* Morgan & Claypool Publishers, 2006.

[136] S. Wang, R. Lee, and F. L. Teixeira, "Anisotropic-medium pml for vector fetd with modified basis functions," *IEEE Transactions on Antennas and Propagation*, vol. 54, no. 1, pp. 20–27, January 2006.

[137] R. A. Chilton and R. Lee, "The discrete origin of fetd-newmark latetime instability, and a correction scheme," *Journal of Computational Physics*, vol. 224, no. 2, pp. 1293–1306, January 2007.

[138] J. Alvarez, L. D. Angulo, M. F. Pantoja, A. R. Bretones, and S. G. Garcia, "Source and boundary implementation in vector and scalar dgtd," *IEEE Transactions on Antennas and Propagation*, vol. 58, no. 6, pp. 1997–2003, 2010.

[139] J. C. Nédélec, *Acoustic and Electromagnetic Equations.* Berlin, Heidelberg: Springer-Verlag, 2001.

[140] K. Sankaran, "Accurate domain truncation techniques for time-domain conformal methods," Ph.D. dissertation, ETH Zurich, Switzerland, 2007.

[141] J. M. Jin and W. C. Chew, "Combining pml and abc for finite element analysis of scattering problems," *Microwave and Optical Technology Letters*, vol. 12, no. 4, pp. 192–197, July 1996.

[142] Y. Xiao and Y. Lu, "Combining pml and abc for scattering problem," *IEEE Transactions on Magnetics*, vol. 37, no. 5, pp. 3510–3513, September 2001.

[143] R. J. Leveque, *Finite-Volume Methods for Hyperbolic Problems.* Cambridge: Cambridge University Press, 2004.

[144] B. Engquist and A. Majda, "Radiation boundary condition for the numerical simulation of waves," *Mathematics of Computation*, vol. 31, pp. 629–651, 1977.

[145] R. Higdon, "Absorbing boundary conditions for difference approximations to the multi-dimensional wave equation," *Mathematics of Computation*, vol. 47, pp. 437–459, 1986.

[146] ——, "Numerical absorbing boundary conditions for the wave equation," *Mathematics of Computation*, vol. 47, pp. 65–90, 1987.

[147] J. Blaschak and G. Kriegsmann, "A comparative study of absorbing boundary conditions," *Journal Computational Physics*, vol. 77, pp. 109–139, 1988.

[148] J. P. Bérenger, "A perfectly matched layer for the absorption of electromagnetic-waves," *Journal of Computational Physics*, vol. 114, no. 2, pp. 185–200, October 1994.

[149] ——, "Numerical reflection from fdtd-pmls: A comparison of the split pml with the unsplit and cfs pmls," *IEEE Transaction on Antennas and Propagation*, vol. 50, no. 3, pp. 258–265, March 2002.

[150] K. P. Hwang and J. M. Jin, "Application of a hyperbolic grid generation technique to a conformal pml implementation," *IEEE Microwave Guided Wave Letters*, vol. 9, no. 4, pp. 137–139, April 1999.

[151] R. Otin, "Regularized maxwell equations and nodal finite elements for electromagnetic field computations," *Electromagnetics*, vol. 30, pp. 190–204, 2010. [Online]. Available: http://prod.informaworld.com/10.1080/02726340903485489

[152] A. J. Jerri, "The shannon sampling theorem-its various extensions and applications: A tutorial review," *Proceedings of the IEEE*, vol. 65, no. 11, pp. 1565–1596, nov. 1977.

[153] J. H. Williamson, "Low-storage runge-kutta schemes," *Journal Computational Physics*, vol. 35, no. 1, pp. 48–56, March 1980.

[154] M. H. Carpenter and C. A. Kennedy, "Fourth-order 2n-storage runge-kutta schemes," *NASA-TM-109112*, pp. 1–24, 1994.

[155] A. Taflove, *Computational Electrodynamics: The Finite-Difference Time-Domain Method.* Boston: Artech House, 1995.

[156] J. R. Montejo-Garai and J. Zapata, "A high-order non-conforming discontinuous galerkin method for time-domain electromagnetics," *IEEE Transaction on Microwave Theory and Techniques*, vol. 43, no. 6, pp. 1290–1297, June 1995.

[157] F. Alessandri, M. Chiodetti, A. Giugliarelli, D. Maiarelli, G. Martirano, D. Schmitt, L. Vanni, and F. Vitulli, "The electric-field integral-equation method for the analysis and design of a class of rectangular cavity filters loaded by dielectric and metallic cylindrical pucks," *IEEE Transaction on Microwave Theory and Techniques*, vol. 52, no. 8, pp. 1790–1797, August 2004.

[158] A. C. Woo, H. T. G. Wang, M. J. Schuh, and M. L. Sanders, "Benchmark radar targets for the validation of computational electromagnetic programs," *IEEE Antennas and Propagation Magazine*, vol. 35, no. 1, pp. 84–89, February 1993.

[159] M. Taskinen and P. Yla-Oijala, "Current and charge integral equation formulation," *IEEE Transactions on Antennas and Propagation*, vol. 54, no. 1, pp. 58–67, January 2006.

[160] M. Taskinen and P. S. Vanska, "Current and charge integral equation formulations and picard's extended maxwell system," *IEEE Transactions on Antennas and Propagation*, vol. 55, no. 12, pp. 3495–3503, December 2007.

[161] H. S. Consortium. (2008) Hirf se project. [Online]. Available: http://www.hirf-se.eu

[162] S. G. Garcia. (2011) Ugrfdtd em solver. [Online]. Available: http://maxwell.ugr.es/ugrfdtd/

[163] X. Q. Sheng and Z. Peng, "Analysis of scattering by large objects with off-diagonally anisotropic material using finite element-boundary integral-multilevel fast multipole algorithm," *IET Microwaves, Antennas and Propagation*, vol. 4, no. 4, pp. 492–500, April 2010.

List of Publications

Journals Papers

P1 Accuracy Antenas

P2 J. Alvarez, L. D. Angulo, A. R. Bretones, C. M. Jong and S. G. Garcia, "A Discontinuous Galerkin Time-Domain method for the accurate modelling of wideband antennas," *IEEE Transactions on Antennas and Propagation*, vol. (To appear), no. –, pp. –, Month 2013.

P3 J. Alvarez, L. D. Angulo, A. R. Bretones and S. G. Garcia, "A leap-frog discontinuous Galerkin time-domain method for HIRF assessment," *IEEE Transaction on Electromagnetic Compatibility*, vol. (To appear), no. –, pp. –, Month 2013.

P4 H. Lin, M. F. Pantoja, L. D. Angulo, J. Alvarez, R. G. Martina and S. G. Garcia, "FDTD modeling of graphene devices using complex conjugate dispersion material model," *IEEE Microwave and Wireless Components Letters*, vol. (To appear), no. –, pp. –, Month 2012.

P5 J. Alvarez, L. D. Angulo, A. R. Bretones and S. G. Garcia, "3D discontinuous Galerkin time domain method for anisotropic materials," *IEEE Antennas and Wireless Propagation Letters*, vol. (To appear), no. –, pp. –, Month 2012.

P6 J. Alvarez, L. D. Angulo, A. R. Bretones and S. G. Garcia, "A spurious-free Discontinuous Galerkin Time Domain for the accurate modeling of microwave filters," *IEEE Transactions on Microwave Theory and Techniques*, vol. 60, no. 8, pp. 2359–2369, August 2012.

P7 G. G. Gutierrez, S. F. Romero, J. Alvarez, S. G. Garcia, and E. P. Gil, "On the use of FDTD for hirf validation and certification," *Progress In Electromagnetics Research Letters*, vol. 32, pp. 145–156, 2012.

P8 L. D. Angulo, J. Alvarez, S. G. Garcia and A. R. Bretones "Discontinuous Galerkin Time-Domain Method for GPR Simulation of Conducting Objects," *Near Surface Geophysics*, vol. 9, no. 3, pp. 257–263, June 2011.

P9 J. Alvarez, L. D. Angulo, M. A. Fernandez Pantoja, A. R. Bretones and S. G. Garcia, "Source and boundary implementation in vector and scalar DGTD," *IEEE Transactions on Antennas and Propagation*, vol. 58, no. 6, pp. 1997–2003, June 2010.

P10 S. G. Garcia, F. Costen, M. Fernandez Pantoja, L. D. Angulo and J. Alvarez, "Efficient Excitation of Waveguides in Crank-Nicolson FDTD," *Progress In Electromagnetics Research Letters*, vol. 17, pp. 39–46, 2010.

P11 J. Alvarez, I. Gomez-Revuelto, J. M. Alonso, L. E. Garcia-Castillo and M. Salazar-Palma, "Fully Coupled Multi-Hybrid FEM-MoM-PO Method for Scattering and Radiation Problems," *Electromagnetics*, vol. 30, no. 1 & 2, pp. 3–22, January 2010.

Conference Proceedings

P9 J. Alvarez, L. Angulo, M. Bandinelli, H. D. Brüns, M. Francavilla, S. Garcia, R. Guidi, G. Gutierrez, C. Jones, M. Kunze, J. P. Martinaud, I. Munteanu, M. Panitz, J. P. Parmantier, P. Pirinoli, Z. Řezníček, G. Salin, A. Schröder, P. Tobola and F. Vipiana, "HIRF interaction with metallic aircrafts. A comparison between TD and FD methods," *Proc. EMC Europe 2012*, Rome, Italy, September 2012.

P10 G. Gutierrez, S. F. Romero, J. Alvarez, S. G. Garcia and E. Pascual Gil, "Strategies for HIRF Simulations using FDTD," *Proc. EMC Europe 2012*, Rome, Italy, September 2012.

P11 J. Alvarez, L. Angulo, M. Bandinelli, H. D. Brüns, M. Francavilla, S. Garcia, R. Guidi, G. Gutierrez, C. Jones, M. Kunze, J. P. Martinaud, I. Munteanu, M. Panitz, J. P. Parmantier, P. Pirinoli, Z. Řezníček, G. Salin, A. Schröder, P. Tobola and F. Vipiana, "EV55: A numerical workbench to test TD/FD codes in HIRF EMC assessment," *Proc. EUROEM European Electromagnetic 2012*, Toulouse, France, July 2012.

P12 J. Alvarez, E. Pascual Gil and S. G. Garcia, "From Current Methods to Finite Elements for EMC in Aerospace," *New and future Trends in Simulation, NAFEMS Seminar*, Madrid, Spain, October 2011.

P13 J. Alvarez, S. Gonzalez Garcia, L. D. Angulo and A. C. Rubio Bretones, "Computational Electromagnetic Tools for EMC in Aerospace," *PIERS Proceedings*, pp. 1840–1844, Marrakesh, Morocco, March 2011.

P14 L. D. Angulo, J. Alvarez, A. R. Bretones and S. G. Garcia, "Time Domain Tools in EMC Assesment in Aeronautics," *Proc. EMC Europe 2010*, Wroclaw, Poland, September 2010.

P15 J. Alvarez, L. D. Angulo, S. G. Garcia, M. A. Fernandez Pantoja and A. C. Rubio Bretones, "A comparison between centered/upwind nodal/vector basis formulations of DGTD," *Proc. 2010 IEEE AP-S/URSI-USNC International Symposium*, Toronto, Canada, July 2010.

P16 L. D. Angulo, J. Alvarez, S. G. Garcia, M. A. Fernandez Pantoja and A. C. Rubio Bretones, "CDGTD: A new reduced-error method combining FETD and DGTD," *Proc. of 2010 IEEE AP-S/URSI-USNC International Symposium*, Toronto, Canada, July 2010.

P17 J. M. Alonso-Rodriguez, E. Pascual-Gil, and J. Alvarez, "Test Case 1. PLACYL. Test Case 2. Dilectric Cube. Test Case 3. Cylinder with Cavity. Test Case 4. Multilayer Conesphere," *Proc. Workshop EM ISAE Radar Signatures*, Toulouse, France, November 2008.

P18 J. Alvarez, I. Gomez-Revuelto, J. M. Alonso, L. E. Garcia-Castillo and M. Salazar-Palma, "Método Multi-Híbrido FEM-MoM-PO para el Anáisis de Problemas de Dispersión y Radiación," *XXIII Simposium Nacional de la URSI*, Madrid, Spain, September 2008.

P19 J. Alvarez, I. Gomez-Revuelto, L. E. Garcia-Castillo and M. Salazar-Palma, "Fully Coupled Multi-Hybrid FEM-MoM-PO Method for the Analysis of 3D Scattering and Radiation Problems," *9th International Workshop on Finite Elements for Microwave Engineering*, Bonn, Germany, May 2008.

Curriculum Vitae

Personal Data

Name:	Jesus Alvarez
Nationality:	Spanish
Date of birth:	October 21, 1978
E-mail:	jesus@ieee.org

Education

2008 – 2012:	University of Granada, Spain.
	Ph.D. in Physics & Space Science.
	Specialization in Applied Physics.
	Dissertation: XXXXXXXXXXXXXXXXXXXXXX"
	Advisor: Dr. Salvador Gonzalez Garcia
2006 – 2008:	University Carlos III of Madrid, Spain.
	M.Sc. Multimedia & Communications.
	Specialization in Signal Processing.
	Special award of Master Multimedia & Communications.
	Dissertation: "Fully Coupled Multi-Hybrid FEM-MoM-PO Method for the Analysis of 3D Scattering and Radiation Problems"
	Advisor: Dr. Luis Emilio Garcia-Castillo
1996 – 2001:	University of Cantabria, Spain.
	M.Sc. Telecommunications Engineering.
	Specialization in Radiocommunications.
	Dissertation: "Design, Mounting and Characterization of the First 17 GHz Transmitter Prototype of WIND-FLEX System"
	Advisor: Dr. Amparo Herrera Guardado

Professional Experience

2006 – current: Sr. EMC/Antenna Engineer – Cassidian, EADS-CASA, Spain.
Aviation & Aerospace
Involved in the development of state of the art computational electromagnetic (EM) simulation tools (HIRF SE, UGRFDTD, HPTESP-MAT, SEMBA).
Responsible for the definition, development and integration of new technologies (R&T) in the EMC department.
Expert on EM simulation: antennas, HIRF, RCS, lightning and EMC.
Responsible for antenna integration (performance, coupling and installation) in military aircrafts; Eurofighter 2000 and UAVs (ATLANTE, Talarion).
Responsible for controlling and assessing electromagnetic environmental effects (E3) on aerospace systems during design, production, and integration in the programs cited above.

2008 – current: Researcher – University of Granada, Spain.
Scientific Research
Doctor of Philosophy Ph.D. at Electromagnetism Group, University of Granada.
Current research interests include time and frequency domain computational electromagnetics methods: Discontinuous Galerkin Time Domain (DGTD) Method, Finite Difference Time Domain (FDTD), Method of Moments (MoM), fast algorithms for integral equations, and High Performance Computing (HPC).

2009 – current: Part-time Lecturer Master Degree in Aircraft Systems Integration. University Carlos III of Madrid, Spain.
Higher Education
A program oriented to develop competencies and skills for employees working for airframe manufacturers, (Airbus Military, Cassidian and Eurocopter). Involved in and responsible for Antenna integration subject, showing the engineering process for the integration of the complete set of antennas on a complex platform (airframe, ground station, etc.).

2007 – 2009:   Part-Time Lecturer – University Carlos III of Madrid, Spain.
Higher Education
Teaching engineering subjects ("Communications Electronics" and "Systems and Circuits") to under-graduate students (Telecommunication Engineering).

2002 – 2006:   Electrical Engineer – RYMSA, Spain.
Defense & Electronics
Company specialized in design/manufacturing of antennas and electronic systems.
Definition and development of new products, taking active part in the design, prototype and certification/qualification phases. Responsible for the electrical design, test campaigns (electrical, mechanical, environmental and EMC) and industrialization of prototypes.
Planning and management of equipment manufacturing and system integration.
Technical support to the commercial department.
Main projects: SAAR 2000. Surveillance Radar Pedestal System; Satellite Base Stations boarded on High Speed Trains; LPI. RADAR Array Antenna System boarded on Military Ships; Land RADAR Antenna. Reflector Antenna System for Coast Vigilance.

2002 – 2002:   Communications Engineer Internship – X64, Matosinhos, Portugal.
Communications & Electronics
Company specialized in design/manufacturing of wireless terminals.
Analysis and definition of the integration of Bluetooth and IEEE 802.11 protocols in X64 wireless terminals.